Synthesis, structural and physical studies of doubly ordered perovskite NaLnCoWO6 : pursuing new multiferroics based on hybrid improper ferroelectricity

Peng Zuo

To cite this version:

Peng Zuo. Synthesis, structural and physical studies of doubly ordered perovskite NaLnCoWO6 : pursuing new multiferroics based on hybrid improper ferroelectricity. Micro and nanotechnologies/Microelectronics. Université Grenoble Alpes, 2017. English. NNT : 2017GREAI113 . tel-01756965

HAL Id: tel-01756965

https://theses.hal.science/tel-01756965

Submitted on 3 Apr 2018

Communauté
UNIVERSITÉ Grenoble Alpes

THÈSE

Pour obtenir le grade de

DOCTEUR DE LA COMMUNAUTE UNIVERSITE GRENOBLE ALPES

Spécialité : **2MGE : Matériaux, Mécanique, Génie civil, Electrochimie**

Arrêté ministériel : 25 mai 2016

Présentée par

Peng ZUO

Thèse dirigée par **Céline DARIE,** MCF HDR, Université Grenoble Alpes, et codirigée par **Holger KLEIN**, MCF HDR, Université Grenoble Alpes et **Claire COLIN,** MCF HDR, Université Grenoble Alpes

préparée au sein de **l' Institut Néel** CNRS Grenoble
dans **l'École Doctorale IMEP2**

Synthèses, études structurales et physiques de doubles pérovskites ordonnées $NaLnCoWO_6$: recherche de nouveaux composés multiferroïques basés sur la ferroélectricité hybride impropre

Thèse soutenue publiquement le **10 octobre 2017**
devant le jury composé de :

Dr. Catherine BOUGEROL
Directrice de Recherche au CNRS, Institut Néel, Présidente
Prof. Nathalie VIART
Professeur de l'Université de Strasbourg, IPCMS, Rapporteur
Dr. Mauro GEMMI
Coordinateur du Centre de Nanotechnology Innovation, Pisa, Rapporteur
Prof. Philippe GHOSEZ
Directeur du CESAM, Université de Liège, Membre

Contents

Abstract

In this study, new magneto-electric materials were synthesized on the basis of the very recently recognized ferroelectric inducing mechanism, hybrid improper ferroelectricity, and structural and physical properties characterizations were carried out on these new phases.

Two classes of materials were focused on: the Ruddlesden-Popper oxides $NaRMO_4$ (R=Y, La; M= Mn, Cr) and the doubly ordered perovskites $NaLnCoWO_6$ (Ln= Y, La, Pr, Nd, Sm, Eu, Gd, Tb, Dy, Ho, Er, and Yb). Attempts to synthesize the former class failed to give the target phases. All compounds in the latter class were prepared successfully by solid-state reactions at high temperature, among which the compounds $NaLnCoWO_6$ (Ln=La, Pr, Nd) were prepared at ambient pressure while the other nine compounds were synthesized at high pressure.

The structural study of the doubly ordered perovskite family $NaLnCoWO_6$ was performed by synchrotron X-ray powder diffraction (SXRPD) and neutron powder diffraction (NPD). Based on the Rietveld refinement of the SXRPD patterns, the space groups were assigned. $NaLnCoWO_6$ (Ln=La, Pr, Nd) compounds crystallize in the centrosymmetric *C2/m* symmetry, whereas the other nine new compounds crystallize in the polar space group $P2_1$. Second harmonic generation measurements on powder confirmed the non-centrosymmetric structure of the new compounds. Symmetry mode analysis demonstrates that the amplitude of the induced polar mode increases with a decreasing Ln cation size. The amplitude of the polarization was estimated from the refined structures, and can be as large as ~$20\mu C/cm^2$.

A structural phase transition was observed by NPD in $NaLaCoWO_6$ with a large temperature hysteresis of ~150K. In addition, stripes were observed on the high-resolution transmission electron microscopy (TEM) images in the high temperature phase. The periodicity of this superstructure is $12a_p$ along either the $[100]_p$ or $[010]_p$ direction. Further investigations by scanning TEM and electron energy loss spectroscopy revealed that the contrast of the stripes is due to a structural modulation rather than a compositional variation. Octahedral tilt twinning models were built with different tilting schemes to fit the observed SXRPD and NPD patterns. The tilting scheme $a^-a^-c^0$ describes successfully the data. The low temperature phase was unambiguously determined to possess the polar space group $P2_1$.

Magnetic and electric properties were experimentally characterized. All $NaLnCoWO_6$ compounds order antiferromagnetically below T_N which is between 4 and 13K. Curie-Weill fits were performed for all compounds, yielding reasonable effective magnetic moments compared to the theoretical ones. Weiss temperatures were all determined to be negative further indicating that antiferromagnetic interactions are dominant in these systems. Magnetic structures were determined for four $NaLnCoWO_6$ (Ln= Y, La, Tb, and Ho) compounds, of which two have non-magnetic Ln cations (Y and La) and two have magnetic ones (Tb and Ho). Magneto-dielectric coupling was experimentally observed in compounds $NaLnCoWO_6$ (Ln=Y, Tb, Ho) by dielectric measurements as a function of temperature and magnetic field. Polarization was derived for the Y and Ho compounds from pyroelectric current measurement, however, only the $NaYCoWO_6$ compound demonstrates a polar behavior which cannot be switched. This is the first evidence that electric polarization can be induced by the magnetic ordering in the $AA'BB'O_6$ class materials.

Acknowledgement

This work was mainly done in Institute NEEL, Grenoble, France, covering synthesis, structural and physical characterizations and taking three years. Indeed, this project gives me a comprehensive training on solid state materials research, with deeper knowledge, skillful technical practice, and presenting as well as writing exercises. Learning so many from this project, I would thank my three supervisors of my PhD study, Dr. Céline DARIE, Dr. Holger KLEIN and Dr. Claire V. COLIN. Your abundant research experience, critical thinking, and rigorous attitude towards scientific research are so impressive to me and influenced me. Whenever I met any problems, you are always ready to give timely advices to me and help me enthusiastically. Thank you all!

Moreover, I also want to acknowledgement my colleagues in Institute NEEL for providing me technical help during the measurements. Thank Murielle Legendre and Céline Goujon, for your helpful support on synthesis; thank Olivier Leynaud for your help on lab X-ray diffraction; thank Sébastien Paris for always keeping SEM healthy; thank Philippe Plaindoux for help on thermal characterizations; thank Géraldine Dantelle and Corinne Felix for your support on SHG measurements; thank Pierre Bordet for your fruitful discussions on Rietveld refinement; thank Eric Eyraud and Didier Dufeu for your help on magnetization measurements; thank Pierre Lachkar for support on heat capacity measurements; thank Frederic Gay for your help on electric measurements.

Those external colleagues should not be forgotten! I would acknowledge the neutron source Institut Laue-Langevin for allocating us beam-time on the beamlines D2B and D1B, and the technical support from Emmanuelle Suard, Vivian Nassif, and Sofien Djellit. The synchrotron source SOLEIL is also acknowledged for providing us beam-time on the beamline CRISTAL, and thank the technical support from Erik Elkaim. I also want to thank the French network METSA for providing us beam-time on STEM and the technical support on all STEM experiments from Hanako Okuno at MINATEC, Grenoble.

Finally, I want to save some space for my family. Thank you, all of my loved ones, for your long term support, care and love!

Chapter 1: Introduction

1.1 Multiferroic Materials

Originally multiferroic materials were defined as materials showing more than one ferroic property, namely ferroeletricity, ferromagnetism and ferroelasticity, combined in the same phase (see Figure 1.1).[1] Nowadays, the term “multiferroics” represents the materials combining ferroelectricity with any kind of magnetic order.[2] In some particular case, for instance spin driver multiferroics, electric and magnetic properties may be coupled. In realization of magneto-electric (ME) coupling in a single phase, the magnetic properties can be controlled by the electric field, or vice versa. Materials presenting this coupling are attracting intense research efforts for their fundamental physics as well as technological applications. In order to meet the ever increasing demand in storage capability of memory devices, multiferroics can be employed in the four-state memory.[3] Magneto-electric multiferroics can also lead to energy-efficient devices with electric field writing and magnetic field reading.[4]

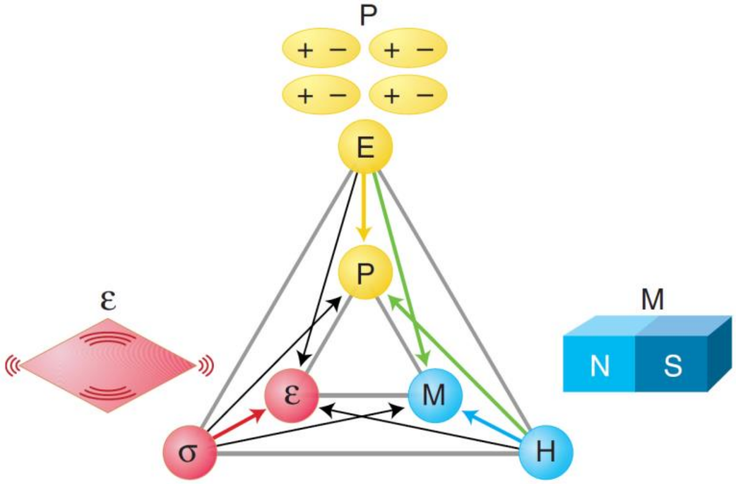

Figure 1.1 Ferroic properties related to multiferroics: ferroelectricity (P), ferroelasticity (ε) and (anti)ferromagnetism (M). In a ferroic material, one ferroic property is spontaneously formed. While multiferroic materials combine at least two of these ferroic orderings, e.g the ferroelectric and (anti)ferromagnetic orderings are combined in magneto-electric multiferroics. [5]

In known multiferroic materials, the origin of the various magnetic orders is based on the same principle: the unpaired electrons present in the partially filled *d* or *f* orbitals of the transition metal atoms or the rare earth atoms. In contrast, there are various mechanisms for the generation of ferroelectricity. According to Khomskii[6], the known multiferroics can be classified into two categories: Type I and Type II.

Type I: **Ferroelectricity and magnetism have different origins**. The polarization in conventional perovskite ferroelectrics is generated from the displacements of transition metal ions with an empty d shell, the electric dipoles arise from the off-center position of the transition metal ions. In contrary, the generation of magnetism needs unpaired electrons in the partially filled d shell of transition metal ions. This is the well-known “d^0 vs d^n problem”.[7] As a result, the approach to achieve multiferroic materials is to obtain a ferroic ordering from different ions individually. Alternative mechanisms of generating spontaneous polarization are due to lone electron pairs (e. g. $BiFeO_3$[8]), charge ordering (e. g. $TbMn_2O_5$[9]) or the “geometric” mechanism ($YMnO_3$[10]). A schematic view of these mechanisms is demonstrated in Figure 1.2. In general, type I materials are rather good ferroelectrics with a large spontaneous polarization and a high ordering temperature. Magnetic ordering appears at a distinct temperature; therefore the coupling between the ferroelectric and magnetic ordering is fairly weak.

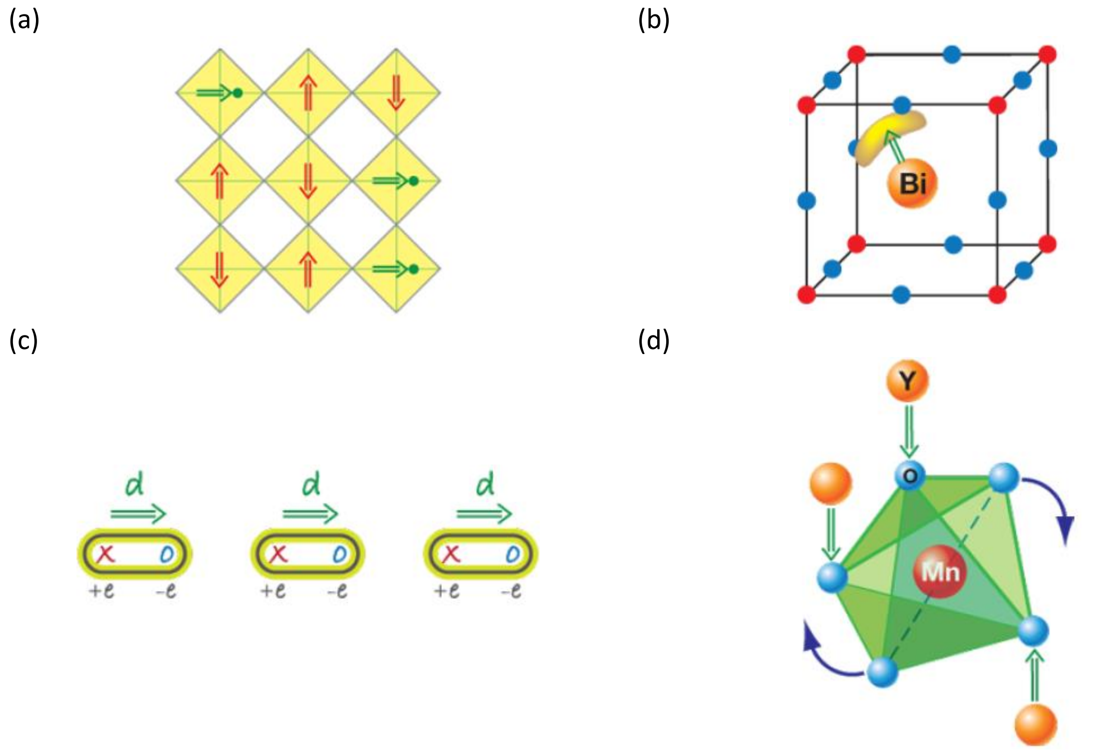

Figure 1.2 Different origins of ferroelectricity in the Type I multiferroics.[6] (a) in perovskites, a d^0 ion (green circles) responsible for ferroelectricity and a d^n ion (red) responsible for magnetism are mixed in the same phase, off-center shifts of the d^0 ions in the oxygen octahedra (yellow plaquettes) result in the polarization and the magnetic ordering is represented by red arrows; (b) $BiFeO_3$ is an example of ferroelectricity generation which is due to lone electron pairs (yellow "lobes") of Bi^{3+}; (c) the mechanism of ferroelectricity arising from the charge ordering, which is due to inequivalent sites with different charges and inequivalent bonds; (d) the "geometric" mechanism of the polarization generation is demonstrated in $YMnO_3$[10], the tilting of the rigid MnO_5 body results in the simultaneous appearance of the two "up" dipoles (green arrows) and one "down" dipole (green arrow), so that a net polarization exists.

Type II: **Multiferroics of spin origin**. In this class of multiferroics, ferroelectricity is induced by the magnetic ordering. There are two types of Type II multiferroics according to the magnetic structures which induce the ferroelectricity. In the first group, the ferroelectricity arises from a spiraling magnetic structure, mainly the cycloid type as explained in Figure 1.3. Examples of the first group are $TbMnO_3$[11] , and $MnWO_4$[12]. In these compounds, spin-orbit coupling is generated through an anisotropic exchange interaction (for instance Dzyaloshinskii-Moriya effect). Because the exchange interaction invocated is weak, the induced polarization is very small in comparison to classical ferroelectrics. However the ME coupling is large because the direction of the polarization is linked to the direction of the spins. In the other group of Type II multiferroics, the ferroelectricity results from a collinear magnetic structure type "up-up-down-down". The ferroelectricity in this case comes from the exchange striction where magnetic coupling varies from parallel and anti-parallel spin configurations. Ca_3CoMnO_6[13] is a good representative of this type multiferroics which is illustrated in Figure 1.4. In this case the polarization generated is larger but the ME coupling is weaker because the direction of the polarization is linked to the crystal symmetry and not to the spins.

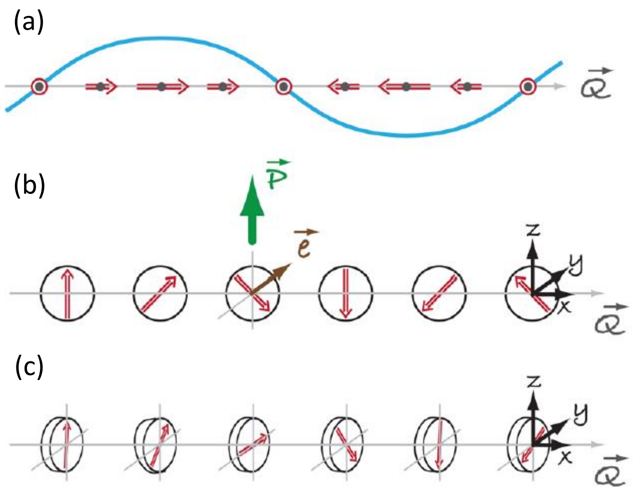

Figure 1.3 Magnetic structures of the Type II multiferroics where the ferroelectricity is generated from the spiraling magnetic structures.[6] (a) the state of sinusoidal spin density wave, where magnetic moments point along one direction but different in magnitude, this structure is centrosymmetric so that no polarization is generated; (b) the cycloidal spiraling magnetic structure where spins rotate in the **x**-**z** plane, consequently the polarization along the **z**-axis exists; (c) the so-called "proper screw" where the spins rotate in a plane perpendicular to **Q**, the inversion symmetry is broken and the polarization might exist.[14]

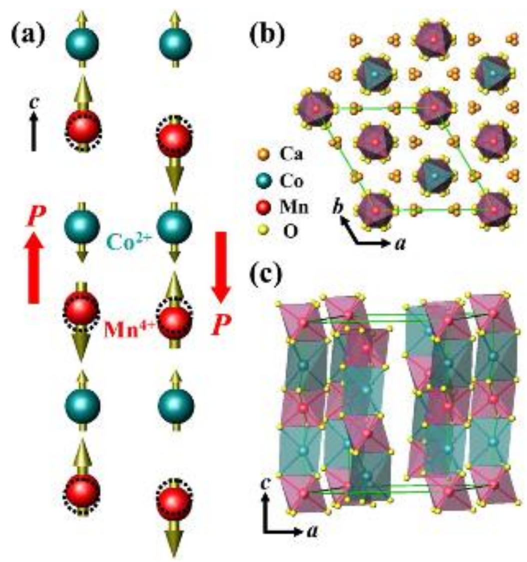

Figure 1.4 (a) the mechanism of ferroelectricity generated through symmetric exchange striction in Ca_3CoMnO_6, the spins order in the up-up-down-down sequence while the Co^{2+} and Mn^{4+} ions order alternatively, which induces the electric polarization. The opposite electric directions generated from two possible magnetic configurations and the undistorted atomic positions in dashed circles are presented. (b) and (c) show the structure of the Ca_3CoMnO_6 chain magnet.[13]

From the discussion above, it is clear that either of the two types of known multiferroics has its own drawbacks. New materials with optimized properties useful for real applications are still to be found and are subject of active research.

1.2 Hybrid Improper Ferroelectricity (HIF)

For the sake of new multiferroic materials, a new mechanism combining ferroelectricity and (anti)ferromagnetism from the same lattice instability is desired.[15] A pioneering effort in this direction was demonstrated by Bousquet *et al.*[16], where the improper ferroelectric polarization was generated in the artificial superlattice $PbTiO_3$/$SrTiO_3$ due to the coupling of two rotational modes of oxygen octahedra. At the bulk level of $PbTiO_3$, a zone-boundary distortion involving tilts of oxygen octahedra is suppressed except at the surface where both a polar distortion and oxygen octahedral tilting can coexist.[17][18] In contrary, for bulk $SrTiO_3$ oxygen rotations result in a nonpolar antiferrodistortion and ferroelectrity is suppressed,[19] however, both distortions can coexist in the presence of pressure[19] or epitaxial strains.[20][21][22] Different volume fraction ratios between $PbTiO_3$ and $SrTiO_3$ were studied by Bousquet *et al.*, who found that the improper ferroelectricity arises from the coupling of two oxygen rotational modes and that it is essentially an interface effect. Figure 1.5 shows the $PbTiO_3$/$SrTiO_3$ superlattice with the constitution ratio of 1:1 grown on a [001] $SrTiO_3$ substrate, and three energy lowering symmetry modes condensed in the superlattice from the prototype *P4/mmm* unit cell.[16] The mode Γ^-_3 shown in Figure 1.5 (a) represents the polar mode where atoms move along the **z**-axis and out-of-plane. Figure 1.5 (b) and (c) correspond to the other two symmetry modes, both of which contain oxygen rotations. In both cases, the oxygens rotate around the **z**-axis, where the M^-_4 mode is out-of-phase while the M^+_2 mode is in-phase. Each mode of the latter two individually only results in a nonpolar symmetry, it is the combination of both that gives rise to a spontaneous polarization. Meanwhile, the energy is lowered more by the combination of the two nonpolar rotational modes than either of them individually.[23]

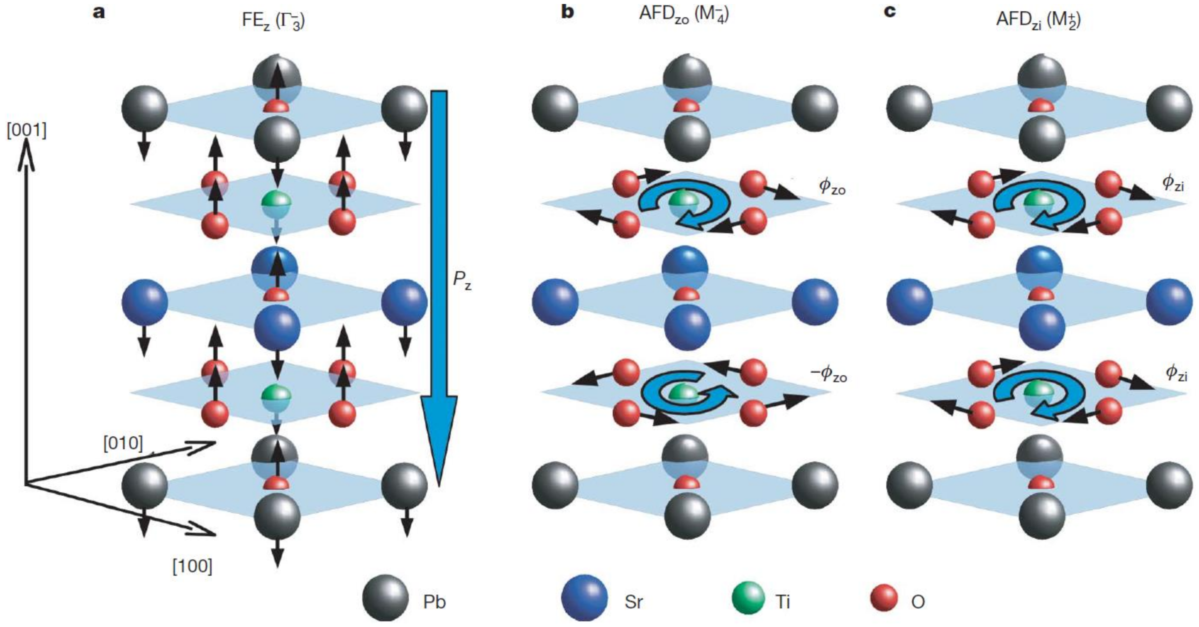

Figure 1.5 The three symmetry modes in the $PbTiO_3/SrTiO_3$ 1:1 superlattice related to the prototype *P4/mmm* unit cell. (a) FE_z (Γ^-_3 mode) which results in the polarization; (b) AFD_{zo} (M^-_4 mode) represents the out-of-phase oxygen atoms rotation around the **z**-axis by an angle ϕ_{zo}; (c) AFD_{zi} (M^+_2 mode) is the in-phase oxygen atoms rotation round the **z**-axis by an angle ϕ_{zi}.[16]

This discovery opened a distinct routine to generate ferroelectricity by the coupling of oxygen rotational modes. In addition, oxygen octahedral rotations have a profound effect on spin interactions in perovskites and related materials.[23] As a result, this mechanism is potentially promising to realize a strong coupling in multiferroics at room temperature.

Soon after this study, a term "Hybrid Improper Ferroelectricity (HIF)" was given to describe the phenomenon where two nonpolar rotational modes induce ferroelectricity.[15] The Ruddlesden-Popper compound $Ca_3Mn_2O_7$ was investigated by first-principles calculations in the study by Benedek *et al.*[15]. The polar ground state of $Ca_3Mn_2O_7$ was attributed to the symmetry reduction from the prototype *I4/mmm* to the polar *A2₁am* structure. Group theory reveals that three symmetry modes are involved in this symmetry reduction: a polar zone-center mode Γ^-_5, an oxygen rotational mode X^+_2 and an oxygen octahedral tilting mode X^-_3. The combination of the distortion modes X^+_2 and X^-_3 results in the formation of the polar mode, as the polarization has a non-zero value only in the presence of the coupling of the two former modes. The improper coupling can be described by a trilinear term in the free energy:

$$F = \alpha P Q(X^+_2) Q(X^-_3) \qquad \text{Equation (1.1)}$$

Where ***F*** is the free energy, ***α*** is the coupling coefficient, ***P*** is the spontaneous polarization, $Q(X^+_2)$ and $Q(X^-_3)$ are the amplitudes of the distortion modes X^+_2 and X^-_3, respectively. A schematic view of the structure of $Ca_3Mn_2O_7$ is shown in Figure 1.6. The magnetic structure of $Ca_3Mn_2O_7$ in the ground state was calculated to be G-type antiferromagnetic in the same study. Spins point along the **z**-axis with a net canted moment along the **x**-axis.

Since octahedral rotations are closely affected by the magnetic ordering in perovskites and related materials, the HIF mechanism is a promising candidate in the tool box to achieve a strong ME coupling with a large polarization at high temperature.

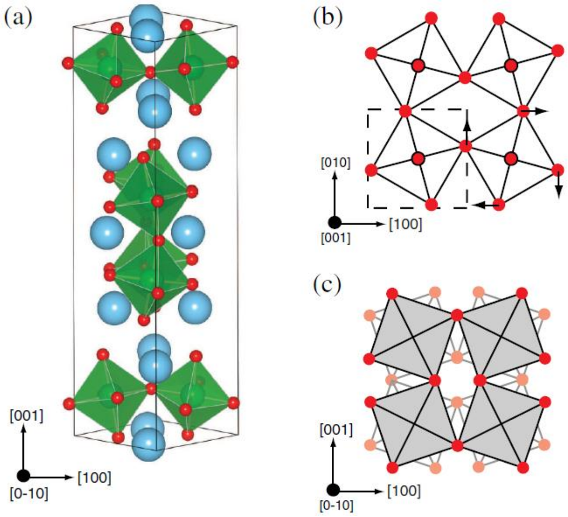

Figure 1.6 The distorted structure of $Ca_3Mn_2O_7$. (a) the polar *$A2_1am$* structure of $Ca_3Mn_2O_7$, the blue spheres represent Ca ions, small red spheres represent O atoms, and Mn ions in green sit inside the oxygen octahedra; (b) the rotational mode X^+_2, the dashed square denotes the parent *P4/mmm* unit cell; (c) the tilt mode X^-_3. The coordinate system of the parent I4/mmm structure was referred to all axes.[15]

Inspired by the observations from compounds possessing HIF, further effort was made on understanding a more general rule to design materials with such properties in terms of structure and chemistry. Perovskites and related materials are the focused candidates as HIF has been proven to occur in these materials in the pioneering work and these materials have the flexibility to tune their physical properties by cation substitution.

Perovskites

Taking the group-theoretical analysis and the crystal chemistry into account, Rondinelli and Fennie [24] concluded that HIF could be induced in layered perovskites constructed from two different *Pnma* building blocks (ABO_3 and $A'B'O_3$). Surprisingly, the space group *Pnma* is nonpolar as established by two octahedral rotations shown in Figure 1.7. Figure 1.7 (a) shows the in-phase octahedral rotation mode M^+_3 around the **z**-axis and (b) shows the out-of-phase octahedral rotation mode R^+_4 around both the **x** and **y**-axes with displacements of the *A*-site.[23] The space group *Pnma* has the most common rotational modes observed in perovskites ABO_3, making it promising for synthesizing many new ferroelectrics with HIF in this strategy. Another appealing aspect is that the *A*-site cations have the possibility to displace in an anti-polar manner between neighboring *A*-site layers in *Pnma* perovskites as shown in Figure 1.7 (c). Even though the overall polarization of this structure is zero, the ferroelectric polarization is established within a certain *AO* layer. It is natural to realize that a spontaneous polarization would arise from a non-cancellation of polarizations between neighboring *AO* layers.

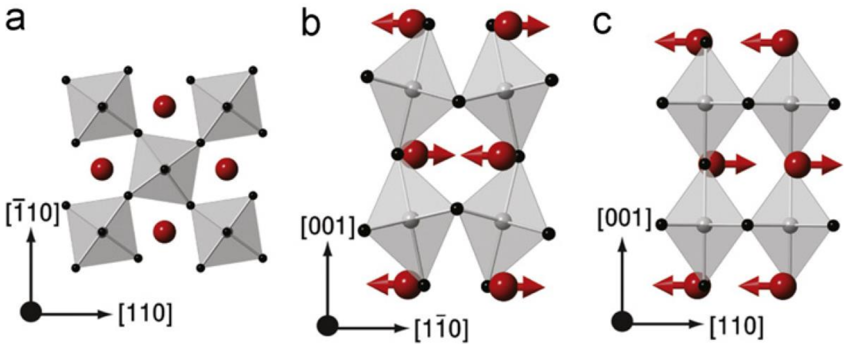

Figure 1.7 The symmetry modes in the *Pnma* structure: (a) the mode M^+_3 corresponds to the in-phase octahedral rotations around the **z**-axis; (b) the mode R^+_4 corresponds to the out-of-phase octahedral rotations around the **x**- and **y**-axes together with the displacement of the *A*-site cations; (c) anti-polar displacement of the *A*-site cations without any rotation.[23]

For the sake of creating a net polarization, the symmetry aspect should be investigated first.

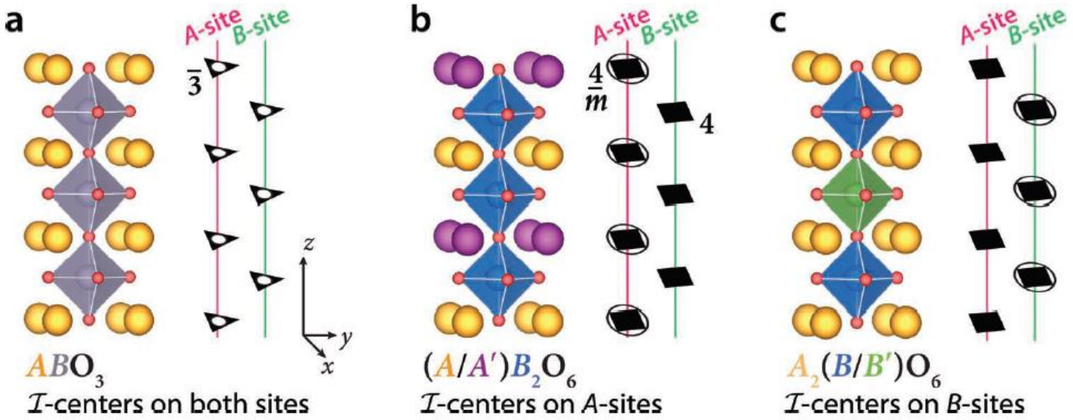

Figure 1.8 The Chemical Criterion for rotational-induced ferroelectricity in layered perovskites constructed from two different ABO_3 perovskites. (a) in the ideal perovskite with the space group *Pm-3m*, inversion centers (*I*) lie on both the *A* and *B* sites, and the three-fold rotoinversion symmetry element is the highest site-symmetry operator. (b) in the presence of *A/A′* layering in the ideal perovskite by substitution of the A site cations, the inversion center on the *B* site is lifted; and (c) in the presence of *B/B′* layering in the ideal perovskite by substitution of the *B* site cations, the inversion center on the *A* site is lifted. [24]

As shown in Figure 1.8 (a), both the *A*- and *B*-sites sit on an inversion center and three mirror symmetry elements are perpendicular to the coordinate axes. If the octahedral rotation modes M^+_3 and R^+_4 are applied to the ideal perovskite, the inversion centers at the *B*-site are still preserved while the mirror symmetry is broken. The net displacement of the *A*-site cations is attributed to the broken mirror symmetry.[23] In order to get a net polarization from the *AO* layers, it is necessary to lift the inversion centers at the *B*-site, or in other words, to have inequivalent *A*-sites between neighboring *AO* layers. As shown in Figure 1.8 (b), the inversion centers at the *B*-site are lifted in the structure with alternating *AO/AO′* layers. While substituting the *B*-site cation by another *B′* cation as shown in Figure 1.8 (c) preserves the inversion centers at the *B*-site. As a result, a certain cation ordering, e.g. the layered *A/A′* ordering, is required for the octahedral rotation induced ferroelectricity defined by Rondinelli and. Fennie.[24] This requirement is called the Chemical Criterion. However, the Chemical Criterion alone is not sufficient. The Energetic Criterion, the other rule, has to be satisfied also. This means that the ground state of both building blocks ABO_3 and $A'BO_3$ must each contain the corresponding octahedral rotations and the 1/1 $ABO_3/A'BO_3$ superlattice is desired.[24] For instance, first-principle techniques were employed to test these design rules, the combination of $LaGaO_3$/$YGaO_3$ was demonstrated to have a strong HIF from the octahedral rotations. Either of the building blocks, $LaGaO_3$ or $YGaO_3$, has a ground state symmetry *Pnma* exhibiting the tilt pattern $a^-a^-c^+$ individually. The symmetry of the superlattice was driven to *Pmc2₁* by rotations with a tilt pattern $a^-a^-c^+$ as well.[23] Just as pointed out above, the La and Y cations displace in the LaO and YO layers in an anti-polar way. Since the La/Y layered ordering removed the inversion centers at the B-site, the polarization induced by the cation displacement between neighboring layers cannot be cancelled totally, giving rise to a net polarization as shown in Figure 1.9. If there is only one constituent possessing the appropriate rotations, it could be possible to induce the same rotation pattern in the second constituent,[25] however, the induced polarization would be much smaller.[24] A net energy gain to the polar structure from the coexistence of octahedral rotations is also a necessary condition for HIF.[24]

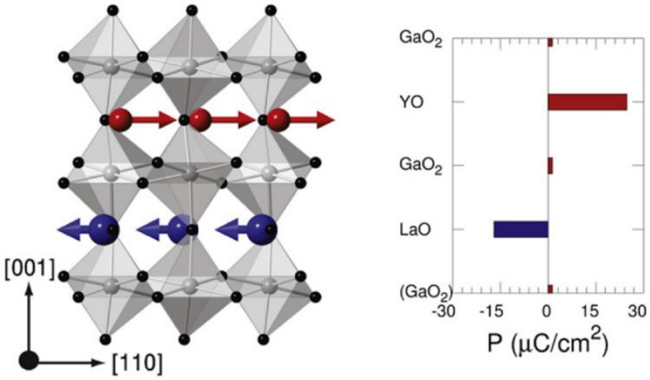

Figure 1.9 The superlattice constructed by $LaGaO_3$/$YGaO_3$, a net polarization is generated from two nonpolar octahedral rotations and the anti-polar displacement of layered A-site cations. Since the A-sites are inequivalent, the polarizations induced by cation displacement in alternating layers cannot be cancelled exactly, giving rise to a net polarization.[23][24]

Recently, a more comprehensive study on how to generate polar perovskites was carried out by Young *et al.*.[26][27] Three key factors were defined to be crucial to lift the inversion centers: distortions, cation ordering and chemical considerations. Consistent with a previous study, 15 distinct combinations of octahedral rotations were investigated and it was concluded that the inversion centers at the *A*-site can only be lifted by the out-of-phase rotations. In order to further lift the inversion centers at the B-site, a systematic study by combining the 15 distinct rotation patterns with various cation ordering schemes was performed as shown in Figure 1.10. These rotation patterns are described by the Glazer's notation[28], where the characters *a*, *b*, and *c* represent the coordinate axes corresponding to [100], [010] and [001], respectively, and the symbols +, - and 0 stand for in-phase tilting, out-of-phase tilting or no tilting along one axis successively. Each intersection in the tables was divided into four smaller parts, each of them corresponds to a centrosymmetric (CS), polar (P), enantiomorphic (E) and second harmonic (SH) crystal class, respectively. As illustrated in the upper right corner, the number in each smaller part represents how many unique space groups are produced by this combination.

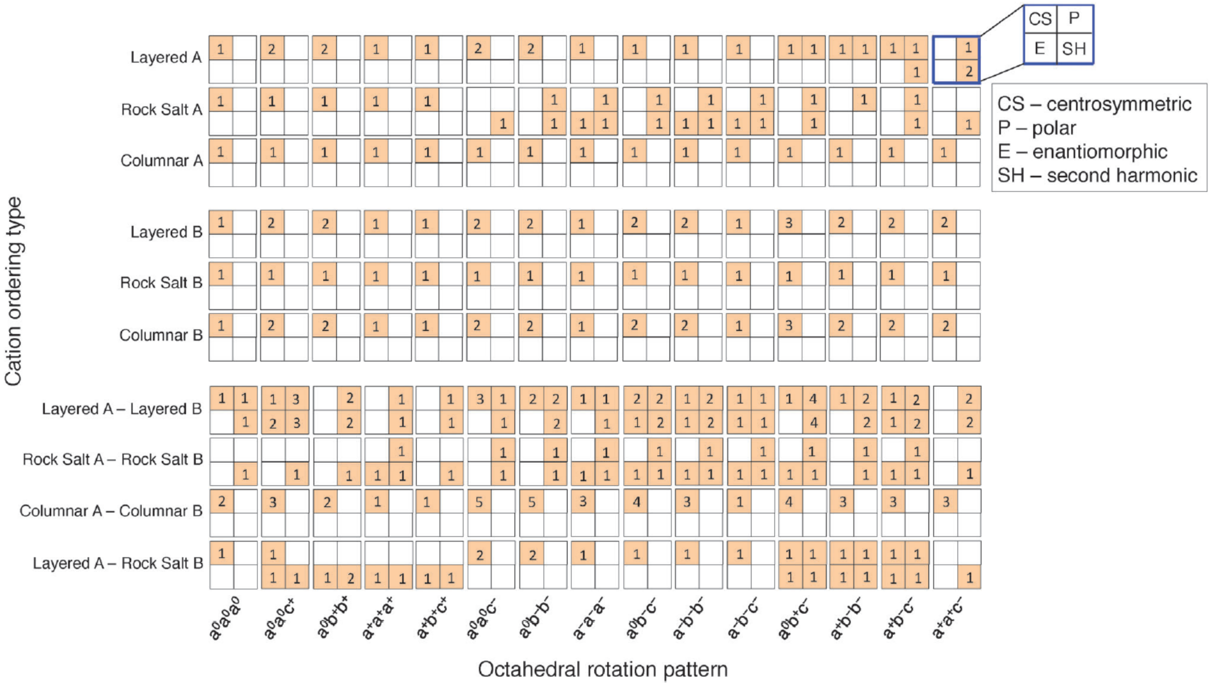

Figure 1.10 Summary of various combinations between cation ordering and 15 distinct rotational patterns. The top three rows considered ordering only on the A-site including the layered ordering, the columnar ordering and the rock-salt ordering; while the middle three rows considered ordering only on the B-site also including the layered ordering, the columnar ordering and the rock salt ordering; the remaining part considered the combined A- and B-site ordering. The outcomes of all combinations produced a centrosymmetric (CS), polar (P), Enantiomorphic (E) or second harmonic (SH) crystal class. The numbers in the boxes represent how many unique space groups of a given type are produced by the corresponding combination.[27]

Firstly, only the A-site cation ordering was considered: along [001] (Layered A), along [110] (Columnar A) and along [111] (Rock Salt A). In total, 105 combinations of the A-site cation ordering and rotation patterns were considered. As shown in the first three rows, for layered ordering only mixed rotation patterns were able to lift all inversion centers; for columnar ordering it was not possible to lift the inversion symmetry with any rotation pattern; while for the rock-salt ordering both out-of-phase and mixed rotation patterns could break the inversion symmetry. Then, if only the B-site cation ordering was considered, there were also a total of 105 combinations. However, no rotation patterns could result in lifting all inversion centers for all the possible B-site cation orderings as shown in the middle three rows in Figure 1.10. Finally, the combined A-site and B-site cation ordering was evaluated. Various combinations of the A- and B-site cation ordering (Layered A-Layered B, Rock Salt A-Rock Salt B, Columnar A-Columnar B, and Layered A-Rock Salt B) were combined with 15 distinct rotation patterns, which produced a total of 330 combinations. For both combinations of Layered A-Layered B and Rock Salt A-Rock Salt B, at least one noncentrosymmetric metric can be produced by each rotation pattern which was attributed to fact that the ordering alone cooperatively lifted the inversion symmetry. However, only centrosymmetric structures were produced in all combinations between the Columnar A-Columnar B ordering and all rotation patterns, indicating the cation ordering along [110] is not a good routine to create polar compounds. Surprisingly, in-phase rotations resulted in broken inversion symmetry for Layered A-Rock Salt B ordering, which was opposite to the observation in the A-site only ordering. It was supposed that the in-phase rotations displayed a handedness and lifted the inversion centers at the B-site. The rock-salt type ordering of the B-site further lifted the inversion centers at the A-site, resulting in a non-centrosymmetric symmetry.

In addition, chemical aspects, such as the tolerance factor, octahedral rotation patterns, the global instability index, the ionic size, and the valence difference, were also evaluated. The tolerance factor and the global instability index were used to predict the stability and octahedral rotations, nevertheless, others factors should be considered as well otherwise they could be misleading. The selection of octahedral rotations had to take the specific cation ordering into account as discussed above. For the A-sites, a difference in size could stabilize the structure and a layered ordering was mostly observed as it could alleviate the A and A’ size mismatch. A large valence difference in the B-sites was required, and typically the B-sites ordered in a rock-salt type to have the maximum separation between the highly charged cations.

The ideal ferroelectric property should have a large spontaneous polarization and a low switching barrier. In order to optimize the HIF, the microscopic mechanism was investigated by Mulder *et al.*.[29] A larger polarization needs the structure to be more distorted, meanwhile, a more distorted structure must result in a higher switching barrier from one state to the other. The best deal is to compromise on these two factors. From this study, it was found that the degrees of octahedral rotations were proportional to the average tolerance factors of the two building blocks ABO_3/$A'BO_3$ constituting the superlattice which is easily understood. However, contrary to one’s intuition, the polarization was independent of the average tolerance factor. It was supposed that the coupling coefficient α in Equation (1.1) was related to the tolerance factor difference of the two building blocks, which indicated that the polarization also depended on the size difference of the A- and A’-site cations. This is nontrivial as the HIF originates from the displacements of the A- and A’- site cations in opposite directions. The larger the tolerance factor difference, the larger the relative displacements which results in a bigger polarization. This reveals that HIF is not only attributed to the coupling of octahedral rotations but also a coupling to the anti-polar displacements. As a consequence, in order to obtain a HIF with a larger polarization and a lower switching barrier, one must select two building blocks ABO_3/$A'BO_3$ where both the average tolerance factor and the tolerance factor difference are at a maximum.

Various investigations were carried out to demonstrate HIF in several compounds. Superlattices, for example, $BiFeO_3$/$LaFeO_3$[30], $ASnO_3$/$A'SnO_3$ (A, A’= Ca, Sr and Ba)[31], $AGaO_3$/$A'GaO_3$ (A, A’= La, Pr, and Nd)[32], were studied with first principles techniques. HIF was observed in all these. The doubly ordered perovskite $NaLaMnWO_6$ was synthesized and proved to possess the polar space group $P2_1$.[33] Fukushima *et al.*[34] decomposed the polar structure in terms of symmetry modes with respect to its parent paraelectric *P4/nmm* symmetry, and the two primary rotation modes and the induced polar mode were defined. Using the point charge model it was estimated that the spontaneous polarization could be as large as ~16 μC/cm^2. Furthermore, a theoretical study was taken on nine doubly ordered perovskites $AA'MnWO_6$ (A= Na, K, Rb; A’= La, Nd, Y).[35] A variety of factors including the tolerance factor, symmetry mode amplitudes, bond valence sums, and layer decomposed dipoles were considered. It was concluded that the largest factor affecting the polarization is the size of the A’-site cation, the amplitudes of the two rotational modes and the induced polar mode increased with decreasing A’-site cation sizes. Meanwhile, the decomposition into layered dipoles revealed that the polarization of the A’O layer remained nominally the same for a given A’ cation. The A-site cation size was then an influencing factor on the polarization such as that a larger one resulted in a smaller cancellation of the polarization in the A’O layer. The electronic contribution to the polarization was also taken into the account in this investigation. Consistent with the previous study, the tolerance factor is a rather a poor indicator for the polarization. The best candidate for the polarization enhancement in this study proved to be $KYMnWO_6$, which was predicted to have a polarization ~26μC/cm^2.

Ruddlesden-Popper (RP) Oxides

As discussed above, the RP oxide $Ca_3Mn_2O_7$ also yielded the phenomenon of HIF.[15] Since the structures of the RP oxides are very closely related to perovskites, it is very likely that a general rule can also be defined for the RP oxides to induce the HIF. In order to figure out the general rule, a systematic theoretical investigation was carried out by Mulder *et al.* [29] on nine $A_3B_2O_7$ RP compounds with a variety of tolerance factors. However, it was found, unlike the perovskites, that the polarization is monotonic function of the tolerance factor. For the sake of understanding this phenomenon, it is necessary to examine the origin of the polarization in $A_3B_2O_7$ compounds. The distorted structure of n=2 RP compound $A_3B_2O_7$ is illustrated in Figure 1.11(a). The local inversion symmetry of the individual octahedron is lifted in presence of the interface between the rock-salt layer and the perovskite layer. As a result, the specific cation ordering is not required as in the case of perovskites. In addition, the anti-polar displacements of the A-site cation are also observed as a consequence of the $a^-a^-c^+$ octahedral rotations. A net polarization, the HIF, is generated between the AO layers at the interface and between the perovskite blocks since they are inequivalent positions with respect to the symmetry. However, this polarization due to non-cancellation is rather small, and the observed polarization is largely attributed to the extra AO layer in the unit cell. Therefore the overall polarization mostly depends on one type of the A-site cation displacement, leading to the polarization monotonically changing with the tolerance factor. As shown in the case of perovskites, the tolerance factor difference also plays a role in deciding the polarization. The effect of this factor was also examined by substitution of the A-site cations in $(ABO_3)_2A'O$. When fixing the A-site cation and replacing the A' cation by a cation of a different size, the same rule as the one concluded from perovskites was observed: the polarization increased as the tolerance factor difference increasing while the switching barrier decreases down as the average tolerance factor increases. However, some contradiction was observed when fixing the A'-site cation while substituting the A-site cation by cations of different sizes. Despite the switching barrier decreasing as the average tolerance factor increases, the polarization was independent of the tolerance factor difference. A case study was investigated as shown in Figure 1.12. When the A-site cation was the same as the one on the A'-site, e.g. in $(CaSnO_3)_2CaO$ (see Figure 1.12 (a)), the inversion symmetry was broken as pointed above, and the polarizations of the neighboring AO and A'O layers nearly cancelled out. The overall polarization mainly comes from one CaO layer. When the A and A' are not the same any more, the story is very different from that in perovskites. If the A'-site cation is substituted by a larger cation, e.g. Ba (see Figure 1.12(b)), the polarization of the AO or A'O layers cannot cancel that of its counterpart. The larger size of the A'-site cation resulted in a much smaller polarization. As a consequence, the overall polarization was approximately the double of the CaO layer polarization. Instead, if the A-site cation is replaced by a larger cation, e.g. Ba as well (see Figure 1.12(c)), the CaO polarization was reduced by the BaO layers even though the average tolerance factor increased. The $a^-a^-c^+$ ground state of n=1 RP compounds $(ABO_3)A'O$ (where A and A' are different) is also polar. After an investigation of 214 n=1 RP compounds, Balachandran *et al.* also found that simple octahedral rotations and Jahn-Teller ordering are insufficient to lift the inversion center, in addition, if in combination with each other or with A- or B-site cation ordering, the inversion symmetry can be lifted. [36]

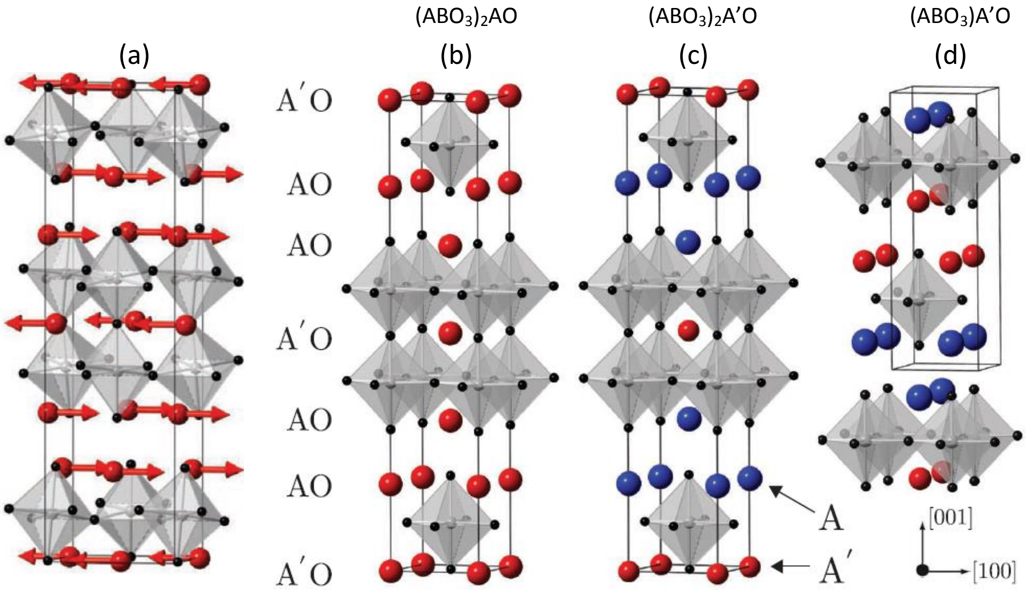

Figure 1.11 The structures of Ruddlesden-Popper oxides. (a) The A-site cation displacement in the $a^-a^-c^+$ n=2 RP structure ; (b) the undistorted n=2 RP structure with a single A-site cation; (c) the n=2 RP structure with two different A-site cations, the A cation is in the interface layer while the A' cation is in the layer between perovskite blocks; (d) the n=1 RP structure with two different A-site cations. [29]

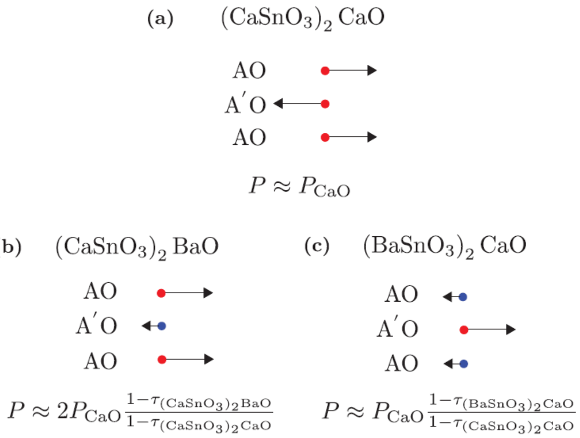

Figure 1.12 The polarization contributions from the AO and A'O layers, where (a) A=A'; (b) only A' is substituted by a larger cation; (c) only A is replaced by a lager cation. [29]

The HIF was demonstrated experimentally in several following studies in RP such as the n=1 RP $NaRTiO_4$ (R denotes the rare-earth) family[37], the n=2 RP $(Ca,Sr)_3Ti_2O_7$ family crystals[38] and the n=2 RP $Ca_3(Ti, Mn)_2O_7$ family[39].

1.3 Doubly Ordered Perovskites AA'BB'O_6

1.3.1 Structures of the Known Doubly Ordered Perovskites AA'BB'O_6

Recently, attention has turned to the rather unexplored class AA'BB'O_6. The first compound synthesized of this class was $NaLaMgWO_6$ in 1984, and its unit cell was determined as monoclinic in dimensions of $\sqrt{2}a_p*\sqrt{2}a_p*2a_p$ (where a_p represents the unit cell parameters of the aristrotype perovskite).[40] The cations Na^+ and La^{3+} at the A- and A'-sites, respectively, had a layered ordering, while the other two cations

Mg^{2+} and W^{6+} at the B- and B'-sites, respectively, ordered in a fashion of rock-salt. Following this compound, there were several other ordered AA'BB'O$_6$ compounds being synthesized, as shown in Table 1.1.

Table 1.1 A Summary of Known Doubly Ordered Perovskites AA'BB'O$_6$.

Compound	Crystal Class	Space Group	Cation Ordering	Unit cell Dimensions	Reference
NaLaMgWO$_6$	Monoclinic	$P2_1$ or $P2_1/m$	Layered A/A' Rock salt B/B'	$\sqrt{2}a_p*\sqrt{2}a_p*2a_p$	[40]
		$C2/m$		$2a_p*2a_p*2a_p$	[41]
NaLnMgWO$_6$ (Ln= Ce, Pr, Nd, Sm, Eu, Gd, Tb, Dy, Ho)	Tetragonal for Ce and Pr; Monoclinic for all others		Layered A/A' Rock salt B/B'	$\sqrt{2}a_p*\sqrt{2}a_p*2a_p$	[42]
NaLaMgTeO$_6$	Monoclinic		Layered A/A' Rock salt B/B'	$\sqrt{2}a_p*\sqrt{2}a_p*2a_p$	[43]
NaLaCaWO$_6$	Monoclinic	$P2_1/m$	Layered A/A' Rock salt B/B'	$\sqrt{2}a_p*\sqrt{2}a_p*2a_p$	[44]
NaLaScNbO$_6$	Tetragonal	$P4/nmm$	Layered A/A', Rock salt B/B', neither complete	$\sqrt{2}a_p*\sqrt{2}a_p*2a_p$	[41]
NaLnMnWO$_6$ (Ln= La, Ce, Pr, Nd, Sm, Gd, Tb, Dy, Ho)	Monoclinic	$P2_1$	Layered A/A' Rock salt B/B'	$\sqrt{2}a_p*\sqrt{2}a_p*2a_p$	[45] [42]
NaLnFeWO$_6$ (Ln = La, Nd)	Monoclinic	$P2_1$	Layered A/A' Rock salt B/B'	$\sqrt{2}a_p*\sqrt{2}a_p*2a_p$	[46]
NaLaCoWO$_6$	Monoclinic	$P2_1/m$	Layered A/A' Rock salt B/B'	$\sqrt{2}a_p*\sqrt{2}a_p*2a_p$	[47]
NaNdCoWO$_6$	Monoclinic	$P2_1/m$	Layered A/A' Rock salt B/B'	$\sqrt{2}a_p*\sqrt{2}a_p*2a_p$	[45]
NaLaNiWO$_6$	Monoclinic	$P2_1/m$	Layered A/A' Rock salt B/B'	$\sqrt{2}a_p*\sqrt{2}a_p*2a_p$	[47]
KLaMnWO$_6$	Tetragonal	$P4/nmm$	Layered A/A' Rock salt B/B'	$\sqrt{2}a_p*\sqrt{2}a_p*2a_p$	[45]
KLaMgTeO$_6$	Monoclinic		Layered A/A' Rock salt B/B'	$\sqrt{2}a_p*\sqrt{2}a_p*2a_p$	[43]
KLaMgWO$_6$	Monoclinic		Layered A/A' Rock salt B/B'	$\sqrt{2}a_p*\sqrt{2}a_p*2a_p$	[48]
KLaCaWO$_6$	Monoclinic		Layered A/A' Rock salt B/B'	$\sqrt{2}a_p*\sqrt{2}a_p*2a_p$	[44]

Given the aristotype perovskite ABO$_3$ adopts the symmetry *Pm-3m*, when half of the B-site cations are substituted by another cation kind B' into A$_2$BB'O$_6$, the rock-salt type ordering at the B-sites is the most preferred.[49] This ordering reduces the symmetry to *Fm-3m* in the absence of octahedral tilting.[50] Large differences in size and charge are very critical for the cation ordering. These differences drive the cations to occupy different crystallographic positions within the structure.[41] In the rock-salt type ordering, the B and B' cations are the most separated.[51][52] In order to understand the preference of this ordering, it is necessary to consider the bonding aspects. In the rock-salt ordering of the B-sites, each anion is surrounded by one B and one B' cation (see Figure 1.13 (a)), as a consequence, it can move toward the smaller B’ cation and away from the larger B cation to optimize the bonding.[52] In contrast, if the B and B’ cations order in a layered fashion (see Figure 1.13 (b)), then one-sixth of the anions are bonded with two of the more charged B’ cation while another one-sixth of the anions are bonded with two less charged B cations, and the remaining anions are coordinated by one B and one B’ cation, which is violating to Pauling’s fifth rule, stating that all ions of the same type should sit in the same environment if possible.[52] As a result, the rock-salt ordering of the B/B’ cations is more preferred.

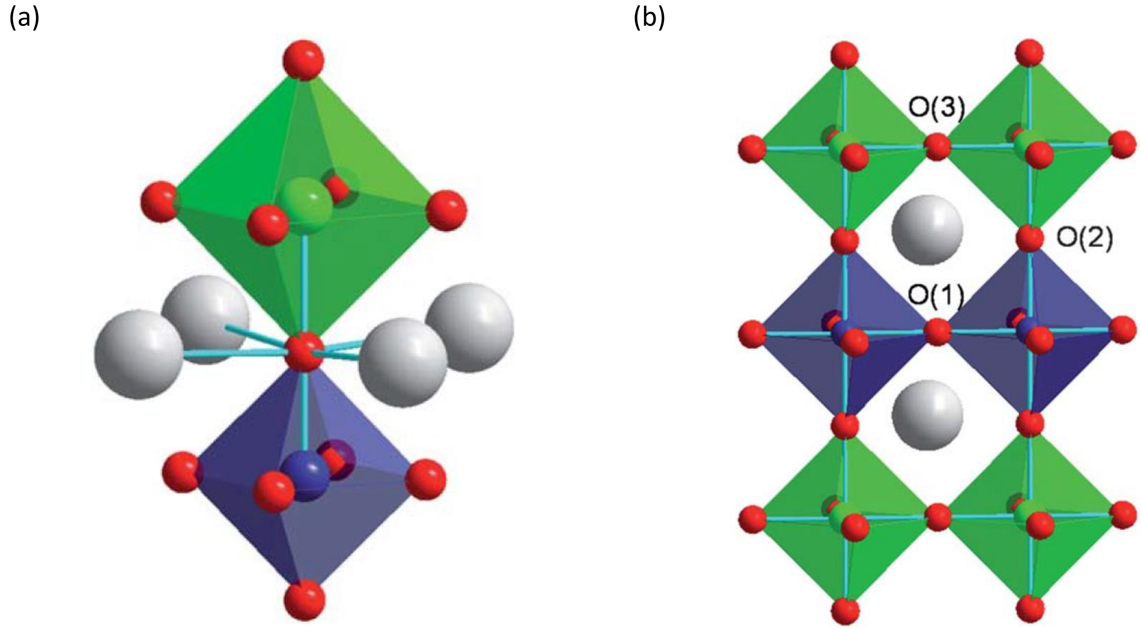

Figure 1.13 The crystal structure of $A_2BB'O_6$ with (a) rock salt ordering and (b) layered ordering of the B/B’ cations. The spheres stand for different ions, A (grey), B(blue), B’(green) and anion (red).[52]

Furthermore, when half of the A-site cations are substituted by another cation kind A’, leading to a compound $AA'BB'O_6$, the A and A’ cations will order into a layered manner alternately. The combination of layered and rock-salt cation ordering further reduces the symmetry to *P4/nmm* in the absence of octahedral tilting.[41] The bonding must be investigated again in order to understand the layered A/A’ ordering. In the case of rock-salt ordering at the A/A’-sites (see Figure 1.14 (a)), the anion is at an inversion site coordinated by two A cations and two A’ cations, making it impossible to shift to relieve lattice strains arising from the A/A’ size mismatch.[52] This problem does not exist in the structure of layered A/A’ ordering (see Figure 1.14 (b)), two thirds of anions are surrounded by two A cations and two A’ cations, making it is possible for these anions to displace in the presence of a significant A/A’ cations size difference.[52] However, the remaining one-sixth of anions are surrounded by four A cations and the other one-sixth are surrounded by four A’ cations, where the problem of the same ions in different environments is encountered again. The layered ordering was proved to be established only in the presence of second-order Jahn-Teller (SOJT) distortions of the highly charged B’ cation.[41] A systematic investigation on the effect of the B’ cation on the layered ordering was performed by Dachraoui *et al.*.[53] Four compounds were chosen such as $NaLaBB'O_6$ (B=Mn, Fe; B’= Nb, Ta). Mn^{3+} and Fe^{3+} were selected to compare cations with and without first-order Jahn-Teller (FOJT) effect, respectively. And Nb^{5+} and Ta^{5+} were selected for the B’ cation in order to compare cations with large differences of SOJT effect. A local layered A/A’ ordering was observed in all four compounds, without a rock-salt B/B’ ordering. It was found that the SOJT effect of the B’ cation is a must for short-range layered A/A’ ordering, however, the long range layered A/A’ ordering could only be established in the presence of the B-site ordering. The degree of the short range ordering is highest in $NaLaMnNbO_6$ and lowest in $NaLaFeTaO_6$, as expected that a stronger SOJT effect increased the range of layered ordering at the A/A’-sites. More pronounced local orthorhombic distortions were observed in Mn^{3+} containing compounds, which was attributed to the FOJT effect of the Mn^{3+} ions.

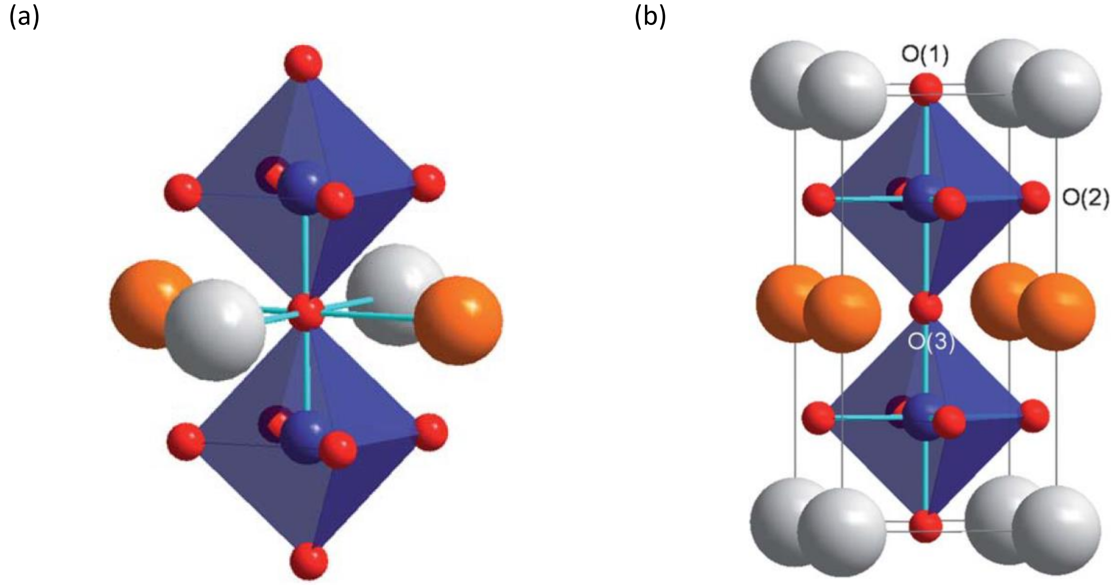

Figure 1.14 The crystal structure of $AA'B_2O_6$ with (a) rock-salt ordering and (b) layered ordering of the A/A’ cations. The spheres stand for different ions, A (grey), A’(orange), B(blue) and anion (red).[52]

As stated above, the cation ordering can reduce the symmetry of $AA'BB'O_6$ only to *P4/nmm* in the absence of octahedral rotations. However, octahedral rotations are very common in perovskites in order to adapt the size effect of ions. Taking the combination of layered A/A’ ordering, rock-salt B/B’ ordering and 12 distinct tilting schemes, a group theoretical study predicted the possible structures of $AA'BB'O_6$ compounds (see Figure 1.15).[41] The tetragonal symmetry is retained in the presence of rotations around only the **c**-axis, $a^0a^0c^-$ and $a^0a^0c^+$, and the in-phase rotations of equal magnitude around both the **a**- and **b**-axes, $a^+a^+c^0$. If the latter turns out to be out-of-phase, the symmetry is reduced to monoclinic while the unit cell dimensions stay the same. The combinations of these basic tilting schemes further reduce the symmetry. The absence of tilting schemes such as $a^-a^-c^-$ and $a^+a^+c^+$ was attributed to the fact that the tilts around the **a**- and **b**-axes are no longer required to be of the same magnitude as the tilt around the **c**-axis destroys sufficient symmetry elements. As a consequence, they are included in the $a^-b^-c^-$ or $a^+b^+c^+$ schemes.

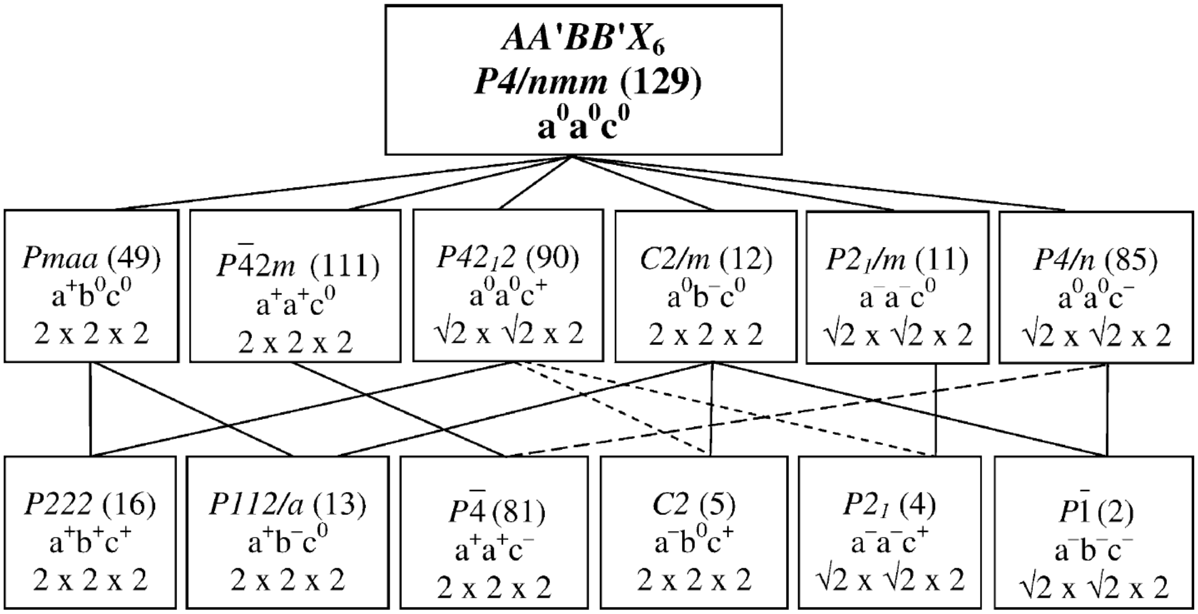

Figure 1.15 A summary of possible AA'BB'O_6 structures predicted by group theoretical methods considering the layered A/A', rock salt ordered B/B' and 12 distinct tilting schemes. Each box shows the space group, tilting scheme using Glazer's notation, and approximate unit cell dimensions in terms of the unit-cell parameter of the undistorted *Pm-3m* perovskite. The group-subgroup relationships are denoted by lines, where the solid line represent possible continuous transitions and the dashed lines represent discontinuous transitions.[41]

1.3.2 Structure Modulations

A transmission electron microscopy (TEM) study of $NaLaMgWO_6$ revealed a modulated structure with a pattern of stripes as shown in Figure 1.16.[54] Satellite reflections were observed around $(100)_p$, $(010)_p$ and $(110)_p$ (the subscript "p" means that the pattern is indexed corresponding to the ideal *Pm-3m* perovskite structure) in the selected area electron diffraction (SAED) pattern along the zone axis $[001]_p$. The spacing between the satellite reflections indicated an extra periodicity of $12a_p$ (a_p is the unit cell parameter of the ideal *Pm-3m* perovskite structure) along the directions of $[100]_p$ and $[010]_p$. HRTEM images corresponding to the SAED pattern shown in Figure 1.16(a) are presented in Figure 1.16 (b) and (c). Alternative dark and bright stripes contrast with a width of $6a_p$ for either of them appeared along two perpendicular directions in the corresponding two domains. The periodicity of the stripes was consistent with the $12a_p$ periodicity observed from the SAED pattern along $[100]_p$ and $[010]_p$. The fast Fourier transform (FFT) of the domains A and B in Figure 1.16 (b) were performed as shown in Figure 1.16 (d) and (e), respectively. The SAED pattern in Figure 1.16 (a) corresponds to a superposition of the patterns of both domains.

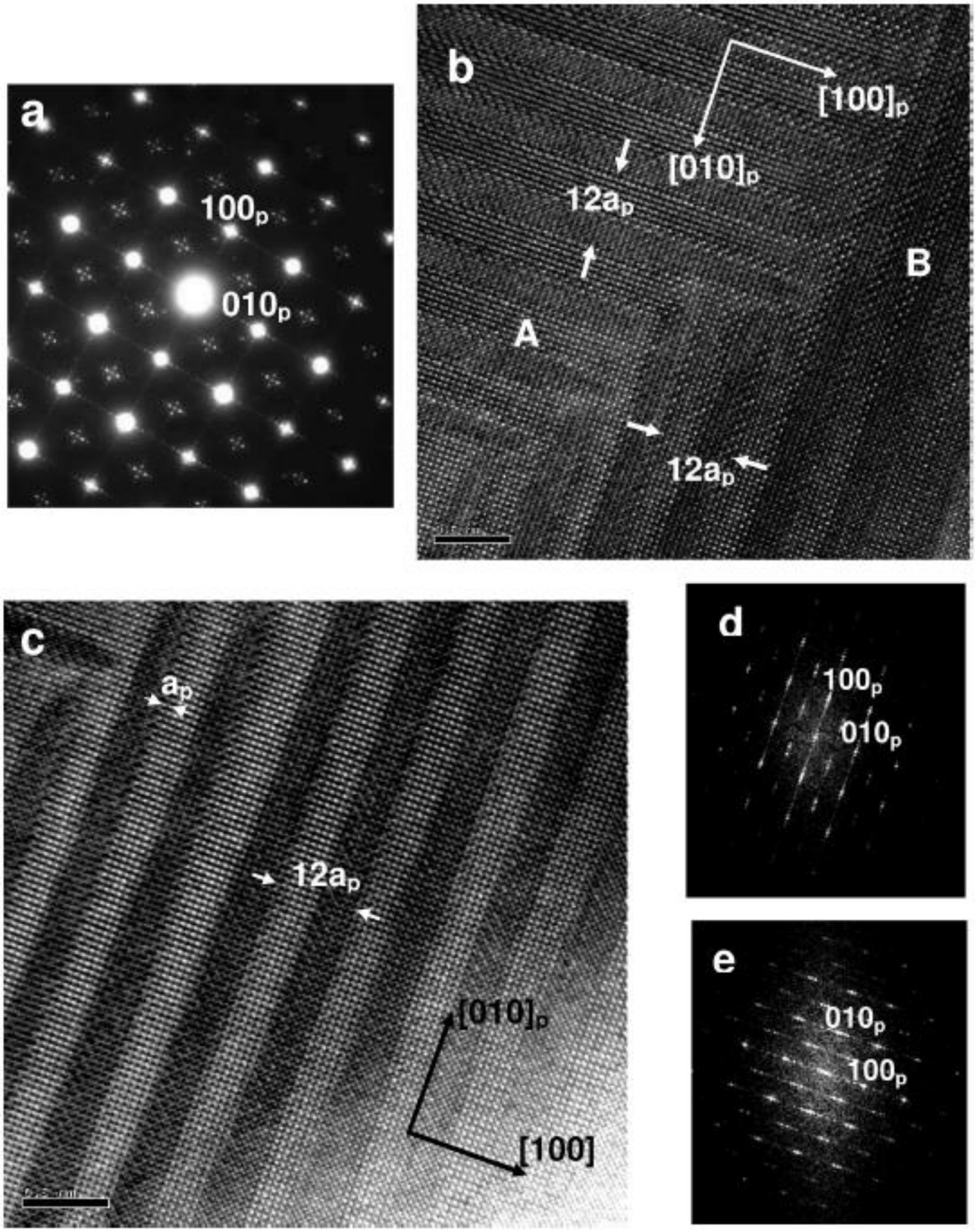

Figure 1.16 The TEM study of $NaLaMgWO_6$. (a) the SAED pattern along the $[001]_p$ zone axis; (b) and (c) are HRTEM images corresponding to the $[001]_p$ zone axis; (d) and (e) are the FFT of the domains A and B in (b).[54]

A further examination was taken on the chemical composition. A contrast difference with the same periodicity as the stripes observed in the corresponding HRTEM image (see Figure 1.17 (b)) appeared in the ADF-STEM image shown in Figure 1.17 (a). Based on this, a variation of chemical composition was proposed and further investigated by EELS. Line-scans of STEM-EELS were performed along the red line shown in Figure 1.17 (a), collecting at the La $M_{4,5}$ edge. The result of EELS in Figure 1.17 (d) yielded that the La content varied with the same periodicity appearing in the ADF-STEM image from stripes to stripes.

The observed compositional modulation was along one of the main perovskite directions. Besides the compositional modulation, octahedral tilt twinning and the corresponding twinning of the B-site cation displacements were also proposed to be responsible for the contrast difference appearing in HRTEM images. Five distinct models to explain the compositional modulation were proposed and examined, the authors argued that the model with alternating stripes $Na_{1.33}MgWO6$ and $NaLaMgWO_6$ was the most preferred. The phase separation was observed to be not completely developed in a few crystals.

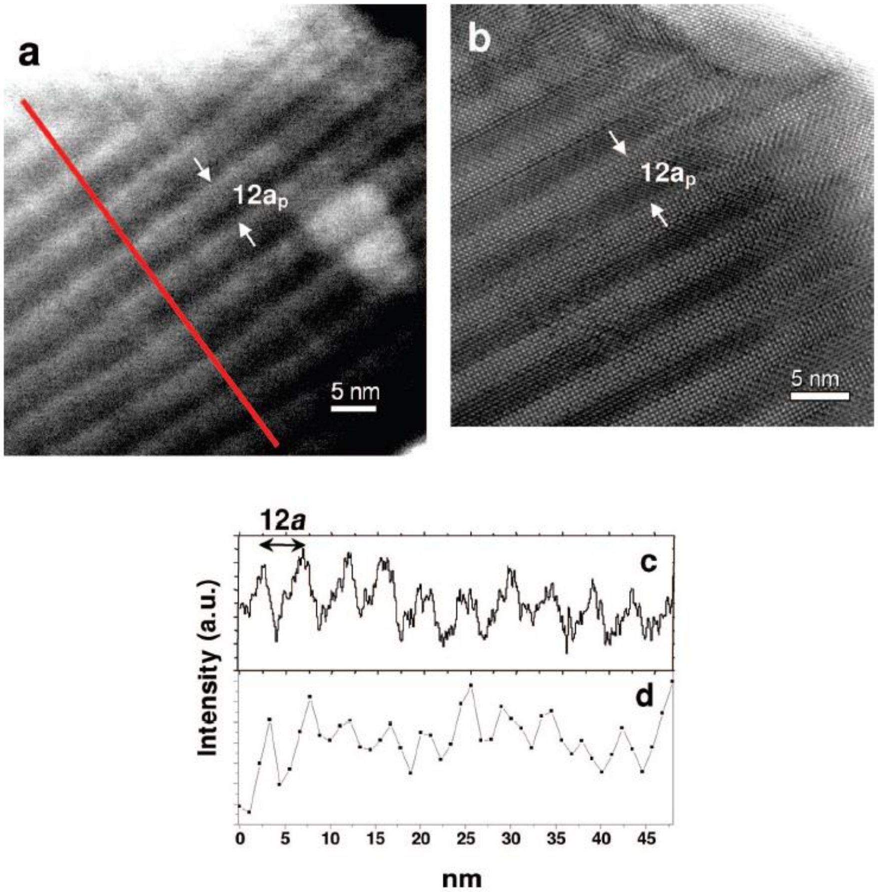

Figure 1.17 The chemical compositional study of $NaLaMgWO_6$. (a) is the ADF-STEM image and (b) is the HRTEM image along the $[001]_p$ zone axis; (c) the intensity variation of the ADF-STEM image along the corresponding STEM-EELS line scan indicated by the red line in (a); (d) the STEM-EELS line scan intensity variation of the La $M_{4,5}$ edge.[54]

In a following study[55], various models based on octahedral twinning were built (see Figure 1.18). Through a comparison of the simulated NPD patterns with the experimentally observed NPD pattern (see Figure 1.19), the model composed by the tilting scheme $a^-a^-c^0$ was believed to be most plausible. The twin boundaries did not generate a mirror plane or any other symmetry element in the structure (Figure 1.18 (b)). It is the rock-salt ordering at the B/B'-sites that does not allow the mirror symmetry. In addition, the octahedra lying across the twin boundaries have different sizes and central atoms, leading to the absence of any symmetry relationship between them. The model considered the twin boundaries running in only one direction, resulting in breaking the equivalence of the **a-** and **b-**axes so that the tilt angles were not necessarily the same along the **a-** and **b**-axes. Therefore, the true tilt scheme would be $a^-b^-c^0$, where the two tilt angles were nearly the same. A further consideration combined both the compositional modulations and octahedral tilting. TEM images of different models were simulated and compared with the experimental one in Figure 1.20. The model *A* only took the octahedral tilt twinning into account, however, it did not reproduce the alternating stripes pattern. A twinned displacement of W^{6+} ions along the **b**-axis was added to the model *B*, once again, no stripes pattern was obtained with this model. Then compositional variations were added to models *C* and *D*, both of them could reproduce the experimental pattern, indicating a compositional modulation is required to explain the observed pattern. It was supposed that the larger Na^+ ion was too large for the sites sitting at the twin boundaries and that it would be replaced by the smaller La^{3+} ions and vacancies on either side of the La^{3+} ion, since the A-site coordination environment at the twin boundaries is different from elsewhere in the crystal.

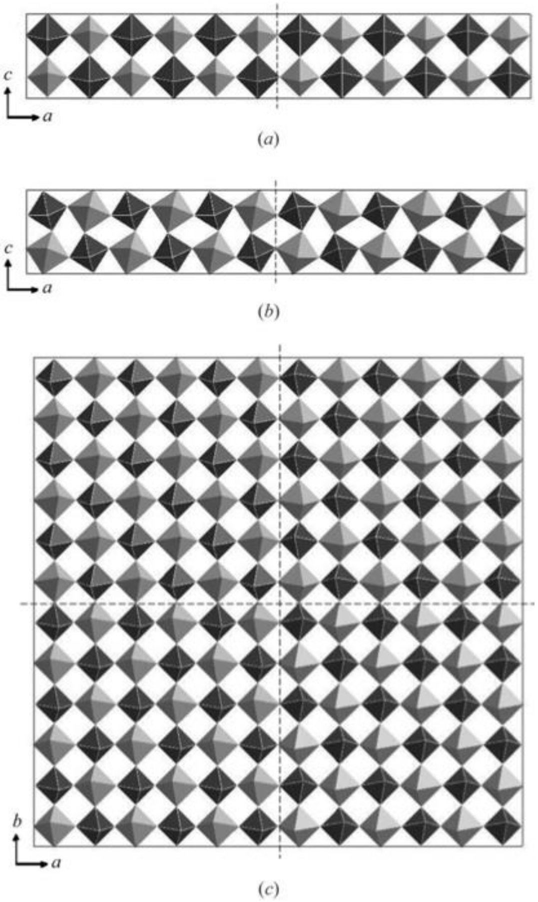

Figure 1.18 Models with octahedral tilt twinning were built to explain the satellite reflections in NPD data. (a) is the unit cell in dimensions of 12a_p*2a_p*2a_p with $a^-b^0b^0$ tilting and the tilt boundary was in one dimension; (b) the unit cell in dimensions of 12a_p*2a_p*2a_p with $a^-a^-c^0$ tilting and the tilt boundary was in one dimension; (c) the unit cell in dimensions of 12a_p*12a_p*2a_p with $a^-b^0b^0$ tilting and the tilt boundary was in two dimensions. W centered octahedra are in dark grey while Mg centered octahedra are in lighter grey. The A-site cations are not displayed for clarity. Dashed lines inside the unit cell stand for the tilt boundaries. [55]

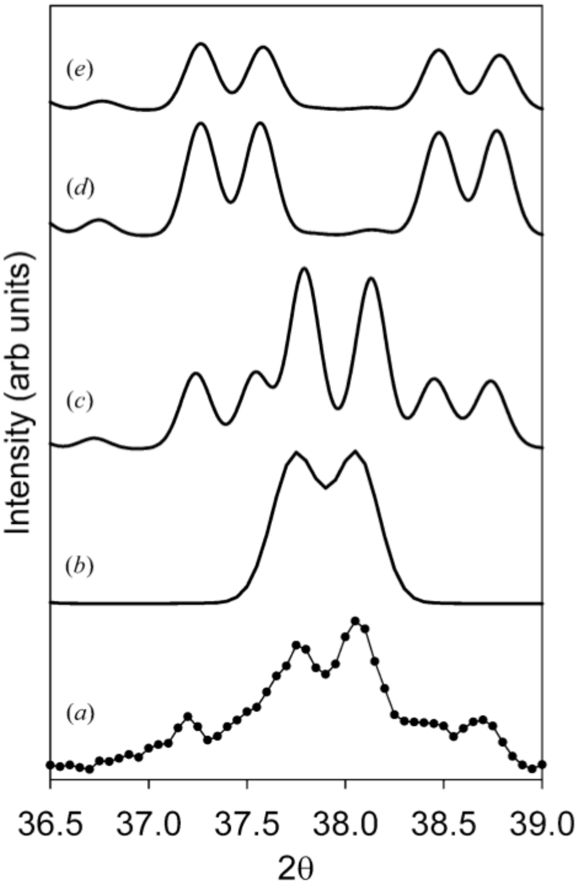

Figure 1.19 A comparison of NPD pattern between (a) the experimentally observed, (b) the calculated from space group *P*2$_1$, (c) the simulated using $a^-a^-c^0$ tilting and the one dimensional tilt boundaries, (d) the simulated using $a^-b^0b^0$ tilting and the one dimensional tilt boundaries, and (e) the simulated using $a^-a^-c^0$ tilting and the two dimensional tilt boundaries.[55]

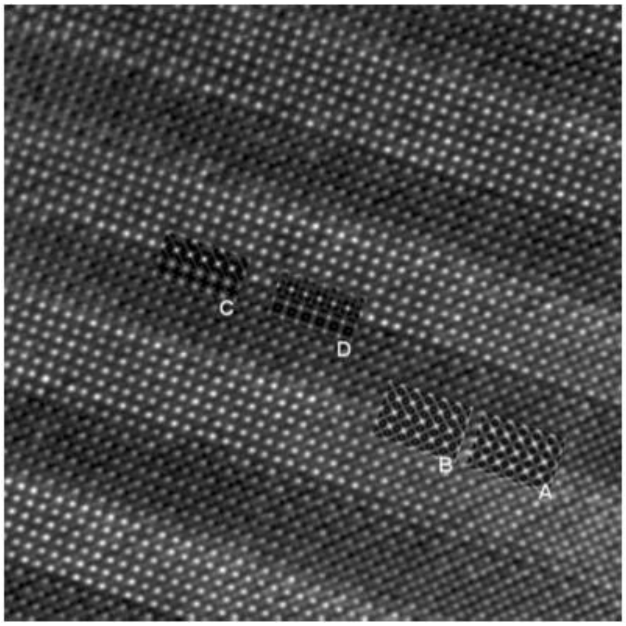

Figure 1.20 A comparison between the experimentally observed HRTEM image and the inserted simulated ones along the $[001]_p$ zone axis.[55]

Another modulation pattern was also observed in the $KLaMnWO_6$ compound by TEM as shown in Figure1.21.[56] The SAED pattern (see Figure 1.21 (a)) is along the $[001]_p$ zone axis. Satellite reflections were observed along $[100]_p$, $[010]_p$, $[110]_p$ and $[1\text{-}10]_p$ directions, indicating the existence of a modulated structure. The distances between satellite reflections revealed that the new periodicity due to the modulated structure is $10a_p$ along both $[100]_p$ and $[010]_p$ directions. A chessboard pattern with dark areas intercalated with bright areas was observed in the corresponding HRTEM image (see Figure 1.21 (b)). The size of the dark areas and bright areas is ~5ap*5ap, which is consistent with the $10a_p$ periodicity derived from the SAED pattern in Figure1.21 (a). Chemical composition was examined by both HAADF-STEM imaging and STEM-EELS. A chessboard pattern with contrast differences composed of dark and bright areas was also observed in the HAADF-STEM image recorded on this compound (see Figure 1.22 (a)), indicating a possible compositional modulation. Collections of STEM-EELS line-scans were carried out at both the La $M_{4,5}$ and the Mn $L_{2,3}$ edges. Line scans along different directions yielded that the La content was modulated while the Mn content was uniform. In addition, satellite peaks were also observed in NPD data. In order to explain these satellite reflections, a model as shown in Figure 1.23 was built. The dimensions of the unit-cell in this model was $10a_p$*$10a_p$*$2a_p$, and made up by four smaller blocks. The tilting scheme $a^-a^-c^0$ was employed except at the tilt boundaries which were inserted every five octahedra along both the **a-** and **b**-axes. A simple Rietveld refinement based on this model was performed, and all satellite peaks in the 2θ range, for instance 37.0°-40.0°, could be well explained. Two models were proposed by considering both octahedral rotations and compositional modulations (see Figure 1.24). Model 1 considered the A-site coordination environment being slightly different at the tilt boundaries from what it was away from the boundaries. If La^{3+} or vacancies were more favorable in this different environment, then the La rich regions might prefer to nucleate in the vicinity of the in-phase tilt boundaries. In contrast, if the in-phase tilts were formed for the sake of relieving stress related to the different lattice parameters of the separated phase, then the model 2 is more favored. The HAADF-STEM image was compared with these two models, and a better agreement was found with Model 2, although it was difficult to rule out a hybrid between these two models.

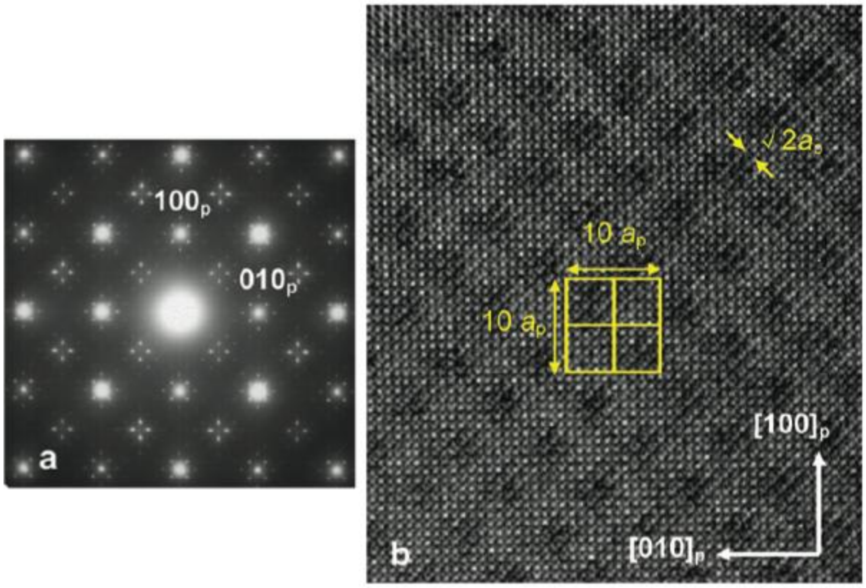

Figure 1.21 TEM study of the $KLaMnWO_6$ compound. (a) SAED pattern and (b) the corresponding HRTEM image along the $[001]_p$ zone axis. [56]

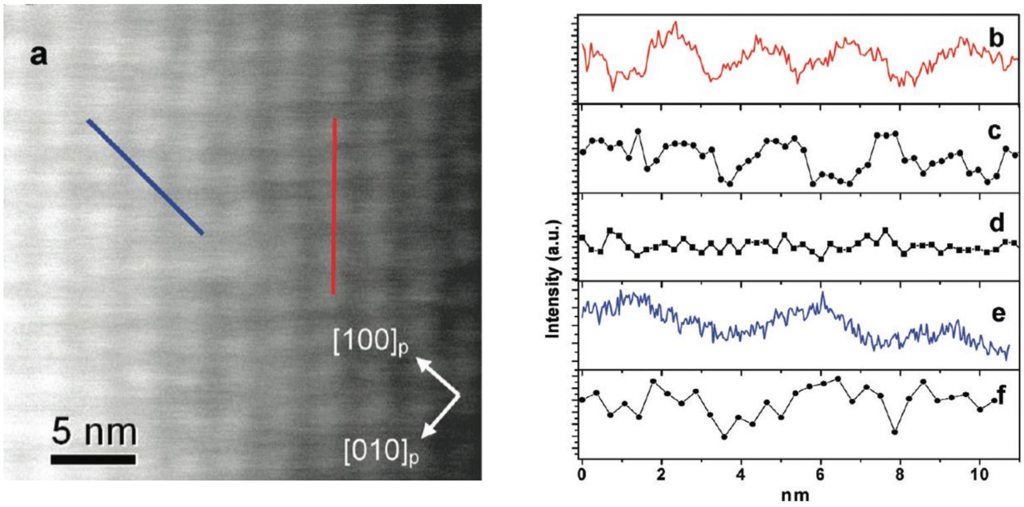

Figure 1.22 Chemical compositional study of the $KLaMnWO_6$ compound. (a) HAADF-STEM image along the $[001]_p$ zone axis, (b) the variation of contrast intensity of the HAADF-STEM image from the STEM-EELS lines scan following the red line in (a) which is the $[110]_p$ direction, (c) the variation of the La $M_{4,5}$ edge signal intensity, obtained from the STEM-EELS line scan along the $[110]_p$ direction, (d) the variation of the Mn $L_{2,3}$ edge signal intensity, obtained from the STEM-EELS line scan along the $[110]_p$ direction, (e) the variation of contrast intensity of the HAADF-STEM image from the STEM-EELS lines scan following the blue line in (a) which is the $[100]_p$ direction, (f) the variation of the La $M_{4,5}$ edge signal intensity, obtained from the STEM-EELS line scan along the $[100]_p$ direction.[56]

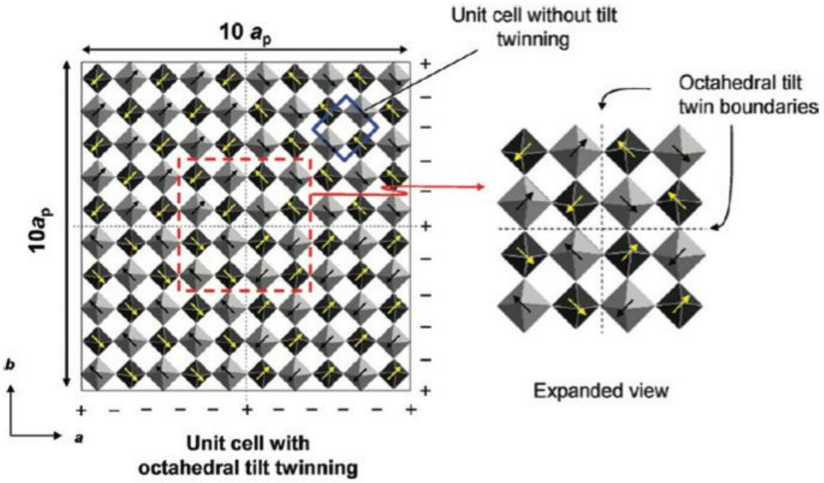

Figure 1.23 The model unit cell in dimensions of $10a_p*10a_p*2a_p$ with octahedral tilt twinning for $KLaMnWO_6$. The symbols – and + indicate the corresponding interface is out-of-phase and in-phase, respectively. The direction in which the apex oxygen is displaced is indicated by the arrows. An expanded view of the central region is shown in the right. The A-site cations are not displayed for clarity. Dashed lines inside the unit cell stand for the tilt boundaries.[56]

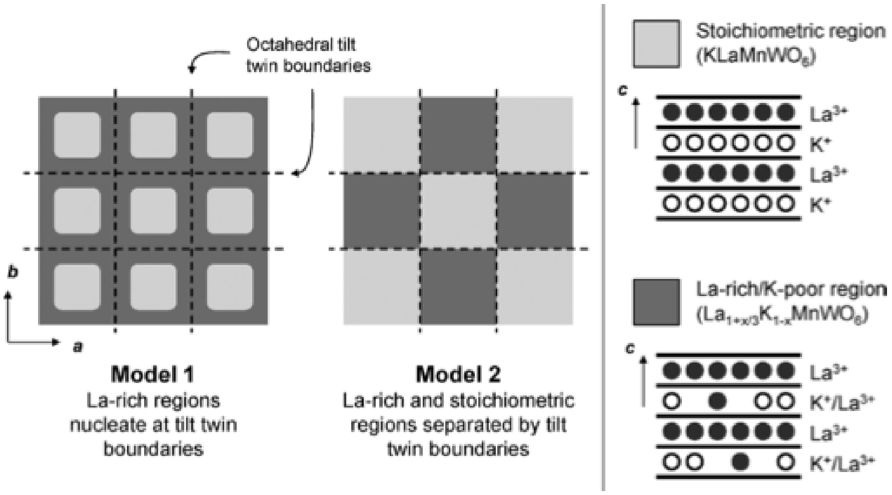

Figure 1.24 Two models to describe how do the compositional modulation and octahedral tilt twinning coexist.[56]

Modulated structures were also reported in some other doubly ordered perovskites. A chessboard pattern was observed in $NaNdMgWO_6$, SAED and HRTEM imaging studies concluded that the supercell in the modulated structure was as large as $14a_p$*$14a_p$*$2a_p$.[57] In addition, HAADF-STEM imaging confirmed the chemical compositional modulation also existed in this compound. Ordered regions with doubled (110) d-spacing in the **a**-**b** plane were separated by two dimensional periodic antiphase boundaries. $NaCeMnWO_6$ and $NaPrMnWO_6$ had incommensurately modulated structures, primarily consisting of two types of domains in the form of chessboard pattern, meanwhile, stripes were also found in some crystals.[58] The average periodicity in $NaCeMnWO_6$ was $14.9a_p$ while it was $21.7a_p$ in $NaPrMnWO_6$. Octahedral tilt twinning and chemical compositional modulations were also proposed in these two compounds. A pattern of alternating stripes contrast with a periodicity $12a_p$ was also observed in $NaLaFeWO_6$.[46] Incommensurate modulation was also observed in $KLaCaWO_6$ with a chessboard pattern, both SAED and HRTEM imaging revealed the supercell had dimensions ~$9.4a_p$*$9.4a_p$ along both **a-** and **b**-axes.[44] A pattern of alternating stripes contrast along the [110] direction was firstly observed in $NaLaCaWO_6$, with a periodicity $16a_p$.[44] Chemical compositional modulations were observed in both $KLaCaWO_6$ and $NaLaCaWO_6$. It was thought that the tolerance factor was a key consideration to predict the morphology and the modulation directions, for instance, from $NaLaMgWO_6$ to $NaNdMgWO_6$ the modulation pattern changed from one-dimensional alternating stripes to a two-dimensional chessboard pattern when reducing the tolerance factor from 0.953 to 0.937. However, the changes in tolerance factors of $KLaCaWO_6$ and $KLaMnWO_6$, from 0.932 to 0.970, did not modify the modulation manner, both of them showed a chessboard pattern modulation.[44] As a consequence, this kind of modulation observed in doubly ordered perovskites seems more complicated.

1.3.3 Physical Properties

1.3.3.1 Magnetic Properties

Magnetic properties are the most widely investigated properties for this class of materials compared to other physical properties. A systematic magnetic investigation was carried out on the $NaLnMnWO_6$ (Ln= La, Ce, Pr, Nd, Sm, Gd, Tb, Dy, and Ho) series compared to their counterpart series $NaLnMgWO_6$ (Ln= Ce, Pr, Nd, Sm, Eu, Gd, Tb, Dy, and Ho).[42] In the $NaLnMnWO_6$ series, the magnetic behavior changes as the radii of the rare-earth cations decrease. It was noted that there are two magnetic sublattices containing Ln^{3+} and Mn^{2+}, respectively. The study of the $NaLnMgWO_6$ series gave complementary information on the magnetic behavior of the Ln^{3+} sublattice in the absence of magnetic cations at the B-site. Taking both series into account, the coupling between the two magnetic sublattices in the $NaLnMnWO_6$ series would be better understood. In the $NaLnMnWO_6$ series, antiferromagnetic behavior was observed in all studied compounds, with Néel temperatures (T_N) varying from 10K to 13K. The Weiss constant was observed decreasing with the size of the rare-earth cations, which was attributed to weaker superexchange interactions from more distorted structures. A slight upturn in the magnetic susceptibility of $NaSmMnWO_6$ and $NaDyMnWO_6$ was observed at 3K and 4K, respectively. This was due to either a second magnetic phase transition or the presence of a small amount of a paramagnetic impurity. More than one transition temperature was also found in $NaPrMnWO_6$ and $NaTbMnWO_6$. At least three transitions were proposed for $NaPrMnWO_6$, T_N was defined at 11K for a transition from paramagnetic to antiferromagnetic, then at 8 K there was an upturn in the magnetic susceptibility just like the ones observed in some other compounds. A following transition was at 5 K with the magnetic susceptibility decreasing rapidly. The examined phase was believed pure and the same phenomenon happened again in another sample batch. No detailed explanation regarding these transitions was given. For $NaTbMnWO_6$, a second transition at 9K followed the paramagnetic to antiferromagnetic transition at 15K.[45] In the $NaLnMgWO_6$ series, no Curie-Weiss behavior was observed in $NaSmMgWO_6$ and $NaEuMgWO_6$, and the van Vleck magnetic behavior was observed in both of them. In contrast, all others could be fitted with Curie-Weiss law. The measured magnetic moments were very close to the theoretical ones. The negative Weiss constant for all compounds suggested that they were potentially antiferromagnetic although no transition temperatures were observed experimentally for any of them down to 2K which indicates the exchange interactions between the rare-earth cations are very weak.

Three compounds $NaLnMnWO_6$ (Ln=La, Nd, and Tb) of the series discussed above were studied to determine their magnetic structures by neutron diffraction data.[33] $NaLaMnWO_6$ provided a reference to study the magnetic ordering of Mn^{2+} in the absence of magnetic rare-earth cations. Two propagation vectors (½, 0, ½) and (0, ½, ½) were tested and it was found difficult to rule out one from the other since the unit-cell parameters *a* and *b* were so close. Since the refinement with the vector (½, 0, ½) was slightly better, then this vector was concentrated on. A moment of 3.99 μ_B per Mn^{2+} ion was derived from the refined magnetic structure, compared with the theoretical value 5 μ_B. There are two magnetic cations Nd^{3+} and Mn^{2+} in the compound $NaNdMnWO_6$. Both magnetic sublattices ordered simultaneously at 11 K with an incommensurate propagation vector (0, 0.48, ½). The derived magnetic moment of Nd^{3+} was 3.23 μ_B compared to a theoretical value of 3.62 μ_B. While a total maximum moment for Mn^{2+} was 6.11 μ_B, this large value was attributed to the mixing in of excited states or an orbital component. The two magnetic sublattices were not found strongly correlated. As discussed above, two transitions were derived from $NaTbMnWO_6$ at 15 K and 9 K, respectively. As a consequence, the resulting magnetic structures were investigated separately at 11 K and 6 K. The magnetic structure at 11 K was hardly indexed by a single propagation vector, instead, the combination of two vectors, one commensurate (½, 0, ½) and one incommensurate (0, 0.427, ½), could explain all peaks well. Both of these two vectors were involved in describing the magnetic ordering of both Mn^{2+} and Tb^{3+}. The necessity of combing two propagation vectors was attributed either to some degree of phase separation within the crystal, or to the two vectors only corresponded to a single phase in which the ordering had a commensurate propagation vector but this propagation vector was modulated by an incommensurate component. Interestingly, when the sample passed through the second transition at 9K, a single propagation vector (½, 0, ½) was sufficient to describe the magnetic structure at 6 K. The magnetic satellite peaks were suppressed while the intensity of fundamental reflections increased. So that the magnetic structure at 11 K was a superposition of two propagation vectors. The measured magnetic moment of Tb^{3+} was 7.73 μ_B, in contrast to its theoretical value 9.72 μ_B. The magnetic moment of Mn^{2+} was 5.12 μ_B.

From all the investigations above, it was evidenced that the sublattice of Ln^{3+} was influenced by the ordering of Mn^{2+} ions. No magnetic ordering was observed in the $NaLnMgWO_6$ series without magnetic cation at the B-site, once the B-site was substituted by a magnetic ion (e.g. Mn^{2+}) both magnetic rare-earth cations and the magnetic transition metal cations order simultaneously (e.g. $NaNdMnWO_6$ and $NaTbMnWO_6$). On the other hand, the presence of Ln^{3+} cations also had a relative effect on the ordering of Mn^{2+}.[33] The refined magnetic moments of both rare-earth cations and Mn^{2+} mainly lay within the **a**-**b** plane for both $NaNdMnWO_6$ and $NaTbMnWO_6$, which was supposed to be an effect of the layered A-site ordering resulting in anisotropic exchange interactions. However, this was not the case for $NaLaMnWO_6$ where the rare-earth cation was not magnetic. In principle, there are two pathways for the superexchange interactions between the primary magnetic cations at the B-site (e.g. Mn^{2+}), one is the nearest-neighbor ions connecting through ~90° Mn-O-O-Mn pathway and the other is the next-nearest-neighbor through a ~180° Mn-O-W-O-Mn pathway.[33] It was argued that the latter was more plausible.[33][45] The large distances between the magnetic Mn^{2+} cations could explain the low ordering temperature T_N. It was also noted that the Weiss temperature in magnitude decreased with a decreasing average size of the A- and A'-sites. As the tolerance factor became smaller, the linearity of the Mn-O-W-O-Mn chains decreased resulting in a reduction of orbital overlap, so that the strength of the exchange interactions was reduced. This explains why the Weiss temperature decreased in magnitude when the size of the A/A' site cations became smaller. If the Mn-O-O-Mn pathway was dominating in the superexchange interactions, then each Mn^{2+} ion would be tetrahedrally coordinated to its nearest Mn^{2+} neighbors, which would lead to magnetic frustration. Octahedral tilting was supposed to relieve the frustration.

A few other doubly ordered perovskites $AA'BB'O_6$ were studied in terms of magnetism. $KLaMnWO_6$ was also an antiferromagnet below its T_N of 6K.[45] $NaLaFeWO_6$ and $NaNdFeWO_6$ were both reported to order antiferromagnetically below their corresponding T_N, 25 K and 21 K, respectively.[46] Attempts were made to determine the magnetic structures of both $NaLaFeWO_6$ and $NaNdFeWO_6$. However, for $NaLaFeWO_6$ no magnetic contributions were observed from NPD data down to 12K, although the transition temperature was determined to be around 25 K. This was attributed to either the net magnetic moment being so small that it was hardly detectable, or the magnetic contributions could only be observed below 12 K. The magnetic structure of $NaNdFeWO_6$ could be described by the propagation vector (½, 0, ½), with two magnetic sublattices Fe^{2+} and Nd^{3+}. In the refined model, both magnetic cations ordered mainly within the **a**-**b** plane which was consistent with what was observed from $NaNdMnWO_6$ and $NaTbMnWO_6$. The magnetic study on $NaLaBB'O_6$ (B=Mn, Fe;B'=Nb, Ta) revealed that both $NaLaFeTaO_6$ and $NaLaFeNbO_6$ present dominant antiferromagnetic interactions while $NaLaMnTaO_6$ and $NaLaMnNbO_6$ are dominated by ferromagnetism.[53] In accordance with the absence of a structural long-range ordering on the B-site, none of them demonstrated long range magnetic ordering in the NPD measurements.

1.3.3.2 Dielectric Properties

Dielectric properties were rather less studied experimentally compared to the magnetic properties. Dielectric properties and possible magneto-electric coupling were investigated on $NaLnFeWO_6$ (Ln=La, and Nd).[46] No ferroelectric response was detected for either of them in the temperature range 5 – 300 K, and neither was the ME coupling observed in zero magnetic field or a field of 10 T at the magnetic transitions. Another experimental study on $NaLnMnWO_6$ (Ln=La, Nd, and Tb) also revealed that there was no ferroelectric polarization detected in these compounds.[59] However, Young *et al.*[35] argued that this could be due to the polycrystalline samples and difficulties in poling sintered ceramic pellets.

1.4 Motivation and Outline

As introduced at the beginning of this chapter, both the known Type I and Type II multiferroic materials have their drawbacks, leaving them not suitable for real applications. New materials are being demanded combining both ferroelectric and (anti)ferromagnetic properties in a single phase with a large polarization and a strong ME coupling for technological interests. Novel routines are needed to create such magneto-electric multiferroics. HIF provides a distinct mechanism from the previous ones to generate ferroelectric polarization in layered perovskites and related materials. The coupling of two nonpolar octahedral rotation modes has been demonstrated to be able to induce a polar mode. In addition, octahedral rotations also fairly affect the exchange interactions between magnetic ions. Considering both aspects of the polarization and the magnetism, the mechanism of HIF is potentially able to strongly couple these two properties, meanwhile, to generate a large polarization.

On the basis of HIF, we explored two classes of materials: the Ruddlesden-Popper oxides $NaRMO_4$ (R= Y or La; M= Mn or Cr) and the doubly ordered perovskite family $NaLnCoWO_6$ (Ln= Y, La, Pr, Nd, Sm, Eu, Gd, Tb, Dy, Ho, Er and Yb), pursuing new multiferroic materials.

Ruddlesden-Popper oxides have been shown to demonstrate HIF, both theoretically and experimentally. One remarkable example is the family $NaRTiO_4$ (R= rare-earths)[37], these compounds were reported to lift the inversion symmetry by octahedral rotations. A natural thought to further couple the magnetism and ferroelectricity is to introduce a magnetic ion into the *B*-site (e.g. substitution to Ti here). In this thesis work, intensive attempts were made to synthesize Ruddlesden-Popper oxides $NaRMO_4$ (M= Mn, Cr) containing magnetic ions. However, these attempts failed. A summary of these attempts is listed in Chapter 2.

Doubly ordered perovskites $AA'BB'O_6$ are the other class of materials which were proposed theoretically to present HIF. However, this class of materials has been rather less explored and only a few real compounds have been synthesized experimentally. A theoretical investigation on $AA'MnWO_6$ compounds revealed that the size of the A' rare earth cations plays the crucial role in determining the polarization.[35] Here, we focused on partially new Co based doubly ordered perovskites with the purpose to study the structural and magneto-electric properties evolution as a function of the rare-earth size.

All synthesis work will be discussed and summarized in Chapter2. Methods and techniques for the structural and physical properties study will be introduced in Chapter 3. Structural determination on the basis of Rietveld refinements will be discussed in Chapter 4. Phase transition and modulated structure of

$NaLaCoWO_6$ will be addressed in Chapter 5. Physical properties characterizations will be discussed in Chapter 6. Finally, an overall summary and perspectives will be given in Chapter 7.

Chapter 2: Synthesis and Phase Identification

Synthesis attempts to prepare the doubly ordered perovskite family $NaLnCoWO_6$ (Ln= Y, La, Pr, Nd, Sm, Eu, Gd, Tb, Dy, Ho, Er, and Yb) and introduce magnetic ions (Mn and Cr) into the RP oxides $NaRTiO_4$ (R=Y, La) were performed and will be discussed in this chapter. The relevant synthesis techniques at both ambient pressure and high pressure will be introduced in chapter section 2.1. The differential thermal analysis technique was employed to assist the synthesis work and will be introduced in the beginning of chapter section 2.2. The products of these synthesis attempts were preliminarily characterized by techniques such as X-ray powder diffraction, scanning electron microscopy and energy-dispersive X-ray spectroscopy, all of which will be introduced in chapter section 2.2. Then, in chapter section 2.3, detailed information concerning the synthesis attempts will be addressed. All samples in this study were synthesized by solid state reaction at high temperature (~1000 °C). The doubly ordered perovskites La, Pr, Nd were prepared at ambient pressure while all the other new compounds were prepared at high pressure (~5GPa). Unsuccessful attempts on $NaLaNiWO_6$, $NaNdNiWO_6$ and $NaLaCuWO_6$ (chapter section 2.3.4) and RP oxides (chapter section 2.4) are summarized at the end of this chapter.

2.1 Solid-State Reaction at High Temperature

2.1.1 Ambient Pressure

It is easy to recognize from the name of this technique "Solid-State Reaction" itself that reactions take place between bulk reactants, and solid products are formed finally. During the reaction, atoms have to diffuse from one place to another in order to meet their favorite partners to form the final product. However, more than often, it is quite difficult and takes a long time for atoms in solid-state materials to diffuse.[60] Controlling the diffusion rate is critical to get a time saving reaction and a homogenous product. High temperature is able to provide atoms with energy to overcome the diffusion activation energy barrier. At high temperature, atoms have a much higher diffusion rate and could move more freely to react. As stated above, since the reaction happens between various solid materials, the diffusion distance and the homogeneity are also important parameters to consider. A shorter diffusion distance will make it easier for atoms to meet their partners and a homogenous starting mixture will apparently result in a homogenous product more easily. These two can be facilitated by grinding the starting materials to a mixture of fine powders and making a compact pellet. Even though approaches are applied to improve the completion of the reaction, one or more re-grinding and re-annealing are frequently needed. Last but not least, it is important to have a correct stoichiometric starting mixture. Nonetheless, some elements may be inserted in excess in the starting mixture on purpose, i.e. to compensate for the volatile loss or to get a more favorite impurity if it is difficult to remove all impurities at the same time.

From time to time, high temperature solely is not enough to get a stable phase. Pressure is another fundamental thermodynamic parameter just like temperature, which could influence the reaction. For the sake of enhancing the stabilization, high pressure is required. More details will be discussed in the following part.

2.1.2 High Pressure

High pressure synthesis techniques provide an extra approach to prepare new and novel materials.[61][62] Pressure makes a significant difference to the reaction equilibria, which stabilizes metastable or badly distorted phases. These phases often possess fantastic properties and technological interests. Another effect of pressure is on the reaction rate. In a solid-state reaction, starting materials have to reach an intermediate state before the reactant state. Applying pressure is capable to decrease the energy barrier to reach the intermediate state, therefore, increasing the reaction rate.[63][64]

The apparatus for high pressure synthesis is more complicated than the furnaces used for ambient pressure synthesis. Pressure originates from the hydraulic press. Two devices are employed in this study: the Belt system[65] and the Conac system[66]. Both of them can provide high temperature and high pressure (HT-HP) conditions at the same time.

A picture of the Belt system is shown in Figure 2.1(a), the extreme conditions that can be reached are 1500 °C and 8 GPa. The maximum sample volume that can be prepared in a single synthesis is 0.04cm^3 (~100 mg considering mass), a sketch of the sample container and all auxiliary components is shown in Figure 2.1 (b). All starting materials are put into a capsule made of Au or Pt, these two capsule materials are selected because they are sufficiently inert in most cases. The capsule has a cross section diameter of 3 mm, this small size makes it possible to reach a high pressure, while, compromising with instrumental requirements and cost. At temperatures higher than 1000 °C, the Pt capsule is more favorable since this high temperature is close to the melting temperature of Au. For instance, under the pressure of 5 GPa, the melting point of Au is around 1227 °C[67] while it is around 1827 °C for Pt[68]. The melting temperature is pressure dependent so that it is better to have a check before performing an experiment in order to decide which capsule is more suitable. The powder in the capsule is compressed before being encapsulated, more final product will be obtained if the starting powder is as compact as possible. The encapsulated capsule is surrounded by a pyrophyllite tube and covered by a pyrophyllite cap at each end. All of these can be well filled into a graphite furnace tube. The graphite tube acts as the heater and the heat is generated from the electric current flowing through it. Two pieces of pyrophyllite cell and Teflon gasket aid to fix the sample and the furnace at the center of the middle plate of the Belt system. The pyrophyllite cells also act as the media to transmit the hydrostatic pressure to the sample in all directions. The graphite furnace and the inner capsule are electrically separated by the pyrophylite caps and tube.

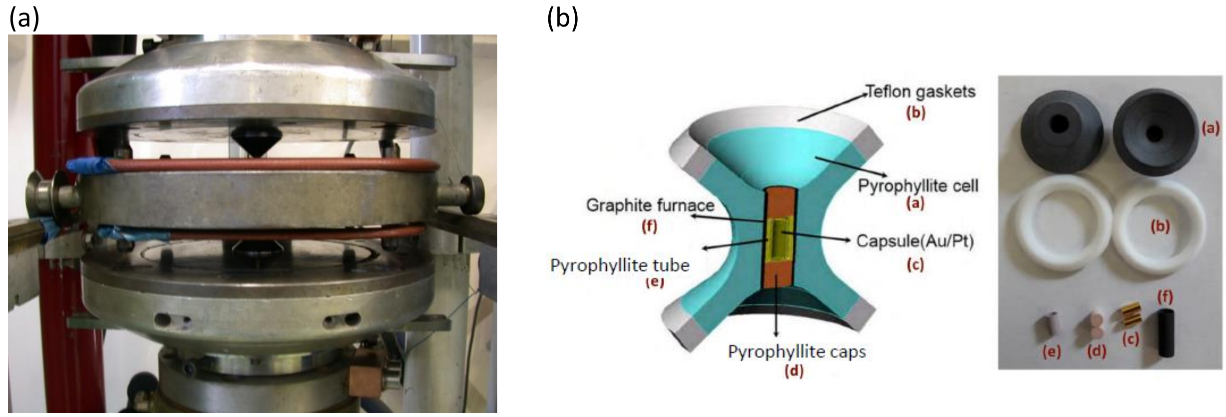

Figure 2.1 (a) A real picture of the Belt system, (b) a sketch of the cell to contain and fix the starting materials for synthesis in the Belt system, a real picture of different components in this cell is also shown. [M. Legendre at Institut NEEL]

Pressure is transmitted from the apparatus to the reaction unit by two tungsten carbide pistons in the shape of a cone in the directions of top-down and bottom-up, respectively. For a HT-HP synthesis, first the pressure is increased slowly. When the target pressure is reached, an electric current starts to be applied to increase the temperature. The high temperature and high pressure conditions can coexist simultaneously which makes HT-HP synthesis possible.

The other device, the Conac system, is in a different configuration compared to the Belt system. A picture of the Conac 40 system is shown in Figure 2.2(a). The extreme conditions can be reached in this system are 1500 °C and around 7 GPa. An advantage of Conac system is that the sample volume can be as large as 0.80 cm^3 (~ 2g considering mass). The main principles of preparing the sample reaction unit are quite similar to the ones used in the Belt system as illustrated in Figure 2.2(b), except that the components of molybdenum slices and copper electric contacts are placed at the two ends of the entire unit to conduct electric current to the graphite furnace. Differently from the Belt system where the reaction unit sits at the center of the middle plate and pressure comes from top and bottom pistons, the Conac system only has two plates. As the volume of the sample is much larger than the one in the Belt system in a single synthesis, it needs much more higher forces to obtain the same pressure compared with the Belt system. However, the capability of applying forces is limited, which means that the Conac system can only reach a lower maximum pressure compared to the Belt system. Meanwhile, a larger quantity of the sample also requires a longer reaction time in the Conac system.

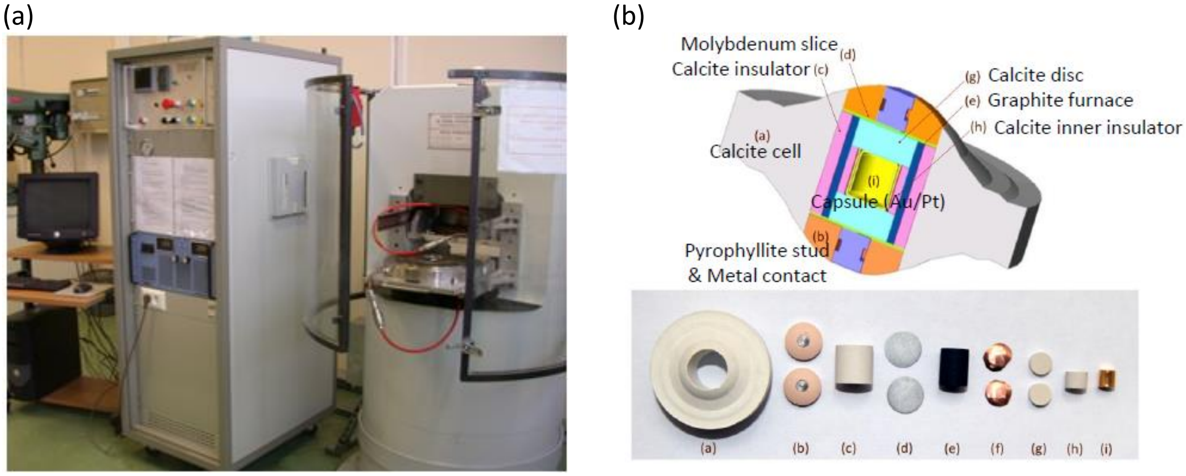

Figure 2.2 (a) A real picture of the Conac system, (b) a sketch of the cell to contain and fix the starting materials for synthesis in the Conac system, a real picture of different components in this cell is also shown. [M. Legendre at Institut NEEL]

2.2 Thermal Analysis and Phase Identification Techniques

2.2.1 Differential Thermal Analysis (DTA)

Thermal analysis is a convenient and widely used technique to track the solid-state reaction procedure. DTA measurement is based on the temperature difference between the inert reference and the sample studied.[69] For example, in this study, Al_2O_3 was taken as the reference since it is thermally inert up to around 1900 °C. The reference and the sample are measured under identical conditions, the differences in temperature between them are recorded as a function of temperature (or time) during both heating and cooling procedures. As the reference material is thermally stable, there is no thermal change happening to it. As a result, any transformation of the sample can be detected from the temperature difference, because heat capacity change is involved in all phase changes. If the sample temperature increases faster than that of the reference, then an exothermic process happens. In contrary, if the sample temperature increases more slowly than that of the reference, then an endothermic process takes place. In this study, DTA measurements were mainly employed as an approach to determine out a good reaction temperature. Besides the high sensitivity of this technique to probe the thermal changes during a reaction, it only needs a small amount of starting materials (tens of mg) and takes a shorter time (~30 min) for a quick examination on the reaction conditions. Even though the product of the DTA measurement is normally composed of several phases due to kinetic issues, it is already able to provide information on whether the target phase is producible or not.

2.2.2 X-ray Powder Diffraction (XRPD)

Basically, to understand the structure of crystallized materials is of primary importance for further and deeper understanding on the properties of thesematerials. However, atoms are too small to be observed directly by visible light (~4000 to ~7000 Å).[70] Fortunately, the wavelengths of X-rays lie in the order of atomic sizes and interatomic spacings, making it suitable for probing the atomic structure of crystals. X-rays are a kind of electromagnetic radiation, with wavelengths between ~0.1 Å and ~100 Å. The most frequently used in crystallographic study are those with wavelengths lying between ~0.5 Å and ~2.5 Å, since the observed shortest interatomic spacings in both organic and inorganic materials are of the same order. Nonetheless, it is very difficult to image individual atoms by focusing X-rays via a lens, because the refraction index of X-rays is close to unity for all materials. This makes a direct observation on atoms impossible. Nature never lets things down, an indirect approach, X-ray diffraction, acts as an alternative approach to study the crystalline structure by transforming the three dimensional ordered structure into reciprocal space. X-ray diffraction is a conventional technique for the structural study, as it is easily accessible in the laboratory and not expensive to perform. The diffraction phenomenon, for all sorts of radiation, can only be established when the radiation wavelength is of the order of the interatomic spacing.

As pointed out above, X-rays are electromagnetic radiations in nature, thus the interaction between X-rays and materials is essentially between the electric component of X-rays and the electrons surrounding atoms. Braggs' Law is mostly used to describe the diffraction phenomenon as shown in Figure 2.3.

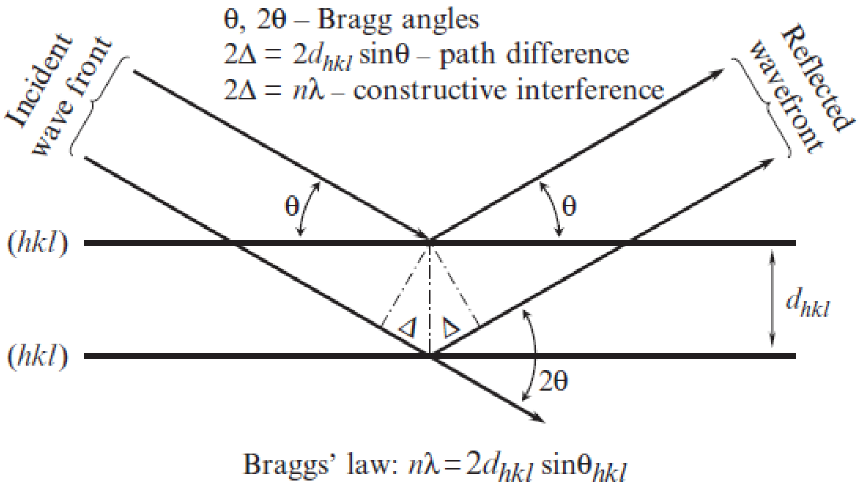

Figure 2.3 Illustration of Bragg's Law.[70]

Imagine there are a set of atomic planes indexed (*hkl*) as shown in this figure, with distances between two neighboring planes d_{hkl}. An incident beam with parallel waves and a constant wavelength λ propagates towards this atomic plane set, the angle between the propagation vector of the incident beam and the atomic planes being defined as θ. Assuming the atomic planes act as mirrors, the incident beam is reflected by the atomic planes into a reflected beam with parallel waves and constant wavelength λ as well. The angle formed between the reflected beam and the atomic planes is also θ as shown in Fig. 2.3. It is easily found that there is a beam propagation path difference 2Δ between waves who interacted with two consecutive atomic planes. The constructive interference is only observed when 2Δ = nλ, where n is an integer, which leads to the formalism of Braggs' Law $2\, d_{hkl} \sin \theta_{hkl} = n\lambda$. Even though the radiation beam is diffracted rather than reflected by atomic planes in reality, Braggs' Law provides a simple way to understand the key parameters involved in the diffraction phenomenon.

Normally, XRPD is used to determine the structure of materials since it is easier to prepare samples in the form of powder rather than big-size single crystals and many materials can only be obtained as powders. When the powder sample is irradiated by X-rays, diffraction phenomena take place for each crystallite according to Braggs' Law. As shown in Figure 2.4 (a), $\mathbf{k_0}$ is the incident beam wavevector, $\mathbf{k_1}$ is the diffraction beam wavevector, and $\mathbf{d^*_{hkl}}$ is the reciprocal lattice vectors. The diffracted wavevectors $\mathbf{k_1}$ from the same planes but different crystallites form a cone with a solid angle 4θ. As a result, a ring is observed from the detector which is called Debye ring. In reality, there are normally many sets of crystallographic planes diffracting simultaneously, then there are many Debye rings generated as shown in Figure 2.4 (b). In a conventional experiment, only the fraction of a narrow rectangle centered at the circumference of the equatorial plane of the Ewald's sphere is measured as the scattered intensity data. It is therefore very important to have a considerable number of grains with complete random orientations for a sufficient intensity statistics and evenly distributed intensity over the Debye rings. Even though XRPD is only able to present a one dimensional projection of the three dimensional reciprocal space, it is able to provide accurate structural information and has been employed for many decades. There are three key factors controlling the quality of the XRPD pattern: the nature and the energy of the radiation, the instrumental resolution and the physical and chemical aspects of the sample itself.

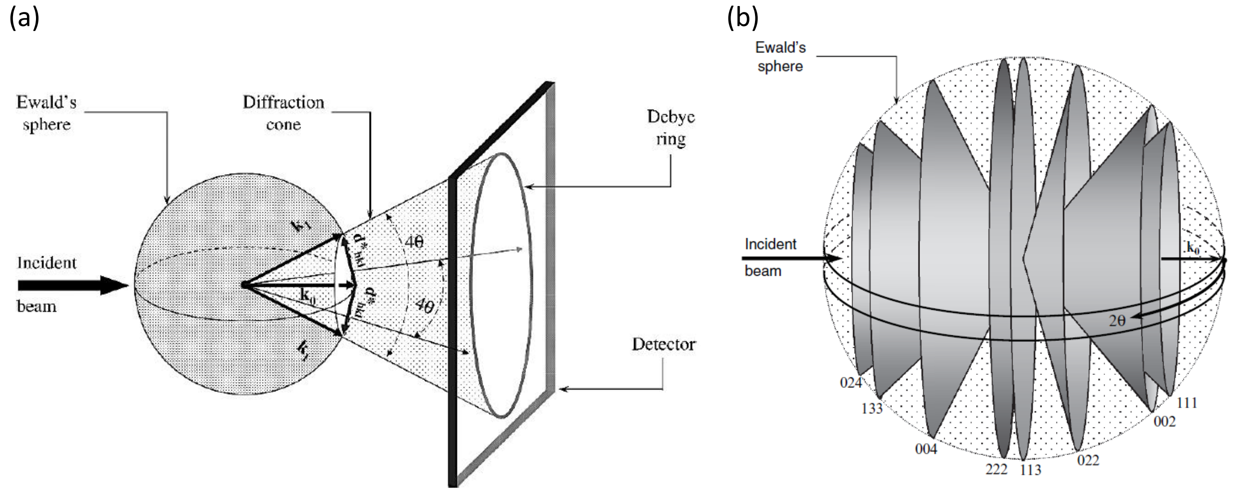

Figure 2.4 (a) the diffraction phenomenon of an infinite number of the completely randomly oriented reciprocal lattice vectors **d*$_{hkl}$** with the same length. A diffraction cone is obtained and the cross section of this cone in the shape of ring is recorded by the detector, the latter ring is called Debye ring. (b) a schematic view of the diffraction cones from various **d*$_{hkl}$** with different (*hkl*) indices.[70]

The XRPD patterns shown in this chapter were measured by the laboratory X-ray diffractometer D5000T (Siemens). It employs the transmission geometry as shown in Figure 2.5, the radiation is Cu Kα1 selected by a Ge (111) primary beam monochromator and the scattered beam is detected by position sensitive detectors. It has the advantage of performing high quality measurements for a small amount of powder in a short period, which is especially crucial for HT-HP synthesis where the sample quantity is normally very small. During the measurement, a transparent sticky tape is used to support the powder sample on the sample holder. As stated above, it is better to have a fine powder and maximize the orientation randomness as much as possible. For all measurements, a step size of 0.032° in 2θ was chosen in order to well define the measured peaks, at least 8 – 12 points needed within one half maximum full-width (without obvious peak overlap) of a well-resolved peak.[70] Concerning the measurement time, for checking starting materials, one hour is sufficient; while for examination of the sample, at least 3 hours were performed to get better statistics. For strongly absorbing samples or high quality data acquisition, longer measuring time is essential.

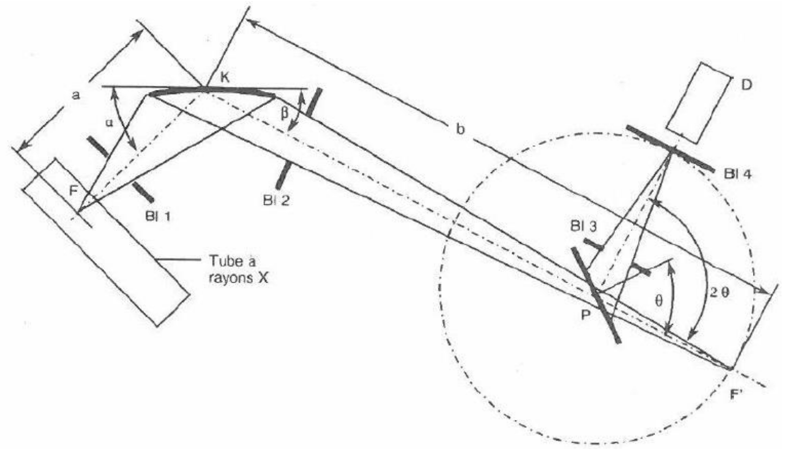

Bl 1: Crystal Entrance Aperture
Bl 2: Crystal Output Aperture
Bl 3: Anti-diffusion Aperture
Bl 4: Aperture of The Detector
D: Detector
F: Focus of The Tube
F': Focus Point
K: Monochromator Crystal
P: Sample

Figure 2.5 The geometry of the D5000T diffractometer in transmission mode.[71][72]

2.2.3 Scanning Electron Microscope (SEM) and Energy-Dispersive X-ray Spectroscopy (EDX)

It must be a pity if a sample is prepared in hand but it cannot be visualized to study its topology and morphology. Optical microscopy is widely used to observe small structures, to gain detailed information on samples from a reflected light signal. However, the wavelength of light limits the resolution of optical microscopy, allowing a magnification only up to 1000-2000 times. For small samples less than 100 nm in one observation dimension, it is very difficult to have a satisfactory image in this magnification range. Electron microscopy is an excellent alternative to optical microscopy, due to its higher resolution which can be up to 0.05 nm, compared to the best resolution of an optical microscope around 500 nm. Besides visualization, more information can be obtained from the interaction between electrons and atoms, like identifying specifically the sort of detected elements.

When the incident beam reaches the sample, electrons start to be inelastically or elastically scattered by the atoms in the sample. However, the interaction volume is normally very small due to the limited energy of incident electrons. As shown in Figure 2.6 (a), the interaction volume has a border which electrons with an average energy equal to the thermal kinetic energy kT. Two factors, the incident beam energy and the atomic number of the elements constituting the sample, have effects on the dimensions of the interaction volume. There are two primary parameters characterizing the interaction processes: the diffusion depth **X_D** is the depth beyond which incident electrons start to be randomly scattered, and the penetration depth **X_R** is the furthest depth that electrons are able to reach with a final energy reduced to the thermal kinetic energy kT. Both penetration depth **X_R** and diffusion depth **X_D** are larger for smaller atomic number elements and higher incident beam energies.

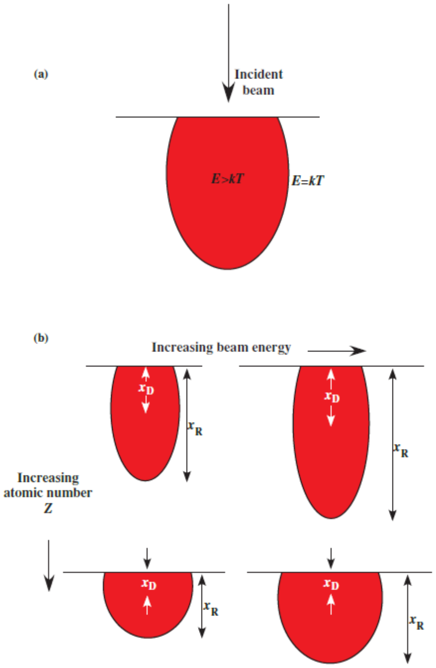

Figure 2.6 (a) The interaction volume of the sample with the electron beam, the boundary is defined as the place where the average energy of electrons reaches the thermal kinetic value kT; (b) The interaction volume depends on both the incident beam energy and the atomic number of the elements in the sample; two parameters X_D, the diffusion depth, and X_R, the penetration depth, can be used to characterize the interaction volume.[73]

A schematic view of signals generated from the interaction between the electron beam and the sample in SEM is shown in Figure 2.7.

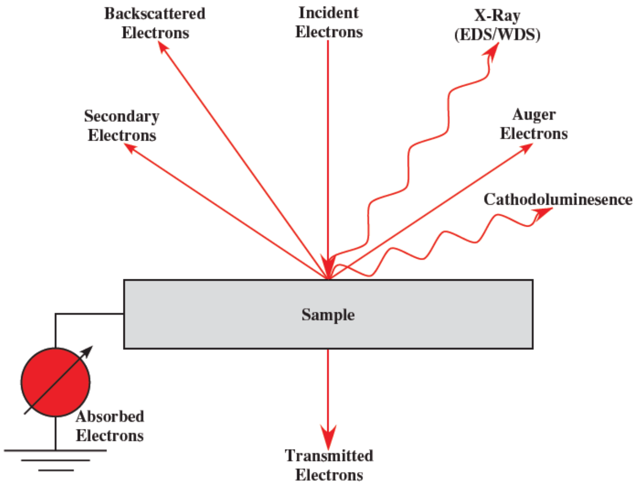

Figure 2.7 A schematic view of various signals generated from the interaction between the incident electron beam and the sample.[73]

The SEM results of this study were obtained on a FESEM Zeiss Ultraplus equipped with secondary electron and backscattered electron detectors and EDX (Bruker).

Secondary Electrons (SE) are electrons excited by either the incident beam or the backscattered electrons. SE have such a low energy (< 50 eV) that only those generated from the surface (10nm in depth) are able to escape and be detected. The signal from SE is therefore a good tool to study the surface topology and morphology. Both the work function of the surface and the incident beam energy play a crucial role in the generation of SE. The intensity of this signal is also influenced by the angle between the incident beam and sample surface, with a higher angle SE are closer to the surface making it easier for them to escape from the surface and to be detected.

Backscattered Electrons (BE) can be either elastically or inelastically scattered by angles greater than 90°. Elastically scattered BE have a comparable energy as electrons in the incident beam. While inelastically scattered BE experience several inelastic interactions with nuclei and electrons before escaping the surface of the sample, if enough energy is still remaining. The signal from BE is very sensitive to the atomic number, the higher the atomic numbers resulting in stronger signals. At the same time it is also influenced by the angle between the incident beam and the sample surface, the higher angle making the generated electrons closer to the surface. As a consequence, BE signal is useful for both compositional and morphological studies.

Ionization of atoms will take place when the energy of the incident beam exceeds the energy required to eject electrons from atoms. The ionization process is accompanied by an inelastic interaction and an energy transfer from the incident electrons to the atoms. The excited atoms decay to their ground state by emission of X-rays. Emitted characteristic X-rays have specific energies corresponding to the differential energies between certain shells. Every element has its own characteristic X-ray energies. EDX takes advantage of this characteristic X-ray signal to study compositional information qualitatively and quantitatively. EDX is able to collect the excited X-rays signal highly efficiently over a wide energy range, simultaneously; however, the energy resolution is sometimes a hindrance resulting in overlap of the characteristic X-rays peaks of different elements.

2.3 Syntheses of Doubly Ordered Perovskites $NaLnCoWO_6$ (Ln= Y, La, Pr, Nd, Sm, Eu, Gd, Tb, Dy, Ho, Er and Yb)

2.3.1 High Temperature and Ambient Pressure

$NaLaCoWO_6$, $NaPrCoWO_6$, and $NaNdCoWO_6$ were synthesized at high temperature under ambient pressure in this study. These three samples were already obtained before, $NaLaCoWO_6$ was firstly synthesized by Arillo *et al.*[47] in 1997, a mixture of $NaNO_3$, $La(NO_3)_3{\cdot}6H_2O$ and $Co(NO_3)_2{\cdot}6H_2O$ and WO_3 was prepared by a sol-gel technique and then sintered at 225 °C for 24h, followed by 500 °C for 72h, finally 900 °C for 72h. $NaPrCoWO_6$ was prepared for the first time by King,[74] the starting materials were Na_2CO_3, La_2O_3, $CoCO_3$ and WO_3, a ternary oxide $CoWO_4$ was prepared as a precursor, then a mixture together with the Na_2CO_3 and La_2O_3 was sintered at 950 °C. $NaNdCoWO_6$ was firstly reported by King *et al.*,[45] a precursor $CoWO_4$ was also prepared in this case and mixed with Na_2CO_3 and Nd_2O_3 as the starting mixture. The final annealing temperature was 975 °C.

Despite the fact that the compounds $NaLaCoWO_6$ and $NaNdCoWO_6$ were obtained before and the recipe is already there, preparing a "pure" sample is not always so easy. Details about the syntheses attempts of these three samples pointed out above are discussed in the following. A summary of the best synthesis conditions can be found in chapter section 2.3.3.

$NaLaCoWO_6$

The first trial in this study was done by using the same starting materials and sintering procedures proposed by Arillo *et al.*[47] without the sol-gel preparation, and the temperature raising rate was set at 2.5 °C/min. The syntheses attempts with starting materials containing nitrate are classified as the nitrate route, in comparison with the other route, the carbonate route, which will be discussed later. The starting powders were pressed into a pellet and then left in an alumina crucible for reaction. The furnace used was a tubular one as shown in Figure 2.8. The compact sample became very loose after sintering which was believed due to the gas produced from decomposing the nitrates. Even though the quality of the product was not satisfactory, it was largely improved after a post-treatment of re-grinding and re-annealing at 900 °C for 12 hours. A pellet was also prepared for the post-treatment. Phase identification was done with XRPD, all stored crystallographic information of compounds composed by any combination of Na, La, Co, W and O elements in the ICDD PDF 4+ database implemented in the *EVA* software of the DIFFRAC Suite (Bruker AXS GmbH, Oestliche Rheinbrueckenstr. 49, D-76187, Karlsruhe, Germany) were compared with the experimentally observed diffractogram. $NaLaCoWO_6$ and Na_2WO_4 were picked out as shown in Figure 2.9. The impurity Na_2WO_4 is very minor and the quality of $NaLaCoWO_6$ is satisfactory. The presence of this impurity is not a big problem since it can be removed by washing.[42] In order to optimize the synthesis method, some other tests were tried as listed in Table.2.1.

Figure 2.8 A picture of the tubular furnace employed.

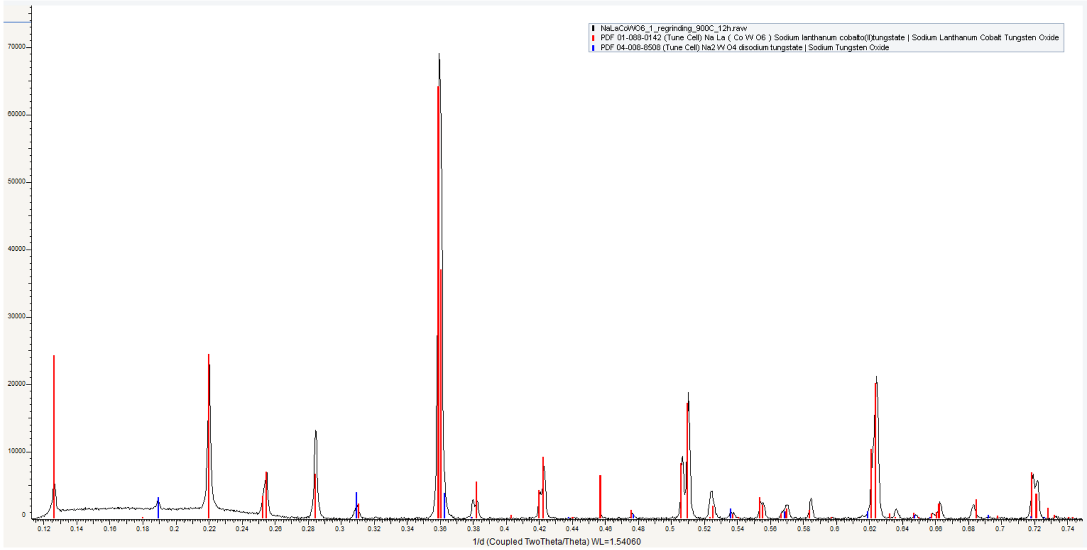

Figure 2.9 The XRPD pattern of the experiment NaLaCoWO_1 after the post-treatment, the black curve is the observed pattern. This pattern was compared with stored phase information in the ICDD PDF 4+ base implemented in the *EVA* application. The red peaks correspond to the target phase $NaLaCoWO_6$, and the blue peaks correspond to the impurity Na_2WO_4.

The reaction duration in the reported literature[47] is very long, a question was raised after the first trial whether it is necessary to have such a long sintering time. Maybe yes, because the nitrates in the starting materials have to decompose before reacting, and the diffusion process after the decomposition could also take time. A test with a short duration for each temperature stage was carried out, and at the end of each stage the products were taken out and checked by XRPD (Experiment reference: $NaLaCoWO_6$_2). The phases in these products are listed also in Table 2.1. After the treatment at 225 °C, all nitrates except $La(NO_3)_3$ already decomposed, while after the treatment at 500 °C, $NaLa(WO_4)_2$, which was a main impurity in this and following tests, already formed with some other intermediate phases. No starting materials could be found any more. At the end of the final stage, the target phase $NaLaCoWO_6$ was obtained together with several impurities. Two post-treatments at 900 °C for 12 hours and 900 °C for 24 hours were applied to improve the quality of the sample. As listed in Table. 2.1, three impurities still remained. As stated above, Na_2WO_4 is not a big issue since it can be washed away by water as reported before,[42] in contrast, $NaLa(WO_4)_2$ and Co_3O_4 seemed more difficult to remove. The appearance of Co_3O_4

could be very annoying since it is a magnetic material. The next parameter to tune was the annealing temperature and its raising rate. Instead of dividing into three annealing stages, the sample was heated straightforward to 900 °C at a much faster speed 10 °C /min (Experiment reference: $NaLaCoWO_6$_3). Unfortunately, given that two post-treatments were operated after the first sintering, there was still the impurity Co_3O_4 which was badly unfavorable. So far, the best recipe was the one in the first experiment, in order to further explore any tunable parameter to optimize the synthesis and avoid interrupting the reaction at 225 °C, the same heating procedure as in the first experiment was employed and the products were taken out at the end of the stage at 500 °C and examined by XRPD (Experiment reference: $NaLaCoWO_6$_4). Nonetheless, the impurities $NaLa(WO_4)_2$ and Co_3O_4 appeared again even after the post-treatment. Then another synthesis was tried by just copying the procedure of the first experiment with another furnace (Experiment reference: $NaLaCoWO_6$_5). It worked well for removing the $NaLa(WO_4)_2$ impurity but the magnetic impurity Co_3O_4 still existed. In parallel, it was noted that the products in the experiment $NaLaCoWO_6$_3 were very close to satisfactory except for the appearance of Co_3O_4. One possible reason could be that the temperature was raised too fast otherwise the nitrates would have more time to decompose, putting them in a more ready state for reaction. Based on this hypothesis, the experiment $NaLaCoWO_6$_6 was performed by increasing the temperature to 225 °C and staying at this temperature for 24 hours to make the reactants ready, and then to 900 °C very rapidly at a rate of 30 °C/min and staying at this temperature for 2 hours. From the result of the experiment $NaLaCoWO_6$_2, it was known that at 225 °C most nitrates in the starting materials would decompose and the result of the experiment $NaLaCoWO_6$_3 suggested that even if the reaction time was limited to 1 hour it was still sufficient for the target phase $NaLaCoWO_6$ to form. These are the reasons why the conditions were selected in the experiment $NaLaCoWO_6$_6. However, this trial did not give a satisfactory product once again.

So far, the conditions in the first experiment were the best ones, in order to produce a larger quantity for the following characterizations, the exact conditions were used in the experiment $NaLaCoWO_6$_7. Surprisingly, the product quality of this experiment was not comparable to the one in the first experiment and the same impurities appearing several times in the precedent experiments formed again even after the post-treatment. The appearance of $NaLa(WO_4)_2$ and Co_3O_4 in a number of syntheses indicated that there may not be sufficient Na, or Na and La in the starting materials. In the target compound $NaLaCoWO_6$, the ratio of cations is 1:1:1:1, while in $NaLa(WO_4)_2$, the component of Na is 0.5, less than 1. Considering Na is volatile at high temperature, some compensation for Na could be required. At the same time, La appeared mainly in $NaLaCoWO_6$ and $NaLa(WO_4)_2$. In $NaLa(WO_4)_2$ the component of La is also less than 1 which could suggest there was a lack of La also. On the other hand, it can be seen that some Co preferred to go into the impurity Co_3O_4 rather than $NaLaCoWO_6$ which could also suggest there is not enough Na and La. So two following tests were tried by either putting only Na in 2% excess (Experiment reference: $NaLaCoWO_6$_8) or putting both Na in 2% excess and La in 5% excess (Experiment reference: $NaLaCoWO_6$_9). It can be seen from the phase information in Table. 2.1 that neither of them could solve the impurity problems effectively. Considering these impurities were very difficult to remove by post-treatment when they once appeared, no further effort was made to these two tests.

Even though the impurities in the experiments above were very difficult to remove, the positive aspect was that the target phase always appeared in the final product.

Table 2.1 A summary of synthesis attempts to prepare $NaLaCoWO_6$ in the nitrate route, despite the fact that $NaLaCoWO_6$ has been obtained in these experiments, the purity of the target phase is far from satisfactory.

Experiment Reference	Staring materials	Synthesis Conditions	Phases
$NaLaCoWO_6$_1	$NaNO_3$, $La(NO_3)_3{\cdot}6H_2O$, $Co(NO_3)_2{\cdot}6H_2O$, WO_3	225 °C for 24 hours, 500 °C for 72 hours, 900 °C for 24 hours; 1st re-annealing at 900 °C for 12 hours; 2.5 °C /min temperature raising rate for all.	$NaLaCoWO_6$, Na_2WO_4 (little)
$NaLaCoWO_6$_2	$NaNO_3$, $La(NO_3)_3{\cdot}6H_2O$, $Co(NO_3)_2{\cdot}6H_2O$, WO_3	225 °C for 2 hours, 500 °C for 2 hours, 900 °C for 10 hours; 1st re-annealing at 900 °C for 12 hours; 2nd re-annealing at 900 °C for 24 hours; 2.5 °C /min temperature raising rate for all.	225 °C: WO_3, $La(NO_3)_3$, Co_3O_4 500 °C: $NaLa(WO_4)_2$, La_2WO_6, Na_2WO_4, Co_3O_4, $Na_5La(WO_4)_4$, $La_{14}W_8O_{45}$, $Na_{0.6}CoO_2$ 900 °C: $NaLaCoWO_6$, Na_2WO_4, $La_{14}W_8O_{45}$, Co_3O_4, $NaLa(WO_4)_2$, $La_6W_2O_{15}$, La_6WO_{12} 1st re-annealing: $NaLaCoWO_6$, Na_2WO_4, $NaLa(WO_4)_2$, Co_3O_4(quite few) 2nd re-annealing: $NaLaCoWO_6$, Na_2WO_4, $NaLa(WO_4)_2$, Co_3O_4(decreased)
$NaLaCoWO_6$_3	$NaNO_3$, $La(NO_3)_3{\cdot}6H_2O$, $Co(NO_3)_2{\cdot}6H_2O$, WO_3	900 °C for 1 hour with temperature raising rate 10 °C /min; 1st re-annealing at 900 °C for 12 hours; 2nd re-annealing at 900 °C for 24 hours; 2.5 °C /min temperature raising rate for the latter two.	900 °C: $NaLaCoWO_6$, Na_2WO_4, $NaLa(WO_4)_2$, Co_3O_4 1st re-annealing: $NaLaCoWO_6$, Na_2WO_4 (decreased), Co_3O_4(decreased) 2nd re-annealing: $NaLaCoWO_6$, Na_2WO_4, Co_3O_4(decreased)
$NaLaCoWO_6$_4	$NaNO_3$, $La(NO_3)_3{\cdot}6H_2O$, $Co(NO_3)_2{\cdot}6H_2O$, WO_3	225 °C for 24 hours, 500 °C for 72 hours, 900 °C for 24 hours; re-annealing at 900 °C for 12 hours; 2.5 °C /min temperature raising rate for all.	500 °C: $NaLa(WO_4)_2$, La_2WO_6, $Na_5La(WO_4)_4$, Co_3O_4, Na_2WO_4 900 °C: $NaLaCoWO_6$, $NaLa(WO_4)_2$, Na_2WO_4, Co_3O_4, $La_2W_3O_{12}$ Re-annealing: $NaLaCoWO_6$, $NaLa(WO_4)_2$, Na_2WO_4, Co_3O_4
$NaLaCoWO_6$_5	$NaNO_3$, $La(NO_3)_3{\cdot}6H_2O$, $Co(NO_3)_2{\cdot}6H_2O$, WO_3	225 °C for 24 hours, 500 °C for 72 hours, 900 °C for 24 hours; re-annealing at 900 °C for 24 hours; 2.5 °C /min temperature raising rate for all.	900 °C: $NaLaCoWO_6$, Na_2WO_4, $LaCoO_3$, $Na_{0.54}WO_3$, Co_3O_4 Re-annealing: Na_2WO_4, $NaLaCoWO_6$, $LaCoO_3$, $La_{0.14}WO_3$, Co_3O_4
$NaLaCoWO_6$_6	$NaNO_3$, $La(NO_3)_3{\cdot}6H_2O$, $Co(NO_3)_2{\cdot}6H_2O$, WO_3	225 °C for 24 hours with temperature raising rate 2.5 °C/min, 900 °C for 2 hours with temperature raising rate 30 °C/min	900 °C: $NaLaCoWO_6$, $NaLa(WO_4)_2$, Na_2WO_4, $La_2W_3O_{12}$, Co_3O_4, WO_3

Experiment Reference	Staring materials	Synthesis Conditions	Phases
$NaLaCoWO_6$_7	$NaNO_3$, $La(NO_3)_3 \cdot 6H_2O$, $Co(NO_3)_2 \cdot 6H_2O$, WO_3	225 °C for 24 hours, 500 °C for 72 hours, 900 °C for 24 hours; Re-annealing at 900 °C for 12 hours; 2.5 °C /min temperature raising rate for all.	900 °C: $NaLaCoWO_6$, Na_2WO_4, $NaLa(WO_4)_2$, Co_3O_4, $La_6W_2O_{15}$ Re-annealing: $NaLaCoWO_6$, $NaLa(WO_4)_2$, Na_2WO_4, Co_3O_4, Na_xWO_3
$NaLaCoWO_6$_8	$NaNO_3$ (2% excess), $La(NO_3)_3 \cdot 6H_2O$, $Co(NO_3)_2 \cdot 6H_2O$, WO_3	225 °C for 24 hours, 500 °C for 72 hours, 900 °C for 24 hours; 2.5 °C /min temperature raising rate for all.	900 °C: $NaLaCoWO_6$, Na_2WO_4, $NaLa(WO_4)_2$, Co_3O_4, Na_xWO_3
$NaLaCoWO_6$_9	$NaNO_3$ (2% excess), $La(NO_3)_3 \cdot 6H_2O$ (5% excess), $Co(NO_3)_2 \cdot 6H_2O$, WO_3	225 °C for 24 hours, 500 °C for 72 hours, 900 °C for 24 hours; 2.5 °C /min temperature raising rate for all.	900 °C: $NaLaCoWO_6$, Na_2WO_4, $NaLa(WO_4)_2$, Co_3O_4, Na_xWO_3,WO_3

Since the undesired impurities always appeared in all optimized attempts and the good quality of the first experiment could not be reproduced, efforts were made to find another routine rather than changing the temperature increasing procedure, the temperature raising rate, the heating duration, the furnace, the post-treatment and the appropriate starting materials ratio. As stated above, it was observed that the starting materials pellets became loose after sintering which was not favorable in the solid-state reaction. Carbonates and oxides are alternative choices for the starting materials, since Na_2CO_3, $CoCO_3$, and La_2O_3 are common reagents in the lab, and they were used to prepare related compounds in another study,[74][42] therefore they were chosen for further synthesis investigation.

A mixture of Na_2CO_3, $CoCO_3$, La_2O_3 and WO_3 was prepared as the starting material for this new synthesis direction. Na was put in 2% excess to compensate for the loss of Na at high temperature according to King *et al.*[42]. La_2O_3 was pre-heated at 1000 °C before use to remove any absorbed water. This experiment started by a fast DTA test up to 1000 °C with a temperature raising rate of 10 °C/min, a dwelling at this temperature for 30 min, then cooling down to room temperature.

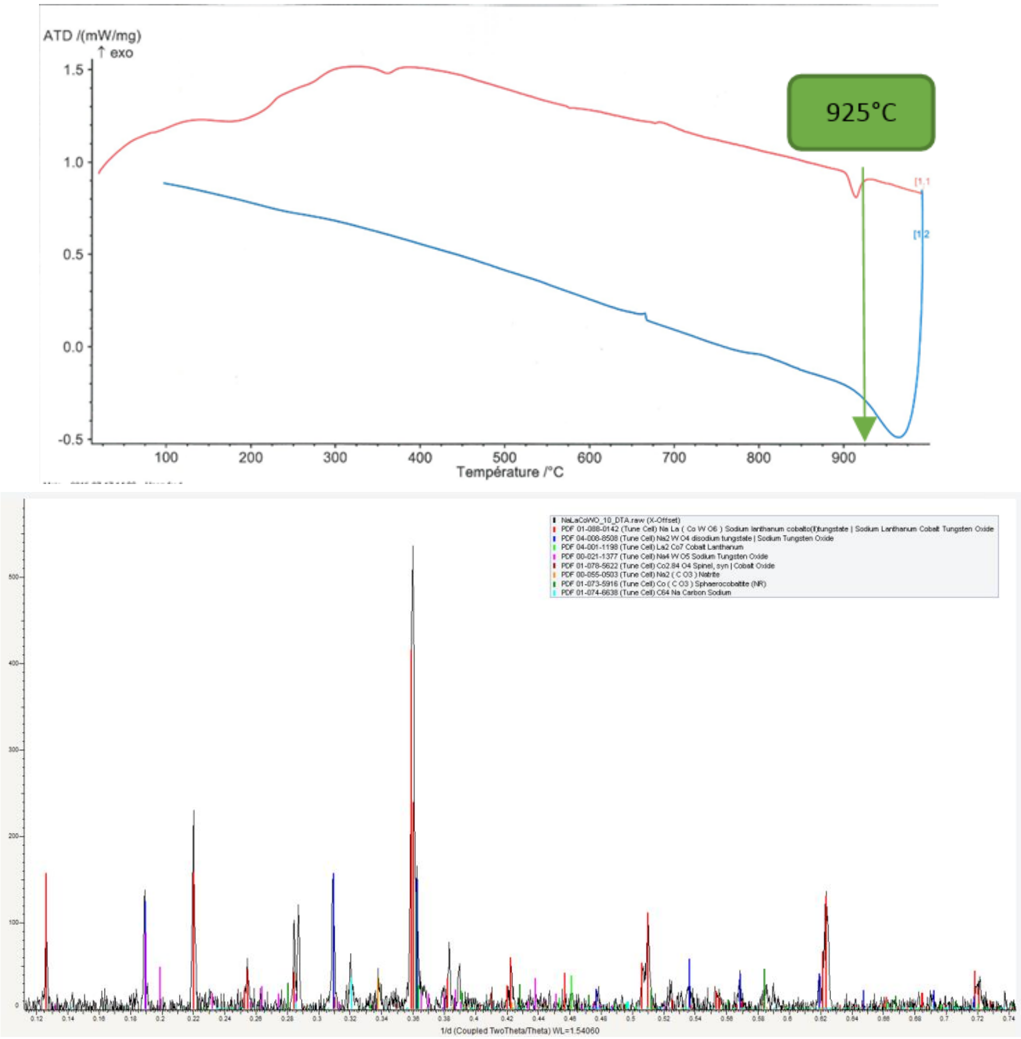
(a)

(b)

Figure 2.10 (a) the DTA result of the experiment $NaLaCoWO_6$_10, the reaction temperature is assigned at 925 °C as pointed out in this figure, the product was examined by XRPD (black curve) in (b), the targeted phase (peaks in red) was well formed in this DTA experiment and took the main part in this product.

The result from the DTA analysis is shown in Figure 2.10 (a), either exothermic or endothermic phenomena related to the process of the chemical reaction could be detected. From the DTA result, 925 °C as pointed out in this figure was picked as the reaction temperature. The product was examined by XRPD as shown in Figure 2.10 (b). Although the reaction duration was very short and the mixture was very loose in this DTA experiment, the target phase $NaLaCoWO_6$ formed and accounted for a big proportion in the product. Several impurities appeared also which could be attributed to kinetic issues. With the same mixture, a new synthesis was programmed heating up to 925 °C with the temperature raising rate of 2.5 °C/min and then dwelling at this temperature for 12 hours in order to have a completion of the reaction, finally cooling to room temperature. A post-treatment was carried out with re-grinding and re-annealing at 925 °C in the same procedure as during the first synthesis cycle. The final product was characterized by XRPD and the phases were identified as shown in Figure 2.11. It is clear that the target $NaLaCoWO_6$ compound was the major phase and the impurity Na_2WO_4 is very minor, no other impurities could be found from this XRPD diffractogram.

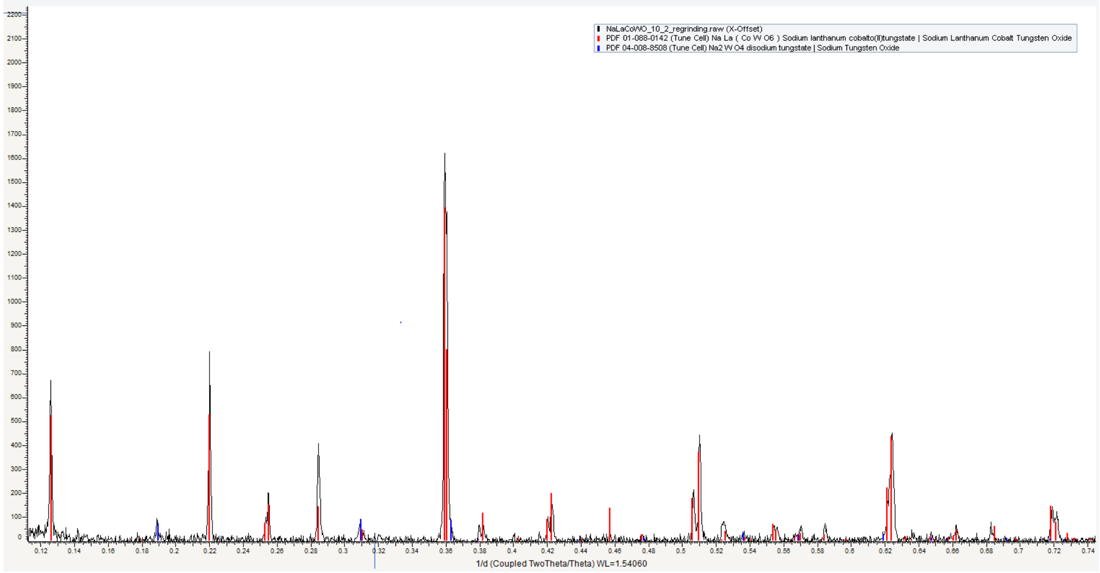

Figure 2.11 the XRPD pattern of the experiment $NaLaCoWO_6$_10 product which was obtained under the synthesis conditions of 925 °C for 12 hours and a post-treatment under the same conditions. The curve in black is the observed XRPD pattern, the red peaks correspond to the target phase $NaLaCoWO_6$, and the blue peaks correspond to the impurity Na_2WO_4. It can be easily seen from the peak intensities that $NaLaCoWO_6$ is the main phase and the impurity Na_2WO_4 is very minor.

This result was encouraging! Na_2WO_4 could be removed by washing,[42] the entire powder sample was put into distilled water and stirred by hand to ensure the impurity Na_2WO_4 was well dissolved. Afterwards, the mixture was filtered with filtration paper "sodipro Ref. 0113P00024". Then only the target phase $NaLaCoWO_6$ was left on the filtration paper and the impurity Na_2WO_4 was gone with the distilled water. The remaining powder with the filtration paper was put into a drying oven at 70°C for several hours. The XRPD result of the washed sample is shown in Figure 2.12. It is clear that the sample after washing was very pure and well crystallized. The same procedure was repeated at least two times, the results were very consistent indicating the reproducibility of this synthesis method. This synthesis with starting materials containing carbonate will be called the carbonate route hereafter and the related conditions are summarized in Table 2.2.

Table 2.2 A summary of synthesis conditions to prepare $NaLaCoWO_6$ in the carbonate route.

Experiment Reference	Staring materials	Synthesis Conditions	Phases
$NaLaCoWO_6$_10	Na_2CO_3 (2% excess), La_2O_3, $CoCO_3$, WO_3	925 °C for 12 hours; 1st re-annealing at 925 °C for 12 hours; 2.5 °C /min temperature raising rate for all.	$NaLaCoWO_6$, Na_2WO_4 (little)

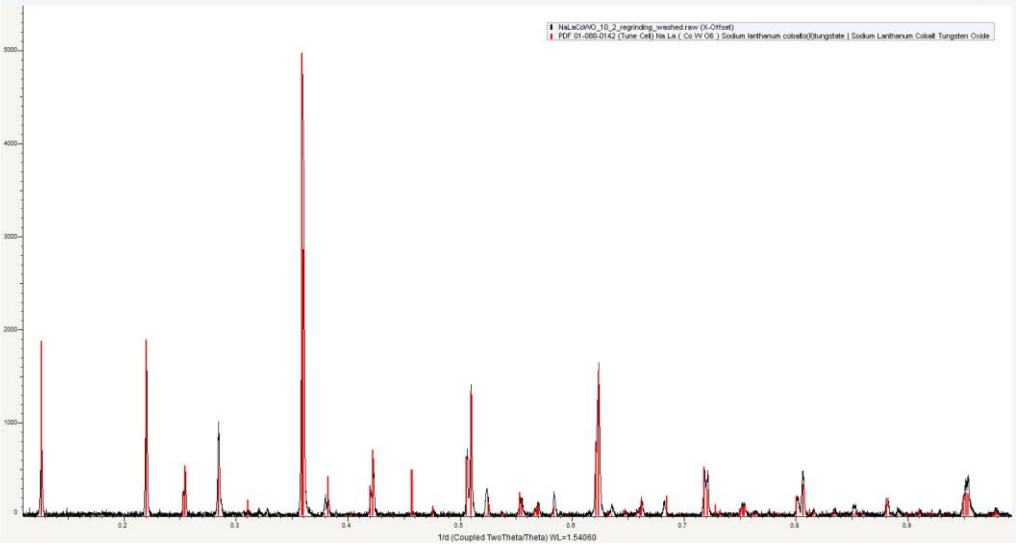

Figure 2.12 the XRPD pattern of the same sample as shown in Figure. 2.11 after being washed. Only the target phase $NaLaCoWO_6$ remained after washing, showing the effectiveness of removing the impurity Na_2WO_4 by washing.

The morphology and composition of the powder sample were studied by SEM and EDX attached to SEM. Figure 2.13 (a) shows the SE SEM image taken from this sample with an accelerating voltage of 3 kV and a working distance of 3 mm. The sizes of particles are not homogenous which suggests different growth processes for different particles. The sample was well crystallized as can be deduced from the formed facets and defined shape which is very consistent with the XRPD pattern. EDX analysis was done for ten distinct spots, characteristic X-ray signals from the elements Na, La, Co, and W were collected and quantified into atomic percentages. A summary of the results from ten spots is listed in Figure 2.13 (b), all the cations were detected and have a ratio very close to the theoretical one. The error bar (Sigma) value is large for Na compared to other elements, which could be attributed to its nature of light element so that the emitted signal was weak leading to a less precise measurement. Oxygen was not quantified since it is a too light element for the emitted signal to be fully detected. With the results of SEM and EDX, it can be concluded that the sample $NaLaCoWO_6$ is well crystallized in the right stoichiometric composition.

(a)

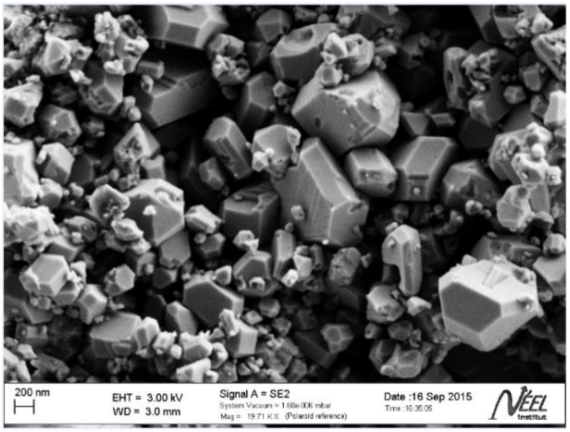

(b)

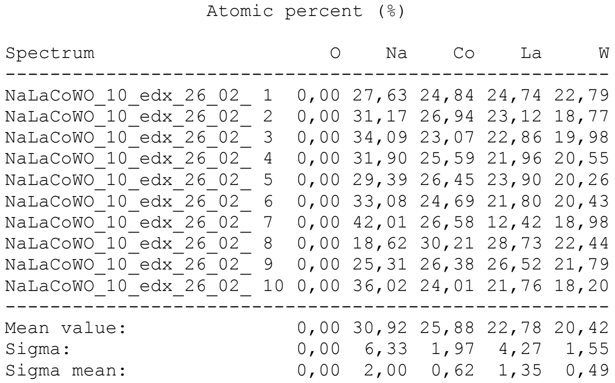

```
                    Atomic percent (%)

Spectrum                      O    Na    Co    La     W
-------------------------------------------------------
NaLaCoWO_10_edx_26_02_ 1  0,00 27,63 24,84 24,74 22,79
NaLaCoWO_10_edx_26_02_ 2  0,00 31,17 26,94 23,12 18,77
NaLaCoWO_10_edx_26_02_ 3  0,00 34,09 23,07 22,86 19,98
NaLaCoWO_10_edx_26_02_ 4  0,00 31,90 25,59 21,96 20,55
NaLaCoWO_10_edx_26_02_ 5  0,00 29,39 26,45 23,90 20,26
NaLaCoWO_10_edx_26_02_ 6  0,00 33,08 24,69 21,80 20,43
NaLaCoWO_10_edx_26_02_ 7  0,00 42,01 26,58 12,42 18,98
NaLaCoWO_10_edx_26_02_ 8  0,00 18,62 30,21 28,73 22,44
NaLaCoWO_10_edx_26_02_ 9  0,00 25,31 26,38 26,52 21,79
NaLaCoWO_10_edx_26_02_ 10 0,00 36,02 24,01 21,76 18,20
-------------------------------------------------------
Mean value:               0,00 30,92 25,88 22,78 20,42
Sigma:                    0,00  6,33  1,97  4,27  1,55
Sigma mean:               0,00  2,00  0,62  1,35  0,49
```

Fig. 2.13 (a) the Secondary Electron (SE) SEM image of the sample $NaLaCoWO_6$_10, the sample is well crystallized which can be observed from the formed facets and defined shapes. EDX analysis in (b) covering ten spots on different particles shows the $NaLaCoWO_6$ composition as expected in this sample.

$NaPrCoWO_6$

With the knowledge of the $NaLaCoWO_6$ synthesis and the reference [74], it was easier to determine the right conditions for the synthesis of $NaPrCoWO_6$. The starting materials were Na_2CO_3, Pr_6O_{11}, $CoCO_3$, and WO_3, where Na was also put into 2% excess. The starting materials were ground to fine powders and pressed into a pellet. An alumina crucible was used as the pellet container. The sample was heated to 950 °C with a temperature raising rate of 2.5 °C/min and dwelling at this temperature for 12 hours. One re-grinding and re-annealing post-treatment under the same conditions was carried out in order to improve the sample quality. Na_2WO_4 also appeared in the product as synthesized, so that the same washing procedure as for the $NaLaCowO_6$ sample was applied to $NaPrCoWO_6$ as well. The powder sample was examined by XRPD. As there was no structural information about $NaPrCoWO_6$ recorded in the ICDD PDF 4+ database and no structural study for $NaPrCoWO_6$ reported, it was impossible to compare the XRPD pattern directly with the $NaPrCoWO_6$ information in the database. Since the size of Pr is very close to that of La, it is reasonable to assume they possess the same structure. As a result, the XRPD pattern was compared with the $NaLaCoWO_6$ model ($P2_1/m$) stored in the ICDD PDF 4+ database implemented in the *EVA* program. The result is shown in Figure 2.14. The peaks after tuning the lattice parameters of the $NaLaCoWO_6$ model fit the $NaPrCoWO_6$ XRPD pattern quite well and the extra peaks were very small, which demonstrated the successful synthesis of $NaPrCoWO_6$ and the high purity of this sample. EDX analysis confirmed the right composition of this sample.

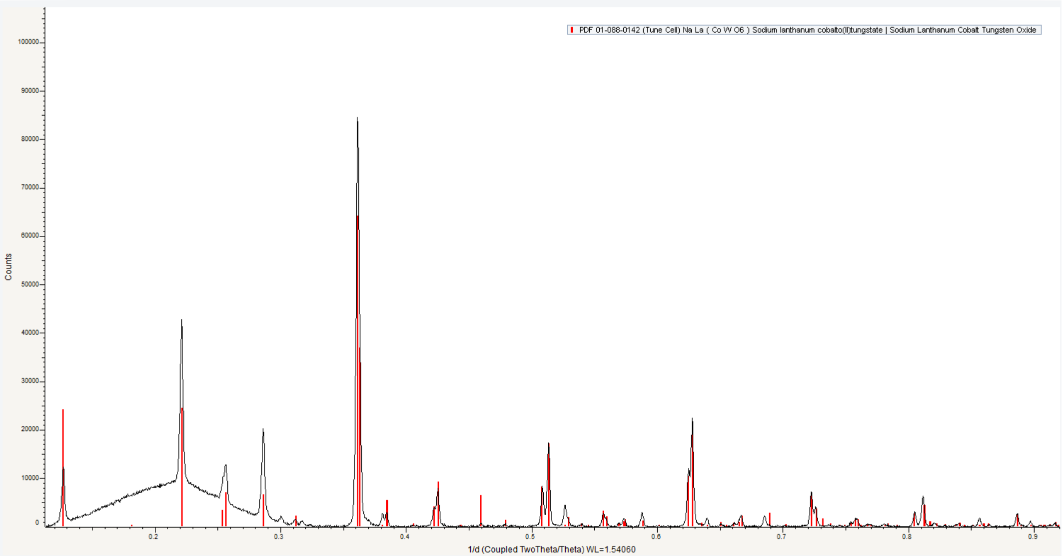

Figure 2.14 The XRPD pattern of the sample $NaPrCoWO_6$ after a post-treatment and washing away Na_2WO_4. The black curve is the observed XRPD pattern, the pattern was compared with the $NaLaCoWO_6$ model (peaks in red) in the ICDD PDF 4+ database base implemented in the *EVA* program. After tuning the lattice parameters of the $NaLaCoWO_6$ model the majority of peaks can be explained indicating the formation of $NaPrCoWO_6$. The extra peaks are very small showing the high purity of the target phase.

It was noted that unlike using La_2O_3 in the $NaLaCoWO_6$ synthesis, Pr_6O_{11} was used as the Pr source in this synthesis. The oxidized state of Ln in $NaLnCoWO_6$ compounds was +3, while in Pr_6O_{11} Pr has a mixed oxidation state of +3 and +4. A trial with starting materials of Na_2CO_3 (Na 2% in excess), Pr_6O_{11}, $CoCO_3$, and WO_3 was carried out in the atmosphere of 5%H_2/95%Ar with DTA. The reduction atmosphere was used to reduce Pr^{4+} to Pr^{3+}. It proved that there was no $NaPrCoWO_6$ formed at all, and the products were mainly Na_2WO_4, WCo_3, W_6Co_7 and $PrO_{1.8}$. So that it was not necessary to reduce the mixed states oxide Pr_6O_{11}, and the synthesis in air already provided a superior sample quality for structural and physical properties characterizations.

$NaNdCoWO_6$

Considering the experimental sequence in time, $NaNdCoWO_6$ was one of the first two compounds attempted to synthesize, together with $NaLaCoWO_6$. It started also with the same procedure reported by Arillo *et al.*[47] and the nitrate route where the starting materials were $NaNO_3$ (5% in excess), $Nd(NO_3)_3·6H_2O$, $Co(NO_3)_2·6H_2O$, and WO_3. A post-treatment was operated at 975 °C for 24 hours, this temperature was selected according to King *et al.*[45]. In all these procedures, the temperature raising rate was 2.5 °C/min. It worked better for $NaNdCoWO_6$ than $NaLaCoWO_6$, the XRPD pattern is shown in Figure 2.15 after the sample was washed to remove the Na_2WO_4 impurity. The main phase was $NaNdCoWO_6$, with minor impurities $NaNd(WO_4)_2$ and CoO. EDX analysis confirmed the $NaNdCoWO_6$ composition in this sample.

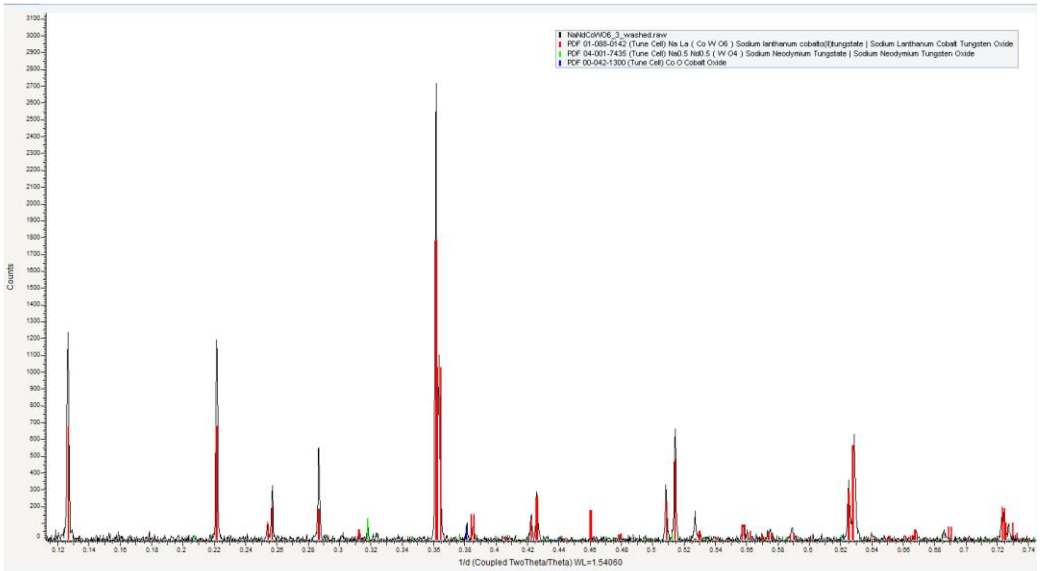

Figure 2.15 the XRPD pattern of the sample $NaNdCoWO_6$ after a post-treatment and washing away Na_2WO_4. The black curve is the observed XRPD pattern, the pattern was compared to the $NaLaCoWO_6$ model (peaks in red) in the ICDD PDF 4+ database implemented in the *EVA* program. After tuning the lattice parameters of the $NaLaCoWO_6$ model the majority of peaks can be explained indicating the formation of $NaNdCoWO_6$. The green peaks stands for the impurity $NaNd(WO_4)_2$, and the blue peaks stead for the impurity CoO. From the comparison of peak intensities between different compounds, it is easily seen that the target phase $NaNdCoWO_6$ is the main phase.

2.3.2 High Temperature and High Pressure (HT-HP)

The compounds $NaLnCoWO_6$ (Ln= Ce, Sm, Eu, Gd, and Tb) were attempted to synthesize at high temperature and ambient pressure.[74] None of them was synthesized successfully in that work, indicating different synthesis mechanisms compared to $NaLaCoWO_6$, $NaPrCoWO_6$ and $NaNdCoWO_6$. In order to explore the syntheses for $NaLnCoWO_6$ with Ln cations smaller than Nd, Gd was selected as a study example to start with. $NaGdCoWO_6$ was already studied in King's work and not synthesized yet, the investigation of $NaGdCoWO_6$ would provide clues not only for $NaGdCoWO_6$ itself but also for the other compounds.

Considering the knowledge discussed in the last section, the first experiment for $NaGdCoWO_6$ was done with starting materials Na_2CO_3 (2% excess), Gd_2O_3, $CoCO_3$ and WO_3. Gd_2O_3 had to be pre-heated at 900 °C for 12 hours before using. The mixture of starting materials was first tested with the DTA facility by increasing the temperature up to 1000 °C at a temperature raising rate of 10 °C/min, dwelling at this temperature for 30 min and then cooling to room temperature in air atmosphere. Not surprisingly, there was no $NaGdCoWO_6$ formed, the product mainly contained Na_2WO_4, Gd_2WO_6 and Co_3O_4, which was consistent with the observation of King. It was easily noted that in the product, the oxidized state of Co was increased from the initial +2 to partially +3. This observation may suggest that it was the change of oxidation state of Co that made the target compound $NaGdCoWO_6$ difficult to form. Therefore an inert atmosphere Ar was added in the same heating procedure, at this time, Co kept a good oxidation state +2 in CoO rather than +3 in Co_3O_4. However, there was still no $NaGdCoWO_6$ formed. A reduction atmosphere 5%H_2/95%Ar was also tried under the same conditions, yet no $NaGdCoWO_6$ was formed neither.

Tuning the atmosphere was not sufficient to synthesize the target compound $NaGdCoWO_6$. If this compound can be synthesized at ambient pressure, there must be another key parameter that should be adjusted to optimize the synthesis, namely the temperature. The highest temperature was extended to 1200 °C with the same starting materials as in air, the temperature raising rate was also 10 °C/min. Nevertheless, $NaGdCoWO_6$ could not be formed this time neither, the products were mainly Gd_2WO_6, Na_2WO_4 and cobalt oxide. In order to obtain a further insight into the reaction process, another DTA experiment was done as following: with the same starting materials and temperature changing rate, to increase the temperature to 1200 °C and then to decrease the temperature to 700 °C and stay at 700 °C for 2 hours, finally to quench to room temperature. Unfortunately, $NaGdCoWO_6$ was not formed neither. The main products were quite similar to the former one: Gd_2WO_6, Na_2WO_4, cobalt oxides and some others.

So far, the atmosphere, the temperature and the heating procedure had been tested to optimize the synthesis, but none of them worked out well to improve the synthesis. As stated at the beginning of this chapter, pressure is another fundamental thermodynamic parameter which can be adjusted to facilitate the synthesis and to stabilize metastable phases. Therefore the synthesis strategy was switched to HT-HP synthesis.

An initial test was done with the same starting materials (Na_2CO_3 (2% in excess), Gd_2O_3, $CoCO_3$ and WO_3) as the precedent experiments done for $NaGdCoWO_6$. The starting materials were pressed into a pellet. In order to prepare the precursor for the HT-HP synthesis under conditions of up to 875 °C for 12 hours, the temperature raising rate was 2.5 °C/min. Then the HT-HP synthesis conditions, 1000 °C (625W, 50W/min) and 5GPa (90 tons, 5 tons/min) for 30 min, were applied to the precursor. It was very exciting that $NaGdCoWO_6$ formed this time even though it was accompanied by some impurities. The presence of $NaGdCoWO_6$ phase indicated the conditions were not so bad, the remaining main problem was most probably due to the reactants. The XRPD examination of the precursor showed that a lot of Co had been oxidized to +3, which was not the appropriate oxidation state +2 in $NaGaCoWO_6$. A further literature check showed that $CoCO_3$ decomposes into Co_3O_4 and CO_2 at 335 °C in air[75], while above 950 °C Co_3O_4 is converted into CoO[76]. So that a new precursor was prepared in the inert atmosphere of Ar and the annealing temperature was selected at 970 °C. These conditions had to make sure that CoO was stable and that it wasn't oxidized into Co_3O_4 in the precursor. With the same HT-HP conditions, a product mostly composed of $NaGdCoWO_6$ (estimated at >90 wt% pure) was obtained, the refined pattern is shown in Fig. 2.16. The Rietveld refinement here is just for an estimation of the purity of the target compound. The detailed and final Rietveld refinements can be found in Chapter 4, where the structural study of all compounds is discussed. EDX analysis confirmed the correct composition of $NaGdCoWO_6$. A faster temperature increasing speed of 250 W/min while all other conditions remained the same was tested also, it proved that the faster speed was worse.

The same synthesis method was applied to other $NaLnCoWO_6$ (Ln= Sm, Eu, Tb, Dy, Ho, Er and Yb) compounds. All of these compounds were obtained with this procedure proving the effectiveness and reproducibility of this method. The compositional study was carried out by EDX analysis, and confirmed the composition of all these compounds.

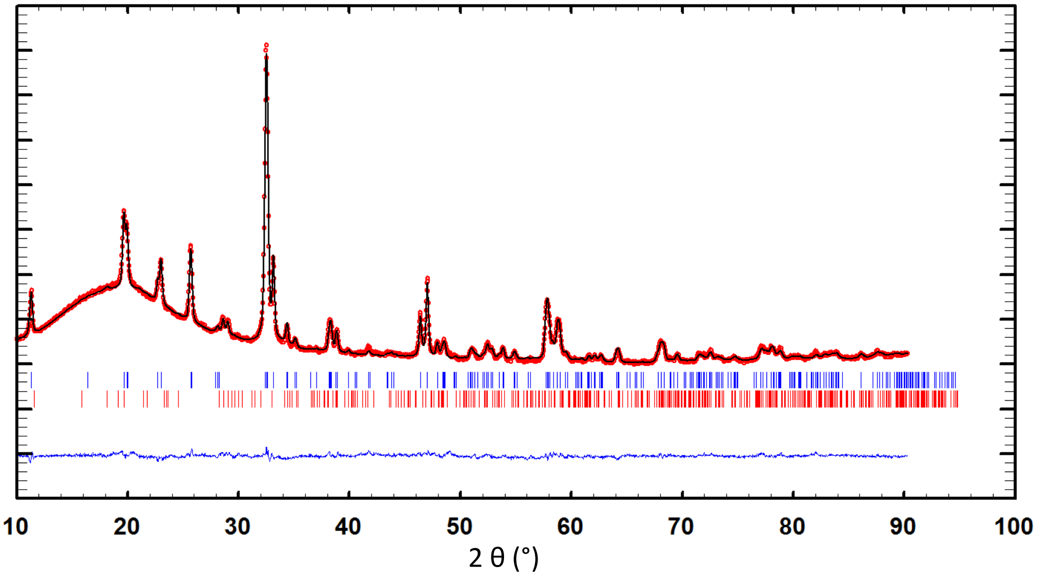

Figure 2.16 The *$P2_1$* Rietveld refinement of the $NaGdCoWO_6$ XRPD pattern, the red open circles are the observed pattern, and the black curve is the calculated pattern. The blue tick marks stand for the allowed (*hkl)* reflections of the target phase $NaGdCoWO_6$, and the red tick marks stand for the allowed (*hkl)* reflections of the impurity Gd_2WO_6. The purity of the target phase $NaGdCoWO_6$ is estimated over 90%.

For all the $NaLnCoWO_6$ (Ln =Sm, Eu, Gd, Dy, and Ho) samples, the purity of the target phase was estimated to be over 90wt%, except for $NaErCoWO_6$ where the purity was estimated only around 20wt% and for $NaYbCoWO_6$ where it was around 75wt%. Even though the target compounds were obtained, the synthesis conditions were not yet systematically studied for optimizing. Optimizing the synthesis conditions and purifying the sample were very crucial for a proper structural analysis, especially in the case of the latter two samples (Er and Yb). A systematic study on synthesis conditions was undertaken on the $NaHoCoWO_6$ compound. Considering that Ho is closer to the smallest rare-earth end side which leads to less stable target compounds, if the best synthesis conditions are found for $NaHoCoWO_6$ the same or close conditions should work for all other compounds.

All tests for optimizing the synthesis conditions of $NaHoCoWO_6$ are summarized in Table 2.3.

$NaHoCoWO_6$_1_HP1 represents the experiment using the precursor prepared at 970 °C in Ar, $NaHoCoWO_6$ was already over 90wt% pure in this experiment. Since it had been shown that increasing the temperature raising rate did not help to improve the $NaGdCoWO_6$ sample quality, this parameter was not tested again. Different reactants for HT-HP synthesis were tried in $NaHoCoWO_6$_2_HP1 and $NaHoCoWO_6$_3_HP1, the reaction conditions were the same except the sources of Ho and W (see Table.2.3). The results of these two tests compared to the $NaHoCoWO_6$_1_HP1 experiment showed that the combination of Na_2WO_4, Ho_2O_3, CoO and WO_3 was the best candidate as the starting materials. Na_2WO_4 was prepared from $Na_2WO_4·2H_2O$ by pre-heating at 110 °C for 5 hours. Ho_2O_3 was pre-heated at 900 °C for 12 hours before using and CoO was obtained by decomposing $CoCO_3$ at 970 °C in Ar for 12 hours. Since the best starting materials were defined, the reaction temperature was tested at 900 °C ($NaHoCoWO_6$_2_HP3), 1100 °C ($NaHoCoWO_6$_2_HP2) and 1200 °C ($NaHoCoWO_6$_4_HP1) separately under the pressure of 5 GPa. The quality of the sample prepared at 1100 °C was comparable to the one prepared at 1000 °C, while the product quality of the remaining two experiments at 900 °C and 1200 °C was worse. From the phases quantification of the two best conditioned experiments $NaHoCoWO_6$_2_HP1 and $NaHoCoWO_6$_3_HP1, it was noted that both of them contained around 1.5wt% of the impurity Ho_2WO_6, which could be a sign of a lack of Na in the starting materials otherwise Ho and W would go into $NaHoCoWO_6$ rather than Ho_2WO_6. Therefore a 3% excess of Na was put in the starting material of the experiment $NaHoCoWO_6$_5_HP1 and the defined best reaction conditions were applied. The hypothesis was verified since the purity of $NaHoCoWO_6$ was increased to 99.60(47)wt% with the presence of a small amount of impurity $NaHo(WO_4)_2$.

Table 2.3 A summary of the HT-HP synthesis attempts for the compound $NaHoCoWO_6$.

Experiment Reference	Starting Materials	Synthesis Conditions	Main Phases
$NaHoCoWO_6$_1_HP1	Na_2CO_3 (Na 2% excess), Ho_2O_3, $CoCO_3$, WO_3	Precursor: 970 °C for 12 hours, in Ar; HT-HP: 1000 °C (625W, 50W/min), 5GPa (90tones, 5 tones/min), 30min	$NaHoCoWO_6$: 93.30 (44)% Ho_2WO_6: 6.70 (19)%
$NaHoCoWO_6$_2_HP1	Na_2WO_4 , Ho_2O_3, CoO, WO_3	HT-HP: 1000 °C (625W, 50W/min), 5GPa (90tones, 5 tones/min), 30min	$NaHoCoWO_6$: 98.35 (51)% Ho_2WO_6: 1.65 (21)%
$NaHoCoWO_6$_2_HP2	Na_2WO_4 , Ho_2O_3, CoO, WO_3	HT-HP: 1100 °C (670W, 50W/min), 5GPa (90tones, 5 tones/min), 30min	$NaHoCoWO_6$: 98.61 (45)% Ho_2WO_6: 1.39 (16)%
$NaHoCoWO_6$_2_HP3	Na_2WO_4 , Ho_2O_3, CoO, WO_3	HT-HP: 900 °C (580W, 50W/min), 5GPa (90tones, 5 tones/min), 30min	More extra peaks related to impurities in XRPD pattern
$NaHoCoWO_6$_3_HP1	Na_2WO_4 , Ho_2WO_6, CoO	HT-HP: 1000 °C (625W, 50W/min), 5GPa (90tones, 5 tones/min), 30min	$NaHoCoWO_6$: 96.97 (46)% Ho_2WO_6: 3.03 (18)%
$NaHoCoWO_6$_4_HP1	Na_2WO_4 , Ho_2O_3, CoO, WO_3	HT-HP: 1200 °C (710W, 50W/min), 5GPa (90tones, 5 tones/min), 30min	Intensities of the strongest peaks are low
$NaHoCoWO_6$_5_HP1	Na_2WO_4 (Na 3% in excess) , Ho_2O_3, CoO, WO_3 (3% less)	HT-HP: 1000 °C (625W, 50W/min), 5GPa (90tones, 5 tones/min), 30min	$NaHoCoWO_6$: 99.60 (47)% $NaHo(WO_4)_2$: 0.40 (09)%
$NaHoCoWO_6$_5_HP2	Na_2WO_4 (Na 3% in excess) , Ho_2O_3, CoO, WO_3 (3% less)	HT-HP: 1000 °C (625W, 50W/min), 3.7GPa (60tones, 5 tones/min), 30min	More extra peaks related to impurities in XRPD pattern
$NaHoCoWO_6$_6_HP1	Na_2WO_4 (Na 3% excess) , Ho_2O_3, CoO (3% excess), WO_3 (3% less)	HT-HP: 1000 °C (625W, 50W/min), 5GPa (90tones, 5 tones/min), 30min	The amount of Ho_2WO_6 increased
$NaHoCoWO_6$_7_HP1	Na_2WO_4 (Na 1.5% in excess) , Ho_2O_3, CoO, WO_3 (1.5% less)	HT-HP: 1000 °C (625W, 50W/min), 5GPa (90tones, 5 tones/min), 30min	$NaHoCoWO_6$: ~98%, $NaHo(WO_4)_2$: ~2%, Some unidentified small peaks
$NaHoCoWO_6$_2_ComRe	Mix sample $NaHoCoWO_6$_2_HP1 & HP2	HT-HP: 1000 °C (625W, 50W/min), 5GPa (90tones, 5 tones/min), 30min	Not improved

The quantifications (wt%) of Main Phases were estimated from the Rietveld refinement implemented in the FullProf Suite.

Some other attempts were also made to further improve the product quality. A lower pressure of ~3.7 GPa ($NaHoCoWO_6$_5_HP2) which could relax the synthesis conditions was tested, yet the result came out worse than that of 5 GPa. As the impurity $NaHo(WO_4)_2$ was present in the $NaHoCoWO_6$_5_HP1 experiment, there might be a lack of Co otherwise all elements would participate in forming the target compound. So 3% excess of Co was also put in the starting materials in the experiment $NaHoCoWO_6$_6_HP1. However, more Co did not help to improve the product, instead the amount of the

Ho_2WO_6 impurity increased. Also the presence of $NaHo(WO_4)_2$ could be a sign of 3% excess of Na being too much because Na appeared in the impurity. 1.5% excess of Na was tested, some small extra peaks related to impurities were observed in XRPD pattern.

Therefore, after comparing the starting materials, the reaction temperature and the pressure, it was concluded that the synthesis conditions in the experiment $NaHoCoWO_6$_5_HP1 were the best, and all other compounds were synthesized based on this method. The final reaction conditions and phase quantifications are summarized in the next section, details won't be discussed for every compound since the syntheses are more or less the same. It could be interesting to comment on $NaErCoWO_6$ and $NaYbCoWO_6$ a little more. As discussed above, the purity of $NaErCoWO_6$ was only around 20wt% with the precursor prepared at 970 °C in Ar. Remarkably, when the starting materials switched to the mixture of Na_2WO_4 (3% excess), Er_2O_3, CoO, WO_3(3% less), the purity increased to 96.92(53)wt% under the same HT-HP reaction conditions. This shows a good choice of starting materials is very crucial for a good synthesis. Increasing the temperature to 1100 °C did improve the quality of the product, where $NaErCoWO_6$ was 98.17(53)wt% pure with 1.83(22)wt% Er_2WO_6 impurity. In contrast, a higher pressure of 6 GPa did not help. Regardless of the high quality of the sample, a post-treatment was carried out under conditions of 1100 °C and 5 GPa. After the post-treatment, the impurity Er_2WO_6 was transformed into $NaEr(WO_4)_2$ is preferable as it had less peaks in XRPD pattern avoiding peak overlapping issues. Meanwhile, the purity of the main phase decreased by a few percent. Similar to $NaYbCoWO_6$, the purity of the target compound largely increased with the new precursor. Whereas, the attempt to transform Yb_2WO_6 into $NaYb(WO_4)_2$ did not work out well. $NaYCoWO_6$ is also among the compounds attempted to synthesize. Because Y is non-magnetic so that $NaYCoWO_6$ can provide a reference to the compounds containing magnetic lanthanide rare earths at the A'-site.

2.3.3 A Summary of the Best Syntheses Conditions of $NaLnCoWO_6$ compounds

The best synthesis conditions of the $NaLnCoWO_6$ (Ln= Y, La, Pr, Nd, Sm, Eu, Gd, Tb, Dy, Ho, Er and Yb) family including at ambient and high pressure are listed in Table 2.4. Phase quantification results from Rietveld method SXRPD refinement implemented in FullProf are also listed. There are some extra peaks related to impurities that cannot be indexed because they are so small that it is very difficult to determine which impurities they are. For reference, the ratio between the highest intensity of the extra peaks and the highest peak intensity ($I_{maxextra}/I_{maxmain}$) of the target phase is calculated in this table. EDX analysis confirmed the compositions of all the targeted compounds.

Table 2.4 The best synthesis conditions for the entire $NaLnCoWO_6$ (Ln= Y, La-Nd, Sm-Er, Yb) series, both the target phase and the impurities were quantified by the SXRPD pattern refinement, the ratio between the highest peak intensity of the extra peaks not indexed yet and the highest peak intensity ($I_{maxextra}/I_{maxmain}$) in the main phase is calculated for each sample.

Sample	Starting Materials	Synthesis Conditions	Main Phase Purity	Impurities	$I_{maxextra}/I_{maxmain}$
$NaYCoWO_6$	Na_2WO_4 (3% Na in excess), Y_2O_3, CoO, WO_3 (3% less)	1100°C, 5GPa, 30min	99.56(18)%	CoO: 0.44(2)%	0.008
$NaLaCoWO_6$	Na_2CO_3 (2% Na in excess), La_2O_3, $CoCO_3$, WO_3	925°C, 12h; re-annealing after regrinding 925°C, 12h; ambient pressure	100%		0.034
$NaPrCoWO_6$	Na_2CO_3 (2% Na in excess), Pr_6O_{11}, $CoCO_3$, WO_3	950°C, 12h; re-annealing after regrinding 950°C, 12h; ambient pressure	99.17(20)%	CoO: 0.58(3)% $NaPr(WO_4)_2$: 0.24(2)%	0.025
$NaNdCoWO_6$	$NaNO_3$ (5% in excess), $Nd(NO_3)_3·6H_2O$, $Co(NO_3)_2·6H_2O$, WO_3	225°C, 24h; 500°C, 72h; 900°C, 24h; re-annealing after regrinding 975°C, 24h; ambient pressure	91.98(18)%	$NaNd(WO_4)_2$: 7.01(4)% CoO: 1.01(3)%	0.009
$NaSmCoWO_6$	Na_2WO_4 (3% Na in excess), Sm_2O_3, CoO, WO_3 (3% less)	1000°C, 5GPa, 30min	98.50(21)%	CoO: 1.16(4)% $NaSm(WO_4)_2$: 0.34(2)%	0.057
$NaEuCoWO_6$	Na_2WO_4 (1.5% Na in excess), Eu_2O_3, CoO, WO_3 (1.5% less)	1000°C, 5GPa, 30min	99.48(16)%	CoO: 0.52(4)%	0.010
$NaGdCoWO_6$	Na_2WO_4 (3% Na in excess), Gd_2O_3, CoO, WO_3 (3% less)	1000°C, 5GPa, 30min	99.35(17)%	CoO: 0.65(4)%	0.017
$NaTbCoWO_6$	Na_2WO_4 (3% Na in excess), Tb_2O_3, CoO, WO_3 (3% less)	1000°C, 5GPa, 30min	99.36(20)%	$NaTb(WO_4)_2$: 0.32 (2)% Tb_6W: 0.32 (2)%	0.015
$NaDyCoWO_6$	Na_2WO_4 (1.5% Na in excess), Dy_2O_3, CoO, WO_3 (1.5% less)	1000°C, 5GPa, 30min	100%		0.040
$NaHoCoWO_6$	Na_2WO_4 (3% Na in excess), Ho_2O_3, CoO, WO_3 (3% less)	1000°C, 5GPa, 30min	99.19(22)%	CoO: 0.35(3)% $Na_2WO_4·2H_2O$: 0.33 (3)% $NaHo(WO_4)_2$: 0.13(1)%	0.037

Sample	Starting Materials	Synthesis Conditions	Main Phase Purity	Impurities	$I_{maxextra}/I_{maxmain}$
$NaErCoWO_6$	Na_2WO_4 (3% Na in excess), Er_2O_3, CoO, WO_3 (3% less)	1100°C, 5GPa, 30min	96.29(18)%	$NaEr(WO_4)_2$: 3.24(4)% Er_2WO_6: 0.47(2)%	0.013
$NaYbCoWO_6$	Na_2WO_4 (3% Na in excess), Yb_2O_3, CoO, WO_3 (3% less)	1100°C, 5GPa, 30min	97.89(20)%	Yb_2WO_6: 2.11(3)%	0.023

2.3.4 Unsuccessful Syntheses Attempts for Other Doubly Ordered Perovskites

Some other doubly order perovskites with different B-site cations (Ni and Cu) were also attempted to synthesize at the beginning, in parallel with the $NaLnCoWO_6$ (Ln=La and Nd) compounds. However, they were not successful either because it was very difficult to obtain a pure target compound or the target phases were not formed in these tests.

Perspective for $NaLaNiWO_6$: even though the target $NaLaNiWO_6$ phase was obtained, its purity was not high enough and accompanied with some other impurities. Considering the sample quality and time, it was decided to concentrate on the $NaLnCoWO_6$ series. From the experience of $NaLnCoWO_6$ compounds syntheses, alternative starting materials with carbonates and oxides, instead of nitrates, may be a good approach to optimize the synthesis of $NaLaNiWO_6$.

A brief summary of these experiments are listed in Table. 2.5 – 2.7.

Table 2.5 A summary of synthesis attempts of doubly ordered perovskites $NaLaNiCoWO_6$.

Experiment Reference	Starting Materials	Synthesis Conditions	Main Phases	Motivation
$NaLaNiWO_6$_1	$NaNO_3$, $La(NO_3)_3·6H_2O$, $Ni(NO_3)_2·6H_2O$, WO_3	225 °C for 24 hours, 500 °C for 72 hours, 900 °C for 24 hours; re-annealing at 1000 °C for 24 hours; 2.5 °C /min temperature raising rate for all	$NaLaNiWO_6$, Na_2WO_4, NiO	To test the method reported in [46]; try to improve the sample quality
$NaLaNiWO_6$_2	$NaNO_3$, $La(NO_3)_3·6H_2O$, NiO, WO_3	225 °C for 2 hours, 500 °C for 2 hours, 900 °C for 10 hours; 1st re-annealing at 900 °C for 12 hours; 2nd re-annealing at 1000 °C for 24 hours; 2.5 °C /min temperature raising rate for all	Na_2WO_4, NiO, $NaLaNiWO_6$, others	To try a shorter heating procedures and a new starting material NiO; try to improve the sample quality
$NaLaNiWO_6$_3	$NaNO_3$, $La(NO_3)_3·6H_2O$, $Ni(NO_3)_2·6H_2O$, WO_3	225 °C for 2 hours, 500 °C for 2 hours, 900 °C for 10 hours; 1st re-annealing at 900 °C for 12 hours; 2.5 °C /min temperature raising rate for all	$La_{14}W_8O_{45}$, Na_2WO_4, $Na_{0.5}La_{0.5}WO_4$, NiO	To test if $Ni(NO_3)_2·6H_2O$ is better than NiO in the starting materials, to compare with $NaLaNiWO_6$_2

Table 2.6 A summary of synthesis attempts of doubly ordered perovskites $NaNdNiCoWO_6$.

Experiment Reference	Starting Materials	Synthesis Conditions	Main Phases	Motivation
$NaNdNiWO_6$_1	$NaNO_3$ (5% excess), $Nd(NO_3)_3{\cdot}6H_2O$, $Ni(NO_3)_2{\cdot}6H_2O$, WO_3	225 °C for 24 hours, 500 °C for 72 hours, 975 °C for 24 hours; 2.5 °C /min temperature raising rate for all	NiO, Na_2WO_4, Nd_2WO_6	To test the method reported [46]
$NaNdNiWO_6$_2	$NaNO_3$ (5% excess), $Nd(NO_3)_3{\cdot}6H_2O$, $Ni(NO_3)_2{\cdot}6H_2O$, WO_3	600 °C for 12 hours; 2.5 °C /min temperature raising rate for all	Na_2WO_4, Nd_2WO_6, $WNiO_4$, $Na_5Nd(WO_4)_4$, $NdNiO_3$, others	To prepare a precursor for HT- HP synthesis
$NaNdNiWO_6$_2_HP1	The product of $NaNdNiWO_6$_2	900 °C (580 W, 50 W/min), 3 GPa (55 tones, 5 tones/min), 30min	$Na_{0.5}Nd_{0.5}WO_4$, WO_3, others	To test HT-HP synthesis

Conclusion: $NaNdNiWO_6$ was not obtained at all, neither has it been reported in the literature. Considering the time, no more effort was made on this compound.

Table 2.7 A summary of synthesis attempts of doubly ordered perovskites $NaLaCuWO_6$.

Experiment Reference	Starting Materials	Synthesis Conditions	Main Phases	Motivation
$NaLaCuWO_6$_1	$NaNO_3$, $La(NO_3)_3{\cdot}6H_2O$, $Cu(NO_3)_2{\cdot}3H_2O$, WO_3	225 °C for 4 hours, 500 °C for 4 hours, 900 °C for 12 hours; 2.5 °C /min temperature raising rate for all	$La_{18}W_{10}O_{57}$, CuO, Na_2WO_4, $Na_{0.5}La_{0.5}WO_4$, $La_2W_{1.25}O_{6.75}$	To test the method reported [46]

Conclusion: $NaLaCuWO_6$ was not obtained at all, neither has it been reported in the literature. Considering the time, no more effort was made on this compound.

2.4 Syntheses of Ruddlesden-Popper Compounds $NaRTi_{1-x}M_xO_4$ (R= Y, La; M= Mn, Cr)

As introduced in Chapter 1, the $NaRTiO_4$ family has been demonstrated to lift the inversion symmetry by octahedral rotations, both experimentally and theoretically.[37] Efforts were made to try to introduce magnetic ions (Mn and Cr) into the B-site, in order to couple the magnetic and ferroelectric properties together. However, no acceptable results were obtained from these synthesis attempts. Even though the syntheses were not successful, the knowledge of these attempts might be helpful for following studies, they are summarized in Table 2.8. Since they are not the main objects discussed in the following chapters, no detailed explanation on this table is given.

$NaYTiO_4$ was already synthesized before[77][78]. The methods used in these two articles are not exactly the same. So in this synthesis work, the first step was to find out a good approach to synthesize the $NaYTiO_4$ parent phase. Based on the two synthesis works stated above, the annealing temperature, the reaction duration and the starting materials were tested. The best starting materials were Na_2CO_3 (30% excess), Y_2O_3 and TiO_2. The best synthesis conditions were: heating up to 900 °C at a temperature raising rate 2.5 °C/min and dwelling at this temperature for 6 hours. EDX analysis confirmed the composition of $NaYTiO_4$. Similar to $NaYTiO_4$, the synthesis conditions of $NaLaTiO_4$ were also explored and it was determined that 850 °C for 6 hours was the best.

As the synthesis conditions had been defined for the parent compounds $NaYTiO_4$ and $NaLaTiO_4$, various attempts on substituting magnetic ions Mn/Cr into the Ti site were tried. All these experiment conditions are summarized in Table. 2.8, the formula of the target phase for each experiment is shown below the experiment reference name.

The goal of the majority of the synthesis attempts was to partially (25% or 50%) substitute Ti by Mn, various parameters such as the temperature, the duration, the atmosphere, the post-treatment, the starting materials as well as HT-HP conditions were examined to try to optimize the synthesis conditions. In addition, Cr was also tried as a substitute for Ti into $NaYTiO_4$. The motivation for each experiment is also summarized in Table 2.8. The products from these trials were characterized by XRPD and EDX, however, no sign of the target compounds were observed. The main phases in each experiment were also listed in this table, they were determined by comparing the measured XRPD pattern and crystallographic information stored in the ICDD PDF 4+ database.

Despite the fact that the target compound was not synthesized, a suspected new phase was formed in the experiment $NaYTiMnO_4$_5_HP1. From the XRPD pattern, there was a set of peaks that could not be indexed by any compound in the ICDD PDF 4+ database. In order to figure out the structure of the suspected new phase, electron diffraction was employed. Unfortunately, this phase was very sensitive to the electron beam, regardless of carefully decreasing the beam intensity. Therefore, the detailed information about this suspected new phase remains unknown.

Table 2.8 A summary of synthesis attempts to substitute Ti by magnetic ions Mn or Cr in the parent Ruddlesden-Popper compounds $NaYTiO_4$ or $NaLaTiO_4$.

Experiment Reference	Starting Materials	Synthesis Conditions	Main Phases	Motivation
$NaYTiMnO_4$_1 ($NaYTi_{0.75}Mn_{0.25}O_4$)	Na_2CO_3 (Na 30% excess), Y_2O_3, TiO_2, MnO_2	DTA: 950°C, temperature raising rate 10 °C/min	Y_2O_3, $Na_{0.5}Y_{0.5}TiO_3$	To find out the best reaction temperature to partially (25%) substitute Ti by Mn
$NaYTiMnO_4$_1 ($NaYTi_{0.75}Mn_{0.25}O_4$)	Na_2CO_3 (Na 30% excess), Y_2O_3, TiO_2, MnO_2	900°C for 6 hours, a post-treatment 900°C for 6 hours, temperature raising rate 2.5 °C/min	$NaYTiO_4$, Y_2O_3	To test temperature and annealing duration conditions to partially (25%) substitute Ti by Mn
$NaYTiMnO_4$_2 ($NaYTi_{0.5}Mn_{0.5}O_4$)	Na_2CO_3 (Na 30% excess), Y_2O_3, TiO_2, MnO_2	900°C for 6 hours, temperature raising rate 2.5 °C/min	Y_2O_3, $Na_2Y_2Ti_3O_{10}$, others	To test temperature and annealing duration conditions to partially (50%) substitute Ti by Mn
$NaYTiMnO_4$_3 ($NaYTi_{0.75}Mn_{0.25}O_4$)	Na_2CO_3 (Na 30% excess), Y_2O_3, TiO_2, MnO_2	DTA: 950°C in O_2, temperature raising rate 10 °C/min	$NaYTiO_4$, Y_2O_3	To test the effect of O_2 and find out the best temperature to partially (25%) substitute Ti by Mn
$NaYTiMnO_4$_3 ($NaYTi_{0.75}Mn_{0.25}O_4$)	Na_2CO_3 (Na 30% excess), Y_2O_3, TiO_2, MnO_2	900°C for 6 hours in O_2, temperature raising rate 2.5 °C/min	$NaYTiO_4$, Y_2O_3, $Na_2Y_2Ti_3O_{10}$, MnO_2	To test temperature and annealing duration conditions to partially (25%) substitute Ti by Mn, O_2 atmosphere to keep Mn^{4+}
$NaYTiMnO_4$_4 ($NaYTi_{0.5}Mn_{0.5}O_4$)	Na_2CO_3 (Na 30% excess), Y_2O_3, TiO_2, MnO_2	DTA: 950°C, temperature raising rate 10 °C/min	Y_2O_3, Mn_2O_3, TiO_2, others	To find out the best reaction temperature to partially (50%) substitute Ti by Mn

$NaYTiMnO_4$_5 ($NaYTi_{0.75}Mn_{0.25}O_4$)	Na_2CO_3 (Na 30% excess), Y_2O_3, TiO_2, MnO_2	600°C for 6 hours, temperature raising rate 2.5 °C/min	Y_2O_3, $Na_4Ti_5O_{12}$, Na_2CO_3, others	To check the reaction at various temperatures, and prepare a precursor for HT-HP synthesis
$NaYTiMnO_4$_5_HP1 ($NaYTi_{0.75}Mn_{0.25}O_4$)	The product of $NaYTiMnO_4$_5	800°C (540 W, 50 W/min), 4 GPa (75 tones, 5 tones/min), 30min	$Na_{0.5}Y_{0.5}TiO_3$, a suspected new phase, others	To test the effect of HT_HP synthesis
$NaYTiMnO_4$_6 ($NaYTi_{0.75}Mn_{0.25}O_4$)	Na_2CO_3 (Na 30% excess), Y_2O_3, TiO_2, MnO_2	700°C for 6 hours, temperature raising rate 2.5 °C/min	Y_2O_3, Na_2TiO_3, others	To check the reaction at various temperatures, and prepare a precursor for HT-HP synthesis
$NaYTiMnO_4$_6_HP1 ($NaYTi_{0.75}Mn_{0.25}O_4$)	The product of $NaYTiMnO_4$_6	800°C (540 W, 50 W/min), 4 GPa (75 tones, 5 tones/min), 30min	Y_2O_3, $Na_{0.5}Y_{0.5}TiO_3$, others	To test the effect of HT_HP synthesis
$NaYTiMnO_4$_7 ($NaYTi_{0.75}Mn_{0.25}O_4$)	Na_2CO_3 (Na 30% excess), Y_2O_3, TiO_2, MnO_2	400°C for 6 hours, temperature raising rate 2.5 °C/min	Y_2O_3, TiO_2, Na_2CO_3, others	To check the reaction at various temperatures, and prepare a precursor for HT-HP synthesis
$NaYTiMnO_4$_8 ($NaYTi_{0.75}Mn_{0.25}O_4$)	Na_2CO_3 (Na 30% excess), Y_2O_3, TiO_2, MnO_2	500°C for 6 hours, temperature raising rate 2.5 °C/min	Y_2O_3, TiO_2, Na_2CO_3, others	To check the reaction at various temperatures, and prepare a precursor for HT-HP synthesis
$NaYTiMnO_4$_9 ($NaYTi_{0.75}Mn_{0.25}O_4$)	Na_2CO_3 (Na 30% excess), Y_2O_3, TiO_2, MnO_2	900°C for 20 hours, temperature raising rate 2.5 °C/min	$NaYTiO_4$, Y_2O_3, $Na_2Y_2Ti_3O_{10}$	To test a longer heating duration for partially (25%) substituting Ti by Mn
$NaYTiMnO_4$_10 ($NaYTi_{0.5}Mn_{0.5}O_4$)	Na_2CO_3 (Na 30% excess), Y_2O_3, TiO_2, MnO_2	900°C for 20 hours, temperature raising rate 2.5 °C/min	Y_2O_3, $Na_2Y_2Ti_3O_{10}$, others	To test a longer heating duration partially (50%) substitute Ti by Mn
$NaYTiMnO_4$_11 ($NaYTi_{0.5}Mn_{0.5}O_4$)	Na_2CO_3 (Na 30% excess), Y_2O_3, TiO_2, MnO_2	700°C for 6 hours, temperature raising rate 2.5 °C/min	Y_2O_3, $Na_{0.5}Ti_2O_4$, Na_2TiO_3, others	To check the reaction at various temperatures, and prepare a precursor for HT-HP synthesis
$NaYTiMnO_4$_11_HP1 ($NaYTi_{0.5}Mn_{0.5}O_4$)	The product of $NaYTiMnO_4$_11	800°C (540 W, 50 W/min), 4 GPa (75 tones, 5 tones/min), 30min	$Na_{0.5}Y_{0.5}TiO_3$, others	To test the effect of HT_HP synthesis
$NaYTiMnO_4$_12 ($NaYTi_{0.5}Mn_{0.5}O_4$)	Na_2CO_3 (Na 30% excess), Y_2O_3, TiO_2, MnO_2	900°C for 6 hours, temperature raising rate 2.5 °C/min	Y_2O_3, $Na_2Y_2Ti_3O_{10}$, others	To check the reaction at various temperatures, and prepare a precursor for HT-HP synthesis
$NaYTiMnO_4$_13 ($NaYTi_{0.5}Mn_{0.5}O_4$)	Na_2CO_3 (Na 30% excess), Y_2O_3, TiO_2, MnO_2	800°C for 6 hours, temperature raising rate 2.5 °C/min	$Na_{0.5}Y_{0.5}TiO_3$, Y_2O_3, others	To check the reaction at various temperatures, and prepare a precursor for HT-HP synthesis
$NaYTiMnO_4$_14 ($NaYTi_{0.5}Mn_{0.5}O_4$)	Na_2CO_3 (30% excess), Y_2O_3, TiO_2, MnO_2	850°C for 6 hours, temperature raising rate 2.5 °C/min	Y_2O_3, $Na_2Y_2Ti_3O_{10}$, others	To check the reaction at various temperatures, and prepare a precursor for HT-HP synthesis
$NaYTiMnO_4$_15 ($NaYTi_{0.5}Mn_{0.5}O_4$)	Na_2CO_3 (30% excess), Y_2O_3, TiO_2, MnO_2	750°C for 6 hours, temperature raising rate 2.5 °C/min	Y_2O_3, others	To check the reaction at various temperatures, and prepare a precursor for HT-HP synthesis
$NaYTiMnO_4$_15 _DTA_like ($NaYTi_{0.5}Mn_{0.5}O_4$)	Na_2CO_3 (30% excess), Y_2O_3, TiO_2, MnO_2	750°C for 10 min, temperature raising rate 10 °C/min	Y_2O_3, Na_2CO_3, others	To test the effect of increasing the temperature rapidly and

				annealing duration very short, just like doing a DTA measurement
$NaYTiMnO_4$_16 ($NaYTi_{0.5}Mn_{0.5}O_4$)	Na_2CO_3 (30% excess), Y_2O_3, TiO_2, MnO_2	700°C for 6 hours, temperature raising rate 2.5 °C/min	Y_2O_3, $Na_{0.5}Ti_2O_4$, Na_2TiO_3, others	To check the reaction at various temperatures, and prepare a precursor for HT-HP synthesis
$NaYTiMnO_4$_17 ($NaYTi_{0.5}Mn_{0.5}O_4$)	Na_2CO_3 (30% excess), Y_2O_3, TiO_2, MnO_2	600°C for 6 hours, temperature raising rate 2.5 °C/min	Y_2O_3, $Na_4Ti_5O_{12}$, Na_2CO_3	To check the reaction at various temperatures, and prepare a precursor for HT-HP synthesis
$NaYTiMnO_4$_17_HP1 ($NaYTi_{0.5}Mn_{0.5}O_4$)	The product of $NaYTiMnO_4$_17	800°C (540 W, 50 W/min), 4 GPa (75 tones, 5 tones/min), 30min	Y_2O_3, $Y_2Mn_2O_7$, $Na_{0.5}Y_{0.5}TiO_3$, TiO_2, MnO, others	To test the effect of HT_HP synthesis
$NaYTiMnO_4$_18 ($NaYTi_{0.5}Mn_{0.5}O_4$)	$NaNO_3$ (30% excess), Y_2O_3, TiO_2, MnO_2	600°C for 6 hours, temperature raising rate 2.5 °C/min	Y_2O_3, $Y_2Ti_2O_7$, $Na_{0.5}Y_{0.5}TiO_3$, others	To test the effect of $NaNO_3$ instead of Na_2CO_3 as the Na source, compared with $NaYTiMnO_4$_17
$NaYTiMnO_4$_19 ($NaYTi_{0.5}Mn_{0.5}O_4$)	$NaNO_3$ (30% excess), Y_2O_3, TiO_2, MnO_2	700°C for 6 hours, temperature raising rate 2.5 °C/min	Y_2O_3, $Y_2Ti_2O_7$, $Na_{0.5}Y_{0.5}TiO_3$, others	To test the effect of $NaNO_3$ instead of Na_2CO_3 as the Na source, compared with $NaYTiMnO_4$_16
$NaYTiMnO_4$_21 ($NaYMnO_4$)	Na_2CO_3 (30% excess), Y_2O_3, MnO_2	600°C for 6 hours, temperature raising rate 2.5 °C/min	Y_2O_3, $Na_2Mn_3O_7$, others	To totally substitute Ti by Mn, prepare a precursor for HT-HP at low temperature, compared with $NaYTiMnO_4$_22
$NaYTiMnO_4$_22 ($NaYMnO_4$)	$NaNO_3$ (30% excess), Y_2O_3, MnO_2	600°C for 6 hours, temperature raising rate 2.5 °C/min	Y_2O_3, $Y_2Mn_2O_7$, $Na_2Mn_3O_7$	To totally substitute Ti by Mn, prepare a precursor for HT-HP at low temperature, compared with $NaYTiMnO_4$_21
$NaYTiCrO_4$_1 ($NaYCrO_4$)	Na_2CO_3 (30% excess), Y_2O_3, CrO_2	DTA: 950°C, temperature raising rate 10 °C/min		To find out the best reaction temperature to totally substitute Ti by Cr
$NaYTiCrO_4$_1 ($NaYCrO_4$)	Na_2CO_3 (30% excess), Y_2O_3, CrO_2	800°C for 6 hours, temperature raising rate 2.5 °C/min	Y_2O_3, $YCrO_3$, Na_2CrO_4, others	To test temperature and annealing duration conditions totally substitute Ti by Cr
$NaYTiCrO_4$_2 ($NaYTi_{0.75}Cr_{0.25}O_4$)	Na_2CO_3 (30% excess), Y_2O_3, TiO_2, CrO_2	DTA: 950°C, temperature raising rate 10 °C/min	Y_2O_3, $NaYTiO_4$, $Na_{0.5}Y_{0.5}TiO_3$, others	To test temperature and annealing duration conditions to partially (25%) substitute Ti by Cr
$NaYTiCrO_4$_2 ($NaYTi_{0.75}Cr_{0.25}O_4$)	Na_2CO_3 (30% excess), Y_2O_3, TiO_2, CrO_2	900°C for 6 hours, temperature raising rate 2.5 °C/min	$NaYTiO_4$, Na_2CrO_4, Y_2O_3	To test temperature and annealing duration conditions to partially (25%) substitute Ti by Cr
$NaLaTiMnO_4$_1 ($NaLaTi_{0.75}Mn_{0.25}O_4$)	Na_2CO_3 (30% excess), La_2O_3, TiO_2, MnO_2	850°C for 6 hours, temperature raising rate 2.5 °C/min	La_2O_3, $Na_2La_2Ti_3O_{10}$, $LaTiO_3$, $Na_{0.5}La_{0.5}TiO_3$	To test temperature and annealing duration conditions to partially (25%) substitute Ti by Mn

Chapter 3: Methods and Technical Aspects of Structural and Physical Study

As presented in the last chapter, a family of doubly ordered perovskites $NaLnCoWO_6$ (Ln= Y, La, Pr, Nd, Sm, Eu, Gd, Tb, Dy, Ho, Er, and Yb) has been synthesized. The preliminary structural and compositional characterizations confirmed the high quality and the right compositions of these samples. In order to further understand the structure-property relationship of these samples, various experiments and analyses were performed. In this chapter, all the methods and technical parts of these experiments will be introduced. The structural study including synchrotron X-ray powder diffraction (SXRPD) and neutron powder diffraction (NPD) will be introduced in chapter section 3.1. Electron diffraction and electron microscopy will be introduced in chapter section 3.2. Physical properties including the magnetic properties and electric properties were characterized by magnetization measurement, specific heat measurement, dielectric measurement and pyroelectric current measurement. In addition, NPD data was collected for the magnetic structure determination. All these aspects concerning physical properties will be introduced in chapter section 3.3.

3.1 Structural Study and Analysis by SXRPD and NPD

3.1.1 Synchrotron X-ray Powder Diffraction (SXRPD)

X-rays can be generated in two ways: either from the impacts of high energy electrons with a metal target in an X-ray tube, or the synchrotron radiation.[70] The laboratory X-ray source employs the first mechanism, however it has drawbacks such as a low efficiency, limited brightness and continuously cooling is necessary to dissipate the heat generated from the impacts. All of these make laboratory sources not suitable for high quality pattern recording, especially when subtle structural features are of interest, e.g. to distinguish close symmetries of $P2_1/m$ and $P2_1$ like in this study. Alternatively, X-rays can also be generated by a synchrotron source when electrons are confined and accelerated in a storage ring. This has the advantages of a continuous spectrum of wavelengths, a high spectral flux, high intensity, high brightness, and extreme collimation,[79] all of which are at the expense of a high cost. All SXRPD patterns were measured at room temperature, except for $NaLaCoWO_6$ which was also measured at 100K with a cryostream system, on the CRISTAL beamline, 2-circle diffractometer at the SOLEIL Synchrotron source, Saint-Aubin, France. The diffractometer is shown in Figure 3.1, it is located at the end of the beamline, 40 m downstream of the U20 undulator.[80] The detection is performed by 21-Si(111) crystal analyzer, fast YAP(Ce) scintillation detectors (Scionix) mounted on the analyzer following the 21-Si(111) crystals. The detectors' signals are then shaped and amplified. In total, 21 independent diagrams are obtained and summed to get the final diffractograms. The radiation wavelength was $\lambda = 0.5818$ Å and an angular range from 0 ° to 65 ° with a 0.002 ° step was scanned in 2θ, except for $NaYCoWO_6$ for which the beam wavelength was $\lambda = 0.5136$ Å and an angular range from 0 ° to 50 ° with a 0.002 ° step.

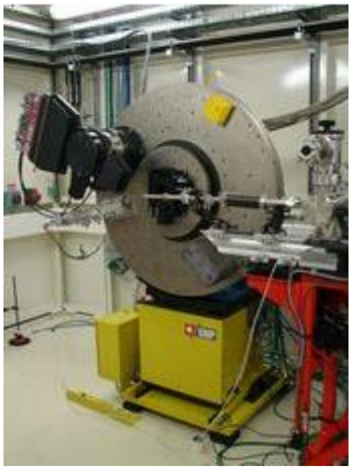

Figure 3.1 The 2-circle diffractometer employed to record the SXRPD data in this study on the CRISTAL beamline, SOLEIL synchrotron source, Saint-Aubin, France.[80]

3.1.2 Neutron Powder Diffraction (NPD)

Similar to X-rays, there are also two approaches to generate neutrons: either in nuclear reactors or by bombarding a heary metal target by accelerated protons (spallation sources).[70] Neutrons produced in the former mechanism have a white spectrum and the maximum of flux is usually obtained within an angstrom wavelength range. However, one of the biggest drawbacks is that the flux is rather low at useful energies and the interaction between neutrons and the samples is weak, so that a large quantity of sample is needed for NPD experiments. In contrast, the neutron flux produced by the way of spallation is highly intense (~100 times higher than in nuclear reactors) and possesses a nearly continuous energy spectrum. Mostly, time-of-fight (TOF) experiments are conducted with spallation neutron sources. We performed the diffraction measurements at Institut Laue-Langevin, Grenoble, France which is a powerful nuclear reactor and one of the most intense neutron sources in the world. All NPD patterns presented here were measured on either the D2B High-Resolution two-axis diffractometer or the D1B high flux two-axis powder diffractometer at ILL. All the diffraction patterns were recorded in the constant wavelength mode. The layouts of the diffractometers are shown in Figure 3.2.[81][82] In the D2B High-Resolution two-axis diffractometer, the detection system is composed of 128 detectors separated at 1.25 ° from each other, a complete diffractogram is obtained by shifting the detection system by 0.05 ° per step and totally 25 steps. The neutron beam wavelength employed was λ = 1.594 Å selected by a Ge (335) monochromator, the data were collected from 0 ° to 160 ° with a 0.05 ° step in 2θ. For these experiments, the $NaYCoWO_6$, $NaLaCoWO_6$, NaPrCoWO6, $NaNdCoWO_6$, $NaTbCoWO_6$ and $NaHoCoWO_6$ samples were selected because all other samples contain rare-earth elements that absorb neutrons strongly. All of the samples were measured at room temperature, except for $NaLaCoWO_6$ which was also measured at 100K.

NPD data for the magnetic structure determination and the phase transition of $NaLaCoWO_6$ were collected on the D1B high flux two-axis powder diffractometer at Institut Laue-Langevin, Grenoble, France. The wavelength was λ = 2.52 Å selected by a pyrolytic graphite (002) monochromator, in the 2θ angle range 0.77°-128.67° with a 0.1° step. The samples $NaYCoWO_6$, $NaLaCoWO_6$, $NaPrCoWO_6$, $NaNdCoWO_6$, $NaTbCoWO_6$ and $NaHoCoWO_6$ were selected to study their magnetic structures because all other samples contain rare-earth elements that absorb neutrons strongly. The patterns were collected a few degrees below and above T_N, and the entire magnetic phase transition processes which were also recorded as a function of the temperature.

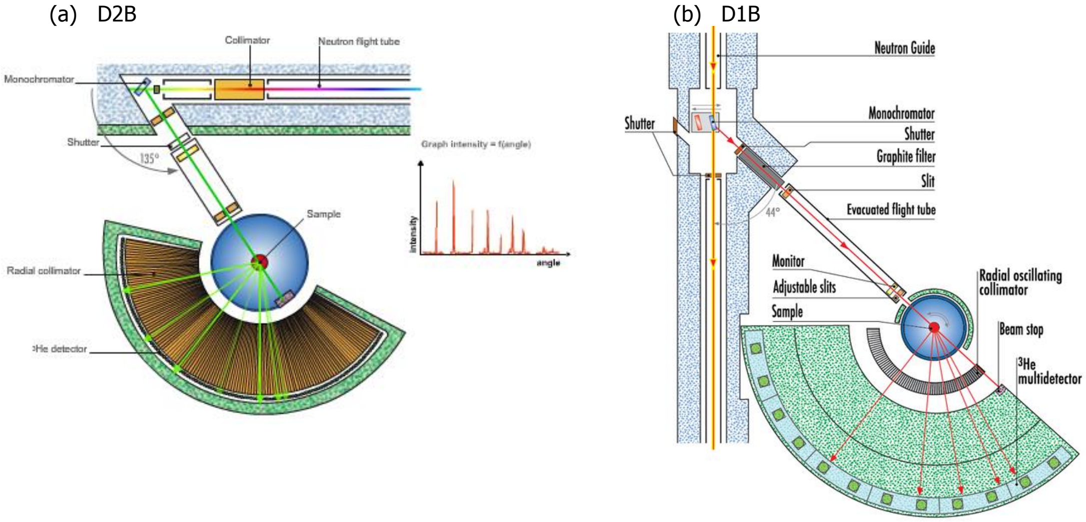

Figure 3.2 The layout of (a) D2B High-Resolution two-axis diffractometer and (b) the D1B high flux two-axis powder diffractometer to record NPD data in this study at Institut Laue-Langevin, Grenoble, France.[81], [82]

3.1.3 Comparison between XRPD and NPD[83]

- Neutrons interact with nuclei, in contrast, X-rays interact with electron clouds surrounding the nuclei. As a result, neutrons are scattered by point-like nuclei resulting in a scattering angle independent form factor, which is in favor of studying a large *Q*-range.
- Since X-rays are scattered by the electron clouds, they are more sensitive to elements with a high atomic number. However, the scattering length of neutrons is not a monotonous function of the atomic number, revealing that light elements could be well probed even in the presence of heavy elements in the same compound. This is very crucial, for example, when studying oxygen octahedral rotations in perovskites that play an important role in determining their physical properties, neutron diffraction is capable to probe the positions of oxygen atoms more precisely to predict the physical properties. Neighboring elements in the periodic table can also be distinguished by neutron diffraction.
- Isotopes can be distinguished as well due to the distinct scattering lengths of different isotopes.
- Neutrons have a high penetration depth due to the weak scattering and usually low absorption in matter.
- Neutrons possess spins, which indicates that neutrons can interact with unpaired electron spins and determine ordered magnetic structures.

3.1.4 Rietveld Refinement

All SXRPD and NPD patterns were refined with the Rietveld method implemented in the FullProf suite[84]. Besides refining SXRPD and NPD data separately, a joint refinement was performed for $NaYCoWO_6$, $NaLaCoWO_6$ (100K patterns), $NaTbCoWO_6$ and $NaHoCoWO_6$. As mentioned above, X-rays are more sensitive to elements with high atomic numbers while neutrons have the advantage of probing light elements such as oxygen. A joint refinement can combine the complementary information obtained from SXRPD and NPD to get a more precise structural model.

Essentially in Rietveld refinements, the least-squares methods were carried out until the difference between the observed pattern and the pattern generated from the calculated model is minimized.[85] These differences are individually weighted proportional to the reciprocal of the variance of the observed intensity. In order to track the quality of refinements, some agreement factors are taken as criteria of the quality of the fit. R_{wp}, the weighted profile R-factor, directly follows the residual minimization process by least-squares methods. Its value is defined by:

$$R^2_{wp} = \Sigma_i w_i(y_{c,i}-y_{o,i})^2 / \Sigma_i w_i(y_{o,i})^2 \qquad \text{Equation (3.1)}$$

where w_i is the weight defined by $w_i = 1/\sigma^2[y_{o,i}]$ (the reciprocal of the variance of the observed intensity), $y_{c,i}$ and $y_{o,i}$ are the calculated and observed intensities at the 2θ angle $2\theta_i$, respectively.

In contrast, R_p is the profile R-factor with equal weights for all points:

$$R^2_{p} = \Sigma_i(y_{c,i}-y_{o,i})^2 / \Sigma_i(y_{o,i})^2 \qquad \text{Equation (3.2)}$$

Assuming there is an ideal model which can explain the observed intensities perfectly, then the average value of $(y_{c,i}-y_{o,i})^2$ will be equal to $\sigma^2[y_{o,i}]$, which means the component $w_i(y_{c,i}-y_{o,i})^2$ equals unity. If there are a total of N data points measured in the pattern, then the formula of the R_{wp} factor reduces to

$$R^2_{wp} = N / \Sigma_i w_i(y_{o,i})^2 \qquad \text{Equation (3.3)}$$

The R-factor R_{exp} is normally used to replace R_{wp} in this case to express the best possible R_{wp} value for a certain set of data.

With the two R-factors defined above, the goodness of fit (χ) can be defined as:

$$\chi = R_{wp}/R_{exp} \qquad \text{Equation (3.4)}$$

However, it is the value of χ^2 that is directly given from the refinement implemented in FullProf. χ^2 should never be smaller than one, otherwise, R_{wp} will be smaller than R_{exp} which is unacceptable. Even when the χ^2 is close to unity, it does not guarantee the refined model is correct; on the other hand, if χ^2 is much larger than unity, it could be attributed either to the problems concerning the model or the data are measured to very high precision.[86] Extending the counting time usually enlarges the difference between R_{wp} and R_{exp}, resulting in a worse χ^2 value. This can be understood considering that with an enormous number of counted points, even minor imperfections would be huge compared to the experimental uncertainties.

The final R-factor is R_{Bragg}, which is calculated in FullProf as:

$$R^2_{Bragg} = \Sigma_{\mathbf{h}}(I_{c,\mathbf{h}}-`I_{o,\mathbf{h}}')^2 / \Sigma_{\mathbf{h}}(`I_{o,\mathbf{h}}')^2 \qquad \text{Equation (3.5)}$$

h represents the Bragg reflections, $I_{c,\mathbf{h}}$ and '$I_{o,\mathbf{h}}$' stand for the calculated and observed intensities. '$I_{o,\mathbf{h}}$' is presented with quotation marks since the intensity is rarely observed directly, so that it is calculated from the Rietveld formula.[87]

It is very difficult to find out a rule-of-thumb to judge the refinement quality although there are several refinement discrepancy indicators discussed above, and even more indicators not being mentioned here. Nevertheless, it is always recommended to check the difference line calculated between the observed and calculated patterns, and examine if the model is reasonable in a chemical sense. In order to give a feeling about the quality of all refinement work in this study, the patterns containing the observed data, calculated data, and the corresponding difference line are given, as well as the agreement factors χ^2, R_p, R_{wp} and R_{Bragg}. R_{exp} is not shown here since it is correlated with R_{wp} by χ^2 as in Equation (3.4).

In all these refinements, the background was defined by linear interpolation of selected points in the pattern, and the profile function used the Thomson-Cox-Hastings pseudo-Voigt model.[88] Within this model, the peak shape is approximately described by a convolution of Lorentzian and Gaussian functions. The variation of Lorentzian and Gaussian half widths as a function of the 2θ angle are considered and described by the instrumental and specimen effects, e.g. the size and strain effects of the powder specimen.

The axial divergence is known as the asymmetry caused by the curvature of the Debye-Scherrer rings approaching either 0 ° or 180 °. An asymmetry correction corresponding to the L. Finger formulation of the axial divergence[89] was applied. The isotropic displacement parameters of oxygen atoms were constrained to be the same in order to reduce the number of refined parameters.

3.1.5 Crystal and Magnetic Structures Drawing

All crystal and magnetic structures drawings were performed with the VESTA program package.[90]

3.1.6 Second Harmonic Generation (SHG)

SHG measurement acts as a complementary technique to the structure refinement, proving either the structure of the examined sample is centrosymmetric or non-centrosymmetric. Powder SHG measurements were carried out using a pulsed Nd:YAG laser system with a 1064 nm beam wavelength, delivering 10 mJ (before the lens) at 10 Hz in 15ps. The beam was focused with a lens of 100 mm focal length and observations were done with a notch filter. All samples were measured under the same conditions.

SHG is only observed in non-centrosymmetric structures, making it a useful tool for detecting the acentric crystals.[91][92] This phenomenon is related to the nonlinear optical effects in dielectric materials. The spatial and temporal distribution of the electrons and atoms are modified by the electric component of the incident light beam, resulting in a displacement of the valence electrons from their normal orbits. This displacement creates electric dipoles. In the case of nonlinearity, the amplitudes of the reradiated waves from these dipoles differ from those that generated them. As a consequence, the distorted reradiation has different frequencies from that of the primary wave. The induced polarization can be expanded as a function of a power series of the electric component of the primary wave. SHG is related to the third term of this function as[92]:

$$\mathbf{P}_l(2\omega) = X^{(3)}_{lmn}\mathbf{E}_m(\omega)\mathbf{E}_n(\omega) \qquad \text{Equation (3.6)}$$

$\mathbf{P}_l(2\omega)$ is the electric polarization component with a frequency 2ω, $\mathbf{E}_m(\omega)$ and $\mathbf{E}_n(\omega)$ are the electric components of the optical waves. $X^{(3)}_{lmn}$ is the third rank tensor, it vanishes to zero in the presence of a centrosymmetric structure so that SHG is only possible in non-centrosymmetric structures.

3.1.7 Point Charge Model[93]

With the structural information of crystals, it is possible to estimate the spontaneous polarization by a point charge model. The polarization is defined as the dipole moments in one unit cell, so that contributions from all ions are summed and divided by the volume of the unit cell:

$$\mathbf{P}_s = (\Sigma_i Q_i * \Delta_i)/V \qquad \text{Equation (3.7)}$$

$\mathbf{P}_s$ is the estimated polarization, Q_i is the electric charge of the i-th ion and Δ_i is the corresponding displacement of this ion, V is the volume of the unit cell.

This model provides a simple way to estimate the spontaneous polarization by considering the ionic contributions only rather than the electronic contributions to the polarization.

3.2 Transmission Electron Microscopy Techniques[94]

3.2.1 Transmission Electron Microscopy[94]

Different from powder diffraction of X-rays and neutrons, TEM has the advantage of studying a single grain as a single crystal and taking local images in the nano scale (1~100 nm). As a consequence, a tiny amount of sample is sufficient to find out a good study object. Electrons are demonstrated to have both particle and wave characteristics in TEM, the relativistic wavelength of the electron beam is approximately 0.00251 nm under the accelerating voltage 200 kV (0.00197 nm for 300kV electrons). Therefore, TEM is able to produce an image resolution at the atomic level. Besides the imaging, various signals can be obtained from the interaction between the electron beam and the sample, the same as discussed in Chapter 2 about SEM. These signals carry information on chemistry and crystallography. In conventional imaging in a TEM a magnified image of the sample can be obtained up to very high magnifications. The contrast in this case mainly stems from the absorption of the electron beam inside the sample. Particle sizes and shapes can be observed on a nanometric scale.

3.2.2 Electron Diffraction

The ED technique provides an alternative way to study the structure of materials, such as whether a material is crystalline or amorphous, the lattice parameters and symmetry of a crystal, and the orientation of the specimen. While the laws of diffraction are the same for electrons and X-rays or neutrons (Bragg's law, Ewald construction etc.) there are some important differences in practice. The strong interaction of electrons with matter necessitates a very thin sample (approximately 10 to 100 nm). This leads to a relaxation of the Bragg conditions for diffraction, meaning that the reciprocal lattice nodes don't have to be exactly on the Ewald sphere in order to yield to a diffracted beam, but it is sufficient that the nodes be in the vicinity of the Ewald sphere. When the crystal is oriented with a crystallographic direction parallel to the incident beam (called zone axis), a plane of the reciprocal lattice will be tangent to the Ewald sphere and many nodes of the reciprocal lattice will therefore be in the vicinity of the Ewald sphere. This is further helped by the small wavelength of the electrons resulting in a very large radius of the Ewald sphere. For X-rays, the typical wavelength is ~0.2 nm which means the radius of the Ewald sphere is ~5 nm^{-1}. In contrast, for ED if the electron beam has an energy of 300 keV, the wavelength is 1.97 pm and the corresponding Ewald sphere radius is 500 nm^{-1}. It is easy to note that the surface of the Ewald sphere in ED is almost planar compared to the array of reciprocal lattice spots, leading to the Bragg condition is nearly satisfied for many planes. Consequently, a large number of diffracted beams can be observed at the same time in a single diffraction pattern.

Normally, diffraction conditions vary from one place to another on the grid, therefore, a restricting aperture is employed to select areas of constant orientation, e.g. a single crystalline particle in a powder. This technique is known as selected area ED (SAED). The positions and intensities of the observed spots in the diffraction pattern yield information about the size of the crystalline unit cell and its symmetry.

3.2.3 High-Resolution TEM (HRTEM) Imaging

The HRTEM imaging technique makes use of the transmitted as well as the diffracted electron beams. When the sample is oriented with a crystallographic direction parallel to the incident beam (zone axis orientation), the diffracted beams are evenly distributed around the transmitted beam. The electromagnetic lenses of the TEM make a large number of diffracted beams interfere with each other and with the transmitted beam in order to from an image of the sample. At high magnification, this interference leads to images that show contrast on an atomic length scale. These images are useful because they give information about geometric motives that constitute the crystal at the atomic level. However, a direct interpretation of the images in terms of atomic positions inside the unit cell is not possible. In fact, atomic columns can give bright or dark contrast depending on the thickness of the sample and the focus or defocus used by the operator.

3.2.4 Scanning TEM (STEM)

A scanning electron beam is employed in STEM just like in SEM. However, unlike in SEM, the electron beam in STEM is transmitted by the sample and the detectors are therefore placed beneath the sample. At each position of the incident beam during the scan one or more of these detectors record the information they receive. An image is then formed where each pixel corresponds to one incident beam position and the grey level of this pixel is a function of the information recorded by the detector. The electron beam can be focused on a very small area, less than 1 Å in diameter, and the resolution of the obtained images can therefore be at the atomic level.

Several detectors are available on a modern STEM collecting either electrons of the transmitted beam, electrons that were scattered to high angles or even detectors capable of recording an electron energy loss spectrum at each pixel of the image. Each detector will give specific information that is used in a particular technique. In the following we will present the techniques that were employed in this work.

3.2.5 High-Angle Annular Dark Field (HAADF) Imaging

The HAADF detector collects scattered electrons at high angles (Figure 3.3). At these high angles the observed signal is mainly from incoherently scattered electrons. As heavy elements are more efficient in scattering to high angles, the contrast in HAADF images depends on the average atomic number Z of the elements in an atom column parallel to the incident beam. Therefore, HAADF imaging is also termed Z-contrast imaging, with brighter contrast corresponding to higher Z elements.

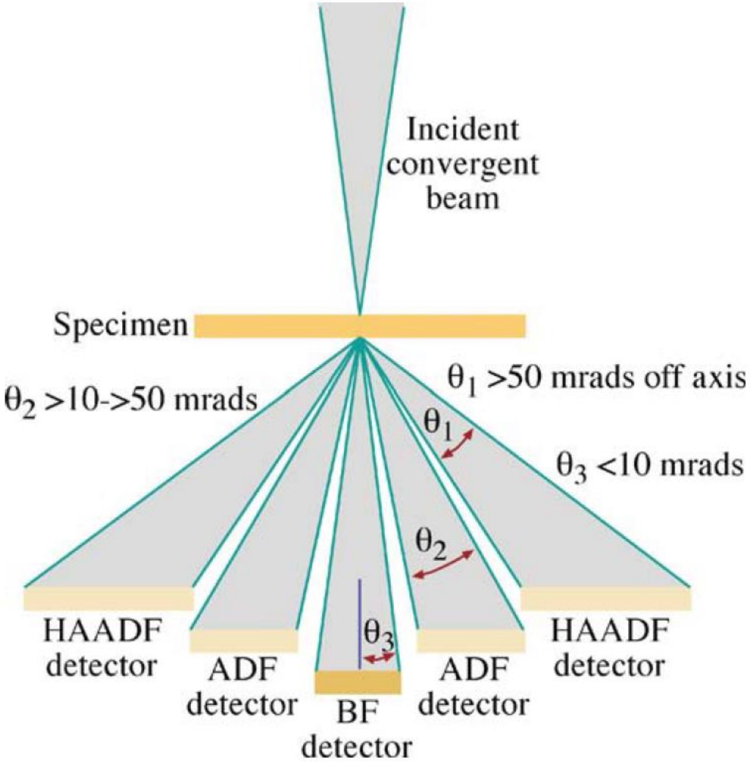

Figure 3.3 A schematic view of the distribution of different detectors, namely BF, ADF and HAADF detectors, in STEM.[94]

3.2.6 Annular Bright Field (ABF) Imaging

The Annular Bright Field detector collects coherently as well as incoherently scattered electrons. Therefore light elements that scatter at small angle are visible in these images. However, Coherent Bragg scattering is also present in the signal obtained, making a direct interpretation of the observed contrasts difficult. [95]

3.2.7 Electron Energy-Loss Spectroscopy (EELS)

EELS is an alternative technique to obtain chemical information on the specimen other than EDX which is discussed in Chapter 2. EELS exploits the fact that during the interaction between the high energy electron beam and the specimen, some electrons lose some of their energy due to a variety of scattering processes. Then, for each position of the electron beam during the scanning process, these inelastically scattered electrons are collected and analyzed to build up a spectrum. Each pixel of the obtained image contains therefore an entire spectrum of the specific energy losses. Any feature of the spectrum can then be selected and translated into a grey level.

From the specific energy of electrons, chemical information can be derived quantitatively and qualitatively. The spectrum curve which stands for the signal intensity decreases rapidly with increasing energy loss. The intensity range is very large with energy limits around 2 keV, where there are only negligible signals. The spectrum can be divided into two parts: the low-loss and the high-loss regions. The low-loss region contains signals regarding the electronic information from the more weakly bound conduction and valence band electrons. Plasmon peaks can be observed in the low-loss region, and the peak intensity can be relative intense. And the high-loss region gives more elemental information from the more tightly bound, core-shell electrons, even details about the bonding and atomic distribution.

Chemical information concerning the elements can be interpreted from the ionization edges, however, the intensities of ionization edges are rather low compared to the spectrum background. An atomic resolution map of any of these features can therefore be obtained yielding valuable chemical information about the specimen.

3.2.8 Experiments

Electron diffraction experiments and high resolution electron micrographs were obtained on the Philips CM300ST transmission electron microscope (TEM) of the Institut Néel. The TEM was operated at 300 kV and has a point to point resolution of 1.9 Å.

The STEM experiments reported in this manuscript were obtained on a FEI Titan Ultimate TEM operated at 200 kV.

3.3 Physical Properties Characterization Methods and Techniques

3.3.1 The Curie-Weiss Law[96]

The magnetic susceptibility (χ) is derived by the Curie-Weiss law in the paramagnetic region for both the ferromagnets and antiferromagnets. The dependence of χ on temperature in the Curie-Weiss law is described by:

$$\chi = C/(T-\theta) \qquad \text{Equation (3.8)}$$

where χ is the magnetic susceptibility, C is the Curie constant, T is the temperature measured in Kelvin (K), and θ is the Weiss temperature. Different ways to plot χ as a function of temperature are shown in Figure 3.4. C and θ can be directly derived from the slope and the intercept with the temperature axis, respectively, from the $1/\chi$-T plot in Figure 3.4 (b). If θ is 0, then the material is essentially paramagnet. Otherwise, the materials is antiferromagnet if $\theta<0$ or ferromagnet if $\theta>0$.

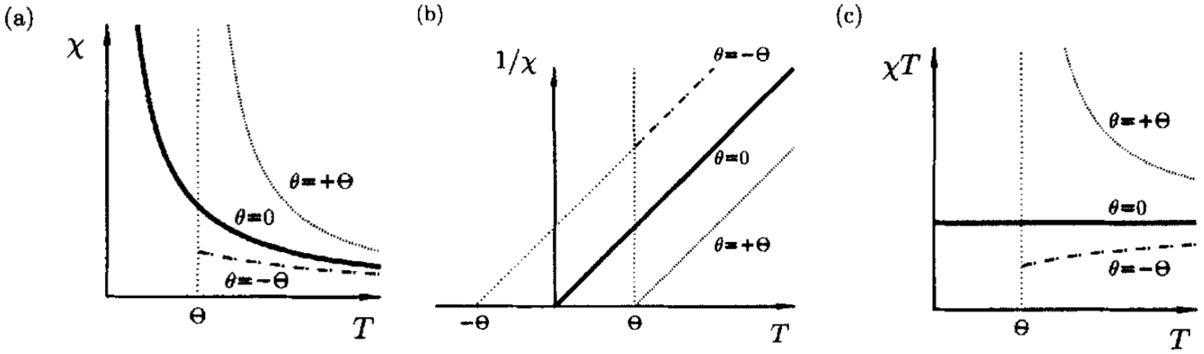

Figure 3.4 The relationships between χ and T described by the Curie-Weiss law. For each plot, three cases are shown: $\theta = 0$ (paramagnet), $\theta > 0$ (ferromagnet) and $\theta < 0$ (antiferromagnet).[96]

Furthermore, the effective magnetic moment can also be derived[97] by:

$$\mu_{eff}= (3k/N\mu^2_B)^{1/2}*(C)^{1/2} \qquad \text{Equation (3.9)}$$

when C is given in cgs units. In Equation (3.9), μ_{eff} is the effective magnetic moment in units of μ_B, k is the Boltzmann constant, N is the Avogadro constant, and μ_B is the Bohr magneton. The constant term is approximately equal to 2.82787.

3.3.2 Magnetic Measurements

The magnetic properties are mainly measured by the commercial squid magnetometer MPMS_XL (MPMS: Magnetic Property Measurement System) manufactured by Quantum Design Inc., and all samples are measured in the states of a powder. This part mainly focuses on introducing the principles of magnetic measurements with the MPMS_XL instrument.

MPMS_XL is typically made up of several systems: the temperature control system, the magnetic field control system, the Superconducting Quantum Interference Device (SQUID) based detection system, the sample handling system and the computer operation system.[98] Several superconducting components are employed in different systems[99]:

-- a superconducting magnet to generate magnetic fields;

-- a superconducting coil to convert magnetic signals into electric signals;

-- a Superconducting Quantum Interference Device (SQUID) to convert current signals into voltage signals;

-- a superconducting magnetic shield to avoid noise.

The SQUID provides an extremely high measurement sensitivity of the MPMS_XL instrument, in fact it is the most sensitive device for magnetic measurements which can reach a sensitivity as small as 10^{-8} emu (1 emu =10^{-3} A*m^2). The magnetic field is generated by the superconducting magnet, which gives a maximum field of 5 T. The sample is placed in a Helium flow cryostat, and the measurable temperature range is between 1.8 K and 400 K. The interface to carry out the measurement and communicate with the instrument is through a dedicated software provided by Quantum Design Inc.. All powder samples were tightly wrapped in a plastic thin film, and then the unit was inserted into the middle part of a plastic straw of diameter ~ 5 mm and length ~ 196 mm. The diamagnetic effects of the plastic components were very small and negligible.

Although SQUID lies in the heart of the highly sensitive magnetic measurement, it does not directly measure the magnetic signal. Instead, it is connected with the superconducting coils to convert a current signal to a voltage signal which is proportional to the magnetic signal from the sample. The superconducting detection coils are composed of three coils which is called a second-order gradiometer, as shown in Figure 3.5 (a). The top and bottom ones are wound clockwise and the middle one is wound counter-clockwise. With such a configuration, the noise from the fluctuations of the magnetic field can be minimized. The counter wound part is responsible for measuring local changes of the magnetic flux density coming from the sample.

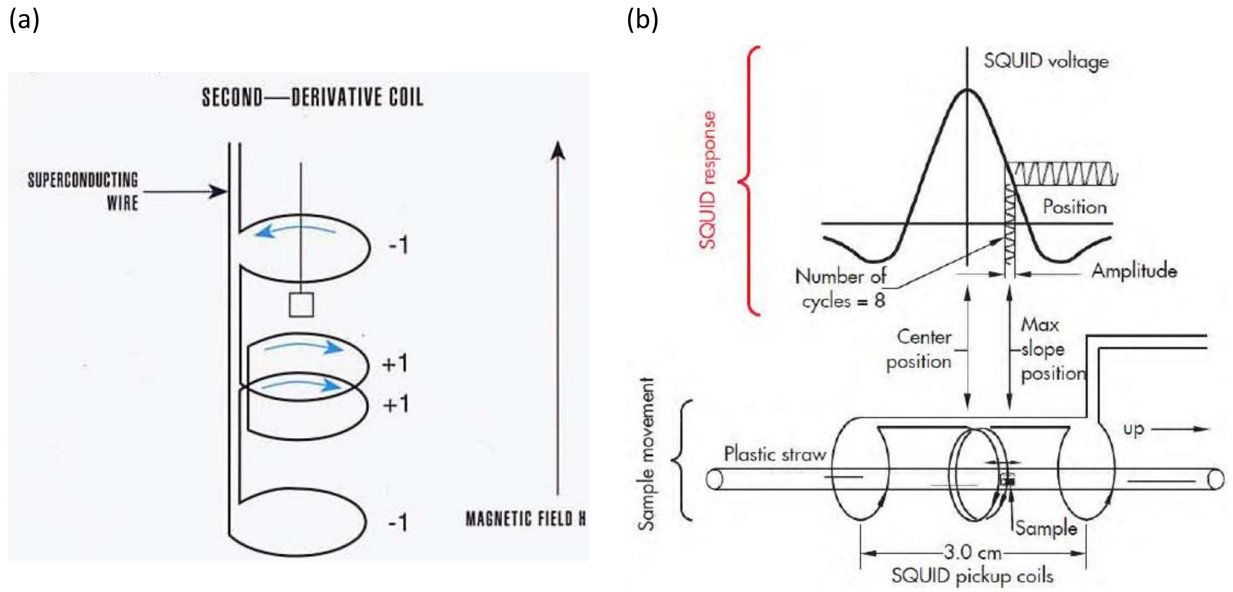

Figure 3.5 (a) The superconducting coil configuration of the second-order (second-derivative) gradiometer in SQUID. (b) The voltage response converted by SQUID as the sample moving in the RSO measurement.[98], [99]

All the measurements were performed in the mode of the Reciprocating Sample Option (RSO), where the sample moves in a reciprocating way in a small amplitude. As the sample moves through the superconducting coils, a current signal is induced in the superconducting coils by the magnetic moments of the sample. Any change of the magnetic flux can be reflected by the change of the persistent current in the superconducting coils. Variations of the voltage signal converted by SQUID from the change of the current signal (see Figure 3.5(b)) are proportional to magnetic signal change and can be analyzed by the system.

The data for a Curie-Weiss fit were collected between 2 K and 300 K in a magnetic field of 1 T, the temperature range 150 K- 300 K was picked for all samples except for $NaYCoWO_6$ (50-150K) and $NaSmCoWO_6$ (50-300K) to do the fit. The data for M-H plots were collected at temperatures of 2 K, 5 K, 10 K, 15 K, 20 K, 25 K, 30 K and 350 K, the magnetic field was scanned from 0 T to 5 T and then back to 0 T with a constant step of 0.1T. Zero-Field Cooling (ZFC) and Field Cooling (FC) measurements were carried out in the magnetic field 0.01 T in the low temperature region (< 20 K). ZFC is a process where the sample is cooled down in the absence of any applied field to a temperature below the transition temperature. Then, a magnetic field is applied and the effect of the magnetic field is continuously measured while raising the temperature to a point which is well beyond the transition temperature. FC is a process where a magnetic field is already applied when the temperature is well above the transition temperature, then the sample is cooled down to a temperature lower than the transition temperature, meanwhile, continuously measuring the effect of the applied field. ZFC and FC are reverse processes to each other, the FC-ZFC process is intended to identify the presence of any ferromagnetic contribution (and therefore hysteretic and history dependent).

3.3.3 Magnetic Structure Determination

Neutrons have been recognized as a very useful tool to study magnetism in condensed matter, and the neutron scattering technique has been widely employed to study the magnetic structure and dynamics.[96] The significance of neutrons for magnetic studies comes from their unique properties.[100]

Neutrons have a spin ½, resulting in a corresponding magnetic moment. Therefore neutrons can directly probe the magnetic moments to reveal the magnetic ordering. The arrangement of the magnetic ordering in a magnetically ordered system can be revealed from the scattering amplitudes which are dependent on the alignment direction of the moments. Furthermore, thermal neutrons have a wavelength (1-3 Å) and an energy (10-80 meV) in the same order of interatomic spacing and thermal excitations, respectively, in crystals. The intensity of the magnetic Bragg peaks reflects the strength of the magnetic ordering, thus, the magnetic order can be tracked as a function of the temperature.

In order to determine a magnetic structure, the propagation vector(s) ***k*** should be defined first of all. The propagation vector(s) describes the dimensions and the propagating direction(s) of the magnetic unit cell with respect to the nuclear structure, because the magnetic unit cell does not necessarily have the same unit cell and propagating directions as the nuclear structure. The propagation vector(s) can be more than one for describing a single magnetic structure, and can be either commensurate or incommensurate, or a combination of both. In this study, the propagation vectors were analyzed from a few low-angle magnetic Bragg peaks by the K-search program implemented in the FullProf Suite. When more than one ***k*** vector was proposed, LeBail refinements with all possible ***k*** vectors were tested to justify which one is better or if they are comparable. The next step was to do the symmetry analysis based on the representation analysis[101], where the magnetic structures were decomposed into irreducible representations based on the propagation vector(s), the space group of the nuclear structure and the atomic positions of the magnetic atom(s). Therefore, determining the correct space group of the nuclear structure is crucial for solving the magnetic structure. This decomposition yields the number of basis vectors from each irreducible representation.[102] The basis vectors for atomic moments are derived by the projection operator technique, which takes a test function and projects from it the component that transforms each irreducible representation. In this study, two programs were employed to do this analysis, the BasIreps application implemented in the FullProf Suite[84] and the SARAh-Representation analysis[103]. The final step was to solve the magnetic structure. The coefficients of the basis functions are the refined variables. It is always helpful to try to start with various combinations of the basis function coefficients, and determine the robust components which always converge to a similar value.

3.3.4 Specific Heat Capacity and Measurements

Heat capacity is defined as the heat absorption or dissipation of an object responding to a temperature change.[104] The heat capacity is an intensive property, so the observed value depends on the amount of the measured object. In order to facilitate the comparison of the heat capacity of different substances, the heat capacity is usually divided by the amount of substance or mass.

The measurements of heat capacity were performed by the Physical Properties Measurement System (PPMS) manufactured by Quantum Design Inc., the main principle of the heat capacity measurement is as following. In Figure 3.6(a), the sample is mounted on the sample platform with the help of adhesive grease. In this study, all the measured samples were prepared in pellets, where the pelletized samples are assumed to be a bulk sample. Considering both the time consuming issue of preparing a large amount of sample and the accuracy factor limited by measuring heat capacity in samples of a small quantity, the most favorable sample mass is between 3 and 5 mg.

At the bottom of the platform, there are one heater which gives the heat pulse to the platform and one thermometer which detects the change of temperature. The sample platform is suspended by thin connecting wires which serve as the electrical leads for the thermometer and heater, as well as the thermal connection between the sample platform and the puck.

When the temperatures of the sample platform and the puck are stable at a certain initial temperature, a power (see Figure 3.6(b)) is applied to the heater in order to transmit a heat pulse to the platform. With this heat pulse, the temperature of the sample platform rises to a certain predetermined temperature (increasing 1% of the initial temperature here). Once the power supply stops, the temperature of the sample platform starts to relax to the puck temperature. Both the processes of heating and relaxing are monitored and recorded by the thermometer as shown in Figure 3.6(c).

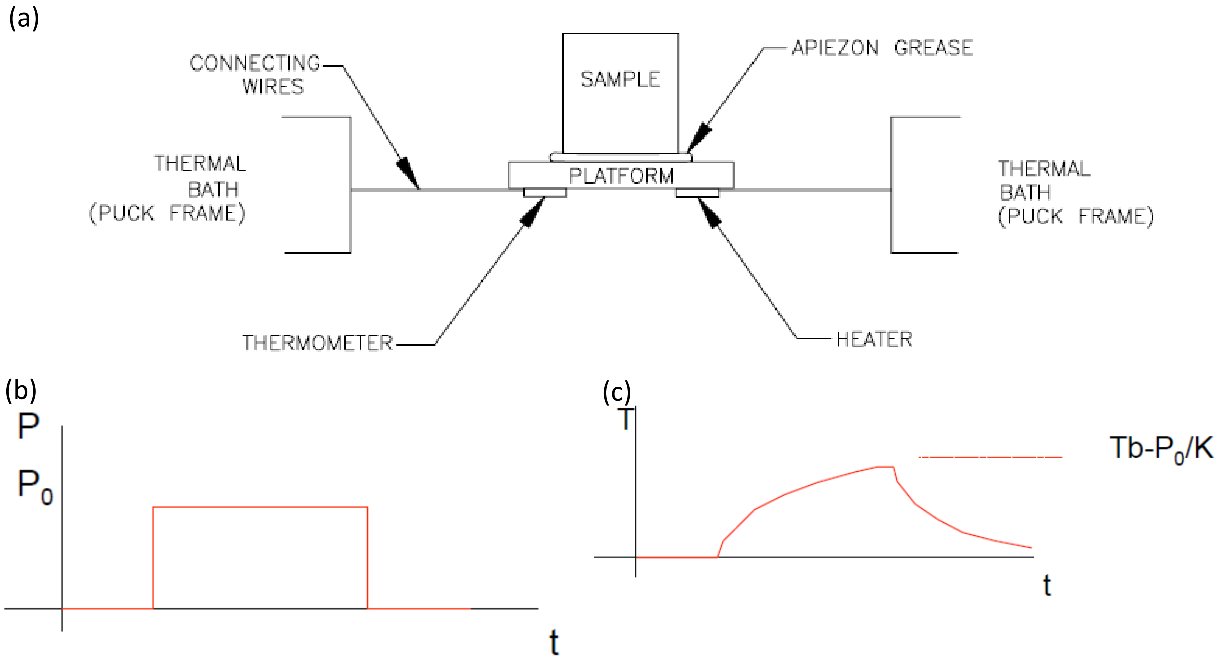

Figure 3.6 (a) a sketch of the sample platform and the puck in PPMS for heat capacity measurement; (b) a description of the power applied the heater when the sample platform and the puck temperatures are stable; (c) the temperature curve of the sample platform recorded from before any power is applied to it until its temperature relaxes to that of the puck.[105][106]

To derive the value of heat capacity, Equations 3.10-3.12 are employed:

$$CdT/dt = -k(T-T_b)+P(t) \qquad \text{Equation (3.10)}$$

$$T=T_b+P_0/k\exp(-\tau/t) \qquad \text{Equation (3.11)}$$

$$\tau = C/k \qquad \text{Equation (3.12)}$$

where C is the heat capacity whose value is to be derived, dT/dt is a description of the change of the temperature with time, k is a constant related to the thermal conductance of the connecting wires, T is the temperature monitored by the thermometer, T_b is the temperature at the beginning of applying the power to the heater, P(t) is the power as a function of time, P_0 is the value of the applied constant power, τ is called time constant with a value given by Equation (3.12).

All parameters except C can be directly measured and recorded by PPMS, so that with Equations (3.10-3.12) the heat capacity value can be deduced.

In this study, the samples $NaYCoWO_6$, $NaLaCoWO_6$, $NaNdCoWO_6$, $NaSmCoWO_6$, $NaGdCoWO_6$, $NaTbCoWO_6$, $NaHoCoWO_6$, and $NaYbCoWO_6$ were selected to do the heat capacity measurements, yielding complementary information on the magnetic ordering. Therefore low temperature range 2 K – 100 K was concentrated on.

3.3.5 Electric Properties and Measurements

The samples for the electric measurements need to be prepared into a pellet with a thickness of ~0.5mm and an as large as possible surface area. The pellets measured in this study were either sintered at high temperature in order to make them compact, for instance, for La, or suitable pellets were directly picked out as synthesized in HT-HP syntheses, for instance, for Y, Tb and Ho. A homogeneous thickness is crucial since it is an important parameter when deriving the capacitance.

All pellets were measured by the four-probe method to extract the electrical impedance. This method is a more precise measurement approach, where the contact resistance of two electrodes for current probing is eliminated. The other two probes are responsible for the voltage measurement.

An equivalent circuit to the AC mode measurement[107] is plotted in Figure 3.7.

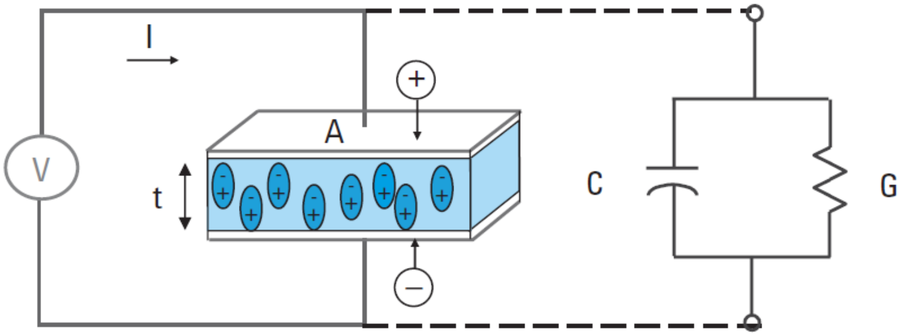

Figure 3.7 A schematic equivalent circuit to the measurement in AC mode to extract the capacitance and resistance.[107]

The pellet in the circuit is equivalent to a capacitor and a resistor in parallel. The capacitor is the dielectric part while the resistor is responsible for the loss current. Both capacitance and resistance are measured either as a function of temperature with or without applying a magnetic field, or at a fixed magnetic field to scan the temperature.

In practice, the capacitance is frequency dependent, therefore, before starting any real measurement, it is crucial to test a variety of frequencies to determine the range where the capacitance remains rather constant and less frequency dependent.

In this study, the capacitances were measured in the temperature cycle 2K-30K-2K with a magnetic field of 0T, 2T, 4T, 6T and 8T, respectively. A larger temperature range between 3K and 300K was also measured for 0T. The magnetic field was also scanned in cycles from 8T to -8T at temperatures 4K, 6K, 8K and 10K, respectively.

The relative electric permittivity ε_r is employed as a benchmark to characterize the dielectric property of all the samples. It is deduced from the equation:

$$C = \varepsilon_0\varepsilon_r A/t \qquad \text{Equation (3.13)}$$

where C is the capacitance in the unit of Farads (F), ε_0 is the permittivity of vacuum which takes a value of $8.85*10^{-12}$ F/m, ε_r is the relative permittivity which is also called the dielectric constant, A is the surface area of the sample in the unit of m^2, t is the thickness of the sample in the unit of m.

Magnetocapacitance is the physical phenomenon which exhibits the magnetic field dependence of the electric capacitance.[108] In order to compare the capacitance variance as a function of the magnetic field, the capacitance differences with respect to the one at 0T are plotted as a function of the applied magnetic field, as:

$$\Delta C_p/C_p(0T)=C_p-C_p(0T)/C_p(0T) \qquad \text{Equation (3.14)}$$

3.3.6 Pyroelectricity

In order to experimentally measure the electric polarization induced by the magnetic ordering, we carried out pyroelectric current measurements. In a polar ionic crystal, the ions displace with changing temperature, resulting in a net dipole moment and a polarization current. The current can be measured and described by:

$$I = p(T)\ A\ dT/dt \qquad \text{Equation (3.15)}$$

where I is the current, p(T) is the pyroelectric coefficient at a certain temperature T, A is the surface area of the electrodes on the sample, and dT/dt is the temperature change rate with respect to time.

Considering the pyroelectric coefficient is the spontaneous polarization change rate with respect to time:

$$p(T) = \partial Ps/\partial T \qquad \text{Equation (3.16)}$$

Taking both Equations (3.13) and (3.14) into account, the spontaneous polarization can be deduced:

$$\partial Ps = Idt/A \qquad \text{Equation (3.17)}$$

As a consequence, the spontaneous polarization is the integration of the current density (I/A) with respect to time.

The measured samples were prepared into pellets. If the sample is synthesized at high pressure, then a piece in the shape of a pellet was selected as synthesized. Silver epoxy was coated on both sides of the pellets as electrodes. Magnetoelectric annealing was performed before any real measurement. It included simultaneously applying an electric field of 400 kV/m (200V applied on sample of typical thickness of 0.5mm) and a magnetic field of 8T in a direction either perpendicular or parallel to the sample at 30K and then cooling the sample down to 2K. Both the electric and magnetic fields were removed at 2K and the wires were left until the circuit was completely discharged. After the poling processes, the pyroelectric current was measured under various magnetic fields (0T, 1T, 2T, 3T, 4T, 5T, 6T, 7T and 8T) and without an electric field when warming the sample up in a speed of 3K/min.

Chapter 4: Structural Study of the Doubly Ordered Perovskites Family $NaLnCoWO_6$ (Ln= Y, La, Pr, Nd, Sm, Eu, Gd, Tb, Dy, Ho, Er, and Yb) by Synchrotron X-ray Powder Diffraction (SXRPD) and Neutron Powder Diffraction (NPD)

In this chapter, the structural study of the entire $NaLnCoWO_6$ series will be discussed, taking advantage of the high quality SXRPD and NPD data collected at room temperature. All compounds are demonstrated to crystallize in monoclinic structures, especially the nine new compounds have the polar space group $P2_1$. Second harmonic generation measurements were carried out in powders for all samples, and it confirmed the non-centrosymmetric structure of the nine compounds. Furthermore, the $P2_1$ polar structures of the nine new compounds were decomposed in terms of symmetry modes, demonstrating that the polar mode is induced by two nonpolar modes in a manner of HIF. The amplitudes of these three major modes were refined for a deeper understanding on the polarization trend as a function of the rare-earth size in this series and it was concluded that all mode amplitudes increase with decreasing the Ln cation size. Finally, the estimated polarizations of $NaLnCoWO_6$ (Ln=Y, Tb, Ho) from the NPD data will be presented, the polarization being as large as ~$20\mu C/cm^2$.

4.1 Structural Analysis for Doubly Ordered Perovskite $AA'BB'O_6$

The aristotype perovskite ABO_3 structure adopts the cubic symmetry of space group *Pm-3m*. This particular structure exhibits a great flexibility of composition by substituting various ions at each site. When two different cations are present in either the A- or the B-site, a large difference in size and/or charge favors the building of a stable ordering. The rock-salt ordering of the B-site cations in $A_2BB'O_6$ is well known, and it changes the structure symmetry from *Pm-3m* to *Fm-3m*, while doubling the unit-cell parameter from 3.8 Å to 7.6 Å.[50] Ordering on the A-site is fairly less common, and if present, a layered ordering on the A/A'-sites is more stable than rock-salt type ordering.[41] When both A-site and B-site orders are simultaneously obtained the unit cell is changed to $\sqrt{2}a_p*\sqrt{2}a_p*2a_p$ (where a_p is the unit-cell parameter of the aristotype perovskite). The resulting $AA'BB'O_6$ structure with layered A/A'-sites and rock-salt ordered B/B'-sites has tetragonal symmetry with space group *P4/nmm*. By tuning the cation sizes, the $BO_6/B'O_6$ octahedra may adopt various tilted arrangements which will further reduce the symmetry. All possible lower symmetry space groups were predicted by Knapp *et al.*[41] by only considering layered A/A' ordering, B/B' rock-salt ordering and $BO_6/B'O_6$ octahedral tilting.

4.2 SXPRD Refinement and Space Group Assignments

SXRPD was performed to investigate the structural aspects of the series. Rietveld refinement was employed to determine the structural parameters for each compound. All unit-cell parameters are listed in Table 4.1 and plotted in Figure 4.1 as a function of the rare-earth cation radius.[109] $NaLaCoWO_6$, $NaPrCoWO_6$, and $NaNdCoWO_6$ are described in a larger unit cell $2a_p*2a_p*2a_p$ while all others adopt a smaller one $\sqrt{2}a_p*\sqrt{2}a_p*2a_p$. To facilitate the comparison, the *a* and *b* unit-cell parameters of $NaLaCoWO_6$, $NaPrCoWO_6$, and $NaNdCoWO_6$ were divided by $\sqrt{2}$ in Figure 4.1(a). All compounds were found to have monoclinic symmetry. Details about the space group assignment for each of them are given in the following part of this chapter.

Table 4.1 The unit-cell parameters, and the formula unit volumes from the SXRPD refinement of all compounds.

Sample	a (Å)	b (Å)	c (Å)	β (°)	V/Z (Å^3)
NaYCoWO$_6$	5.34712(2)	5.52411(2)	7.78938(2)	90.2946(1)	115.04(0)
NaLaCoWO$_6$	7.8347(1)	7.8430(1)	7.8940(1)	90.165(1)	121.27(1)
NaPrCoWO$_6$	7.7900(3)	7.7913(3)	7.86673(5)	90.025(2)	119.366(5)
NaNdCoWO$_6$	7.7736(2)	7.7757(2)	7.86181(6)	90.023(2)	118.801(3)
NaSmCoWO$_6$	5.43629(6)	5.51765(6)	7.8402(1)	90.297(1)	117.585(2)
NaEuCoWO$_6$	5.41229(2)	5.52448(2)	7.82945(5)	90.3220(3)	117.049(1)
NaGdCoWO$_6$	5.40023(5)	5.52331(5)	7.82229(8)	90.2976(6)	116.657(1)
NaTbCoWO$_6$	5.38318(2)	5.51974(5)	7.80868(5)	90.3017(5)	116.011(1)
NaDyCoWO$_6$	5.36328(4)	5.52198(4)	7.79760(4)	90.2986(4)	115.465(1)
NaHoCoWO$_6$	5.34661(1)	5.52114(1)	7.78969(2)	90.2836(2)	114.972(0)
NaErCoWO$_6$	5.33276(1)	5.51783(1)	7.78224(2)	90.2758(1)	114.496(0)
NaYbCoWO$_6$	5.30692(1)	5.50727(1)	7.76784(2)	90.2815(2)	113.513(0)

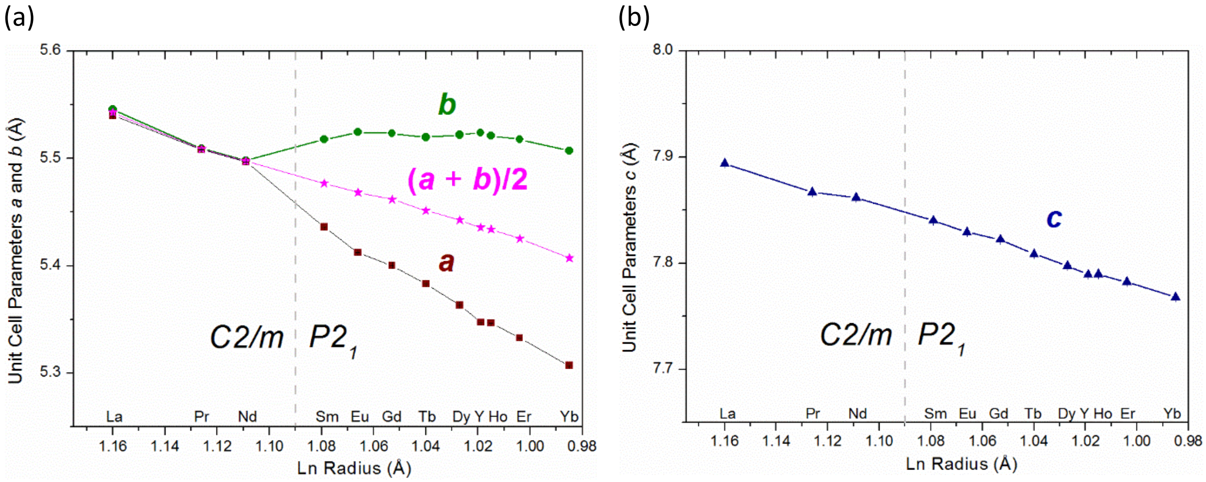

Figure 4.1 Lattice parameters plotted as a function of the eight-coordinated rare-earth site radius. The *a* and *b* parameters of NaLaCowO$_6$, NaPrCowO$_6$, and NaNdCowO$_6$ were divided by √2 for comparison.

The lattice parameters *a*, *b* and *c* decrease slightly from NaLaCoWO$_6$, to NaPrCoWO$_6$ and to NaNdCoWO$_6$. Note in particular that the *a* and *b* parameters are almost identical and that *β* is very close to 90° (Table 4.1) in these three samples, although the refinements clearly indicate that their symmetry is monoclinic.

With a further decreasing size of the Ln site cation, the *a* parameter keeps decreasing while the *b* parameter remains approximately constant, and the *c* parameter decreases continuously.

$NaLaCoWO_6$ was first synthesized by Arillo *et al.* and determined as having the symmetry of space group $P2_1/m$ with lattice parameters $\sqrt{2}a_p*\sqrt{2}a_p*2a_p$ and β close to 90°.[47] In a following study, the structure of $NaLaCoWO_6$ was also determined as monoclinic with a similar unit cell. [110] However, we found it very difficult to refine our SXRPD pattern with space group $P2_1/m$, many peak positions being not accounted for in this description. To determine the correct space group, we considered systematic extinctions and the results of a theoretical analysis,[41] which led to the conclusion that the *C2/m* space group is in better registry. The main differences between the descriptions in $P2_1/m$ and *C2/m* are the unit-cell dimensions and oxygen octahedral BO_6/B'O_6 tilting schemes. For $P2_1/m$, the unit-cell dimensions are $\sqrt{2}a_p*\sqrt{2}a_p*2a_p$ and the tilting scheme is $a^-a^-c^0$ in Glazer's notation, while for *C2/m*, the unit-cell dimensions are $2a_p*2a_p*2a_p$ and the tilting scheme is $a^0b^-c^0$. The same angular regions from the $P2_1/m$ and *C2/m* refinements are compared in Figure 4.2 (a), right and left, respectively. The presented peaks correspond to the $\{224\}_T$ and $\{400\}_T$ (the subscript "T" represents the index referred to the parent *P4/nmm* tetragonal unit cell) reflections, the splitting being due to the monoclinic distortion. Clearly, *C2/m* symmetry is superior in describing the peak positions and splitting, which was also confirmed on other reflections. On the one hand, a further refinement was tried with subgroup *C2*, but it did not improve the refinement, which indicates that the symmetry is not lower than *C2/m*. On the other hand, neither tetragonal nor orthorhombic space groups could be found to well-explain the peak splitting shown, so that space group *C2/m* was assigned to $NaLaCoWO_6$. Note, however, that electron diffraction and high-resolution electron micrographs show the presence of a superstructure in this compound. The presently refined structure only takes into account the average structure. Detailed information concerning this superstructure will be discussed in the next chapter, Chapter 5.

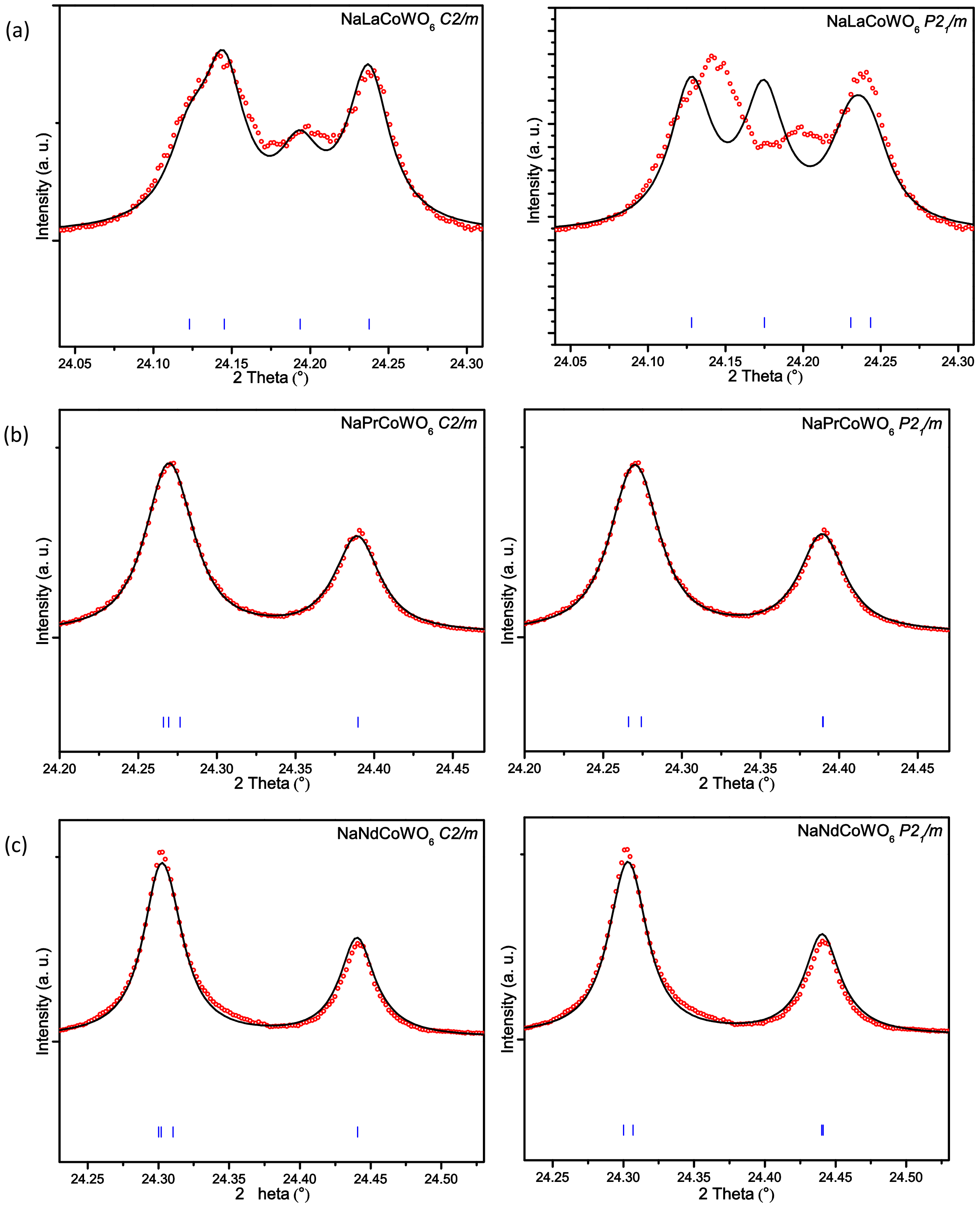
(a)
NaLaCoWO$_6$ C2/m
NaLaCoWO$_6$ $P2_1/m$
Intensity (a. u.)
24.05
24.10
24.15
24.20
24.25
24.30
2 Theta (°)
(b)
NaPrCoWO$_6$ C2/m
NaPrCoWO$_6$ $P2_1/m$
Intensity (a. u.)
24.20
24.25
24.30
24.35
24.40
24.45
2 Theta (°)
(c)
NaNdCoWO$_6$ C2/m
NaNdCoWO$_6$ $P2_1/m$
Intensity (a. u.)
24.25
24.30
24.35
24.40
24.45
24.50
2 heta (°)
2 Theta (°)

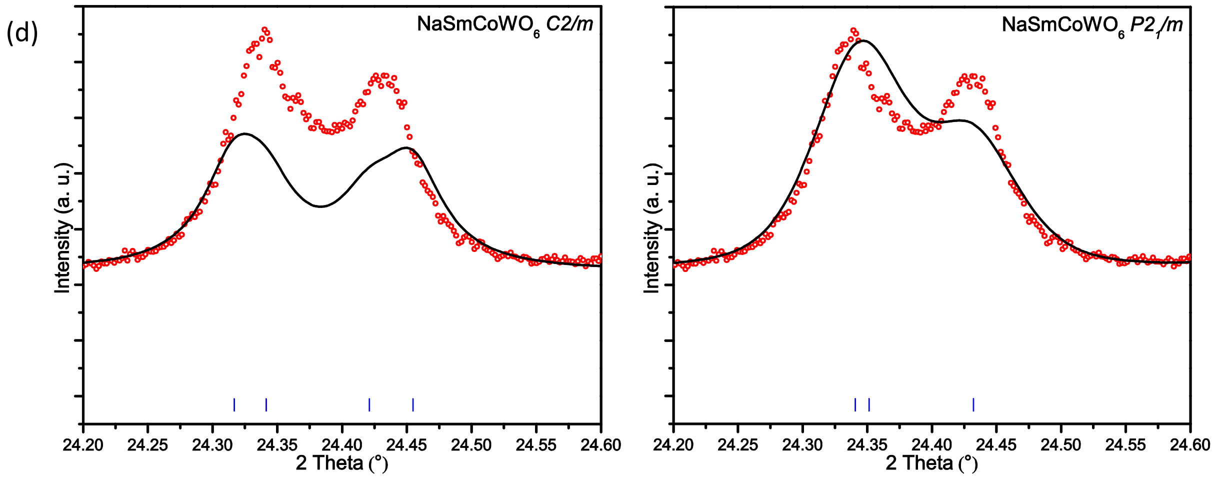

Figure 4.2 Comparison between *C2/m* (left) and *P2₁/m* (right) refinements of the $\{224\}_T$ and $\{400\}_T$ peaks for (a) $NaLaCoWO_6$, (b) $NaPrCoWO_6$, (c) $NaNdCoWO_6$ and (d) $NaSmCoWO_6$, respectively.

$NaPrCoWO_6$ and $NaNdCoWO_6$ have many structural aspects in common. First, the refined unit-cell parameters are very close to a tetragonal metric, which led us to test a refinement using the space group of the tetragonal parent structure *P4/nmm*. Although the fit is rather good, the value of the thermal parameter B_{iso} of the oxygen atoms is very large, indicating that the oxygen positions are not well-described within this symmetry. Therefore, we tried lower-symmetry space groups, of which *C2/m* and *P2₁/m* yielded the best and equally good fits as can be seen in Figure 4.2 (b) and (c). Lower-symmetry space groups were also tried; nevertheless, neither of the corresponding subgroups *C2* nor *P2₁* can provide a better fit. As the space group *C2/m* has a higher symmetry and the refinement reaches convergence more easily than with *P2₁/m*, we retain this space group for both $NaPrCoWO_6$ and $NaNdCoWO_6$. Here also, very complex modulations have been observed in the $NaPrCoWO_6$ and $NaNdCoWO_6$ samples by electron diffraction and high resolution imaging in a transmission electron microscope (TEM). Detailed information concerning these modulations will be addressed in the next chapter, Chapter 5. Even though a mixed occupancy with the Ln cation (Pr and Nd, respectively) was refined for the Na site, the refined occupancies of the Ln cations were very small. The refined $NaPrCoWO_6$ structural parameters are selected as a representative of the *C2/m* compounds, and listed in Table 4.2.

Table 4.2 Crystallographic parameters of NaPrCoWO$_6$ from the SXRPD pattern refinement (*C2/m*) at room temperature.[a]

Atom	Wyckoff Symbol	x	y	z	B(Å^2)	Occupancy
Na	4g	0	0.225(5)	0.5	1.1(2)	0.475(2)
Pr1	4g	0	0.225(5)	0.5	1.1(2)	0.025(2)
Pr2	4h	0	0.246(1)	0	1.03(1)	0.5
Co	4i	0.745(3)	0	0.7467(9)	0.12(2)	0.5
W	4i	0.250(1)	0	0.7338(2)	0.270(4)	0.5
O1	4i	0.02(1)	0	0.707(7)	0.6(1)	0.5
O2	8j	0.714(5)	0.261(7)	0.762(5)	0.6(1)	1.0
O4	4i	0.49(1)	0	0.820(8)	0.6(1)	0.5
O5	4i	0.805(5)	0	0.008(5)	0.6(1)	0.5
O6	4i	0.697(5)	0	0.485(5)	0.6(1)	0.5

[a] Space group *C2/m*, Z=4. Unit cell parameters: a= 7.7900(3) Å, b= 7.7913(3) Å, c= 7.86673(5) Å, β= 90.025(2) °, V/Z= 119.366(5) Å^3. Discrepancy factors: χ^2 = 15.2, R_p=11.2%, R_{wp}= 15.3%, R_{Bragg}= 4.16%.

For all other compounds with smaller Ln site cations the unit cell metrics is clearly not tetragonal since significant differences in the *a* and *b* parameters are observed (see Figure 4.1). Therefore only monoclinic space groups can reasonably be retained for these compounds. To illustrate the refinement of all remaining compounds we choose NaSmCoWO$_6$ since it contains the largest Ln site cation Sm. On the basis of our findings for the three compounds discussed above, we started by refining the SXRPD pattern with *C2/m* and $P2_1/m$ symmetries. The refined *C2/m* pattern showed calculated peak positions that differ from the observed ones (see Figure 4.2 (d)). In contrast, all peak positions could be well-reproduced by the refinement in the $P2_1/m$ space group. A more detailed check on the $P2_1/m$ pattern revealed intensity discrepancies for some peaks. The refinement in the lower-symmetry subgroup $P2_1$ yielded a fit that accounts for peak positions as well as intensities (Figure 4.3). $P2_1/m$ and $P2_1$ share the same extinction conditions and can only be discriminated from peak intensities. The $(210)_{MP}$ and $(022)_{MP}$ (the subscript "MP" represents the index referring to the monoclinic $P2_1/m$ or $P2_1$ unit cell) reflections provide the clearest way to discriminate between $P2_1/m$ and $P2_1$, showing that peak intensities are well-described with $P2_1$, while they are calculated as quasi-null in the $P2_1/m$ case. The following smaller Ln site compounds share the same situation as NaSmCoWO$_6$, and as a result, $P2_1$ was assigned to all of them.

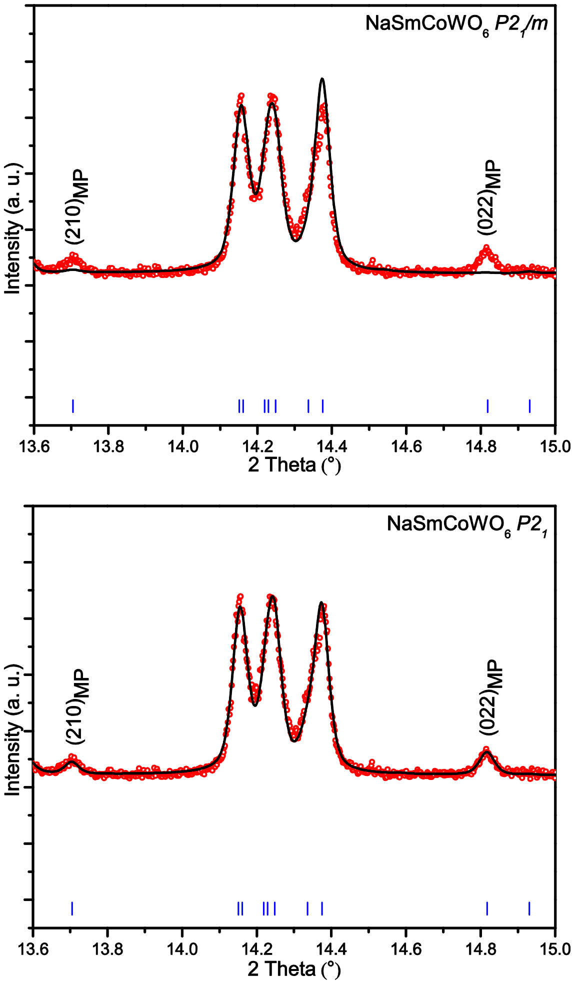

Figure 4.3 *$P2_1/m$* and *$P2_1$* refinements of SXRPD data for the $NaSmCoWO_6$ compound.

Full SXRPD pattern refinements of $NaLaCoWO_6$, $NaPrCoWO_6$, $NaNdCoWO_6$ and $NaSmCoWO_6$ are illustrated in Figure 4.4. The R_{Bragg} factors of all 12 samples fall between 2.00 % and 5.52 %, indicating a high quality of our refinement and correct space group assignments. Detailed information about the unit-cell parameters and agreement factors can be found in the appendix. There are some very small extra peaks not indexed related either to impurities or to the superstructures observed in TEM in the first three cases. Since the intensities of these peaks are very small, it is very difficult to distinguish between these two possibilities and to identify the nature of the possible impurities. Considering the $I_{maxextra}/I_{maxmain}$ values in Table 2.4, these small extra peaks do not influence the final refined structures.

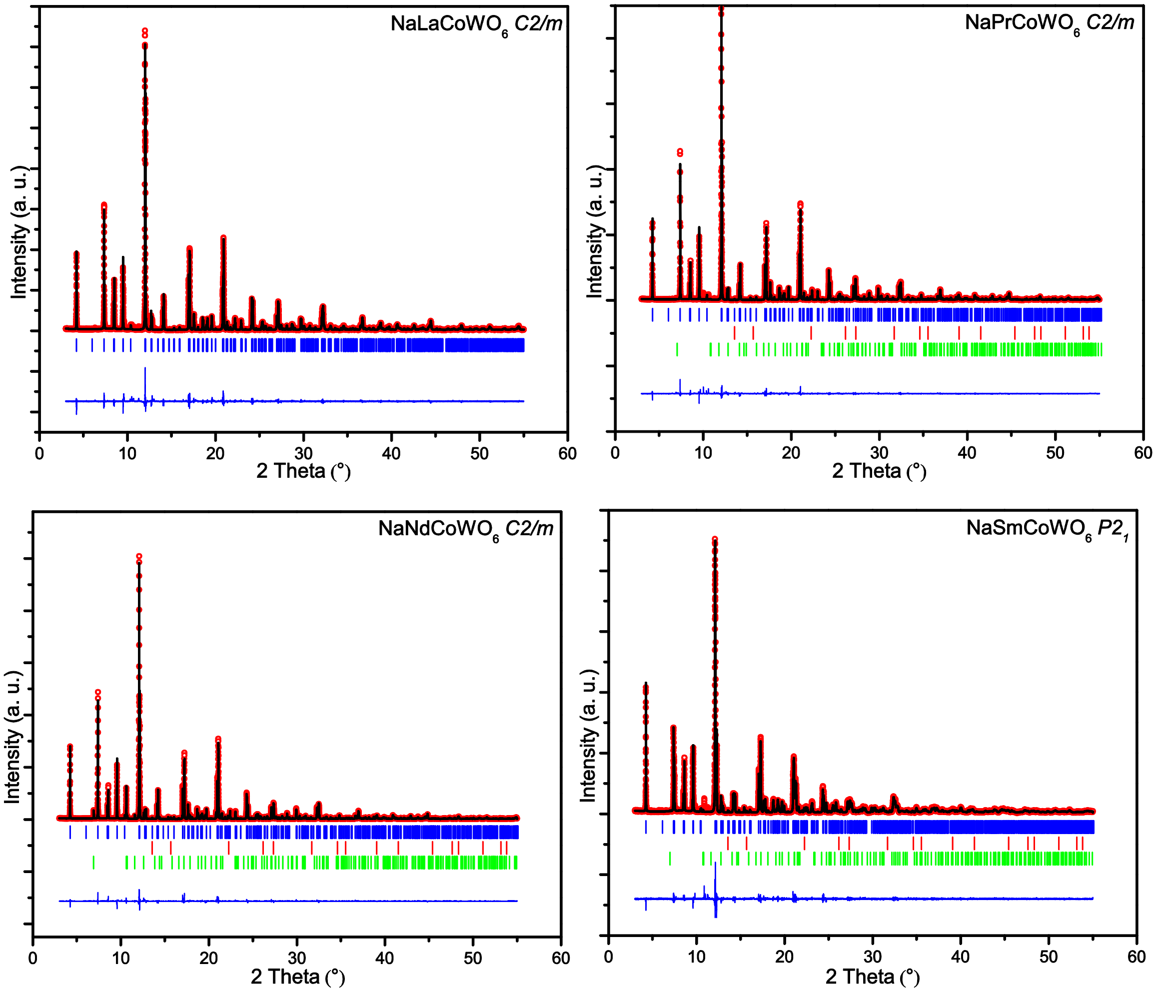

Figure 4.4 Full SXRPD pattern refinements for $NaLaCoWO_6$, $NaPrCoWO_6$, $NaNdCoWO_6$, and $NaSmCoWO_6$. The observed patterns (red circles), calculated patterns (black lines), and the difference lines (blue, at the bottom of each pattern) are shown. Blue tick marks in all cases show allowed (*hkl*) reflections of the main phase. Red and green tick marks stand for allowed (*hkl*) reflections of different impurities, respectively: $NaPrCoWO_6$: CoO (0.58(3)%, red tick mark), $NaPr(WO_4)_2$ (0.24(2)%, green tick mark); $NaNdCoWO_6$: CoO (1.01(3)%, red tick mark), $NaNd(WO_4)_2$ (7.01(4)%, green tick mark); $NaSmCoWO_6$: CoO (1.16(4)%, red tick mark), $NaSm(WO_4)_2$ (0.34(2)%, green tick mark).

To track the structural evolution of the entire series, details of two angular domains of the diffractograms are plotted in Figure 4.5. The compound $NaYCoWO_6$ is not plotted because the SXRPD wavelength is different from the others, but the curve fits well between those of Dy and Ho as could be expected from their cation radii. Figure 4.5 (a) shows the peaks indexed $\{101\}_T$ which split into $(-111)_{MC}$ and $(111)_{MC}$ (the subscript "MC" represents the index referring to the monoclinic *C2/m*) peaks as a result of the reduction of symmetry in $NaLaCoWO_6$, $NaPrCoWO_6$, and $NaNdCoWO_6$. Since the angles for these reflections are very close the splittings are only observed as broadenings of a single peak. As the Ln site is substituted by smaller and smaller rare-earth cations, the $\{101\}_T$ peaks split more and more into $(011)_{MP}$, $(-101)_{MP}$, and $(101)_{MP}$ peaks, as the monoclinic distortion becomes more and more pronounced. The same trend can also be observed in Figure 4.5 (b), where the $\{103\}_T$ and $\{211\}_T$ peaks become more and more split. The evolution of $(210)_{MP}$ and $(022)_{MP}$ peaks, which are key signatures of the presence of the $P2_1$ symmetry as stated above, is also shown in this plot. These two peaks only start to emerge from the $NaSmCoWO_6$ sample, which agrees with our conclusion above that the structure turns to *P2₁* from $NaSmCoWO_6$. Concerning the $NaYCoWO_6$ sample, the same observations are valid, namely, *P2₁* providing a superior fit for the SXRPD pattern. Detailed SXRPD refinement information for all compounds can be found in the appendix.

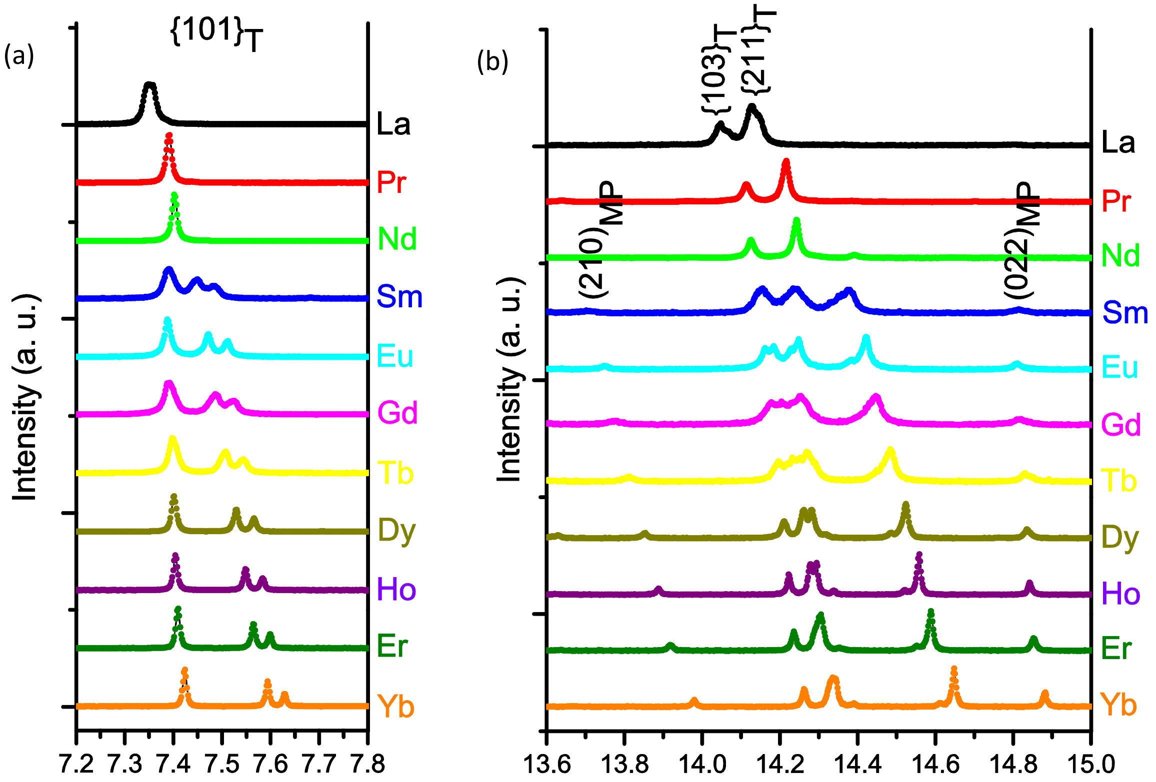

Figure 4.5 Series evolution of SXRPD patterns in (a) 7.2° - 7.7° range showing the $\{101\}_T$ peaks splitting and (b) 13.6° - 15.0° range, showing the $\{103\}_T$ and $\{211\}_T$ peaks splitting and the emerging of key signatures of *P2₁* symmetry peaks $(210)_{MP}$ and $(022)_{MP}$.

For the sake of confirming our conclusions about the space group assignments, powder SHG measurements were carried out on samples of the entire series. With an incident wavelength of 1064 nm, a visible white light signal was observed from $NaLaCoWO_6$, $NaPrCoWO_6$, and $NaNdCoWO_6$, which suggests a centrosymmetric structure for these compounds. This observation is consistent with our SXPRD investigation conclusion that these three have the centrosymmetric *C2/m* symmetry. For all other samples, a visible green light signal was observed. Since the wavelength of green light falls between 495 and 570 nm, this corresponds well to the SHG of the incident beam wavelength 1064 nm, showing that the structures are non-centrosymmetric. This observation is also consistent with our SXPRD conclusion that all of them have the non-centrosymmetric *P2₁* symmetry.

4.3 NPD Refinement and Combined with SXRPD

NPD experiments were conducted on the samples $NaLnCoWO_6$ (Ln= Y, Tb, and Ho) to confirm the details of the SXRPD refinements. The polar $P2_1$ symmetry originates from the oxygen octahedral tilting around the **c**-axis compared to the nonpolar $P2_1/m$. Even though SXRPD data show clear evidence to assign the $P2_1$ space group rather than $P2_1/m$, the limited capability of detecting oxygen positions by X-rays, especially in the presence of heavy atoms such as W and Ln, is a hindrance for the accurate determination of tilts or distortions of the oxygen octahedra that cause the ferroelectric properties of the compounds. In contrast, NPD is able to probe the oxygen positions precisely, providing complementary structural information. To take advantage of the high accuracy of SXRPD and the oxygen sensitivity of NPD combined Rietveld refinements were performed. The joint refinement patterns of $NaYCoWO_6$ are shown in Figure 4.6. The small deviations in the difference line of each pattern and the R_{Bragg} factors 2.48 % (NPD pattern) and 2.29 % (SXRPD pattern) indicate that the quality of the joint refinement is quite high and prove that our $P2_1$ space group assignment is correct. Atomic positions from the joint refinement are summarized in Table 4.3. Details of all joint refinement information can be found in the appendix.

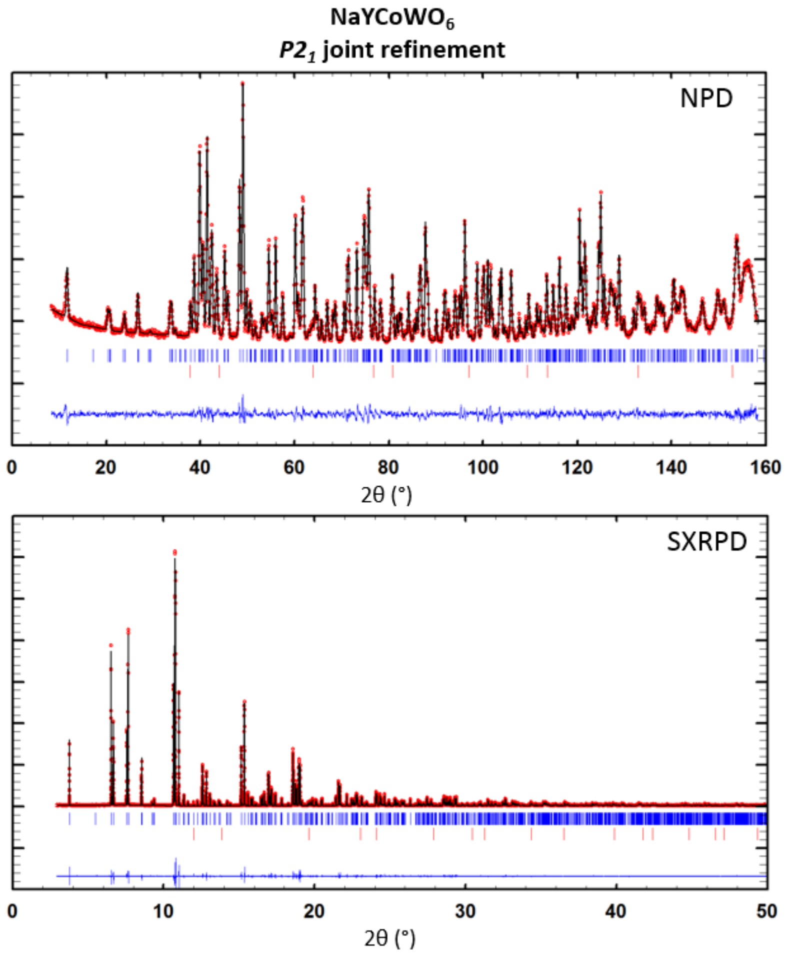

Figure 4.6 $P2_1$ joint refinement of the NaYCoWO$_6$ sample, the NPD pattern (top) and the SXRPD pattern (bottom). The observed patterns (red circles), the calculated patterns (black lines), and the difference lines (blue, at the bottom of each pattern) are shown. Blue tick marks in all cases show allowed (*hkl*) reflections of the main phase. Red tick marks stand for allowed (*hkl*) reflections of a CoO (0.55(4)wt% from NPD) impurity.

Table 4.3 Structural parameters from the $P2_1$ joint refinement of $NaYCoWO_6$ [a]

Atom	Wyckoff Symbol	x	y	z	B(Å^2)	Occupancy
Na	2a	0.250(2)	0.715(2)	0.002(1)	1.03(8)	1.0
Y	2a	0.2658(5)	0.8129(6)	0.5005(3)	0.19(2)	1.0
Co	2a	0.7497(8)	0.759(2)	0.2487(5)	0.06(3)	1.0
W	2a	0.7624(2)	0.75	0.7642(1)	0.022(7)	1.0
O1	2a	0.465(1)	0.555(2)	0.6862(7)	0.32(1)	1.0
O2	2a	0.439(1)	0.526(1)	0.3146(8)	0.32(1)	1.0
O3	2a	0.077(1)	-0.051(1)	0.2159(7)	0.32(1)	1.0
O4	2a	0.053(1)	-0.070(2)	0.7787(7)	0.32(1)	1.0
O5	2a	0.855(1)	0.713(1)	0.5050(8)	0.32(1)	1.0
O6	2a	0.673(1)	0.778(1)	-0.0114(7)	0.32(1)	1.0

[a] Space group $P2_1$, Z=2. Unit cell parameters: a= 5.34712(2) Å, b= 5.52411(2) Å, c= 7.78938(2) Å, β= 90.2946(1) °, V/Z= 115.04(0) Å^3. Discrepancy factors: (NPD) χ^2= 2.39, R_p= 7.92%, R_{wp}= 8.36%, and R_{Bragg}= 2.48%; (SXRPD) χ^2= 1.68, R_p= 11.7%, R_{wp}= 14.0%, and R_{Bragg}= 2.29%.

4.4 Crystal Structures

A schematic view of the $C2/m$ and $P2_1$ structures is shown in Figure 4.7. The dimensions of the $C2/m$ unit cell are $2a_p*2a_p*2a_p$, which is twice as large as than the $P2_1$ unit cell ($\surd 2a_p*\surd 2a_p*2a_p$). Both of them have A/A' layered ordering and B/B' rock-salt ordering. As stated above, SOJT distortions of the B' site stabilize the layered ordering of A/A' cations.[41] Selected bond distances and angles, as well as bond valence sums (BVS) calculated from $NaLaCoWO_6$, $NaPrCoWO_6$ and $NaNdCoWO_6$ SXRPD refinements, and from $NaYCoWO_6$, $NaTbCoWO_6$ and $NaHoCoWO_6$ joint refinements are compared in Table 4.4. The displacements of W^{6+} cations can be confirmed from the comparison of different W-O bond lengths along the **c**-axis. In both structures, W-O6 is always shorter than W-O5 (see Figure 4.7 and Table 4.4), which means the W^{6+} cations tend to move toward the Na layer to have a small energy gap between the empty W 5d orbitals and the filled O 2p orbitals, the so-called SOJT. As a result, the bond strains are released, and a more stable structure is constructed. From the examination of the BVS values, the O6 anions are underbonded, and the O5 anions are overbonded, which is consistent with the observation of W-O bond lengths, shorter W-O distances increasing the corresponding O valence. In contrast, the Co-centered octahedra remain rather symmetric. As mentioned above, the tilting scheme of $C2/m$ is $a^0b^-c^0$, indicating that the octahedral tilt is only around the **b**-axis. The bond angles of Co-O1-W and Co-O4-W indicate the degree of tilting. It is clear from the Co-O4-W bond angle that the tilting is more pronounced in smaller Ln compounds. When the symmetry is reduced to *P2₁*, the structure is more distorted to a tilting scheme $a^-a^-c^+$ in Glazer's notation, which is reflected by the much smaller Co-O-W angles.

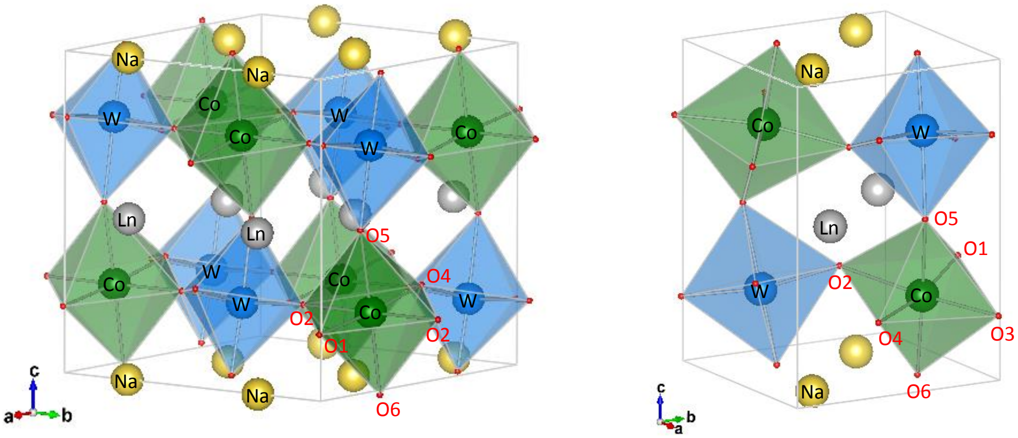

Figure 4.7 The schematic view of the crystal structure of $NaLaCoWO_6$ (*C2/m*, left) and $NaYCoWO_6$ (*P2₁*, right). The spheres are Na (yellow) and Ln (grey), Co (green) and W (blue), the smaller spheres are O (red).

Table 4.4 Selected Bond lengths, BVS and Bond Angles from the SXRPD Refinement of NaLnCoWO$_6$ (Ln = La, Pr and Nd), and the Joint Refinement of NaLnCoWO$_6$ (Ln= Tb, Y, Ho)

	NaLaCoWO$_6$	NaPrCoWO$_6$	NaNdCoWO$_6$	NaTbCoWO$_6$	NaYCoWO$_6$	NaHoCoWO$_6$
	Bond Lengths (Å)					
Co-O1	2.08(8)	2.16(8)	2.16(9)	2.07(2)	2.06(1)	2.07(2)
Co-O2	2.07(6)	2.05(5)	2.04(5)	2.15(2)	2.16(1)	2.15(1)
Co-O3				2.06(2)	2.06(1)	2.06(1)
Co-O4	2.07(8)	2.04(8)	2.12(9)	2.11(2)	2.11(1)	2.10(2)
Co-O5	2.10(5)	2.11(4)	2.17(5)	2.09(1)	2.087(9)	2.07(1)
Co-O6	2.09(5)	2.09(4)	2.06(5)	2.057(9)	2.067(7)	2.082(8)
Co-O Average	2.08	2.08	2.10	2.09	2.09	2.09
W-O1	1.89(8)	1.81(8)	1.79(9)	1.969(9)	2.013(7)	2.008(8)
W-O2	1.86(6)	1.89(5)	1.89(5)	1.968(9)	1.965(7)	1.968(8)
W-O3				1.856(9)	1.877(7)	1.879(8)
W-O4	1.96(8)	2.01(7)	1.94(9)	1.864(9)	1.848(7)	1.853(8)
W-O5	2.08(5)	2.08(4)	2.04(5)	2.093(9)	2.092(7)	2.094(8)
W-O6	1.78(5)	1.77(4)	1.82(5)	1.814(8)	1.822(5)	1.813(7)
W-O Average	1.91	1.91	1.89	1.927	1.936	1.936
	Bond Valence Sums					
Na	0.86(1)	0.86(1)	0.936(9)	0.880(9)	0.926(8)	0.915(9)
Ln	2.36(2)	2.90(2)	2.76(2)	2.95(1)	3.01(1)	3.05(2)
Co	2.11(3)	2.20(3)	2.14(3)	2.05(2)	2.05(1)	2.06(2)
W	6.38(9)	6.69(9)	6.94(9)	6.02(3)	5.88(3)	5.89(3)
O1	1.70(5)	2.13(6)	1.98(6)	2.00(2)	1.93(1)	1.94(2)
O2	2.05(4)	2.14(4)	2.14(3)	1.91(2)	1.90(1)	1.93(2)
O3				2.02(2)	1.98(2)	1.97(2)
O4	2.07(4)	2.17(4)	2.31(5)	1.94(2)	2.00(2)	2.01(2)
O5	1.77(2)	1.93(2)	1.88(2)	1.92(1)	1.95(1)	1.96(1)
O6	2.07(4)	2.13(3)	2.33(3)	2.11(2)	2.10(1)	2.12(2)
	Bond Angles (°)					
Co-O1-W	165.0(7)	164.8(7)	165.3(7)	143.5(5)	142.2(4)	142.9(4)
Co-O2-W	176.2(5)	161.9(4)	163.8(4)	144.3(5)	143.8(4)	143.5(4)
Co-O3-W				148.6(5)	146.2(4)	147.2(4)
Co-O4-W	151.2(7)	143.8(7)	143.6(7)	153.3(6)	151.3(4)	150.9(5)
Co-O5-W	157.9(4)	155.2(3)	153.3(3)	149.2(3)	147.9(2)	148.2(3)
Co-O6-W	156.1(5)	156.3(4)	152.7(3)	153.3(3)	152.1(2)	152.2(3)

4.5 Symmetry Modes Analysis

From the structural viewpoint, the nine $NaLnCoWO_6$ (Ln= Y, Sm, Eu, Gd, Tb, Dy, Ho, Er, and Yb) members in polar $P2_1$ symmetry are potential ferroelectrics. For the sake of a detailed understanding of the origin of the polarization, distortion modes from the parent *P4/nmm* to $P2_1$ symmetry were decomposed and analyzed. The corresponding Group-Subgroup tree is illustrated in Figure 4.8 (a). There are three major distortion modes (Figure 4.8 (b)-(d)): Γ^+_5 describes the out-of-phase tilting around the **b**-axis, Γ^-_1 describes the in-phase rotation around the **c**-axis and Γ^-_5 describes the displacements of Na/Ln cations and oxygens of the BO_6/$B'O_6$ octahedra.[34] The former two modes essentially describe rotations of oxygen octahedra and result in nonpolar structures individually, however, the combination of them is able to induce a polar Γ^-_5 mode in a manner of HIF.[15] In this polar mode, atoms mainly move in the **b**-axis direction, especially Na and Ln cations are displaced in opposite directions. Since the polar mode is closely related to Γ^+_5 and Γ^-_1 nonpolar oxygen octahedral rotations and HIF values, it is necessary to examine the evolution of the amplitude of each mode as the Ln cation is getting smaller. These three major modes were refined from the undistorted structure with FullProf, and the resulting mode amplitudes are plotted in Figure 4.9. As the Ln cation is replaced by smaller ones, the amplitude of the Γ^+_5 mode has a slowly increasing trend, while the Γ^-_1 mode increases very rapidly, as a result, the induced polar Γ^-_5 mode keeps increasing as well. This demonstrates that the Γ^+_5 and Γ^-_1 modes are correlated to the polar mode and a larger polarization is expected in a compound with a smaller Ln cation. All these experimental results are very consistent with precedent theoretical investigations.[35]

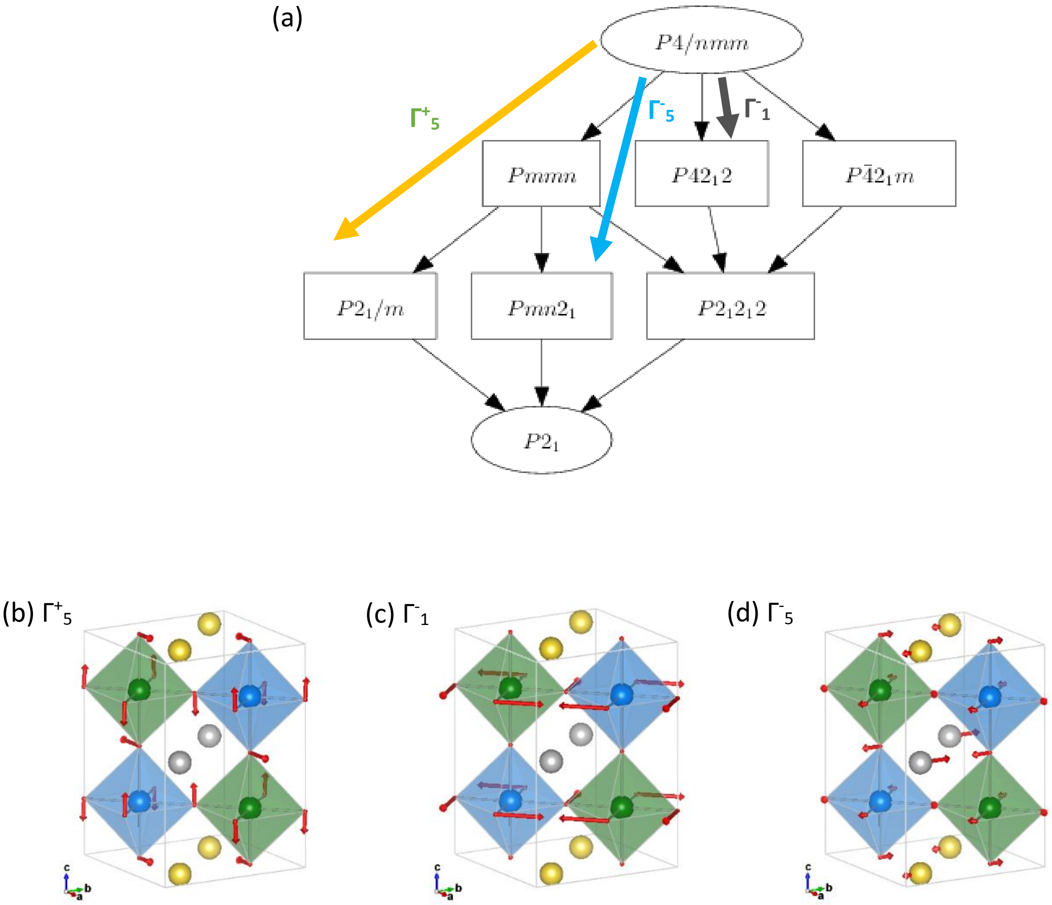

Figure 4.8 (a) Group-Subgroup tree analyzed from the parent *P4/nmm* symmetry to the distorted *$P2_1$* symmetry, three major distortion modes Γ^+_5, Γ^-_1 and Γ^-_5 are illustrated. Schematic views of the three key modes are shown in (b)- (d), the spheres are Na (yellow), Ln (grey), Co (green) and W (blue), the smaller spheres are O (red).

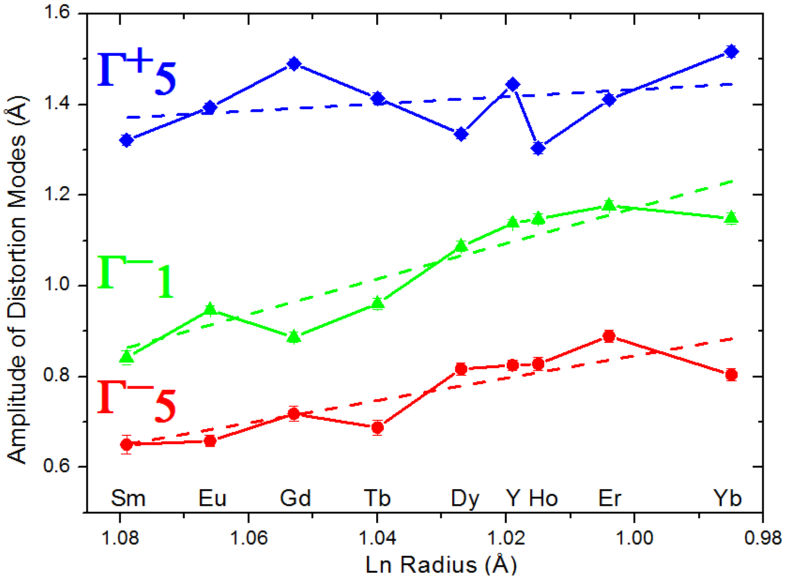

Figure 4.9 Evolution of Γ^{+}_{5} (blue), Γ^{-}_{1} (green), and Γ^{-}_{5} (red) symmetry mode amplitudes as a function of Ln cation size in the *P2₁* polar compounds $NaLnCoWO_6$ (Ln= Y, Sm-Er, Yb). The dashed lines for each curve are linear fits.

Since subtle oxygen displacements are involved in all three key distortion modes, the total spontaneous polarization was estimated from the NPD data. The polarization was calculated by the point charge model with nominal charges (Na= +1, Ln= +3, Co= +2, W= +6 and O= -2), and only ionic contributions are considered. The ferroelectric polarizations are ~20 μC/cm^2 for $NaYCoWO_6$, ~14 μC/cm^2 for $NaTbCoWO_6$, and ~19 μC/cm^2 for $NaHoCoWO_6$. For $NaYMnWO_6$ the theoretical analysis taking both the ionic and electronic contributions into account predicts a polarization of 23.6 μC/cm^2[35], which is quite close to our estimated values.

4.6 Conclusions

In this chapter, the structural studies on the doubly order perovskite family of $NaLnCoWO_6$ (Ln= Y, La, Pr, Nd, Sm, Eu, Gd, Tb, Dy, Ho, Er, Yb) were performed by Rietveld refinements of the SXRPD and NPD patterns collected at room temperature. $NaLaCoWO_6$ has *C2/m* symmetry rather than the previously determined *$P2_1/m$*, and the following Pr and Nd compounds also have the same symmetry although the fit qualities are comparable with *C2/m* and *$P2_1/m$*. All nine other members possess a polar symmetry *$P2_1$*, and the SHG measurement supported this assignment. Our structural study demonstrates that these compounds exhibit the HIF phenomenon, and three major distortion modes from the parent *P4/nmm* structure were analyzed to track the evolution of the entire series. The Γ^{+}_{5} and Γ^{-}_{1} nonpolar modes are correlated to the polar mode, and the trend of the polar mode amplitude increases as the Ln cation becomes smaller. The spontaneous ferroelectric polarization is estimated from the NPD data for three samples, all of these yield reasonable results compared to a theoretically predicted value in a similar compound $NaYMnWO_6$, and can be as large as ~20 μC/cm^2. As stated in this chapter, more complex superstructures were observed by TEM in three compounds $NaLnCoWO_6$ (Ln=La, Pr, and Nd), they are the subject of the next chapter.

Chapter 5: The Special Case of the $NaLaCoWO_6$ Compound

The compound containing La (along with those containing Pr or Nd) shows a number of differences from the compounds containing smaller rare-earth elements. $NaLaCoWO_6$ has been synthesized at ambient pressure and it exhibits a unit cell that is undistinguishable from a tetragonal metric. It is therefore worthwhile to investigate this compound in greater detail, especially when taking into account that other La containing double perovskites have shown peculiar superstructure orders ($NaLaMgWO_6$ [54][55], $KLaMnWO_6$[56]).

In this chapter we will first present in more detail our observations in SXRPD and NPD at room temperature and at low temperature showing that a phase transition occurs. Then the simpler low temperature phase (LTP) structure will be presented. The superstructure in the high temperature phase (HTP) will be the subject of the third part of this chapter before we propose a structural model of the HTP.

5.1 Phase Transition

In Chapter 4 the structure of $NaLaCoWO_6$ at room temperature is given as monoclinic with space group *C2/m* by the SXRPD data. The unit cell was described in dimensions of $2a_p*2a_p*2a_p$ (where a_p is the unit cell parameter of the aristotype perovskite), and the oxygen octahedral tilting scheme $a^0b^-c^0$ in Glazer's notation[28]. Even though it is clear from peak positions in the SXRPD pattern that the real symmetry of $NaLaCoWO_6$ is *C2/m* rather than $P2_1/m$ as previously proposed in the literature[47], the differences stem essentially from the oxygen atom positions. Since the sensitivity of SXRPD to oxygen positions is limited especially in the presence of heavy elements such as W and La, NPD data was collected at room temperature to provide complementary information. The quality of the *C2/m* NPD pattern refinement is not really satisfactory as shown in Figure 5.1 (a). Interestingly, some extra satellite peaks appear in the refined *C2/m* NPD pattern (see Figure 5.1 (b)), which are hardly observed in the corresponding SXRPD pattern (see Figure 5.1 (c)). Then a systematic investigation on impurities and structures pattern according to the theoretical space group predictions by Knapp *et al.*[41] was carried out to try to explain the NPD. The impurity search was performed on the SXRPD pattern in the ICDD PDF 4+ database implemented in the *EVA* software, taking any combination of the elements Na, La, Co, W and O into account. Given that the intensities of extra peaks in the SXRPD pattern are very small, some suspected impurity phases were selected and tested with the NPD pattern refinement. The theoretical study predicted all space groups for $AA'BB'O_6$ compounds considering the A/A' layered ordering, rock-salt ordered B/B' and various schemes of oxygen octahedral tilting. Surprisingly, there is neither an impurity nor an alternative space group that could explain all these satellite peaks in the NPD pattern.

A further electron diffraction investigation of these extra peaks and their link to a superstructure will be presented later in this section.

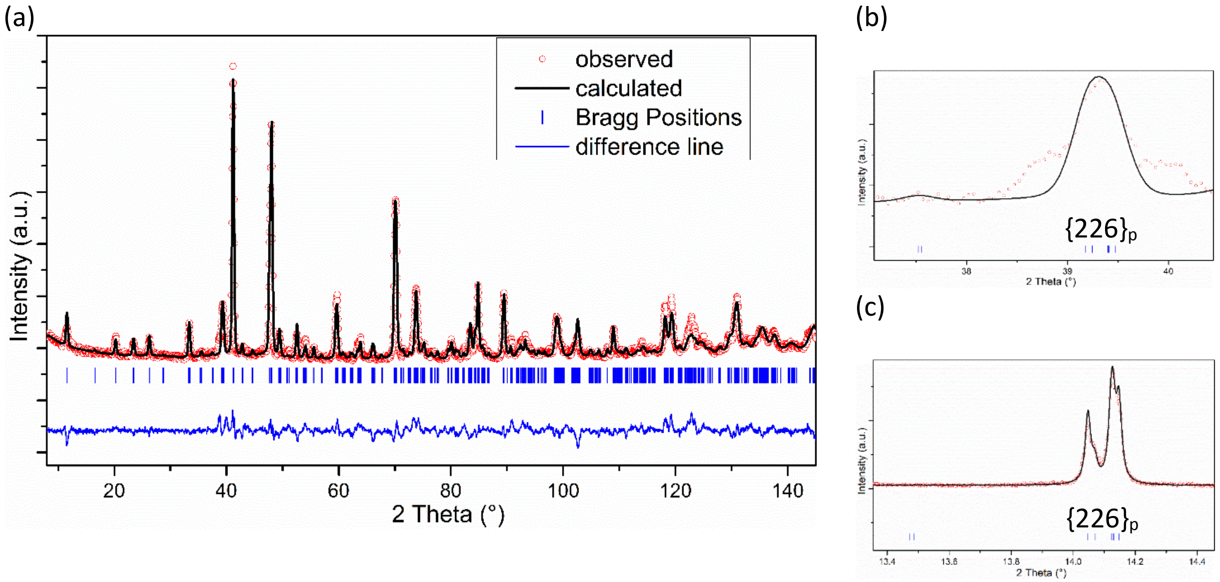

Figure 5.1 (a) The *C2/m* refinement of NPD data collected on D2B at ILL, with a wavelength of 1.594 Å, the quality of the fit is rather poor and much worse than the SXRPD refinement. Extra peaks are observed in the NPD pattern, a typical 2θ region with extra peaks is illustrated in (b). The corresponding SXRPD region is shown in (c), where satellite peaks can hardly be observed.

During low temperature NPD that was performed in order to study a potential magnetic ordering in this compound we observed a phase transition. This transition affects in particular the two shoulders of the peak shown in Figure 5.1 (b). We therefore did temperature dependent NPD measurements on the D1B beamline at ILL. Figure 5.2 shows a cycle of heating from 100 K to 550 K and then cooling down to 100 K again. When heating up from 100K to 550 K, the phase transition starts around 330 K. While when cooling down from 550 K to 100 K in the second step, the transition temperature was observed around 180 K showing an unusually large hysteresis in temperature (~150K) of this phase transition.

(a)

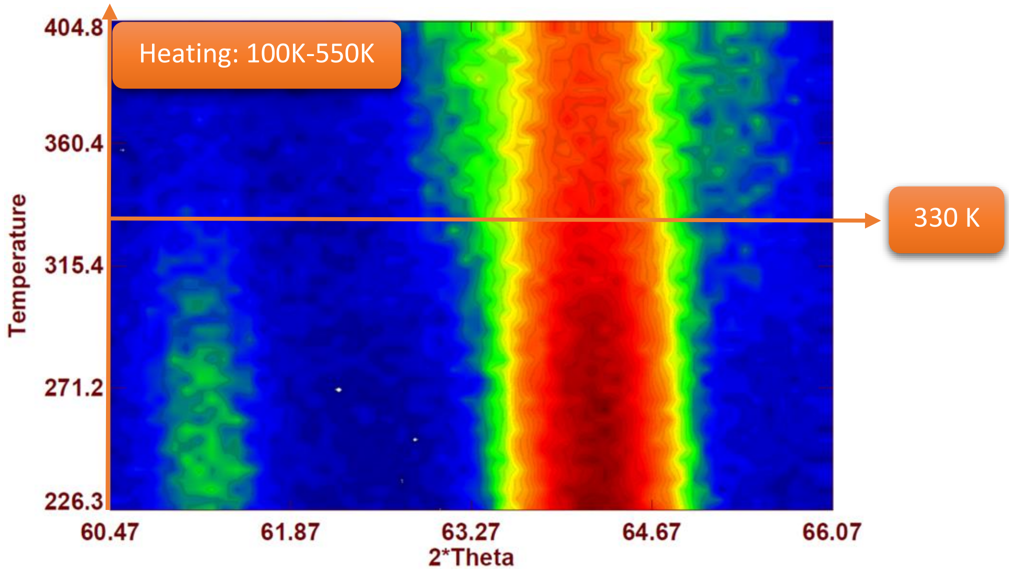

(b)

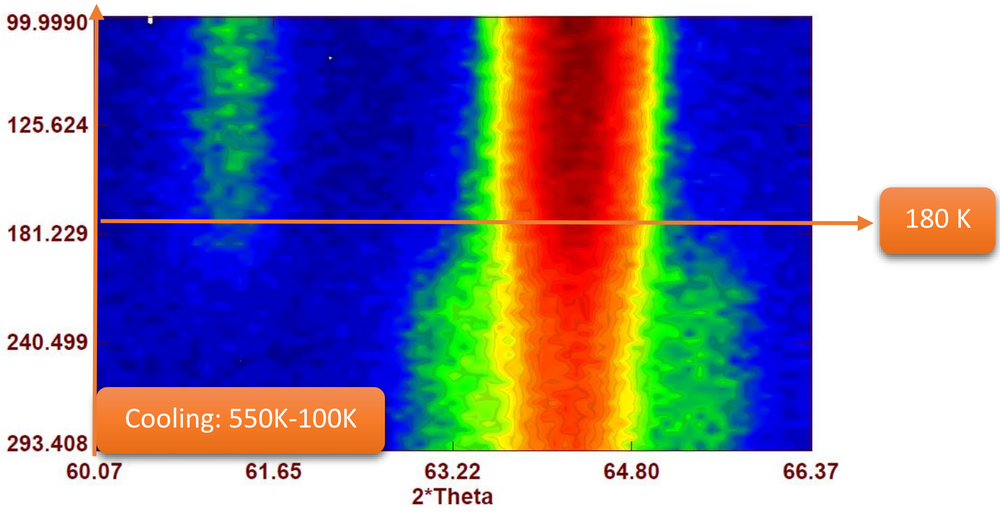

Figure 5.2 The NPD study on the phase transition in a large temperature range (100 K to 550 K). (a) is the heating process from 100 K to 550 K, where the transition temperature is observed around 330 K. (b) is the cooling process from 550 K to 100 K, where the transition temperature is observed around 180 K. Data were collected at D1B at ILL, with a wavelength of 2.52Å.

For the sake of corroborating the phase transition observed in powder diffraction, we investigated the sample by electron diffraction. The advantage of electron diffraction resides in the fact that the interaction of electrons with matter is much stronger than those of X-rays or neutrons. A much smaller sample is therefore sufficient to perform a diffraction experiment. In our case the powder is dispersed onto an amorphous carbon membrane supported by a copper grid.

Introducing an aperture in the image plane and illuminating the sample with a parallel beam allows the observation of the single crystal diffraction of a selected area of the sample, e.g. an individual grain of a powder. In this technique, called selected area electron diffraction (SAED), an entire plane of the reciprocal lattice is visible in one diffraction pattern (Figure 5.3).

The $[001]_p$ zone axis of the sample in its HTP shows an almost square lattice of strong reflections (Figure 5.3 (a)). These reflections can be indexed as the basic reflections of the aristotype perovskite as shown in Figure 5.3 (a), or when indexed in the monoclinic *C2/m* unit cell ($2a_p*2a_p*2a_p$) all strong reflections can be indexed *hk*0 with even *h* and *k*. Since the structure is pseudotetragonal, we can't distinguish between **a** and **b** axes from this kind of diffraction pattern. In the center of the squares, doublets of reflections (surrounding the no intensity spot -½ ½ 0_p circled in red for example) can be observed where the difference vector between the doublet reflections is in the $[100]_p$ (or $[010]_p$) direction of the aristotype perovskite and the distance between the doublet indicates a periodicity of $12a_P$. Corresponding satellite reflections can also be observed around the main reflections. As will be seen in the chapter section 5.3 these doublets and satellites are linked to a superstructure ordering of the phase.

We then cooled the sample in a cooled sample holder filled with liquid nitrogen to the lowest possible nominal temperature of 100 K. The exact temperature of the sample is difficult to evaluate since the electron beam was partially absorbed by the sample and therefore heated the particle during the experiment. The temperature would then be a function of the energy absorbed from the beam and the heat evacuated by thermal conduction from the particle via the carbon membrane to the copper grid and on to the liquid nitrogen cooled heat sink. The exact temperature of the sample is unknown, but in the used conditions of a weak electron beam we can estimate that the temperature of the sample was at most a few tens of degrees above the nominal temperature.

The diffraction pattern at low temperature (see Figure 5.3 (b)) shows some important changes with respect to the ambient temperature diffraction pattern. While the main reflections of the aristotype perovskite are unchanged, taking the spot circled in red for example, the doublets in the center of the squares have greatly diminished in intensity and a strong reflection has appeared in the center of each doublet. The phase transition is therefore linked to the disappearance of the superstructure, however, the transition seems not to be complete in this case as the doublets don't disappear completely. It should be noted that on another particle no transition was observed, the doublet reflections still being visible at low temperature.

Heating the sample back to room temperature yielded an almost complete recovery of the doublets and disappearance of the central reflections (Figure 5.3 (c)). However, since the central reflections didn't disappear completely we further heated the sample by concentrating the electron beam on the sample for 5 minutes. After this additional heating the central spots are no longer visible (Figure 5.3 (d)), indicating a complete reversibility of the phase transition.

So far, the temperature resolved NPD data has demonstrated that $NaLaCoWO_6$ undergoes a crystallographic phase transition with a large hysteresis in temperature (~150 K). Satellite reflections corresponding to a superstructure were observed in the HTP from both NPD and SAED patterns. The spacing of these satellites in the SAED patterns yielded a new periodicity of $12a_p$ along either the $[100]_p$ or $[010]_p$ direction for the superstructure. SAED evidenced that this superstructure is involved in the phase transition, such that it appears in the HTP and disappears in the LTP. Furthermore, SAED study also revealed the reversibility of this phase transition.

However, some key issues are still waiting to be resolved: Since the HTP was determined to possess the *C2/m* symmetry, how is the structure of the LTP? Could it be described by a subgroup of *C2/m* with a lower symmetry? As satellites are observed in the NPD pattern of HTP and the SAED study suggests that the superstructure disappeared in the LTP, how does it look like in the LTP NPD pattern? Is there any satellite peak existing? If the superstructure only appears in the HTP, how is the modulated pattern of the structure? What are the origins of this superstructure? Structural? Chemical? Or both? Can this superstructure be modelized to account for the observed satellites in the NPD pattern of the HTP. With all these questions, we performed Rietveld refinements on the LTP SXRPD and NPD patterns to find the correct space group to describe the LTP structure. Intense STEM investigations including ABF imaging, HAADF imaging, and EELS study were carried out to understand the superstructure to a deeper degree. All of these will be addressed step-by-step in the following part of this chapter.

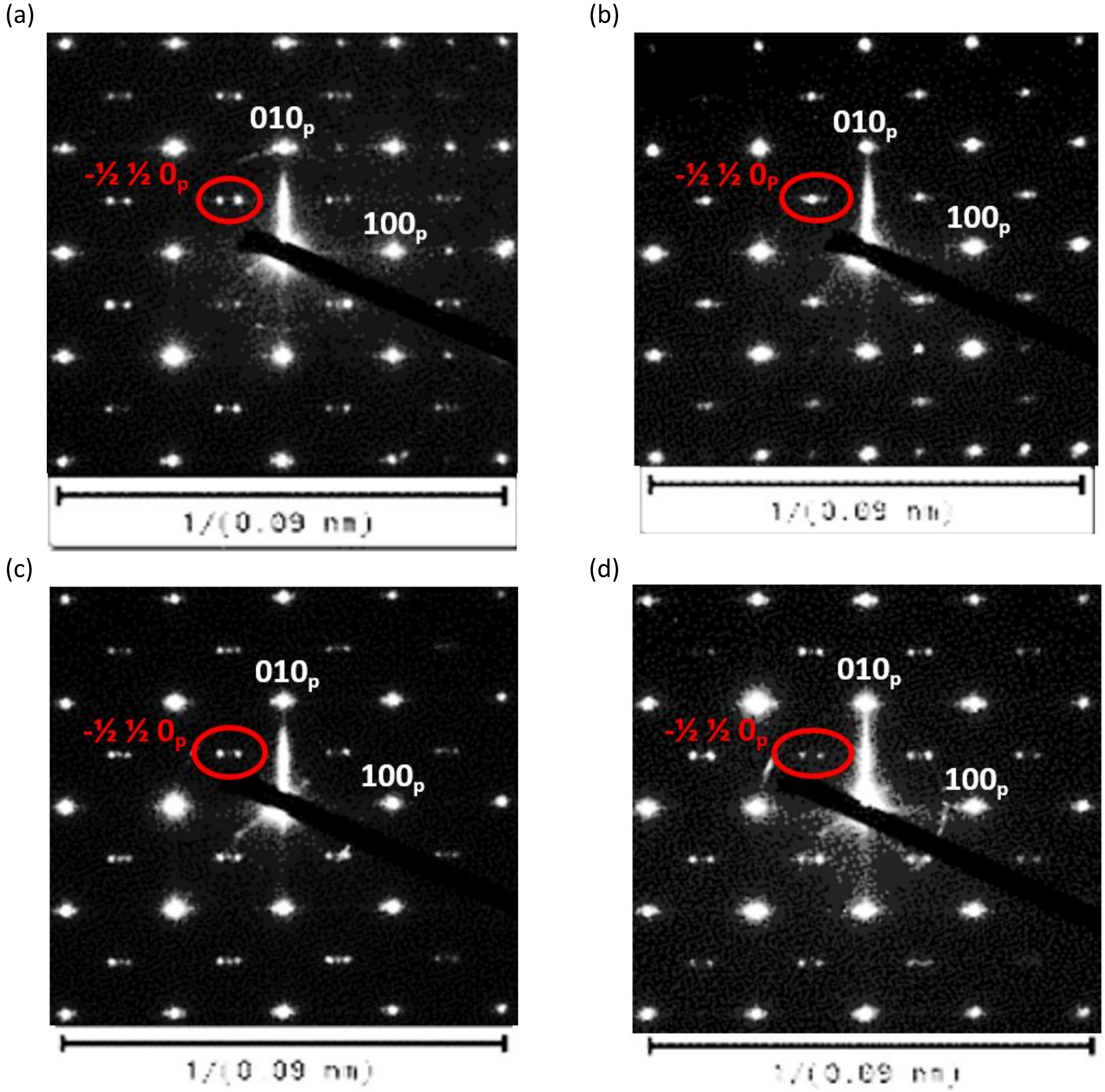

Figure 5.3 The SAED study along the $[001]_p$ zone axis on the phase transition in temperature by TEM: (a) the HTP pattern, (b) cool the sample down to the nominal temperature 100K, (c) heat the sample from 100 K back to room temperature, (d) a further heating with concentrating the beam on the sample for 5 min.

5.2 The LTP Structure

The average structure of HTP has been determined as monoclinic *C2/m* before, however, the LTP symmetry remains unknown. In order to assign the space group to the LTP, a joint refinement combining the SXRPD and NPD data at 100 K was systematically carried out by the Rietveld method. As the HTP possesses the *C2/m* symmetry, it was assumed at the beginning that the LTP had the subgroup *C2* symmetry. However, it was found that the *C2* model can't even explain the peak positions of the observed pattern, which suggests that the LTP has neither *C2/m* nor *C2* symmetry. Taking the systematic extinctions and the theoretical predictions concerning the possible space groups for AA'BB'O_6 as discussed in Chapter

1[41] into account, the space groups $P2_1/m$ and $P2_1$ were concluded to be the best candidates to explain the peak positions. Since these two space groups have exactly the same extinction conditions, the discrimination of them relies on the peak intensities which are related to their tilting scheme of oxygen octahedra. The space group $P2_1/m$ has the tilting scheme $a^-a^-c^0$ while it is $a^-a^-c^+$ for $P2_1$. Considering that the tilting here involves only the oxygen octahedra, NPD is the best technique to distinguish between $P2_1/m$ and $P2_1$ owing to its high sensitivity to probe oxygen positions. The $P2_1$ NPD refinement provides a superior fit than that of $P2_1/m$. A main difference in peak intensities is illustrated in Figure 5.4, showing that the LTP possesses the $P2_1$ symmetry rather than $P2_1/m$.

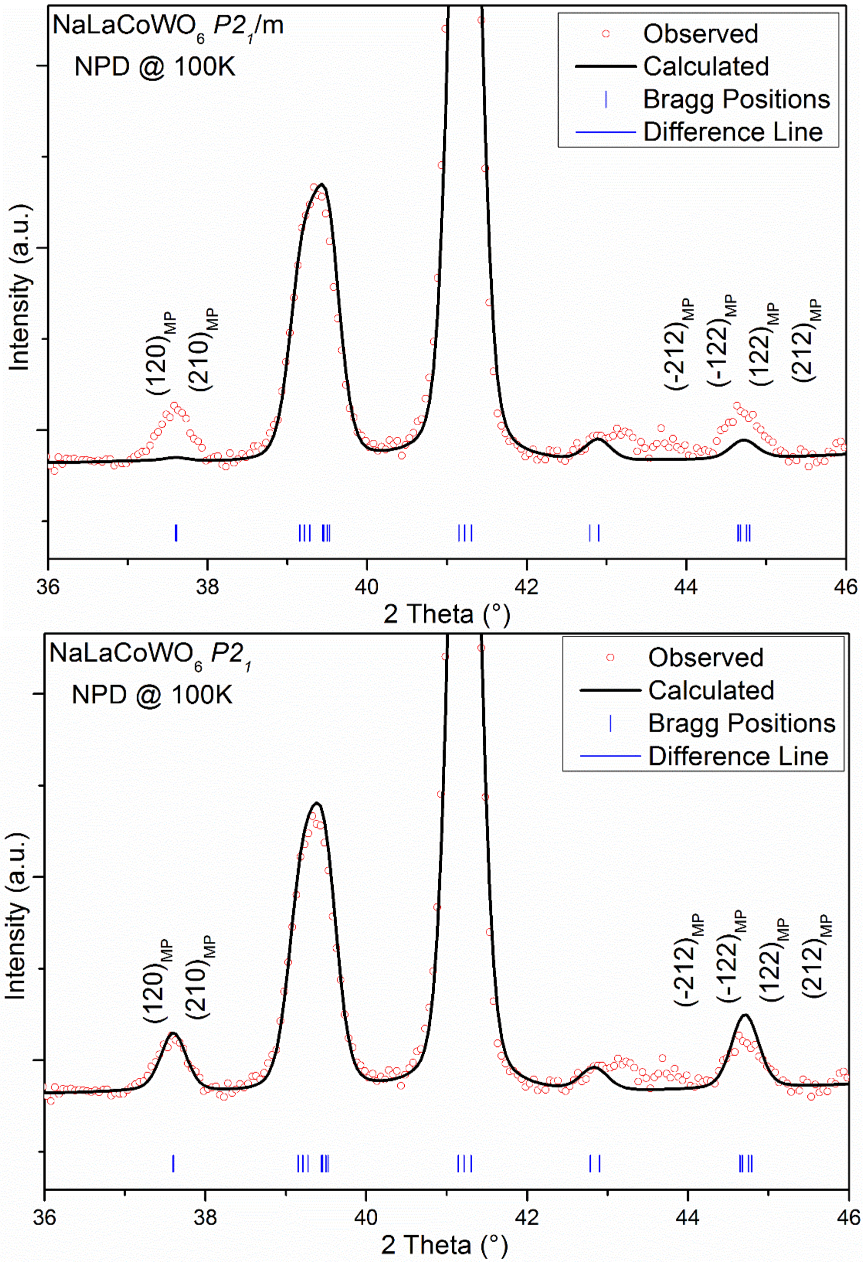

Figure 5.4 A comparison between the $P2_1/m$ and $P2_1$ NPD refinement at 100 K in a selected 2θ region (36° - 46°).

Different respective weights of the NPD/SXRPD data were tested in the $P2_1$ joint refinement on the data collected at 100K. The best global agreement was selected as 1:1, and the corresponding refinement patterns are shown in Figure 5.5. The Bragg factors are 11.4% (NPD) and 5.57% (SXRPD), indicating the correct space group assignment.

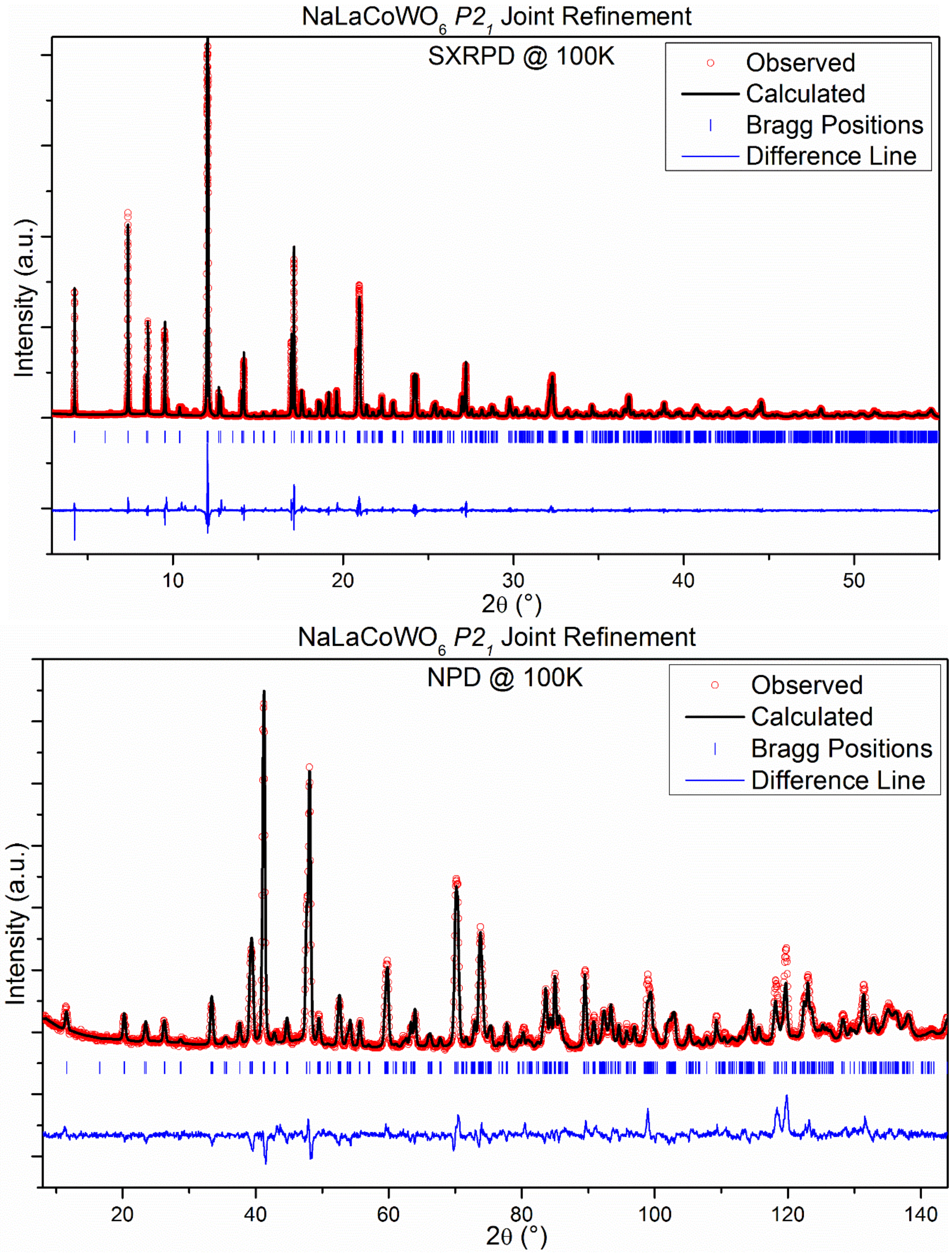

Figure 5.5 The $P2_1$ joint refinement of $NaLaCoWO_6$ combing the SXRPD and NPD data collected at 100 K.

All the refined crystallographic parameters are listed in Table 5.1 and the selected bond lengths, bond angles and the derived bond valence sums of each atom are all listed in Table 5.2. Note that the sodium site was mixed with La in order to have a reasonable B_{iso} value at this site, otherwise, the B_{iso} is negative. The proportions of Na and La on this site were refined with the constraint of full occupancy of the Na site. The refined La proportion is less than 3.5%. Other tests like mixing La at the Na site together with mixing Na at the La site with constraint of fully occupancy of the Na and La sites as well as all elements in stoichiometry were also attempted. In all cases the occupancy deviations of the Na and La sites are not larger than 4% and the fit is no better than the one shown in Figure 5.5 considering the refinement agreement factors. Very similar situations were also observed in the compounds NaPrCoWO$_6$ and NaNdCoWO$_6$ and have been discussed in Chapter 4. All these three compounds were prepared at high temperature and ambient pressure, the possible substitution of Na by Ln could be attributed to the volatility of Na at high temperature.

Table 5.1 Crystallographic parameters of NaLaCoWO$_6$ from the joint refinement ($P2_1$) at 100K.[a]

Atom	Wyckoff Symbol	x	y	z	B(Å^2)	Occupancy
Na	2a	0.233(9)	0.78(1)	-0.001(7)	1.0(2)	0.966(2)
La1	2a	0.233(9)	0.78(1)	-0.001(7)	1.0(2)	0.034(2)
La2	2a	0.253(2)	0.727(2)	0.500(1)	1.28(3)	1.0
Co	2a	0.748(3)	0.768(6)	0.248(1)	0.92(7)	1.0
W	2a	0.7534(8)	0.75	0.7687(4)	1.17(1)	1.0
O1	2a	0.53(1)	0.49(1)	0.715(8)	0.84(5)	1.0
O2	2a	0.51(1)	0.47(1)	0.294(8)	0.84(5)	1.0
O3	2a	-0.01(1)	0.03(1)	0.235(7)	0.84(5)	1.0
O4	2a	-0.05(1)	0.03(1)	0.803(7)	0.84(5)	1.0
O5	2a	0.83(1)	0.78(1)	0.504(5)	0.84(5)	1.0
O6	2a	0.676(9)	0.78(1)	-0.014(4)	0.84(5)	1.0

[a] Space group $P2_1$, Z=2. Unit cell parameters: a= 5.53091 Å, b= 5.53226 Å, c= 7.89281 Å, β= 90.22028 °, V/Z= 120.753 Å^3. Discrepancy factors: (NPD) χ^2 = 7.78, R_p=19.6%, R_{wp}= 19.7%, R_{Bragg}= 11.4%; (SXRPD) χ^2 = 26.9, R_p=14.0%, R_{wp}= 19.1%, R_{Bragg}= 5.57%.

The refined crystal structure is shown in Figure 5.6. The tilting scheme of the $P2_1$ structure adopts $a^-a^-c^+$, and the unit cell is in the dimensions of $\sqrt{2}a_p*\sqrt{2}a_p*2a_p$. It shares the common structure features with other $P2_1$ compounds: the Na/La sites order in layers while the Co/W sites order in a rock-salt type; the SOJT effect of W^{6+} is well reflected from the difference of the W-O5 and W-O6 bond lengths tending to move towards the Na layer. The more distorted LTP $P2_1$ structure, in comparison with the $C2/m$ HTP structure, is reflected from the decreasing of the bond angles such as Co-O1-W (165.0(7)° in HTP) and Co-O2-W (176.2(5)° in HTP). All calculated BVS are very close to the expected valences, indicating the refinement was appropriate and the space group assignment correct.

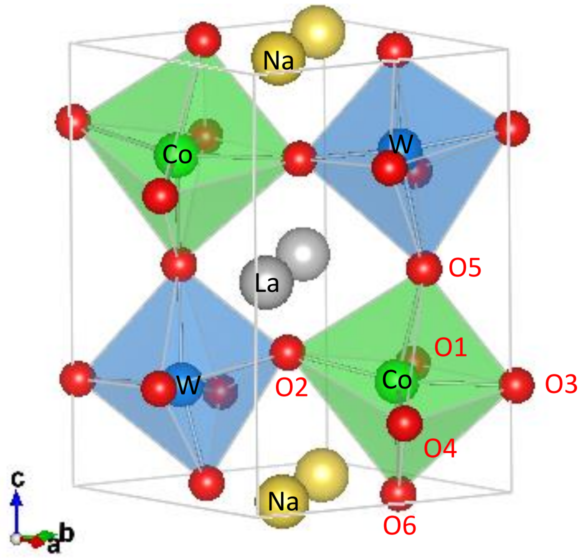

Figure 5.6 Schematic view of the crystal structure of NaLaCoWO$_6$ LTP (*P2$_1$*). The spheres are Na (yellow), La (grey), Co (green), W (blue) and O (red).

Table 5.2 Selected Bond lengths, bond valence sums and bond angles of NaLaCoWO$_6$ from the joint refinement at 100K.

Bond Lengths (Å)		Bond Valence Sums	
Co-O1	2.02(7)	Na	0.84(2)
Co-O2	2.14(7)	La1	2.77(5)
Co-O3	1.96(7)	La2	2.86(4)
Co-O4	2.17(7)	Co	2.24(4)
Co-O5	2.07(4)	W	6.2(1)
Co-O6	2.11(4)	O1	2.14(6)
Co-O Average	2.08	O2	2.01(5)
W-O1	1.92(7)	O3	2.08(6)
W-O2	1.97(7)	O4	1.91(5)
W-O3	1.88(7)	O5	1.96(3)
W-O4	1.91(7)	O6	2.13(4)
W-O5	2.13(4)	Bond Angles (°)	
W-O6	1.77(4)	Co-O1-W	156.2(8)
W-O average	1.93	Co-O2-W	152.8(8)
		Co-O3-W	174.3(8)
		Co-O4-W	154.5(8)
		Co-O5-W	155.9(4)
		Co-O6-W	154.5(4)

5.3 The Superstructure of the HTP

As shown in chapter section 5.1, the diffraction pattern of the $[001]_p$ zone axis shows satellite reflections indicating the existence of a superstructure. Since it is difficult to distinguish whether the propagation direction is $[100]_p$ or $[010]_p$, the following discussions focus on the propagation direction $[1\ 0\ 0]_p$. A high resolution electron micrograph (HREM) of this phase in the same orientation clearly shows a contrast modulation in form of stripes (Figure 5.7). The squares of white dots correspond to the aristotype perovskite unit cell. The stripes are parallel to the edges of these squares and the repeat distance is equal to 12 small squares. This modulation therefore corresponds to the satellite reflections observed in SAED.

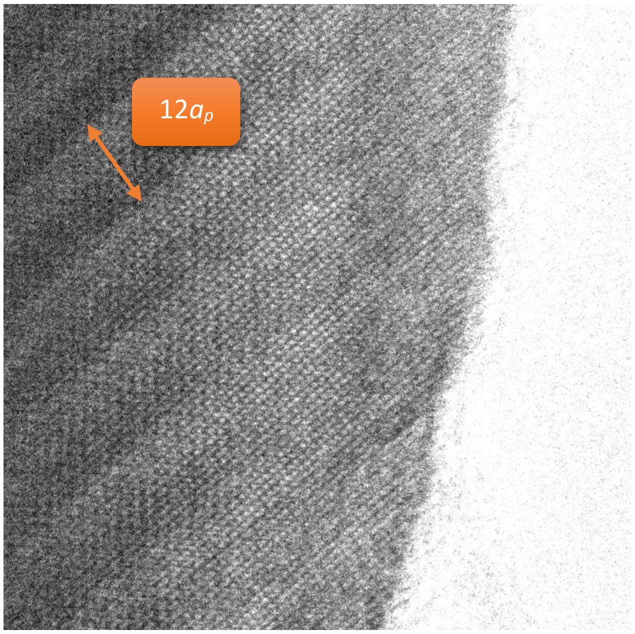

Figure 5.7 The HREM image taken from the high temperature phase of $NaLaCoWO_6$ along the zone axis $[0\ 0\ 1]_p$, a contrast of dark and bright stripes is observed with a periodicity $12a_p$.

Such a modulation was also observed in the related compound $NaLaMgWO_6$ before[54][55]. Two sources were proposed to explain the contrast: octahedral tilt twinning and chemical compositional modulation.

The SAED pattern and the HREM give that the new periodicity regarding the superstructure is $12a_p$ along the $[100]_p$ or the $[010]_p$ direction, details concerning how the structure is modulated remaining, however, a question. Even though we can obtain an atomic resolution in HREM images, a straightforward interpretation of the contrast in such images is not possible. In order to obtain more information we have to turn to other techniques, namely scanning transmission electron microscopy (STEM) with high angle annular dark field (HAADF), annular bright field (ABF) and electron energy loss spectroscopy (EELS).

In STEM a focused beam of very small diameter is scanned across the sample and at each position of the beam an intensity measurement is performed. Each position of the beam corresponds to one pixel of the final image and the measured intensity is then attributed to a grey level in this pixel. The information content of the image then depends on the type of measurement that is done.

In the case of HAADF only electrons that are scattered to high angles are counted. At these angles only incoherently scattered electrons are obtained and the contrast can directly be linked to the atomic numbers Z since the scattering power depends on Z of the elements in one atomic column, heavy elements giving brighter contrasts. This imaging mode is also called Z-contrast imaging.

ABF consists in detecting the electrons in the transmitted beam using an annular detector. The Z-contrast imaging is able to well probe the heavy elements from the bright contrast, however, it has difficulty to reveal the positions of light elements, such as oxygen, when both heavy and light elements are present in the same phase. ABF is the complementary technique to have contrast from both heavy and light elements simultaneously.[95] In addition, ABF also has the advantage that the contrast is rather insensitive to defocus and sample thickness. But the interpretation is not as straightforward since coherent and incoherent scattering is superimposed.

In EELS an energy loss spectrum is recorded for each pixel of the image. The post-experiment treatment then allows selecting element specific regions in the spectrum and thus to obtain images that show elemental maps.

Figure 5.8 shows the HAADF and the ABF images of $NaLaCoWO_6$ in an almost perfect $[001]_p$ zone axis orientation. In the images a contrast corresponding to the superstructure stripes can be observed, but it is very weak. The corresponding EELS images didn't show any compositional variation for any of the four cations. We can therefore conclude that the contrast of the stripes is not due to chemical differences in the stripes.

Tilting the sample, however, changes the contrast in STEM ABF iamges. Figure 5.9 shows a region of the sample where two domains of the superstructure exist showing perpendicular orientations for the stripes. HAADF images and the corresponding diffraction patterns are listed in the left and right column, respectively. The diffraction patterns show how the sample is tilted. When tilting the sample around one axis (**a** or **b**) the contrast in one domain increases (upper part of the image) while it stays weak in the other (Figure 5.9 (a)). Tilting it around the same axis but in the opposite direction again increases the contrast in the same domain (Figure 5.9 (c)). However, note that the dark and bright stripes are inverted as can be seen from the placement of a defect contrast in the upper left part of the images. In Figure 5.9 (a) the dark defect contrast is inside a bright stripe while in Figure 5.9 (c) it is in a dark stripe.

Tilting the sample around the perpendicular axis in one direction (Figure 5.9 (e)) or the opposite direction (Figure 5.9 (g)) changes the contrast in the other domain (bottom part of the image) while leaving it weak in the domain in the upper part of the image. Tilting it along the diagonals **a**+**b** or **a**-**b** makes the contrasts appear in both domains in similar intensity (Figure 5.9 (i) and (k)).

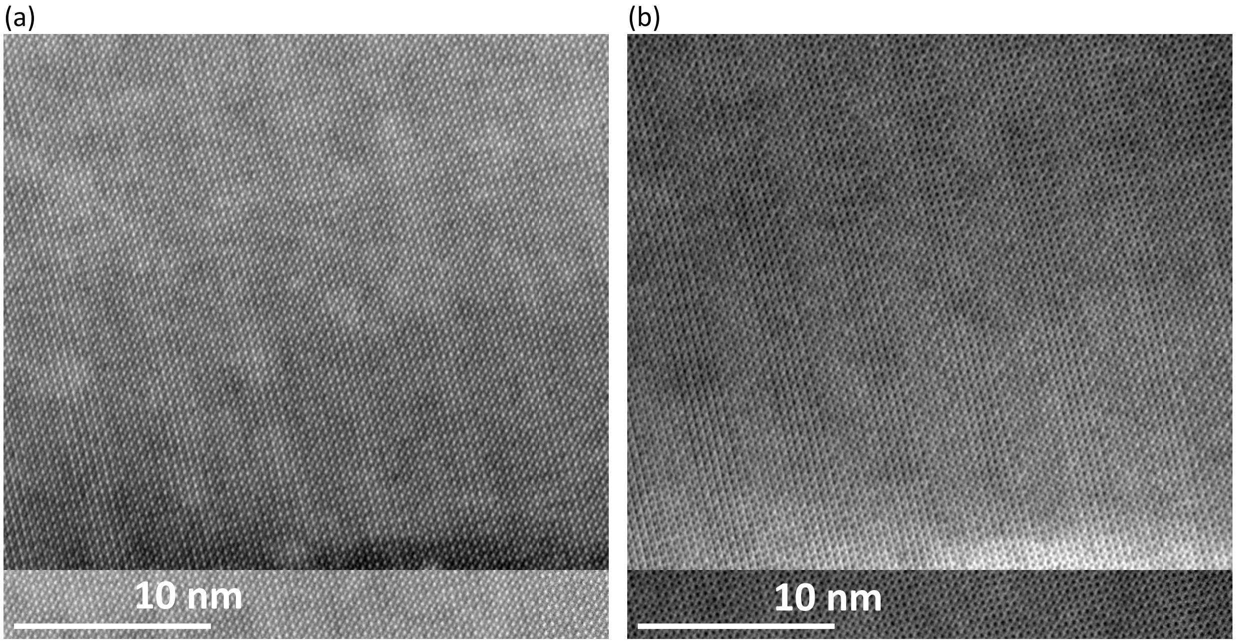

Figure 5.8 (a) the HAADF image of $NaLaCoWO_6$ shows no chemical contrast in the crystal, (b) the STEM ABF image shows very weak stripes contrast under the condition of perfect alignment.

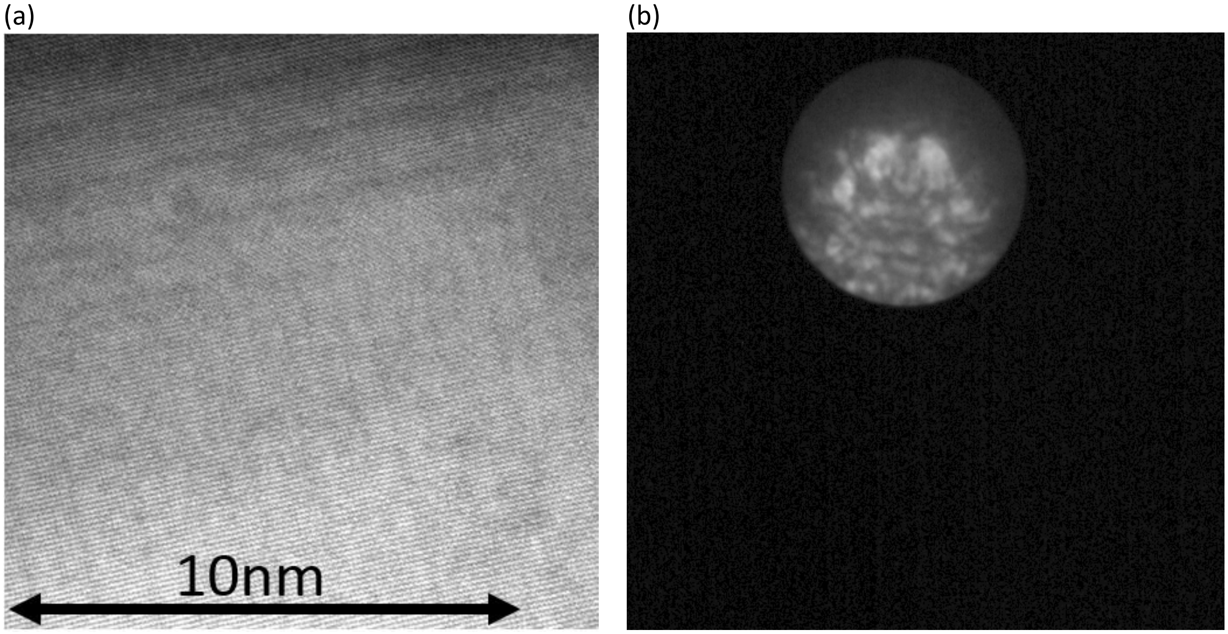

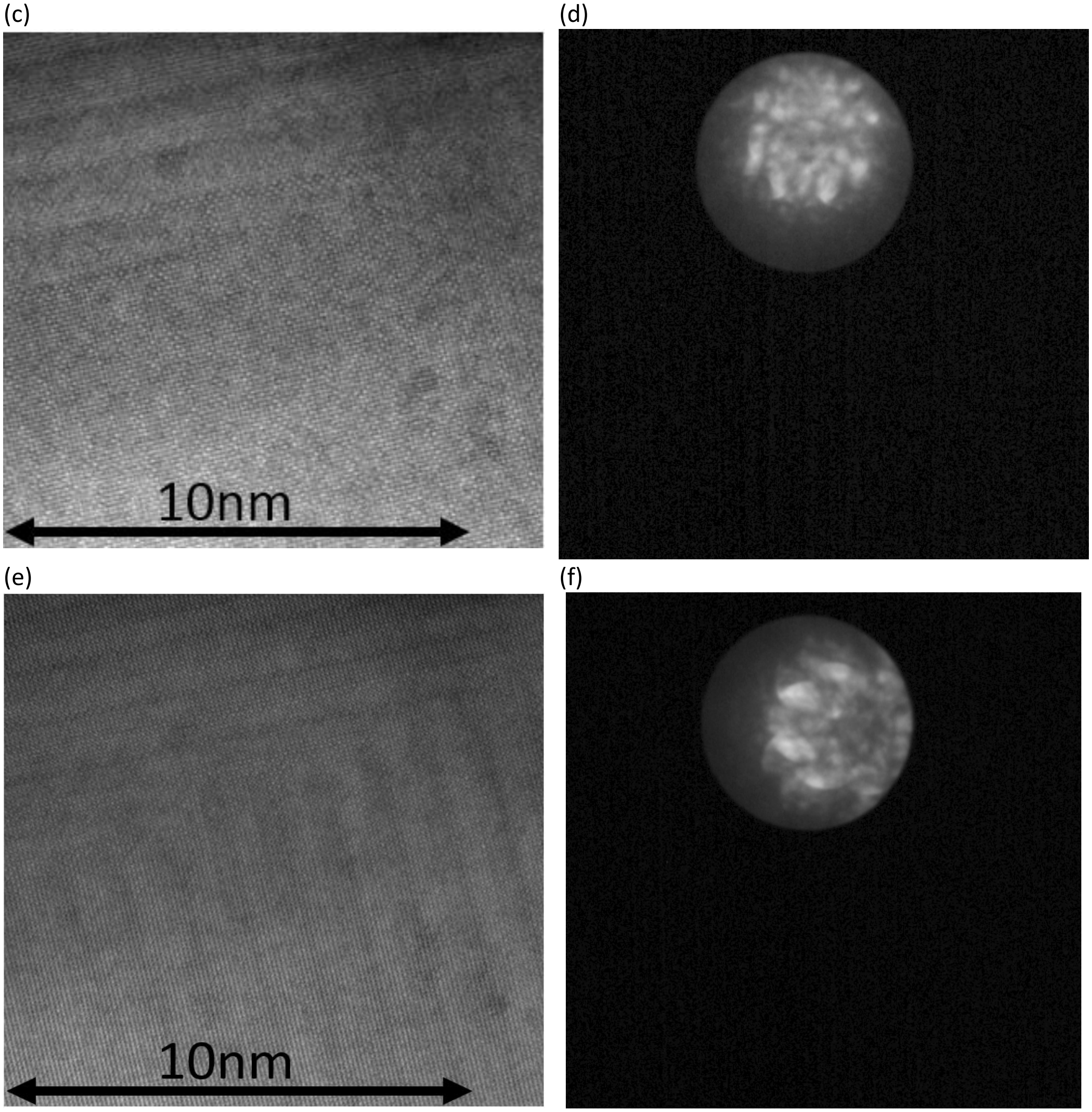

(g) (h)

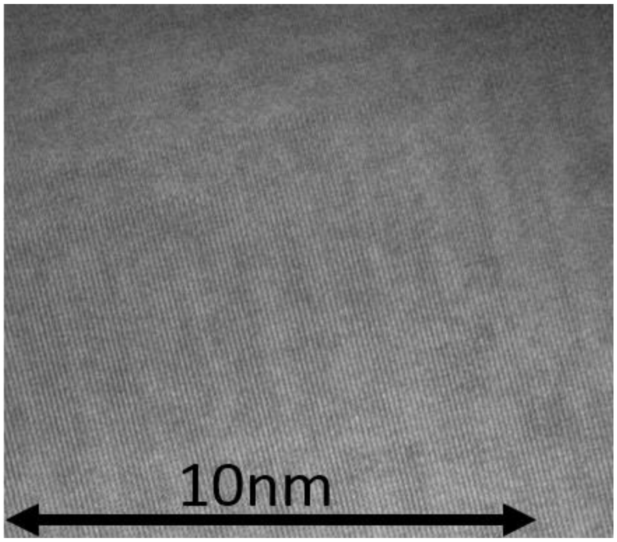

(i)

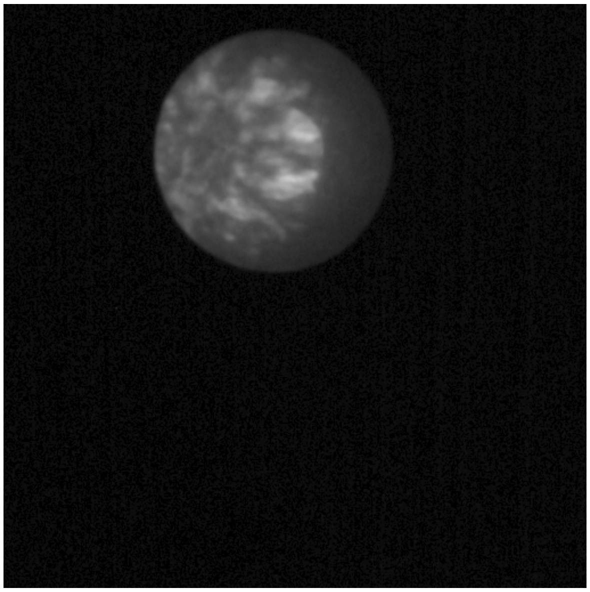

(j)

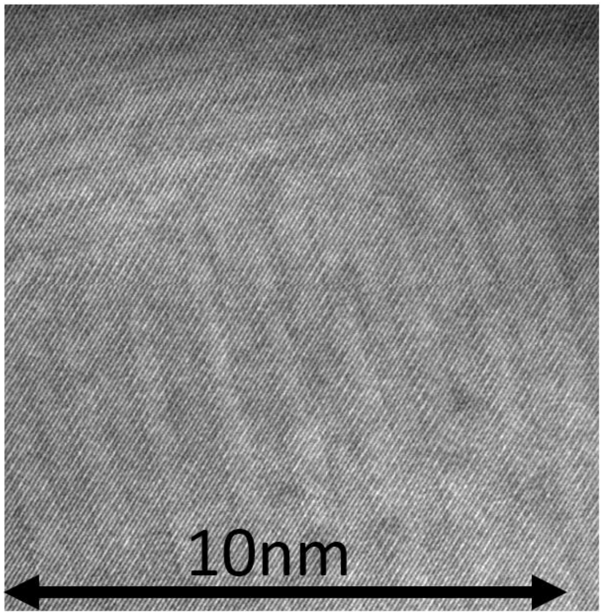

(k)

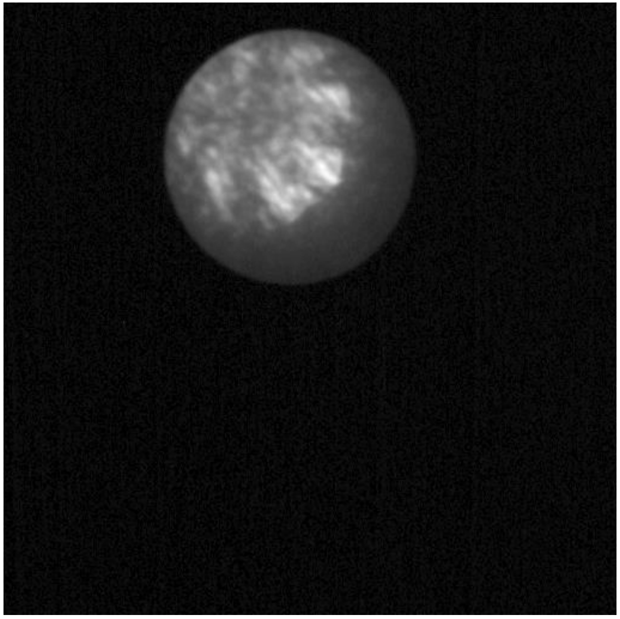

(l)

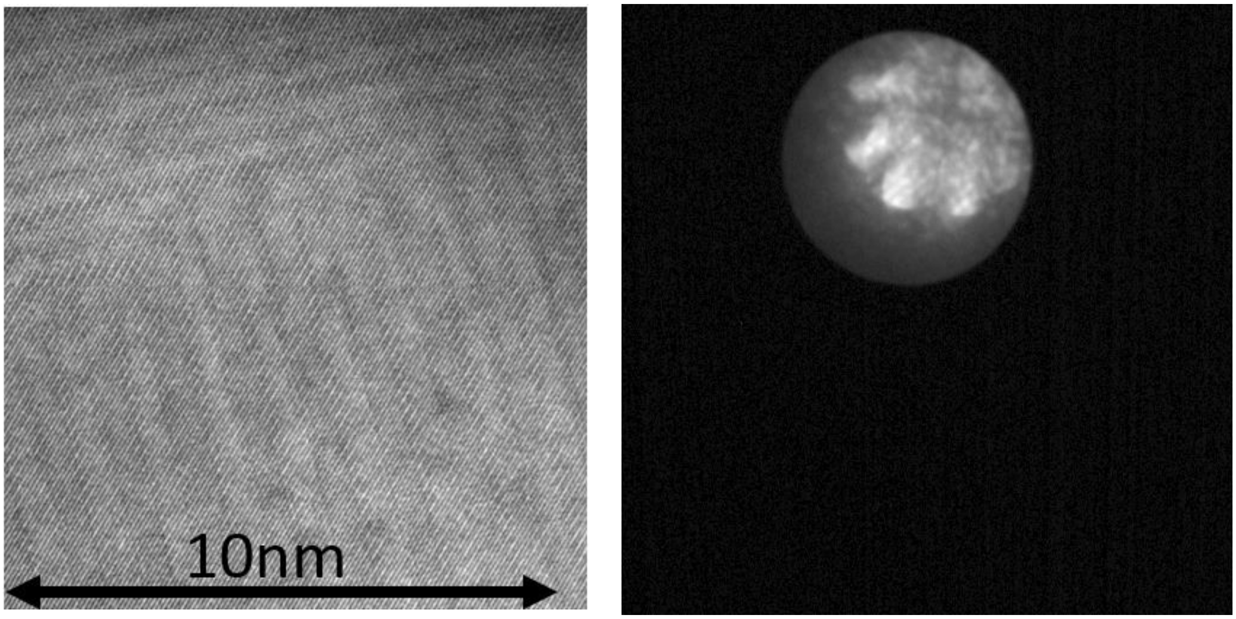

Figure 5.9 The investigation on the relationship between tilting the sample away from the perfect alignment by some tenths of a degree and the stripes contrast in STEM ABF images. (a) and (c) tilt the sample along either **a** and **b**-axis, respectively; and (e) and (g) tilt the sample along the other axis, **b** and **a**-axis, respectively; (i) and (k) tilt the sample along the diagonal **a**+**b** and **a**-**b**, respectively. The corresponding diffraction patterns are shown on the right indicating how the sample is tilted referred to the zone axis.

A sketch drawing (see Figure 5.10) illustrates a possible interpretation of the observed contrast when tilting the crystal. The crystal is supposed to be composed of domains in distinct orientations, each domain tilted by a small angle with respect to its neighbors as shown in Figure 5.10. When the crystal is perfectly aligned along the zone axis $[001]_p$, the incident electron beam is parallel to none of the domain orientations (see Figure 5.10 (a)). Consequently, electrons are evenly scattered and transmitted through the crystal, leaving a uniform pattern with no contrast. However, when the crystal is tilted (see Figure 5.10 (b) and (c)), some domains will be better aligned with the incident beam. In this case, in the aligned domains electron channeling along the atom columns is more effective, resulting in a bright contrast. On the other hand, the other domains are tilted further away from the incident beam direction, as a result, electron channeling is less effective and a dark contrast is observed in the HAADF images.

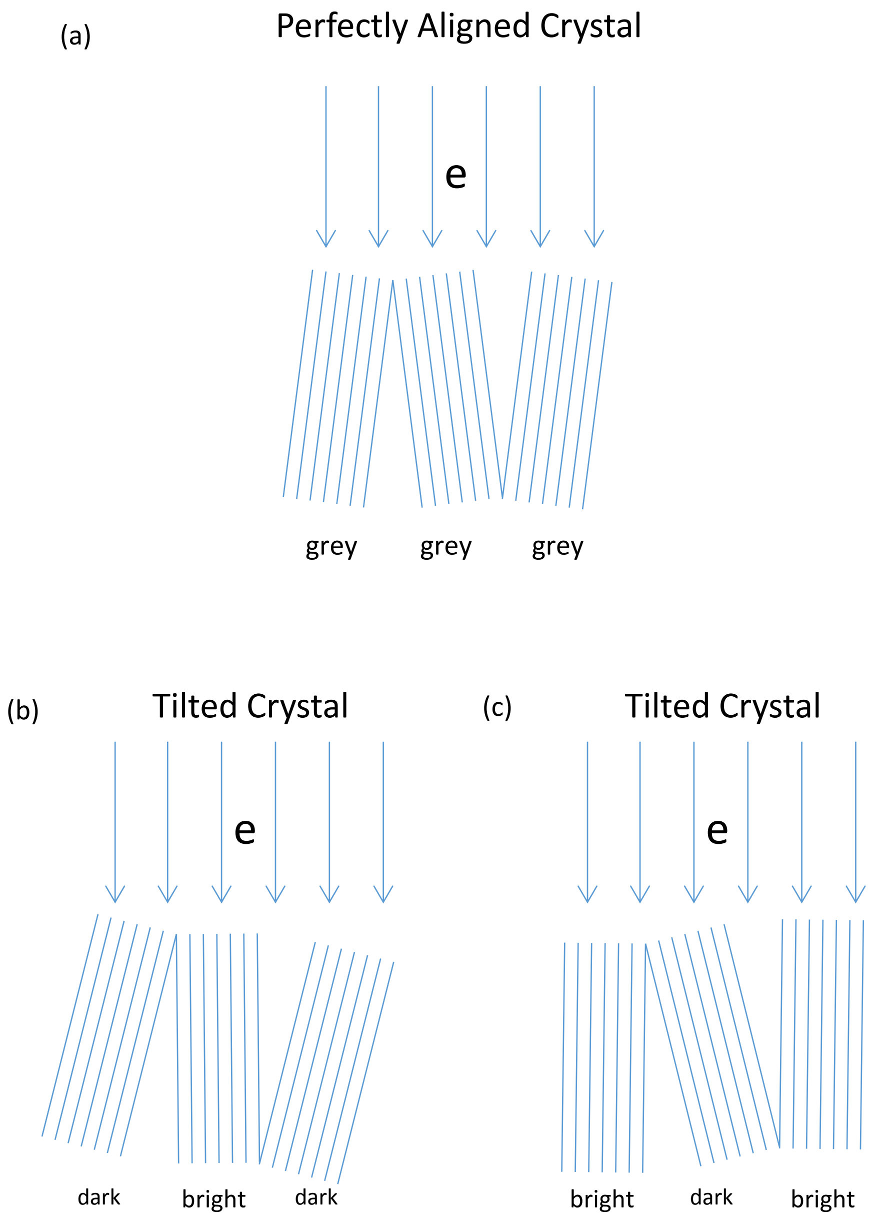

Figure 5.10 A sketch drawing to elucidate the relationship between the crystal tilting and the observed contrast.

Besides $NaLaCoWO_6$, complex superstructures are also observed in $NaPrCoWO_6$ and $NaNdCoWO_6$. The HREM and the corresponding SAED patterns taken along the zone axis $[001]_p$ are illustrated in Figure 5.11. More complex modulated patterns are found in these two compounds.

(a) NaPrCoWO$_6$ (b) NaPrCoWO$_6$

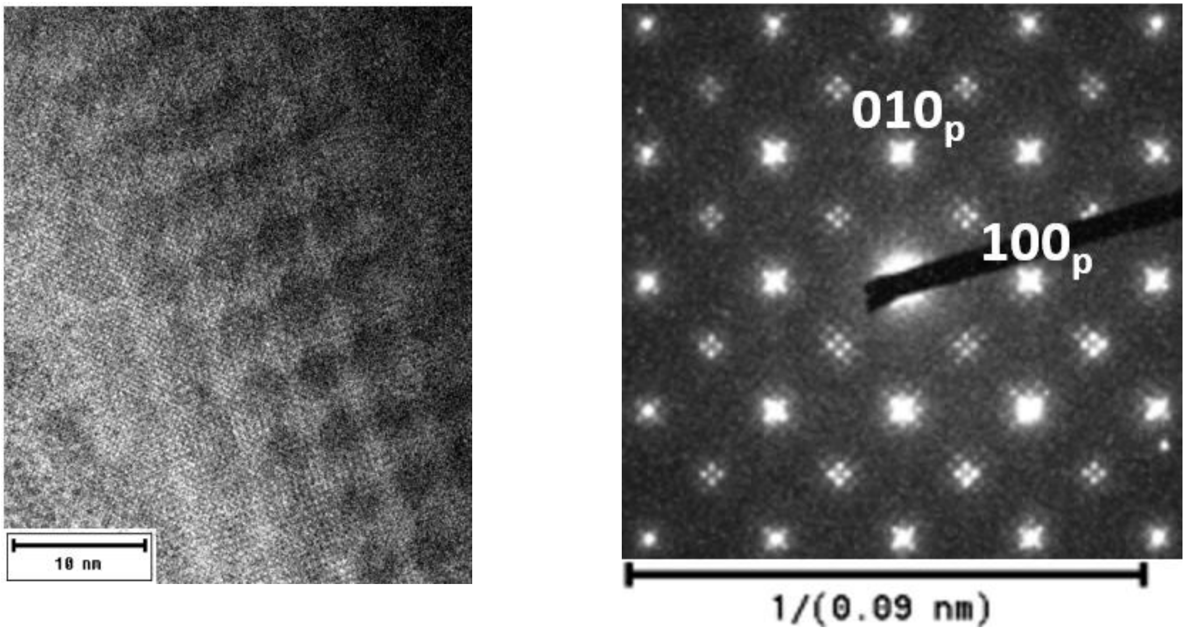

(c) NaNdCoWO$_6$ (d) NaNdCoWO$_6$

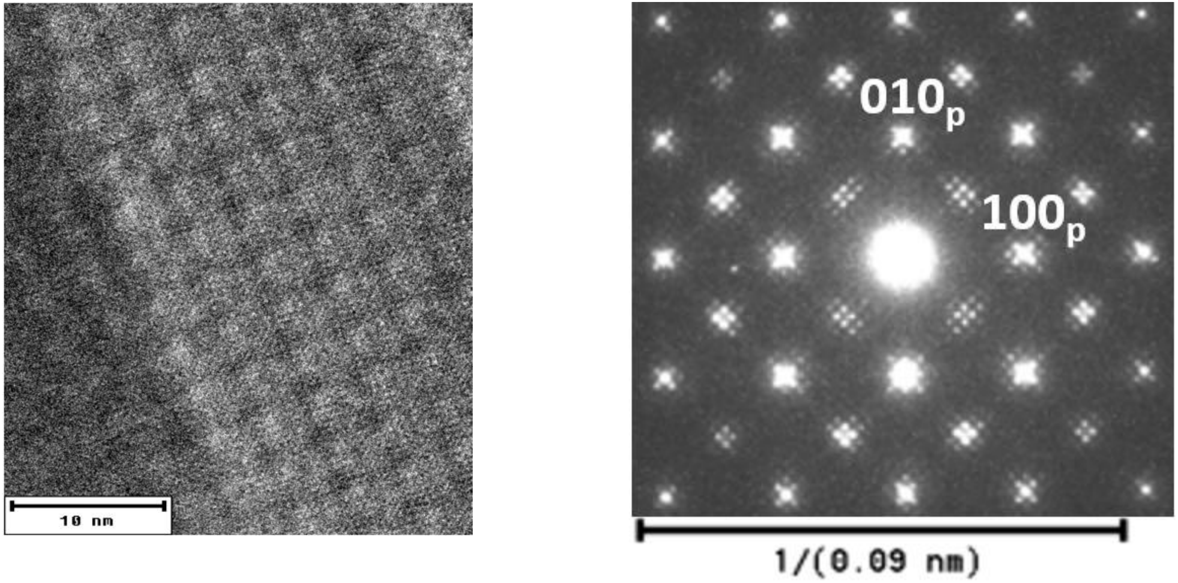

Figure 5.11 Superstructures are also observed in NaPrCoWO$_6$ and NaNdCoWO$_6$, evidenced from the HREM ((a) and (c)) and the corresponding SAED patterns ((b) and (d)) along the zone axis $[001]_p$.

5.4 The Superstructure Models for HTP

Since it is evidenced that the stripes contrast observed in the HTP has nothing to do with the chemical modulation, the contrast is only attributed to the structural effect -- the octahedral tilting. We have built models with oxygen octahedral tilt twinning in order to try to explain the satellite reflections observed in both the NPD pattern and the ABF images. According to the SAED pattern and the stripes contrast pattern in the ABF images, the unit cell of the superstructure has dimensions of $12a_p*2a_p*2a_p$ or $2a_p*12a_p*2a_p$. Based on a previous study on $NaLaMgWO_6$[55], three models are built based on the *C2/m* and *P2₁/m* NPD refinements in order to approach to reality more closely.

Model 1 is based on the *C2/m* NPD refinement. Since the tilting scheme of *C2/m* is $a^0b^-c^0$, which means the octahedra only tilt around the **b**-axis, the superstructure can only propagate along the **b**-axis to have a tilt twinning at the middle of the superstructure unit cell. There is no tilt twinning along the **a**-axis, so that it is impossible to have a tilt twinning along this direction. As a result, the unit cell of Model 1 has dimensions of $2a_p*12a_p*2a_p$ and the tilting scheme $a^0b^-c^0$. To build this model, the y-coordinates of all atoms in the refined unit cell are divided by 6, which yields a first block of the structure. Then 1/6 and 1/3 are added to the y-coordinates of the first block, respectively, to build the second and the third blocks. After this step half of the unit cell is filled Then, the tilt twinning is applied at this antiphase boundary to build the second half of the unit cell. Model 1 is shown in Figure 5.12 (a), the octahedra at the two sides of the tilt twinning boundary are tilted in the same direction along the **b**-axis.

Models 2 and 3 are built based on the *P2₁/m* NPD refinement. Since it is difficult to distinguish whether the propagation direction of the superstructure is along $[100]_p$ or $[010]_p$, Model 2 is made to propagate along the **a**-axis and Model 3 along the **b**-axis. Both of them possess the *P2₁/m* tilting scheme $a^-a^-c^0$. The unit cell of the *P2₁/m* structure has dimensions of $\surd 2a_p*\surd 2a_p*2a_p$, where the **a**-axis is along the $[110]_p$ direction and the **b**-axis is along the $[1\text{-}10]_p$ direction. The first step in building these models is to convert the coordinate axes to be consistent with the aristotype perovskite (which coincides with the *C2/m*) unit cell. The new x-coordinates are thus obtained by $(y_{MP}-x_{MP})/2$ (x_{MP} and y_{MP} are the x and y-coordinates in the *P2₁/m* unit cell, respectively), and the new y-coordinates are $(y_{MP}+x_{MP})/2$. Since there is no difference in the **c**-axis, all the **z**-coordinates are kept the same. Model 2 is modulated along the **a**-axis so that its unit cell is $12a_p*2a_p*2a_p$. The main principle to build the model is the same as that of the Model 1, this time creating a tilt twinning at the middle of the unit cell along the **a**-axis. The unit cell size of Model 3 is $2a_p*12a_p*2a_p$, and the tilt twinning is at the middle along the **b**-axis. All the structures of these models are shown in Figure 5.12.

(a) Model 1: $a^0b^-c^0$

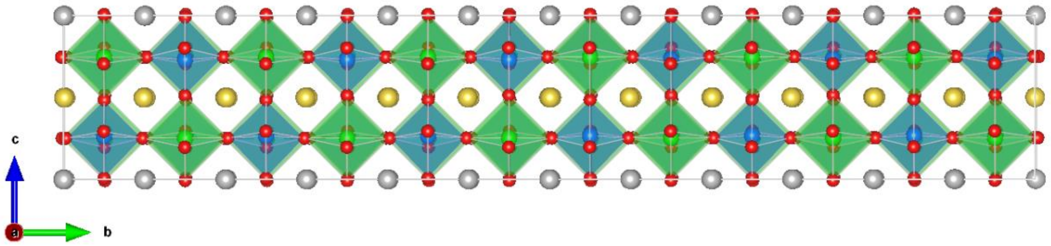

(b) Model 2: $a^-a^-c^0$

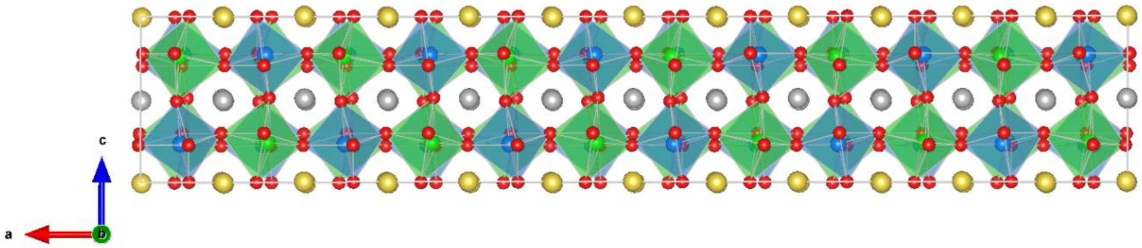

(c) Model 3: $a^-a^-c^0$

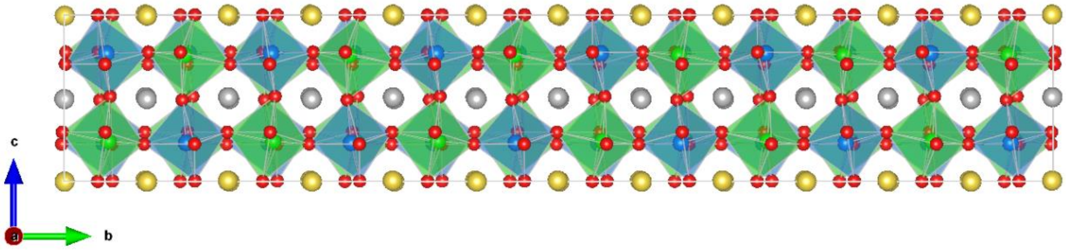

Figure 5.12 The structures of different models with octahedra tilt twinning to describe the structural modulations in HTP. (a) the model based on the *C2/m* NPD refinement with the unit cell $2a_p$*$12a_p$*$2a_p$ and the tilting scheme $a^0b^-a^0$; (b) the model based on the *P2₁/m* NPD refinement with the unit cell $12a_p$*$2a_p$*$2a_p$ and the tilting scheme $a^-a^-c^0$; (c) the model based on the *P2₁/m* NPD refinement with the unit cell $2a_p$*$12a_p$*$2a_p$ and the tilting scheme $a^-a^-c^0$. The spheres are Na (yellow), La (grey), Co (green), W (blue), and O (in red).

In each model, there are 240 atoms in one unit cell, so that it is impossible to refine the diffraction patterns properly. We can only simulate the SXRPD and NPD patterns of all these three models. The lattice parameters used in these simulations are from the *C2/m* SXRPD refinement, with the parameter corresponding to the $12a_p$ direction multiplied by 6. All profile parameters are the same as those in the *C2/m* SXRPD and NPD refinements. Reasonable B_{iso} values are picked for all elements and the atoms of the same element are constrained to have the same B_{iso} value. In the SXRPD pattern simulations, the B_{iso} values were picked directly from the refinement; while in the NPD pattern simulations, B_{iso} values were selected as 0.49 for Na, 0.56 for La, 0.29 for Co, 0.23 for W and 1.0 for O. It is noted that these simulations are only approximations to compare with the observed pattern, nevertheless, they are very close to reality.

A representative 2θ range related to the superstructure in the simulated NPD and SXRPD patterns is shown and compared with the corresponding observed pattern in Figure 5.13. The 2θ range selected in the NPD and SXRPD simulations are in the same Q-range. In the NPD pattern simulations, Model 1 can explain the satellites, which indicates that the satellite peaks come from the new periodicity $12a_p$. In contrast, the main peaks cannot be explained with this model which is attributed to the wrong choice of tilting scheme, so that this model is ruled out. Both Models 2 and 3 can well-explain the positions of all the observed peaks and the relative intensities in this specific region as shown in Figure 5.13 (a). This evidences that the tilting scheme $a^-a^-c^0$ is the one adopted by the oxygen octahedra. Although the propagation directions are different in Models 2 and 3, where the propagation direction is along the **a**-axis for Model 2 and it is along the **b**-axis for Model 3, it is hard to tell which one is better than the other from the simulated patterns. Considering both models are only built as approximations to the reality, some parameters such as the B_{iso} values are not properly refined. As a result, it is not reasonable to tell which one is better than the other from very small features. The simulated SXRPD patterns with these three models are compared in Figure 5.13 (b), the main peaks in the observed pattern are approximately reproduced by the simulations, without any strong evidence about the superstructure like in the NPD data. Refinement attempts were made on the SXRPD patterns in this specific region, however, only lattice parameters can be refined into convergence, no other parameters can be refined any more. From the limited refinements, it is difficult to rule out Model 2 or Model 3 with respect to the other. It still remains a question whether the propagation direction of the superstructure is along $[100]_p$ or $[010]_p$.

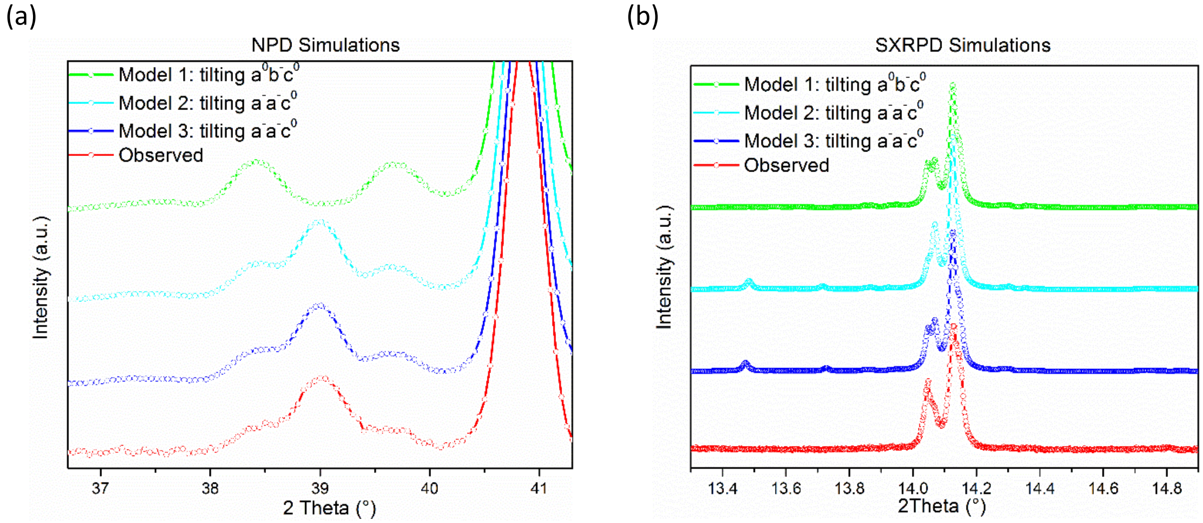

Figure 5.13 A comparison between the simulated (a) NPD and (b) SXRPD patterns of different superstructure models and the observed pattern. The Model 1 (in green) corresponds to the unit cell parameters $2a_p*12a_p*2a_p$ and the tilting scheme $a^0b^-a^0$; the Model 2 (in cyan) corresponds to the unit cell parameters $12a_p*2a_p*2a_p$ and the tilting scheme $a^-a^-c^0$; the Model 3 (in blue) corresponds to the unit cell parameters $2a_p*12a_p*2a_p$ and the tilting scheme $a^-a^-c^0$.

5.5 Conclusions

A structural phase transition is observed in $NaLaCoWO_6$ with a temperature hysteresis as large as 150 K. Some extra peaks are observed in the NPD pattern of the HTP, which can be explained by neither an impurity nor a different space group. The SAED study also observes the satellite reflections in the HTP, a new periodicity $12a_p$ along either $[100]_p$ or $[010]_p$ is derived from the spacing between the satellites. The phase transition is also investigated by the SAED study by cooling the sample down to 100 K and heating up back to room temperature. The satellites became much weaker and tend to disappear at 100 K, and the main reflections which are surrounded by the satellites become stronger at 100 K. When the sample is heated up to room temperature, with the irradiation of the electron beam, it transits from the LTP to the HTP. All these indicate that the satellites are closely related to the phase transition and the reversibility of this transition is confirmed by the SAED study. The structure of the LTP is determined as the polar space group $P2_1$ from both the SXRPD and NPD refinements. In order to get a more precise model of the LTP, a joint refinement combing the SXRPD and NPD patterns is performed. A further TEM study is carried out on the HTP, a contrast of stripes contrast is observed in the HREM images. The contrast is a structural effect since no evidence on chemical modulations is observed from the HAADF images and the EELS data. Three models are built based on the *C2/m* and $P2_1/m$ refinements to explain the superstructure in the HTP. The tilting scheme $a^-a^-c^0$ seems to be the correct one, however, the direction of propagation of the superstructure remains unknown. The small domain size in the high temperature phase prevented further electron diffraction study to verify between these two symmetries *C2/m* and $P2_1/m$.

Chapter 6: Physical Characterizations of the Doubly Ordered Perovskite Family $NaLnCoWO_6$

Within the last two chapters, it has been shown that all doubly ordered perovskites in the $NaLnCoWO_6$ (Ln= Y, La, Pr, Nd, Sm, Eu, Gd, Tb, Dy, Ho, Er, and Yb) family crystallize in monoclinic structures with a Na/Ln layered ordering and a Co/W rock-salt type ordering. The magnetic transition metal cation Co^{2+} is on the B-site for all compounds and on the A'-site the magnetic rare-earth ions are found except for $NaYCoWO_6$ and $NaLaCoWO_6$ where the Ln are not magnetic. Here we present magnetization and specific heat capacity measurements carried out to study the magnetic properties for all samples (chapter section 6.2). Magnetic structures were determined by NPD on selected compounds with or without magnetic rare-earth ions: $NaLnCoWO_6$ (Ln=Y, La, Tb, Ho) (chapter section 6.3). Furthermore, electric properties were investigated by dielectric and pyroelectric measurements on these four samples (chapter section 6.4). Strikingly, the magneto-electric coupling was experimentally observed in $NaLnCoWO_6$ (Ln=Y, Tb, and Ho), and will be discussed also in chapter section 6.4.

6.1 Magnetic Interactions in Doubly Ordered Perovskites $NaLnCoWO_6$

6.1.1 Crystal Fields and Orbital Quenching[96]

The crystal field theory considers the electric field between neighboring atoms in the crystal, and the neighboring orbitals are regarded as negative point charges. A further consideration on the crystal field theory creates another theory, which is known as the ligand field theory. In the ligand field theory, the overlap between the d orbitals on the central ion and orbitals on surrounding ions is also considered. The crystal field effect is strongly dependent on the symmetry of the local environment in the crystal. Based on the configurations of the d orbitals, they can be classified into two classes as shown in Figure 6.1(a). The e_g orbitals point along the coordinate axes, where the d_{z^2} orbital points along the **z**-axis and the $d_{x^2-y^2}$ orbital points along both the **x**- and **y**-axes. Meanwhile, the t_{2g} orbitals point between the coordinate axes, which are denoted as d_{xy}, d_{xz} and d_{yz}.

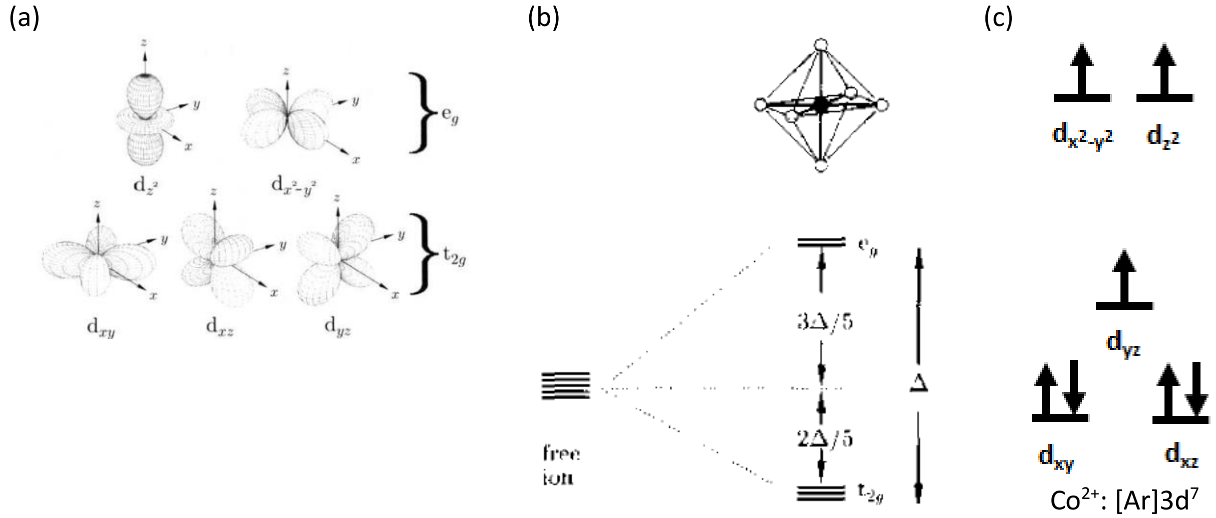

Figure 6.1 (a) The angular distribution of the d orbitals. The orbitals d_{z^2} and $d_{x^2-y^2}$ which point along the coordinate axes are grouped into the e_g orbitals, and the orbitals d_{xy}, d_{xz} and d_{yz} which point between the coordinate axes are grouped into the t_{2g} orbitals. (b) Crystal field splitting in the octahedral environment (c) the 3d electron configuration of the Co^{2+} ion in an octahedral environment in doubly ordered perovskites.

The octahedral environment is shown in Figure 6.1 (b), the neighboring positive charges are located at the points (±r, 0, 0), (0, ±r, 0) and (0, 0, ±r), so that the t_{2g} orbitals have an energy advantage over the e_g orbitals. As a consequence, these five levels split into lower energy levels for the t_{2g} orbitals and higher energy levels for the e_g orbitals.

The electron configuration of Co^{2+} is illustrated in Figure 6.1 (c). The Co^{2+} cation has 7 electrons in the 3d orbital, losing 2 electrons from the 4s orbital of the neutral Co atom. These electrons are arranged in the high spin configuration (S=3/2, L=3, J=9/2). The degeneracy of the t_{2g} orbitals is released by a weak Jahn-Teller effect.

For 3d transition metal ions, the crystal field interaction is much stronger than the spin-orbit interaction. The moment values predicted by considering both the spin and the orbital angular momenta do not always agree with the experimental values. However, if one considers the orbital angular momenta to be equal to zero, the calculated moments show a better agreement with experiment. This effect is called orbital quenching. For 4f ions, the crystal field is not as strong as in 3d ions, so that there is no orbital quenching for 4f ions. In this study, the 3d magnetic cation is Co^{2+} at the B-site. The predicted effective moment is $g_j\sqrt{[J(J+1)]} = 6.63\ \mu_B$ if both angular momenta are considered, and $g_j\sqrt{[S(S+1)]} = 3.37\ \mu_B$ in the condition of orbital quenching. However, the experimentally derived value is 4.90 μ_B from paramagnetic salts, which indicates that the physics behind the moment of Co^{2+} is in between the former two cases. Hence, in this study, the moment 4.9 μ_B is picked as the reference moment for Co^{2+}, all related effective magnetic moments calculated are based on this reference value.

6.1.2 Superexchange Interaction

Exchange interactions are the core of the long range magnetic ordering, they are essentially electrostatic interactions. Electrons on neighboring magnetic atoms can directly interact with each other via the so-called direct exchange. However, in many magnetic materials, indirect exchange interactions have also to be considered. In the so-called superexchange, the non-neighboring magnetic ions interact with each other via non-magnetic intermediary ions which lie between the magnetic ions. This interaction has an advantage in kinetic energy for antiferromagnetism (AFM). The superexchange interaction is strongly affected by the bond angles between the magnetic and non-magnetic ions, because the bond angles are directly linked to the degree of overlap of the orbitals. Given that the superexchange interaction can also to be ferromagnetic, the interaction is much weaker and rather less common than the antiferromagnetic superexchange.

The magnetic transition metal cations Co^{2+} are located on the B-site over the entire series, and interact with each other via the superexchange mechanism. Considering nearest-neighbor (NN) interaction, there are two possible super-super-exchange (SSE) antiferromagnetic pathways Co-O-O-Co to consider. For the next-nearest-neighbor (NNN) interaction, there is only one ~180° Co-O-W-O-Co AFM exchange path. These pathways represented in the **a**-**b** plane are schematically shown in Figure 6.2(a). In the Co-O-O-Co pathway, spins of Co ions of opposite orientation interact with each other with the assist of the 2p orbital electrons of two ligand O atoms. In contrast, in the Co-O-W-O-Co pathway, the 2p electron on the ligand O ion, with opposite spin with respect to the $3d_{x^2-y^2}$ electron on the Co ion, can partially occupy the $3d_{x^2-y^2}$ orbital of the Co ion. And the other O2p electron can interact with the 5d orbitals of the highly charged W^{6+} ion, where the 5d orbitals of W^{6+} are empty. The NN AFM interaction is believed to be the dominant one. The actual values of the exchange interactions are strongly dependent on the orientations of the electronic orbitals which are not trivial to determine.

Finally, when considering only the NN interactions, a face centered cubic (FCC) lattice is formed by the magnetic Co ions (figure 6.2 (b)). Consequently, all these lead the magnetic structure prediction to be complicated, and more effort is needed to understand the magnetic interactions more deeply.

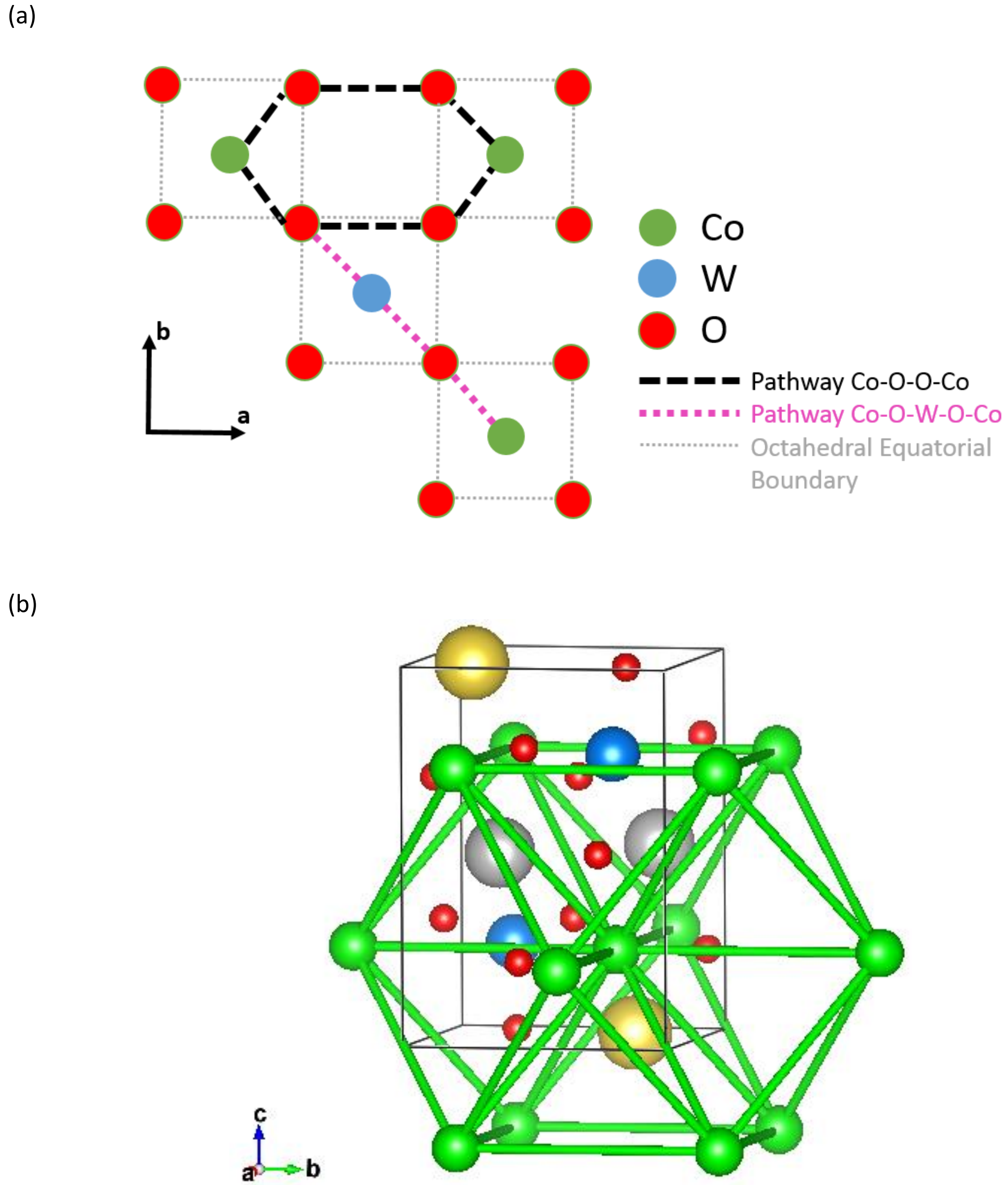

Figure 6.2 (a) Schematic views of the NN and NNN interactions. For NN: Co-O-O-Co SSE interaction and for NNN, Co-O-W-O-Co pathway. (b) face centered cubic compact lattice formed by magnetic Co ions considering only NN interactions.

6.2 Magnetic Properties

6.2.1 Magnetization and Specific Heat Capacity Measurements

All samples were systematically investigated in terms of temperature dependence of the magnetization between 2 and 300K under a magnetic field of μ_0H= 1T in addition to FC and ZFC processes between 2 and 20K under a magnetic field of μ_0H=0.01T. As shown in the second column on the left in Figure 6.3, the antiferromagnetic ordering temperature, i.e. the Néel temperature T_N, was identified from either the infletion point or the maximum of the magnetization curves, except for Gd and Yb where they were absent. The range of Néel temperatures T_N is from 4 K to 13 K, as can be seen in Table 6.1. There are no or very small differences between FC-ZFC curves below the ordering temperature ruling out the existence of a ferromagnetic contribution. The only exception is the $NaLaCoWO_6$ compound where FC and ZFC curves are well separated already above the Néel temperature suggesting that this phenomenon is not intrinsic but related to the presence of an impurity.

Heat capacity (Cp) measurements were carried out to provide further information concerning the magnetic transition process for 8 compounds (Ln= Y, La, Nd, Sm, Gd, Tb, Ho, Yb) (see the middle column of Figure 6.3). The transition temperatures were determined by the maximum slope from the heat capacity curves. The extracted T_N are in good agreement with the ones determined by the temperature dependence of the magnetization. For Gd and Yb, where the transition temperatures were hardly visible from their magnetization measurements, the heat capacity shows a clear signature of the transition and the T_N of Gd and Yb were determined as ~10K and ~7K, respectively. Since there was no non-magnetic reference sample to extract the magnetic entropy from the heat capacity data, efforts were made to fit the observed data with the Debye model. However, these attempts were not very successful. It would be better to prepare the corresponding non-magnetic samples, for example $NaLnMgWO_6$, as references to properly extract the magnetic entropy from the heat capacity measurements.

Below T_N, anomalies were observed in the FC-ZFC and heat capacity measurements of some compounds. The temperatures at which either the curve starts to rise in Cp-T curves or where a kink appears in the M-T curves are listed in the column of T_{an} in Table 6.1. Such anomalies are visible in $NaPrCoWO_6$, $NaNdCoWO_6$, $NaSmCoWO_6$, $NaEuCoWO_6$, $NaGdCoWO_6$, $NaTbCoWO_6$, $NaDyCoWO_6$, and $NaHoCoWO_6$. It is reasonable to attribute these anomalies to magnetic Ln^{3+} ions aligned by the magnetically ordered Co^{2+}. Quite similar phenomena were also observed before in related compounds such as $NaLnMnWO_6$ (Ln=Pr, Sm, Tb, and Dy).[42]

The Curie-Weiss fit was performed from the 1/χ-T plots for all compounds (except $NaYCoWO_6$ and $NaSmCoWO_6$) in the paramagnetic regime, between 150K and 300K where the curve is linear. 1/χ-T plots of $NaYCoWO_6$ and $NaSmCoWO_6$ do not display a linear regime between 150K and 300K and their cases were treated separately. For $NaYCoWO_6$, the Curie-Weiss fit was performed in the temperature range 50K-150K. For $NaSmCoWO_6$, we identified the presence of a ferromagnetic impurity in the M-H curve at 350K (see later). The Curie-Weiss fit was performed in the χ-T plot between 50K and 300K by the function:

$$\chi = \chi_0 + C/(T-\theta) \qquad \text{Equation (6.1)}$$

where χ_0 is the magnetic susceptibility of the magnetic impurity. The refined positive χ_0 indicates that there is indeed a magnetic impurity in this sample, and all other parameters deduced from the fit are listed in Table 6.1.

All M-T curves and the corresponding Curie-Weiss fits can be found in the most left-most of Figure 6.3. All derived magnetic parameters from the Curie-Weiss fits including the Curie constants (C), the Weiss temperatures (θ) and the effective magnetic moments are summarized in Table 6.1. All deduced Weiss temperatures are negative, indicating that antiferromagnetic interactions are dominant for all compounds. For compounds containing magnetic rare-earth cations, the μ_{ref} is calculatd by:

$$(\mu_{ref})^2=(\mu_{Ln})^2+(\mu_{Co})^2 \qquad \text{Equation (6.2)}$$

where all μ_{Ln} take theoretical values tabulated in reference[96], and μ_{Co} takes the value 4.90 μ_B which means that the spin-orbit coupling is not totally ignored. This value is also tabulated in the same reference as the experimentally derived value. The deduced magnetic moments are very close to the expected reference values for all compounds except for the $NaEuCoWO_6$ compound. The large measured effective magnetic moment is attributed to the Van Vleck paramagnetism.[111] Eu is a theoretically non-magnetic ion, however, its first excited state is so close to the ground state in energy that the energy gap is comparable to the thermal energy at room temperature.[112] As a consequence, this state can be thermally populated and contribute a magnetic moment about $3.4\mu_B$[96]. If μ_{ref} takes the magnetic moments from the thermally populated excited states, then it becomes $5.96\mu_B$ with a deviation being largely reduced to 9%.

Table 6.1 The summary of magnetic parameters of the doubly ordered perovskite $NaLnCoWO_6$ family.

Compound	C (emu.K/mol)	θ (K)	μ_{eff}/μ_B	μ_{ref}/μ_B	T_N (K)	T_{an} (K)
$NaYCoWO_6$	2.876(5)	-39.7(2)	4.796(4)	4.90	~8	
$NaLaCoWO_6$	2.86(2)	-30(2)	4.78(2)	4.90	~13	
$NaPrCoWO_6$	3.97(1)	-18.9(8)	5.636(4)	6.07	~11	~5
$NaNdCoWO_6$	4.51(2)	-36.3(9)	6.00(2)	6.09	~11	~4
$NaSmCoWO_6$	3.27(7)	-48(2)	5.11(5)	4.97	~10	~4
$NaEuCoWO_6$	5.36(2)	-85.4(7)	6.55(1)	4.90	~10	~4
$NaGdCoWO_6$	10.10(2)	-5.1(4)	8.99(1)	9.33	~10	~4
$NaTbCoWO_6$	17.27(2)	-22.5(3)	11.753(5)	10.89	~10	~4
$NaDyCoWO_6$	16.694(8)	-7.6(1)	11.554(3)	11.70	~10	~4
$NaHoCoWO_6$	15.98(2)	-1.3(3)	11.305(6)	11.68	~9	~4
$NaErCoWO_6$	12.66(3)	-2.4(6)	10.06(1)	10.77	~4	
$NaYbCoWO_6$	6.10(2)	-35.8(7)	6.98(1)	6.67	~7	

The listed parameters are Curie constant (C), Weiss temperature (θ), effective magnetic moment (μ_{eff}), the reference magnetic moment (μ_{ref}) tabulated[96], the Néel temperature (T_N) and the temperature (T_{an}) where an anomaly occurs below T_N (see text).

In addition to the M-T and heat capacity plots, the isothermal magnetic measurements are also summarized in Figure 6.3. Isothermal magnetic curves were collected for all samples at 2K, 5K, 10K, 15K, 20K, 25K, 30K, and 350K, scanning the magnetic field such as 0T-5T-0T in a 0.1T step with the MPMS_XL.

At high temperature, far above T_N, all samples except Sm behave as a paramagnet where the magnetization linearly increases with increasing magnetic field. In $NaSmCoWO_6$, a clear deviation from the linearity between M and H is visible already at 350K. This may be due to the presence of a ferromagnetic impurity.

The M-H curves measured at the lowest temperature were picked out and listed separately in the right-most column of Figure 6.3. When the temperature is slightly above T_N, the magnetic moments start to order locally and the magnetic field effects are reflected by some degree of curve bending. When the temperature is below T_N, the long range antiferromagnetic order is established, the curves bend and tend to reach the saturated value. The critical magnetic fields of the metamagnetic transition are deduced from the M-H curves measured at 2K (see the right-most column of Figure 6.3), where all samples are fully ordered antiferromagnetically in the absence of an applied field. The metamagnetic transition describes the magnetic field induced change of the magnetic structure in antiferromagnets.[113] When the strength of the applied magnetic field is sufficiently high, the magnetic moments will reorient, leading to another magnetic structure. $NaTbCoWO_6$, $NaDyCoWO_6$, $NaHoCoWO_6$ and $NaErCoWO_6$ exhibit a metamagnetic transition as shown in Figure 6.3. The first order derivative of these M-H curves directly gives the critical magnetic field. Where for Tb the transition point is 1T, for Dy it is 0.8 T and it is 0.7T for both Ho and Er. Furthermore, it is noted that there is a small hysteresis in the M-H curves at 2K for Dy and Er when cycling the magnetic field.

A Summary of Magnetic Parameters of All compounds

NaYCoWO$_6$

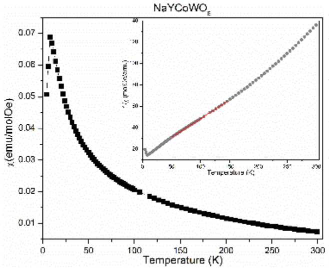

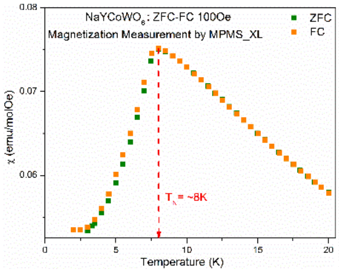

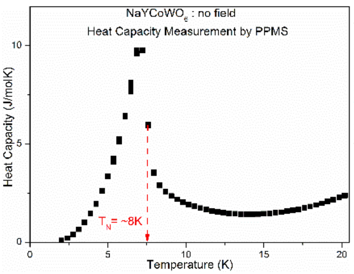

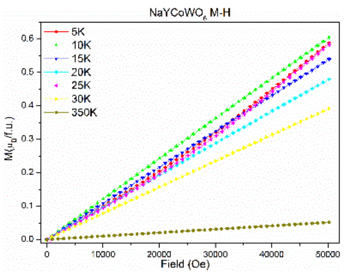

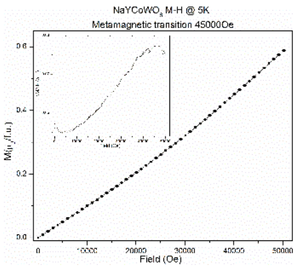

NaLaCoWO$_6$

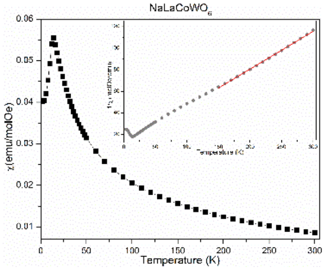

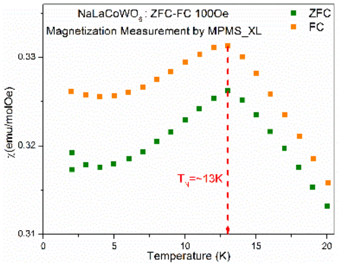

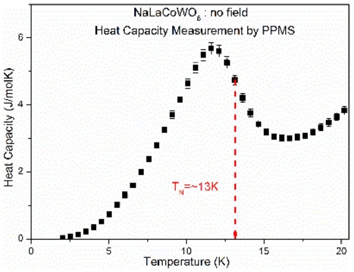

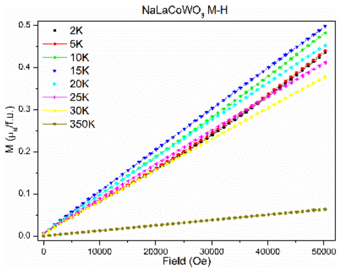

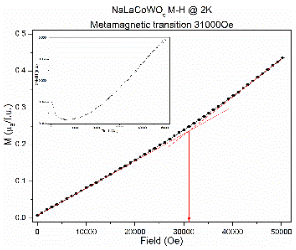

NaPrCoWO$_6$

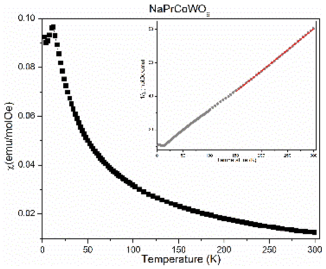

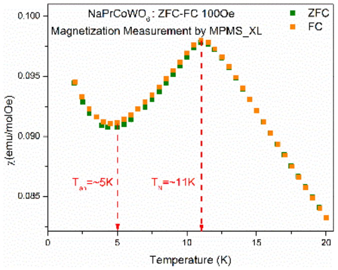

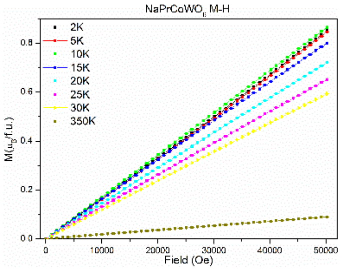

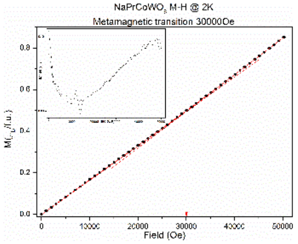

NaNdCoWO$_6$

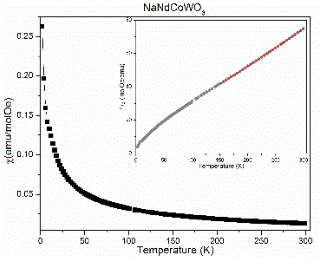

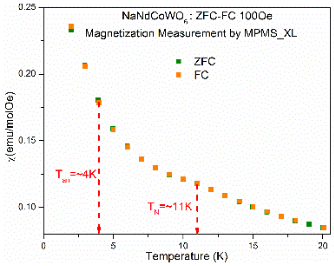

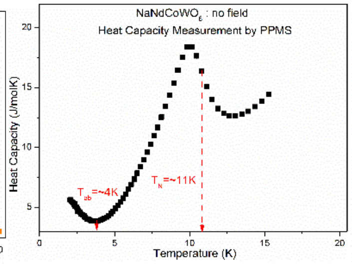

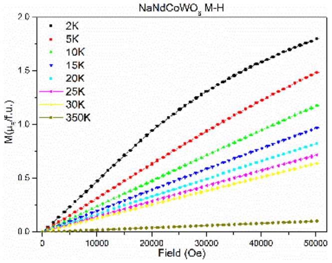

NaSmCoWO$_6$

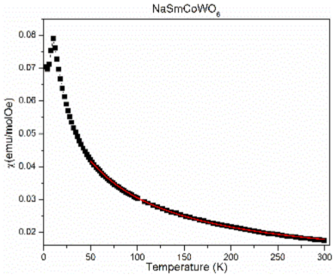

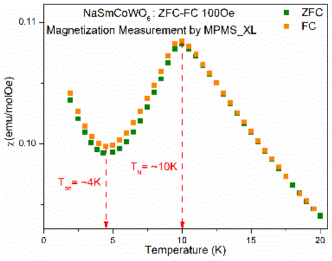

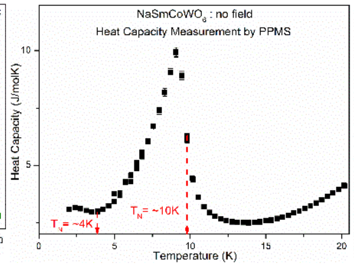

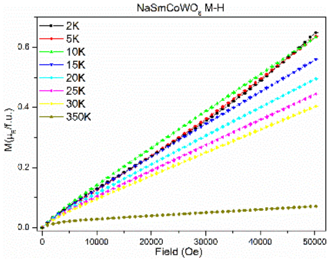

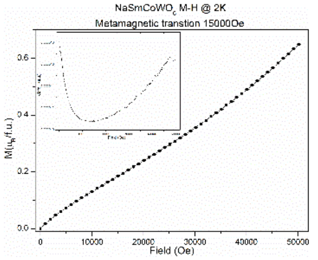

NaEuCowO$_6$

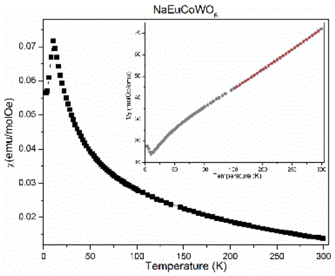

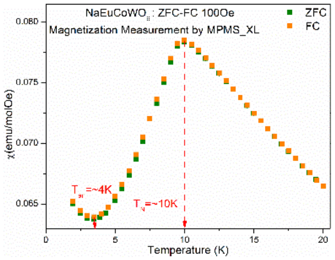

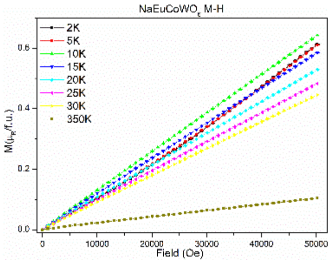

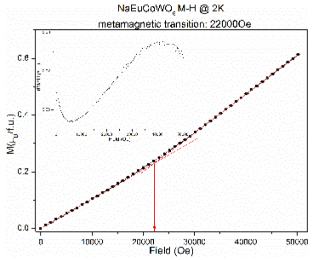

NaGdCoWO$_6$

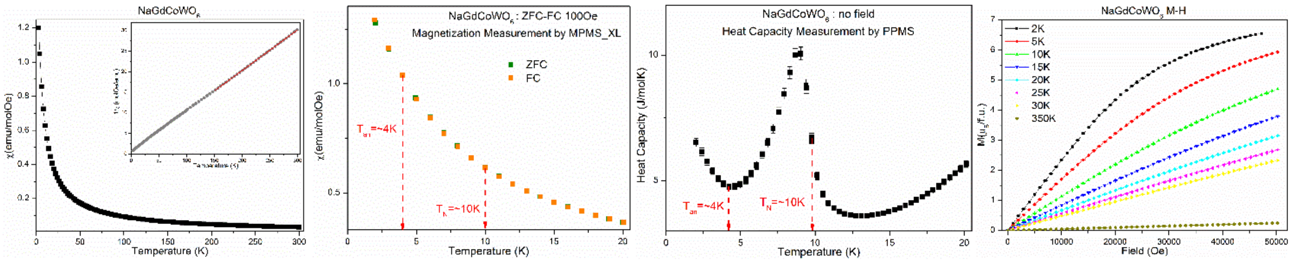

NaTbCoWO$_6$

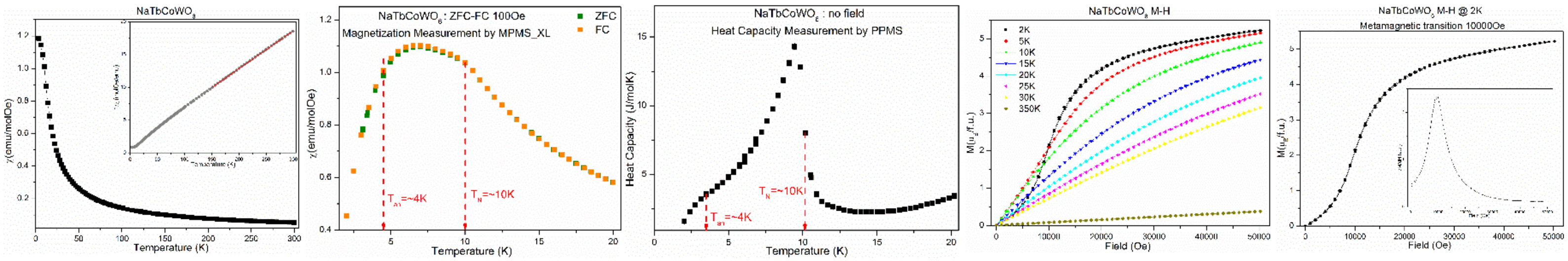

NaDyCoWO$_6$

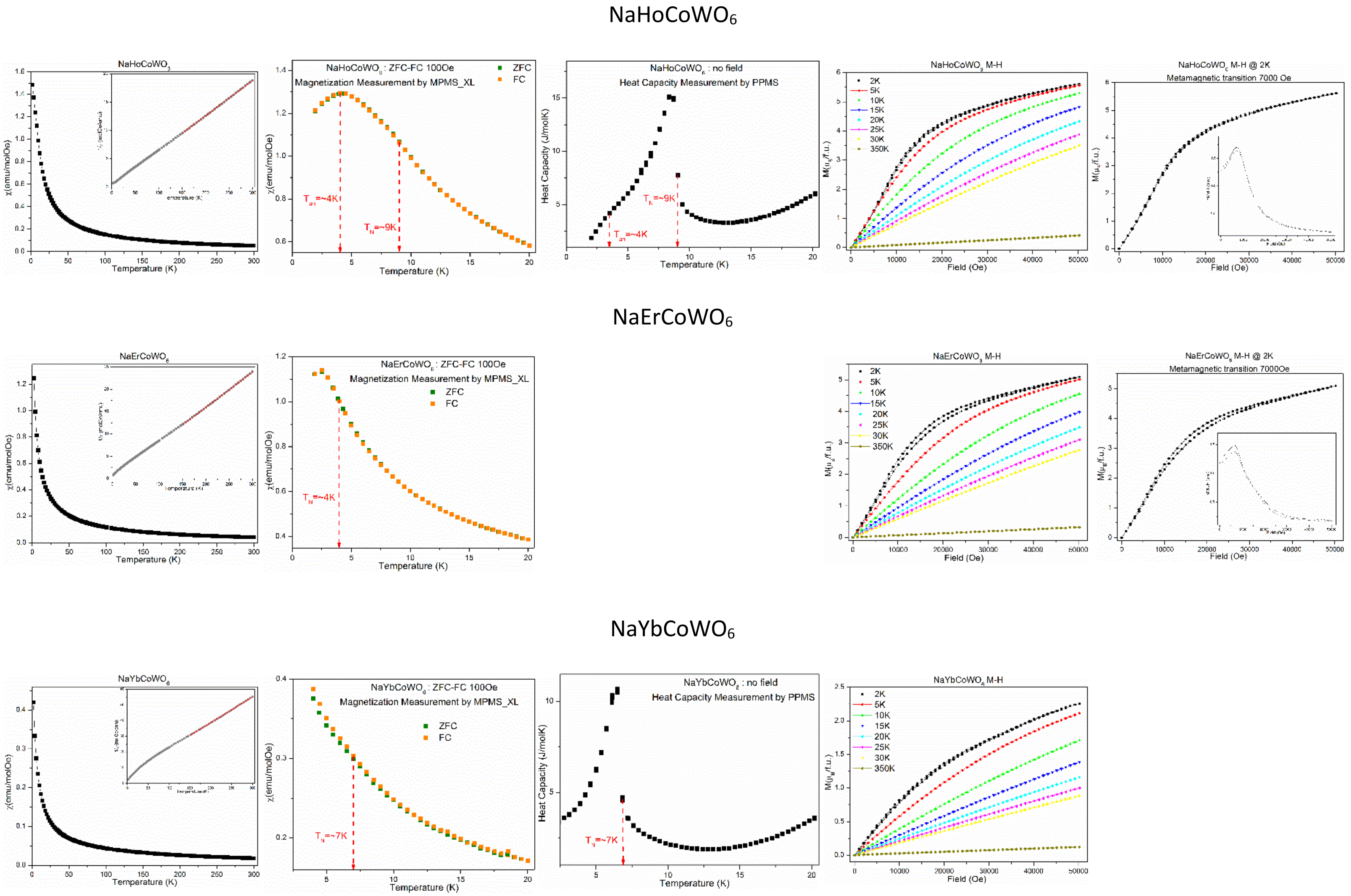

Figure 6.3 The magnetic and heat capacity characaterizations of compounds in the entire series. The left-most column contains the M-T curves (2K-300K, 1T) including the Curie-Weiss fits; the second column on the left contains the ZFC-FC plots where T_N for all compounds is pointed out; the middle column contains the Heat Capacity measurement results for some compounds where the magnetic transition temperatures are pointed out; the second column on the right contains M-H curves at different temperatures (2K, 5K, 10K, 15K, 20K 25K 30K and 350K); the right-most column contains the M-H curves at 2K where a metamagnetic transition is observed and the critical field is defined for some of the compounds.

The plots of T_N as a function of the rare-earth radius are illustrated below in Figure 6.4. The Néel temperature tends to decrease as the rare-earth size decreases.

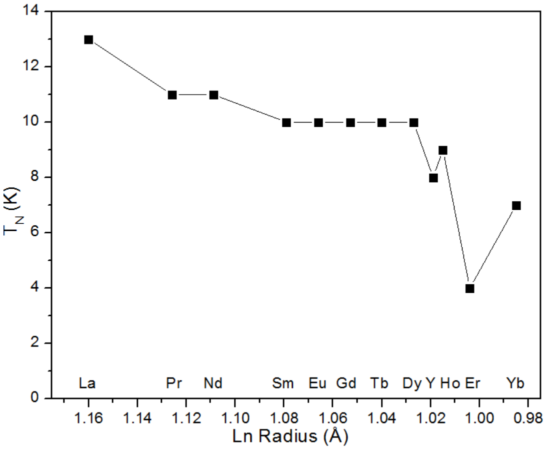

Figure 6.4 The plot of T_N as a function of the size of eight-coordinated rare-earths.

6.2.2 Magnetic Structure Determination

Four compounds, namely $NaYCoWO_6$, $NaLaCoWO_6$, $NaTbCoWO_6$ and $NaHoCoWO_6$, were selected as examples for the magnetic structure determination. These compounds are less neutron absorbing compared to other compounds in this series, and provide a systematic study on compounds without (Y and La) or with (Tb and Ho) magnetic rare-earth cations. In addition, $NaPrCoWO_6$ and $NaNdCoWO_6$ were also measured by NPD, intending to determine their magnetic structures. However, the crystallographic structure of these compounds is still a question of debate due to the presence of 2D modulations (see Chapter 5) making it impossible to determine the magnetic structures.

Long NPD scans were collected a few degrees above and below the magnetic phase transition temperatures of the selected four compounds. These high quality data sets were used to refine the nuclear structure in the paramagnetic phase and the magnetic structure in the AFM phase. In addition, the data were also recorded continuously from 2K up to 300K in order to get a whole view of the magnetic transitions and detect any possible nuclear structure transition. In the following part, the magnetic structure of each compound will be discussed, starting with the simpler ones Y and La and then moving to the more complex compounds Tb and Ho.

6.2.2.1 The Magnetic Structure of $NaYCoWO_6$

The compound $NaYCoWO_6$ has been confirmed to possess the polar structure $P2_1$ by both SXRPD and NPD as discussed in Chapter 4. T_N was determined as ~8K as stated in the last section, the temperature dependent NPD data collected from 2K to 20K is shown in Figure 6.5, once again, confirming that the magnetic transition occurs at ~8K. Long scans were collected at 2K and 20K. The pattern recorded at 20K was refined to get the nuclear structure model for the refinement on the 2K NPD pattern. The lattice parameters for the nuclear structure at 20K are a=5.3140(8) Å, b=5.4919(9) Å, c=7.738(1) Å, and β=90.25(2) °. The refined structure model at 20K is essentially similar to the one obtained from the joint refinement at room temperature. All the magnetic peaks appearing below 8K can be indexed by the commensurate propagation vector **k**= (0.5, 0, 0.5), indicating that the magnetic unit cell doubles along the **a**- and **c**-axes. The determination of the magnetic structure was done by symmetry analysis, following the representation analysis technique described by Bertaut[101]. Calculations were carried out using both the BasIreps program implemented in the FullProf Suite and the SARAh-Representation analysis program. In addition, the magnetic space group was determined with the online program MAXMAGN[114] on the Bilbao Crystallographic Server. For the Co^{2+} cation on the 2a Wyckoff position of the space group *P2₁*, the decomposition of the magnetic representation is $\Gamma_{mag} = 3\Gamma_1^1 + 3\Gamma_2^1$. The basis vectors of the two Irreps are listed in Table 6.2. The magnetic space group associated with both representations is *Pa2₁*.

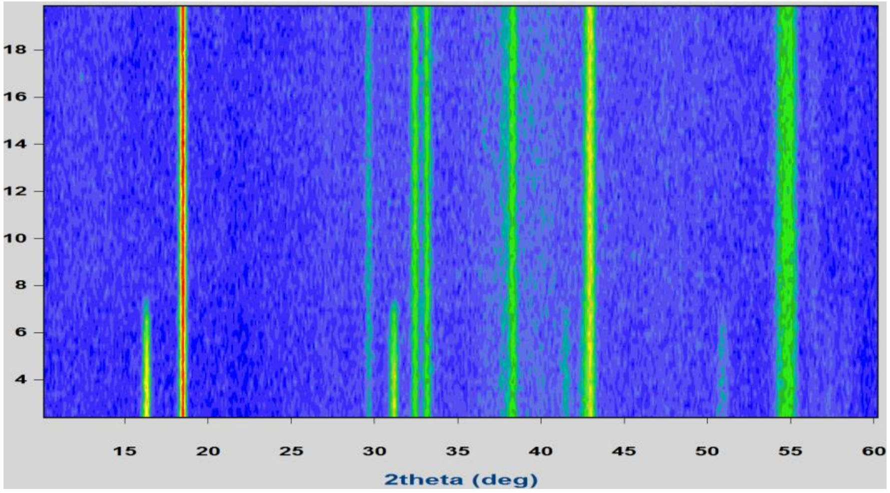

Figure 6.5 Temperature dependence of NPD for $NaYCoWO_6$ as the temperature increasing from 2K to 20K.

Table 6.2 Basis vectors of the irreducible representations for Co^{2+} on the 2a site in the space group *P2₁* with the propagation vector **k**=(0.5, 0, 0.5).[a]

Irrep	Basis Vector	Atom		Irrep	Basis Vector	Atom	
Γ_1	Ψ_1	Co1	1 0 0	Γ_2	Ψ_1	Co1	1 0 0
		Co2	-1 0 0			Co2	1 0 0
	Ψ_2	Co1	0 1 0		Ψ_2	Co1	0 1 0
		Co2	0 1 0			Co2	0 -1 0
	Ψ_3	Co1	0 0 1		Ψ_3	Co1	0 0 1
		Co2	0 0 -1			Co2	0 0 1

[a] Atomic coordinates: Co1= (0.761 0.765 0.250), Co2=(0.239 0.265 0.750)

A systematic study was performed to determine the best model to refine the data. Both representations and various combinations of magnetic moments in different values and directions were tested to figure out the robust component in the refinement. Representation Γ_2 yielded a better description of the peak intensities. The best fit was achieved by a model with the magnetic moment aligned along the **c**-axis (i.e. using only the Ψ_3 basis vector). The corresponding NPD refinement pattern is shown in Figure 6.6. A few extra peaks appeared in the NPD pattern, the strongest of which locates around 29.90° in 2θ. They are attributed to the magnetic reflections of CoO, which is confirmed from the temperature dependent NPD data where the transition temperature was ~291K. The refined nuclear and magnetic structures at 2K are shown in Figure 6.7. The two Co^{2+} cations in the same nuclear unit cell are coupled ferromagnetically, in contrast, the magnetic moments in the adjacent nuclear unit cells along **a**- and **c**- axes are coupled antiferromagnetically. The refined moment takes the value of $2.14(2)\mu_B$, in comparison with the theoretical value of $g_jS=3\mu_B$ for the Co^{2+} ion. The evolution of the Co^{2+} magnetic moment as a function of temperature was derived sequentially from the temperature dependence of NPD data from 2K to 20K and plotted in the inset of Figure 6.6. The magnetic ordering starts to emerge around 8K, which is consistent with the determined T_N = ~8K. The profile of the magnetic moment evolution curve reflects the second-order nature of this magnetic transition.

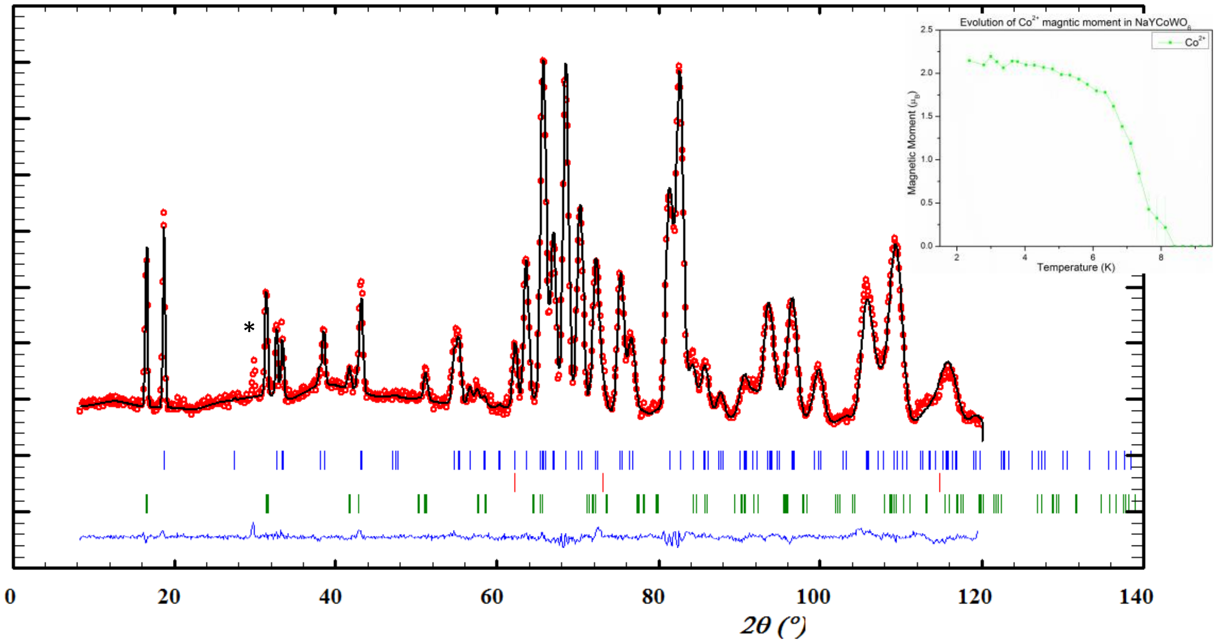

Figure 6.6 The refinement of the $NaYCoWO_6$ NPD pattern collected at 2K with a wavelength of 2.52Å. The observed pattern (red circles), the calculated pattern (black line), and the difference line (blue, at the bottom) are shown. Blue tick marks show allowed (*hkl*) reflections of the nuclear structure of $NaYCoWO_6$. Red tick marks show allowed (*hkl*) reflections of the nuclear structure of the impurity CoO. Green tick marks show allowed magnetic (*hkl*) of the magnetic structure of $NaYCoWO_6$. (χ^2=4.17, R_p=10.4%, R_{wp}=9.46%, R_{nul}=4.63%, R_{mag}=14.7%). The * symbol denotes the position of the magnetic reflection of the CoO impurity. The inset illustrates the Co^{2+} magnetic moment evolution as a function of temperature.

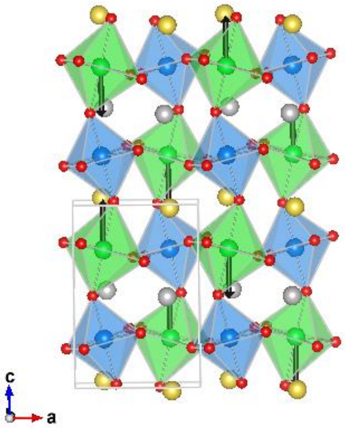

Figure 6.7 The magnetic and nuclear structures of NaYCoWO$_6$. The magnetic structure is described by the arrangement of magnetic moments (black arrows), spheres in the nuclear structure are Na (yellow), Y (grey), Co (green), W (blue) and O (red).

6.2.2.2 The Magnetic Structure of NaLaCoWO$_6$

NaLaCoWO$_6$ acts as the other non-magnetic Ln reference, together with NaYCoWO$_6$. However, the size of La is very different from that of Y, so that La is more a reference for compounds in the larger rare-earth region. As discussed before, the high temperature phase of NaLaCoWO$_6$ was assigned the space group *C2/m*, while the low temperature phase (below 100K) was determined as $P2_1$. The magnetic transition temperature was determined as ~13 K, which was confirmed by the temperature dependence of NPD data from 2K to 20K shown in Figure 6.8. Long scans were collected at 20K and 2K for proper nuclear and magnetic structure refinement. The refined structure model at 20K is essentially similar to the one obtained from the joint refinement at 100K in the low temperature phase of $P2_1$. The refined lattice parameters at 20 K are: a=5.530(2) Å, b=5.524(2) Å, c=7.8815(9) Å, and β=90.29(1) °.

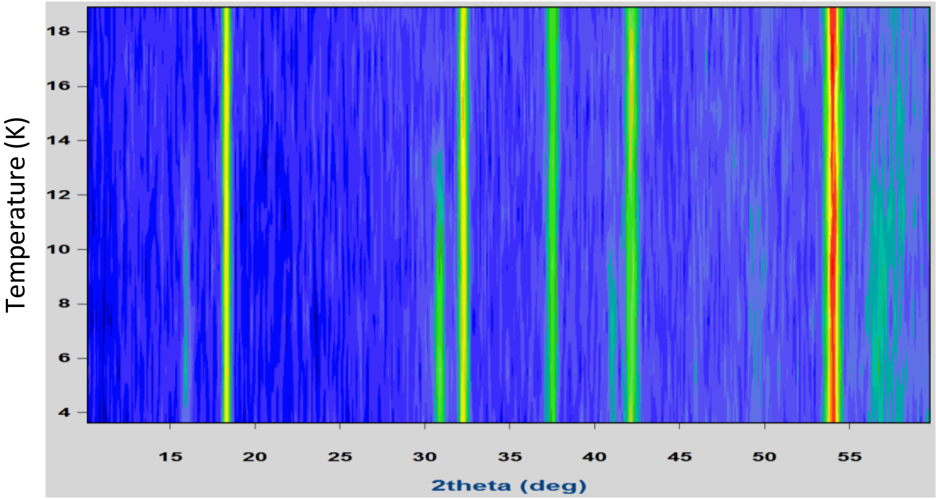

Figure 6.8 The temperature dependent NPD data of NaLaCoWO$_6$ as the temperature increasing from 2K to 20K.

The magnetic peaks in the 2K pattern can be indexed by either of the two propagation vectors: **k**= (0.5, 0, 0.5) or **k**= (0, 0.5, 0.5). It is difficult to rule out one propagation vector with respect to the other by a LeBail fitting, because of the pseudo-tetragonal nature of the unit cell and the limited resolution of neutron diffraction. Satisfactory refinements were obtained with models derived from both k-vectors. We choose to present here the magnetic structure model of highest symmetry compatible with our data. Indeed, the magnetic space group analysis performed by the online program MAXMAGN[114] yielded that the magnetic space group for **k**=(0.5, 0, 0.5), *Pa*2_1, is of higher symmetry than the one for **k**=(0, 0.5, 0.5), *Ps1*. In the magnetic space group *Pa*2_1 the atoms Co1 and Co2 are symmetrically linked (3 parameters) whereas they are independent in *Ps1* (6 parameters). To keep the refinement parameters as few as possible and the higher symmetry, all following discussions concerning the magnetic structure of $NaLaCoWO_6$ will be focused on the models described by the propagation vector **k**= (0.5, 0, 0.5). The representation analysis is the same as for $NaYCoWO_6$.

In order to figure out the better Irrep, various combinations of magnetic moments in different values and directions were tested and compared. However, several models belonging to both representations give a similar fit quality. We present in Figures 6.9 and 6.10 one of these satisfactory magnetic structure models with the corresponding refinement.

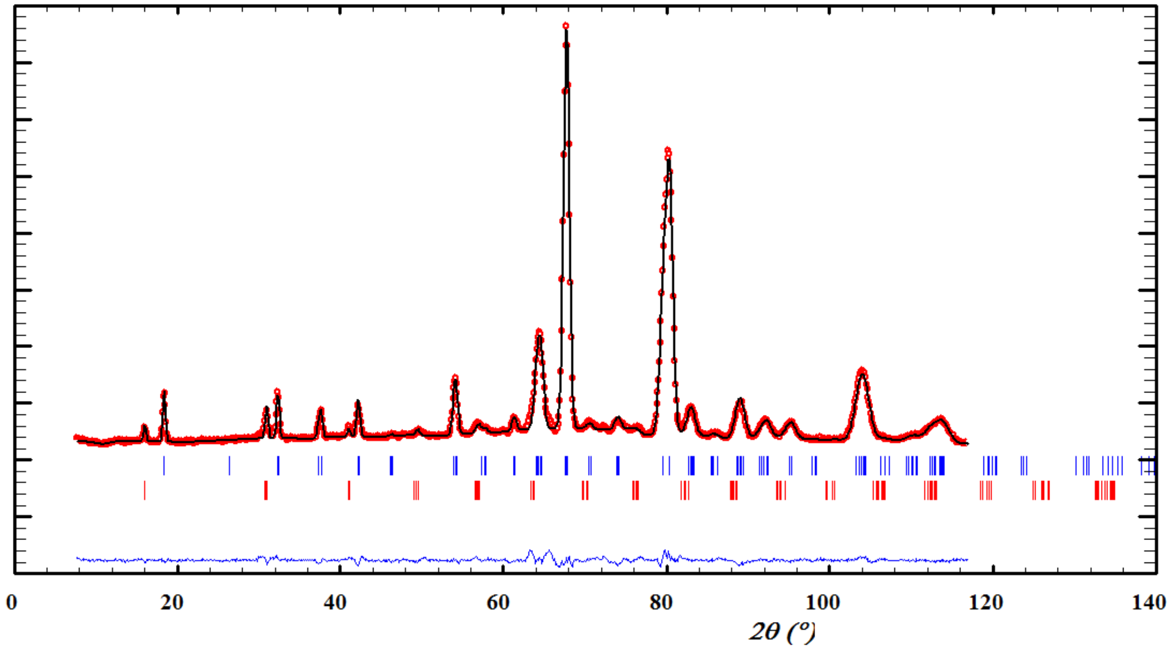

Figure 6.9 The refinement of the $NaLaCoWO_6$ NPD pattern collected at 2K with the propagation vector k= (0.5, 0, 0.5) and a wavelength of 2.52Å. The magnetic structure model on the basis of Γ_2 (χ^2=2.98, R_p=8.75%, R_{wp}=8.25%, R_{nul}=3.18%, R_{mag}=17.3%). The observed pattern (red circles), the calculated pattern (black line), and the difference line (blue, at the bottom) are shown. Blue tick marks show allowed (*hkl*) reflections of the nuclear structure of $NaLaCoWO_6$. Red tick marks show allowed magnetic (*hkl*) of the magnetic structure of $NaLaCoWO_6$.

This magnetic structure model on the basis of Γ_2 is described by the moment components Mx=1.00(2) μ_B and My=0.33(4) μ_B, where the moment along the **c**-axis is zero. The resulting total magnetic moment is 1.05 μ_B in comparison with the theoretical value of 3μ_B for the Co^{2+} ion. The two Co^{2+} in the same nuclear structure unit cell are coupled ferromagnetically along the **a**-axis and antiferromagntically along the **b**-axis. While the Co^{2+} ions in adjacent nuclear structure unit cells are antiferromagnetically ordered along the **a**- and **c**-axes.

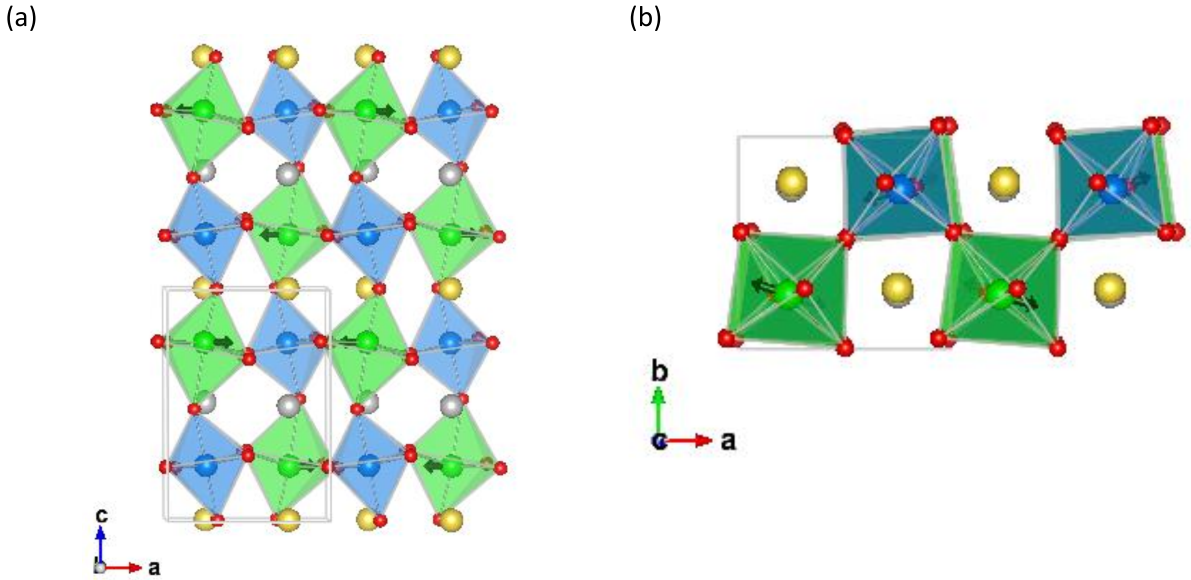

Figure 6.10 The magnetic and nuclear structures of $NaLaCoWO_6$. The magnetic structure is described by the arrangement of magnetic moments (black arrows), viewed along (a) the b-axis and (b) the c-axis. Spheres in the nuclear structure are Na (yellow), La (grey), Co (green), W (blue) and O (red).

6.2.2.3 The Magnetic Structure of $NaTbCoWO_6$

$NaTbCoWO_6$ has been determined to crystallize in the polar space group $P2_1$, with the magnetic transition metal cation Co^{2+} at the B-site and the magnetic rare-earth cation (Tb^{3+}) at the A'-site which is different from the former two compounds discussed. T_N was determined to be ~10K which is confirmed from the NPD data collected from 2K to 20K as shown in Figure 6.11, long scans were recorded at 16K and 2K, above and below the transition temperature in order to properly refine the nuclear and magnetic structures, respectively. The nuclear structure refined from the NPD data at 16K is very similar to the one at room temperature, and the lattice parameters are: a=5.3623(3) Å, b=5.4855(3) Å, c=7.7690(5) Å, and β=90.269(8) °. The magnetic reflections can all be indexed by the propagation vector **k**=(0.5, 0, 0.5). Because Co^{2+} and Tb^{3+} sit at the same Wyckoff position (2a), the representation analysis gives the same decomposition in irreducible representations (Irrep), Γ_1 and Γ_2 for both sites (Table 6.2). The corresponding magnetic space group is P_a2_1.

In order to determine a model describing the observed NPD pattern well, various combinations of initial magnetic parameters were tested and refined. Co and Tb were constrained to belong to the same representation. There are several models that can fit the NPD data well, a model among the best ones is picked to show here. Nevertheless, as stated above, the one shown here is only one example of them. The model picked here is on the basis of Γ_2, the refinement pattern is shown in Figure 6.12. Both Co and Tb have magnetic moments along three coordinate axes. For Co, Mx=-1.59(5) μ_B, My=-0.85(7) μ_B and Mz=-0.80(9) μ_B, resulting in a total magnetic moment of 1.97 μ_B. While for Tb, Mx=7.59(3) μ_B, My=3.89(8) μ_B and Mz=2.0(1) μ_B, resulting in a total magnetic moment of 8.76 μ_B in comparison with the theoretical value of 9.72 μ_B. The evolution of the Co^{2+} and Tb^{3+} magnetic moments as a function of temperature was derived sequentially from the temperature dependent NPD data from 2K to 16K and plotted in the inset of Figure 6.12. Magnetic peaks start to emerge around 10K, which is consistent with the determined T_N = ~10K. The magnetic moments of the Co^{2+} sublattice develop below 10K and saturate rapidly (the value is

$2\mu_B$ at 2K). The ordering of the Co^{2+} sublattice polarizes the Tb^{3+} sublattice as shown in Figure 6.12. The polarized moment of Tb^{3+} at 2K is around $8.5\mu_B$ with no sign of saturation. The corresponding magnetic structure together with the nuclear structure is illustrated in Figure 6.13.

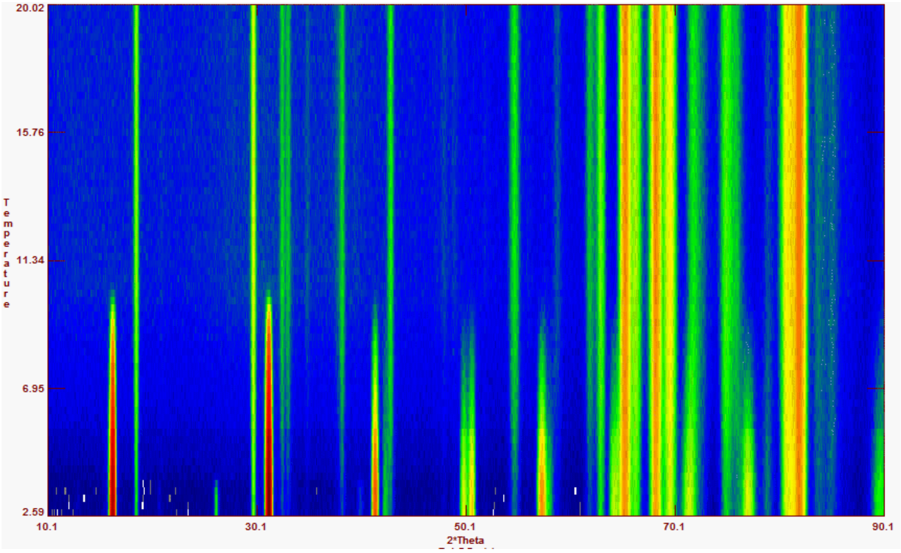

Figure 6.11 Temperature dependent NPD data collected from 2K to 16K for $NaTbCoWO_6$.

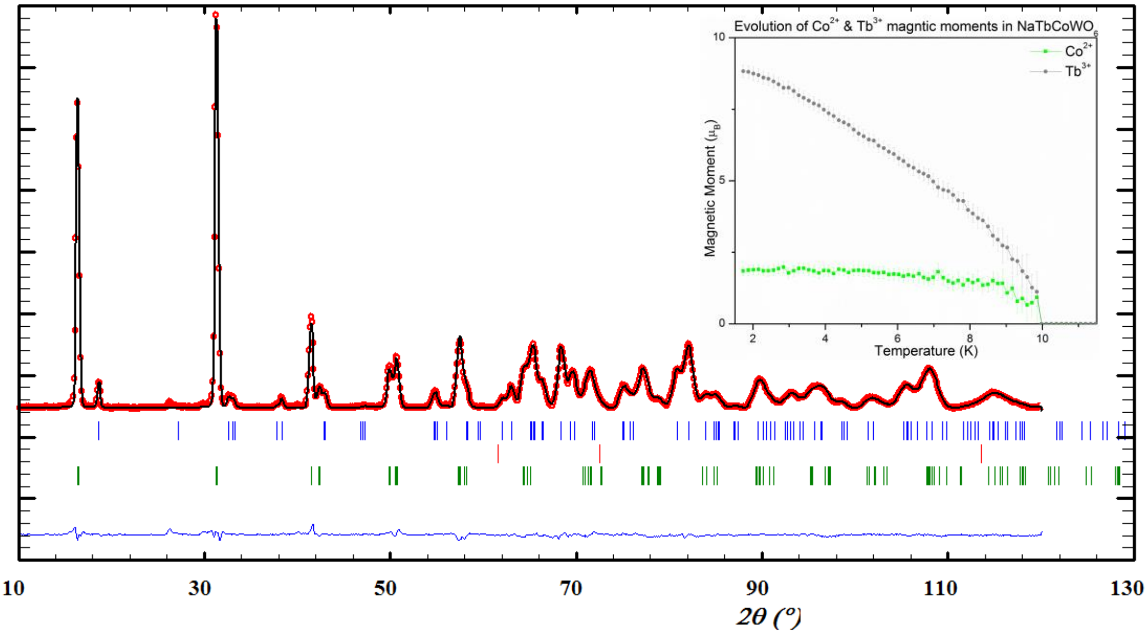

Figure 6.12 The refinement of the $NaTbCoWO_6$ NPD pattern collected at 2K with the propagation vector k= (0.5, 0, 0.5) and a wavelength of 2.52Å. The magnetic structure model on the basis of Γ_2 (χ^2=201, R_p=5.93%, R_{wp}=6.80%, R_{nul}=3.58%, R_{mag}=4.35%). The observed pattern (red circles), the calculated pattern (black line), and the difference line (blue, at the bottom) are shown. Blue tick marks show allowed (*hkl*) reflections of the nuclear structure of $NaTbCoWO_6$. Red tick marks show allowed (*hkl*) reflections of the nuclear structure of CoO, and green tick marks show magnetic (*hkl*) of the magnetic structure of $NaTbCoWO_6$. The inset illustrates the Co^{2+} and Tb^{3+} magnetic moment evolution as a function of temperature.

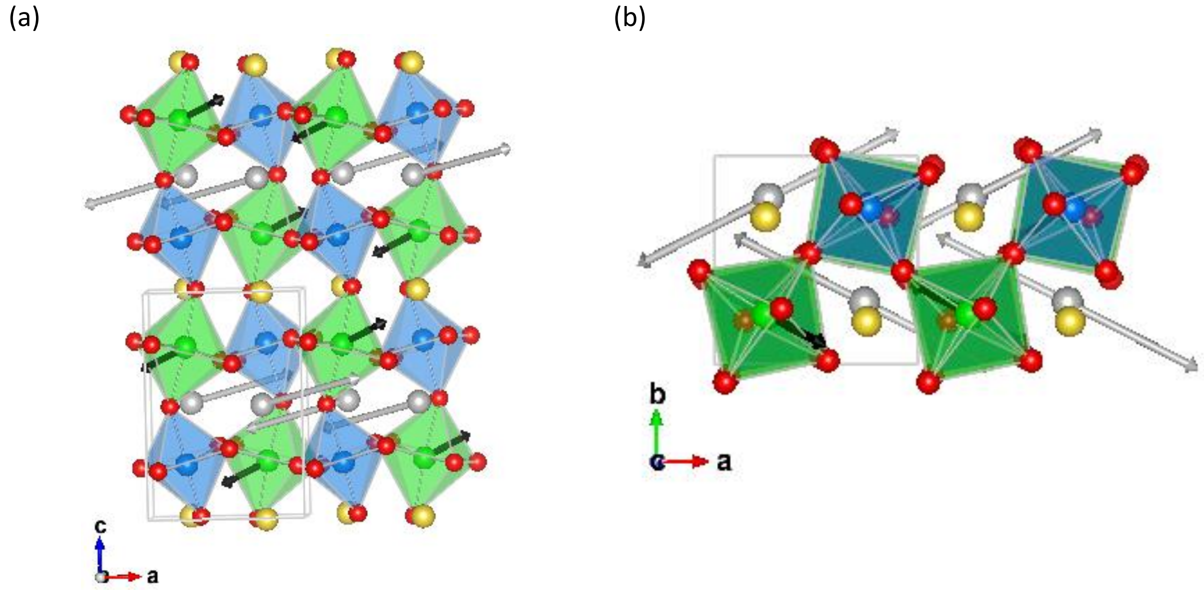

Figure 6.13 The magnetic and nuclear structures of $NaTbCoWO_6$. The magnetic structure is described by the arrangement of magnetic moments (Co: black arrows; Tb: grey arrows), viewed along (a) the b-axis and (b) the c-axis. Spheres in the nuclear structure are atoms Na (yellow), Tb (grey), Co (green), W (blue) and O (red).

6.2.2.4 The Magnetic Structure of $NaHoCoWO_6$

$NaHoCoWO_6$ provides another example which has two magnetic sites where Co^{2+} ions occupy the B-site and Ho^{3+} ions the A'-site. This compound has been assigned the polar space group $P2_1$, and its magnetic transition temperature T_N is determined to be ~9K which is further confirmed from the NPD data collected from 2K to 15K as shown in Figure 6.14. In order to properly refine the nuclear and magnetic structures of $NaHoCoWO_6$, long scans were recorded at 15K and 2K, above and below the transition temperature. The nuclear structure refined from the NPD data at 15K are very similar to the one at room temperature, respectively, and the lattice parameters are: a=5.3208(4) Å, b=5.4960(4) Å, c=7.7470(6) Å, and β=90.27(1) °. All the magnetic peaks can be indexed with the propagation vector **k**=(0.5, 0, 0.5). The representation analysis proposed, once again, the same irreducible representations (Irrep) Γ_1 and Γ_2 for both sites (Table 6.2).

In order to determine a model describing the observed NPD pattern well, various combinations of initial magnetic parameters were tested and refined. A model among the best ones is picked to be shown here. The model picked here is on the basis of Γ_1, the refinement pattern is shown in Figure 6.15. For Co, Mx=-0.85(8) μ_B, My=1.86(6) μ_B and Mz= 0 μ_B, resulting in a total magnetic moment of 2.04 μ_B. While for Ho, Mx=2.10(9) μ_B, My=-4.11(7) μ_B and Mz=5.01(7) μ_B, resulting in a total magnetic moment of 6.81 μ_B in comparison with the theoretical value of 10.6 μ_B. The evolution of the Co^{2+} and Ho^{3+} magnetic moments as a function of temperature was also derived sequentially from the temperature dependence of NPD data from 2K to 15K and plotted in the inset of Figure 6.15. The magnetic ordering starts to emerge around 9K, which is consistent with the determined T_N = ~9K. Quite similar to the $NaTbCoWO_6$ case, the sublattice of Co^{2+} orders below the Néel temperature at 9K, and saturates quickly to a moment close to 2μ_B. The ordering of the Co^{2+} sublattice polarizes the Ho^{3+} sublattice as shown in Figure 6.15, whose magnetic moment increases almost linearly when decreasing the temperature with no sign of saturation until 2K. At 2K, the refined moment of Ho^{3+} is around 6.8μ_B, in comparison with the theoretical saturated magnetic moment of 10.60 μ_B. The corresponding magnetic structure together with the nuclear structure is illustrated in Figure 6.16.

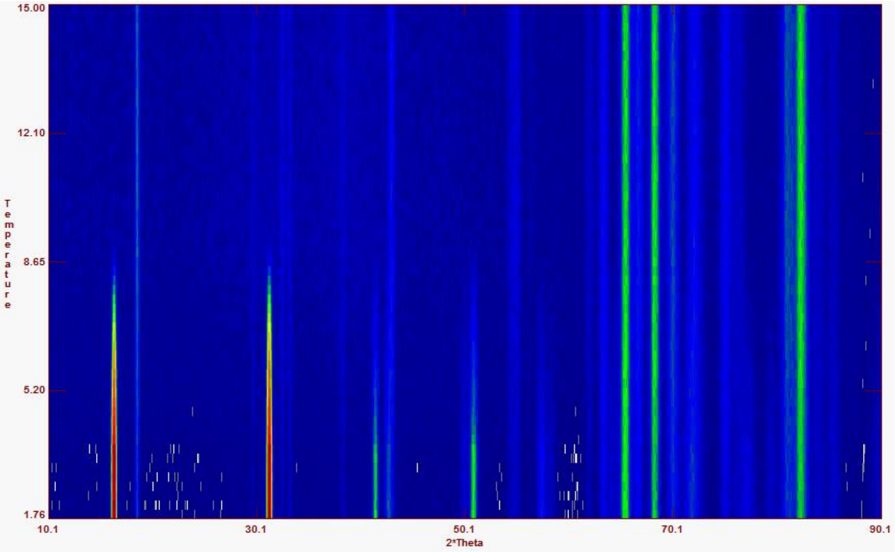

Figure 6.14 Temperature dependent NPD data collected from 2K to 15K for $NaHoCoWO_6$.

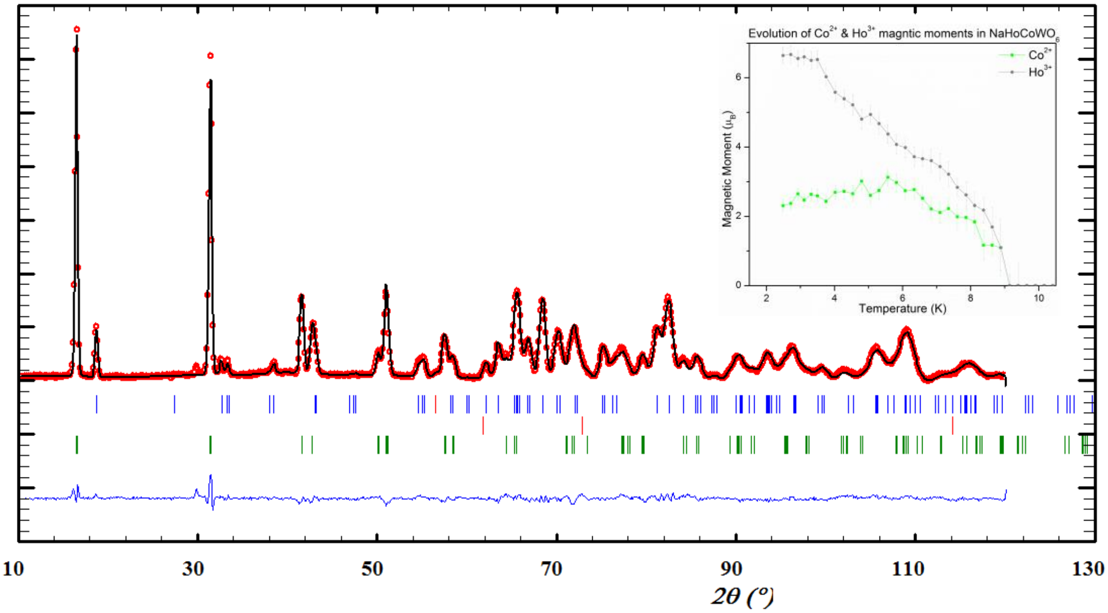

Figure 6.15 The refinement of the $NaHoCoWO_6$ NPD pattern collected at 2K with the propagation vector k= (0.5, 0, 0.5) and a wavelength of 2.52Å. The magnetic structure model on the basis of Γ_1 (χ^2=90.5, R_p=7.83%, R_{wp}=7.78%, R_{nul}=3.97%, R_{mag}=5.97%). The observed pattern (red circles), the calculated pattern (black line), and the difference line (blue, at the bottom) are shown. Blue tick marks show allowed (*hkl*) reflections of the nuclear structure of $NaHoCoWO_6$. Red tick marks show allowed (*hkl*) reflections of the nuclear structure of CoO, and green tick marks show magnetic (*hkl*) of the magnetic structure of $NaHoCoWO_6$. The insets illustrates the Co^{2+} and Ho^{3+} magnetic moment evolution as a function of temperature.

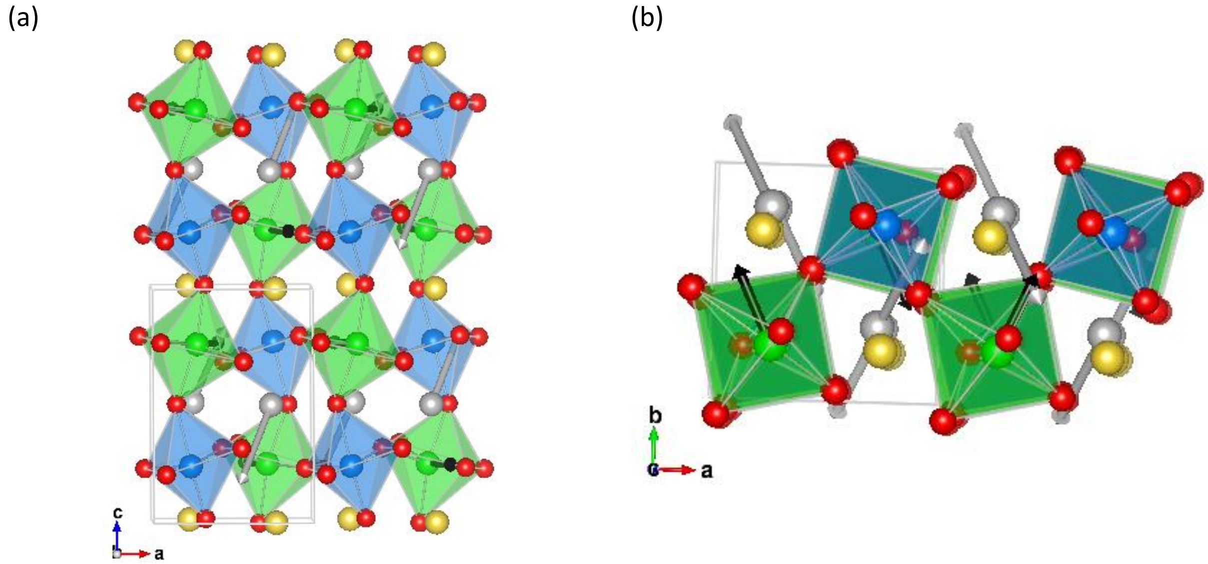

Figure 6.16 The magnetic and nuclear structures of $NaHoCoWO_6$. The magnetic structure is described by the arrangement of magnetic moments (Co: black arrows; Tb: grey arrows), viewed along (a) the b-axis and (b) the c-axis. Spheres in the nuclear structure are Na (yellow), Ho (grey), Co (green), W (blue) and O (red).

6.3 Magneto-(Di)-Electric Properties

The compounds Y, La, Tb and Ho were selected for the dielectric and pyroelectric measurements under magnetic field. The temperature dependence of the dielectric permittivity of the samples Y, La, Tb and Ho were measured at different magnetic fields, namely 0T, 2T, 4T, 6T, and 8T, respectively. The temperature was scanned such as 3K-30K-3K. For the compounds Y and Ho, sharp peaks appear when the temperature goes through T_N in all magnetic field conditions (see Figure 6.17 (a) and (c)), regardless if the process is cooling down or heating up. With increasing the magnetic field, the magnetic ordering temperature is reduced and the peak in the dielectric permittivity is shifted in temperature accordingly. For the Tb compound, even though there is no sharp peak at T_N, it is easily found that there are anomalies at this temperature (see Figure 6.17(b)). All these observations indicate that the magnetic ordering makes a difference in the dielectric permittivity, which means the two properties are coupled, being the signature of the so-called magneto-dielectric coupling. For the La compound, no clear anomaly was seen at the magnetic ordering transition (Figure 6.17(d)).

A larger temperature range from 3K to 300K was also measured for these samples in the absence of the magnetic field, however, no features of any other phase transition was observed for any of them.

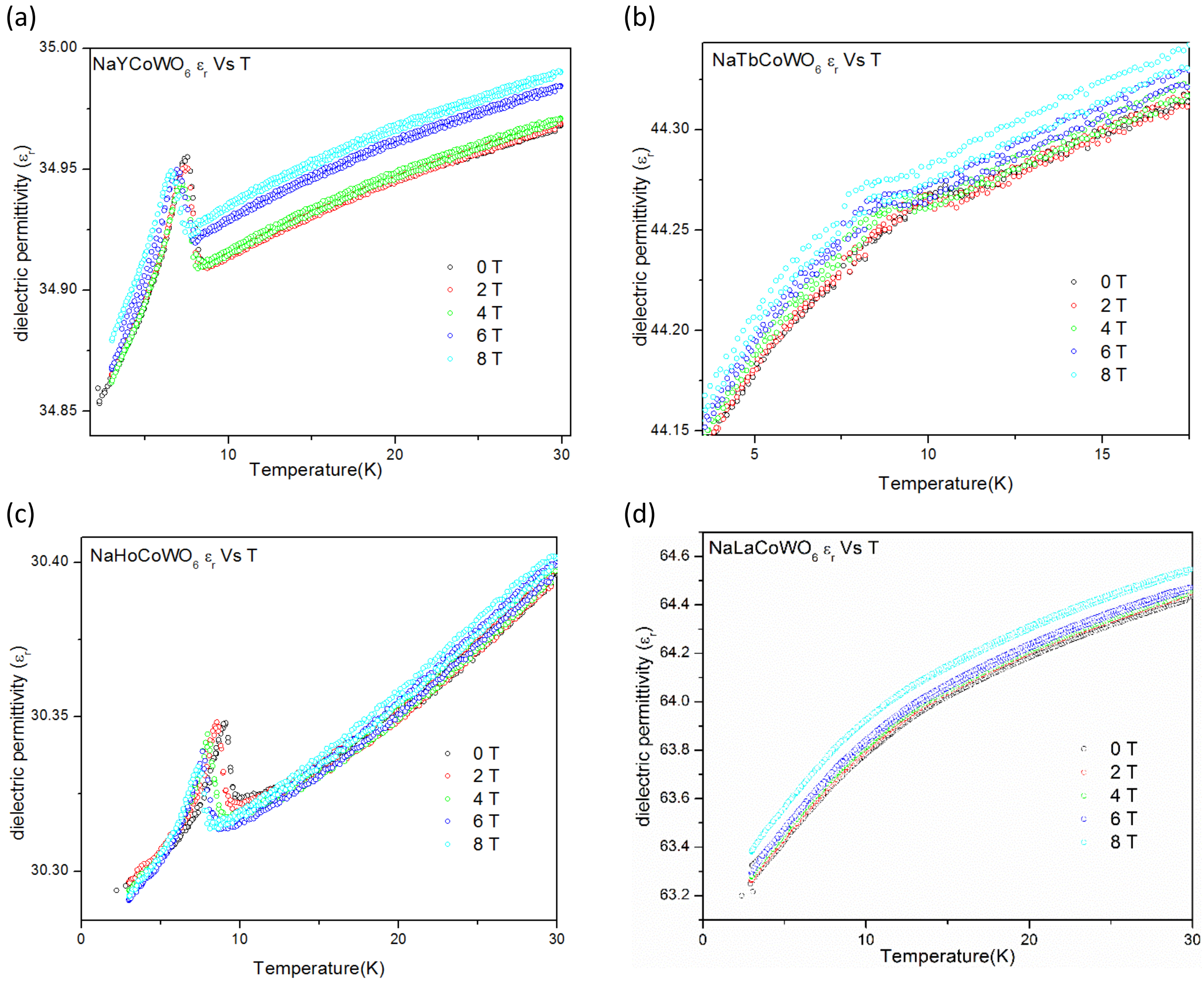

Figure 6.17 The dielectric permittivity of (a) NaYCoWO$_6$, (b) NaTbCoWO$_6$ and (c) NaHoCoWO$_6$, in different magnetic fields, namely, 0T, 2T, 4T, 6T, and 8T, respectively. The temperature cycling is between 3K and 30K.

The magnetic field dependence of the capacitance at fixed temperatures was also measured for the samples Y, Tb, and Ho. The samples were measured at 4K, 6K, 8K, and 10K with the magnetic field cycling from 8T to -8T. The resultant magneto-capacitance which is defined as the relative variation of the capacitance with magnetic field [C(H)-C(0T)]/C(0T)) is plotted in Figure 6.18. These three samples present magneto-capacitive effects that change as a function of temperature. The evolution of the magneto-capacitance with field is complex and non-monotonic. For all the samples the maximum of the magneto-capacitance effect is close to the AFM transition temperature.

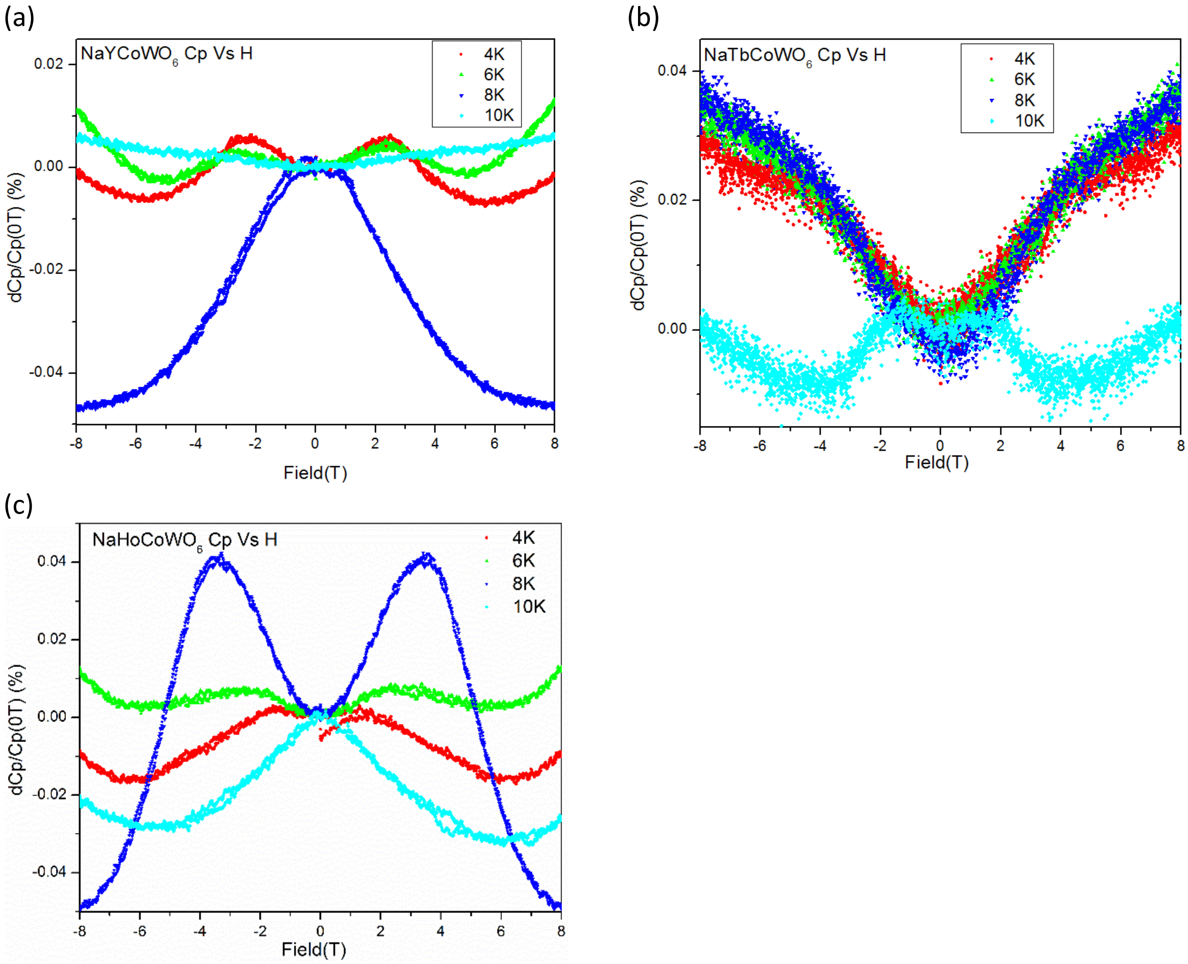

Figure 6.18 The magneto-capacitance plots of (a) NaYCoWO$_6$, (b) NaTbCoWO$_6$ and (c) NaHoCoWO$_6$, at 4K, 6K, 8K, and 10K, respectively. The magnetic field is scanned between 8T and -8T.

To determine if electrical polarization is associated with the magnetic ordering, pyroelectric measurements were carried out on NaYCoWO$_6$ and NaHoCoWO$_6$, as they demonstrated clear magneto-dielectric coupling. However, the pyroelectric current was only detected in NaYCoWO$_6$ and not in NaHoCoWO$_6$. The measurements were performed in various magnetic fields between 0 T and 8 T with an electric poling field of approximately 400KV/m. Under each magnetic field, two measurements were conducted by applying the electric field in the opposite direction, respectively. Figure 6.19 (a) and (b) show the collected pyroelectric current signal and its dependence on the applied magnetic field. Figure 6.19 (a) shows the pyroelectric current measurements with a voltage of -200V. Clearly, the integrated pyroelectric current signal is dependent on the magnetic field, increasing the magnetic field reduces slightly the polarization and the temperature is shifted towards lower temperatures. A similar trend is also observed when the voltage is +200V as shown in Figure 6.19 (b), however, in this case the measured signal is smaller and more noisy. Note thateven though the applied voltages are in the opposite directions in the cases of Figure 6.19 (a) and (b), the measured pyroelectric current is in the same direction, which indicates that the polarization direction was not switched under voltages with opposite sign.

In order to obtain the polarization value, the pyroelectric current was integrated as a function of temperature as shown in Figure 6.19 (c) and (d). Once again, the magnetic field dependent polarization is clearly demonstrated. The maximum measureable polarization is ~0.06 μC/m^2 under the voltage -200V and ~0.10 μC/m^2 under the voltage +200V.

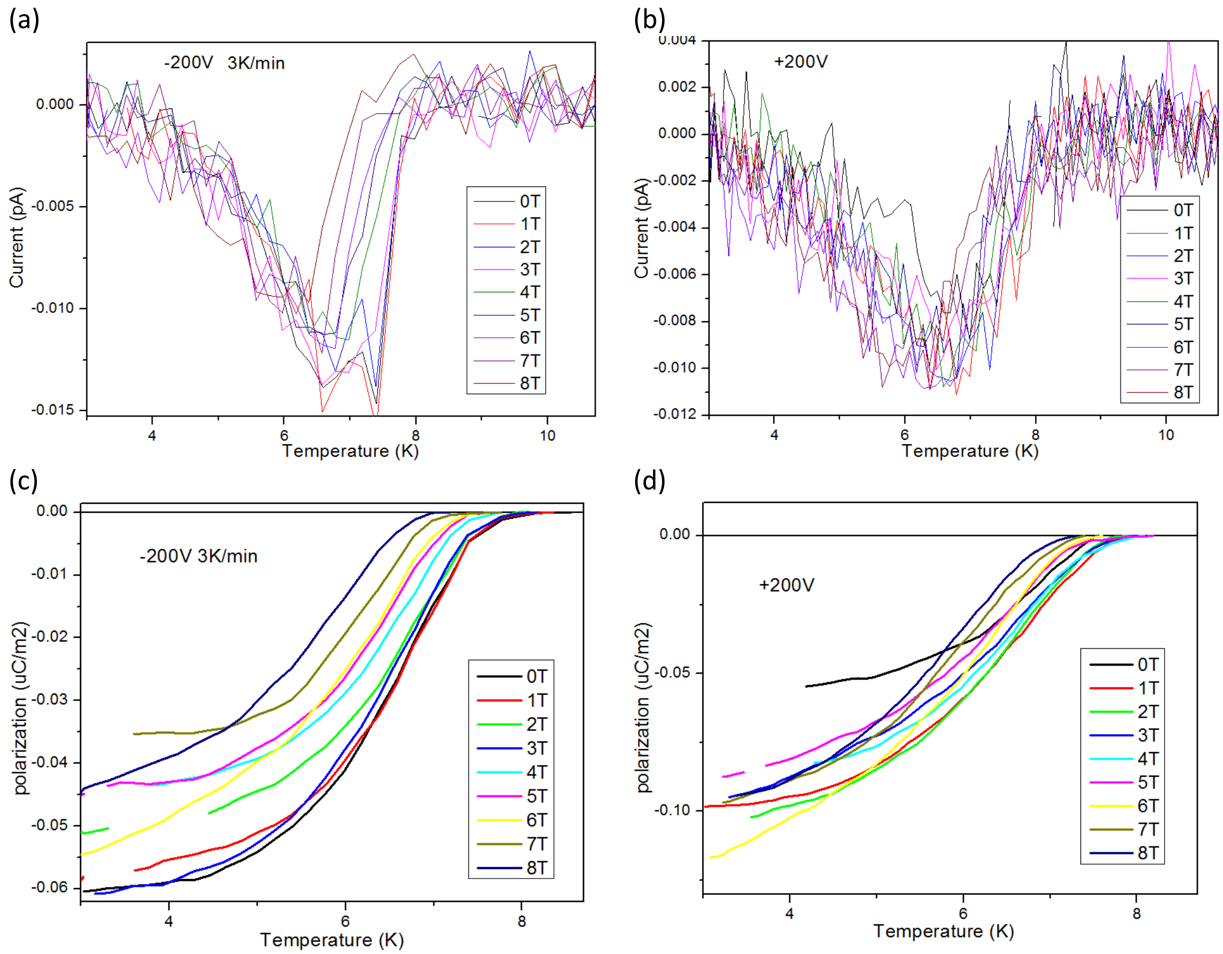

Figure 6.19 The pyroelectric current measurements of NaYCoWO$_6$ with (a) -200V and (b) +200V under various magnetic fields (0T, 1T, 2T, 3T, 4T, 5T, 6T, 7T, 8T), the temperature raising rate is 3K/min; the corresponding derived polarizations from integrating the pyroelectric current signal are plotted in (c) and (d), respectively, as a function of temperature.

6.4 Conclusions

Magnetic and magneto-(di)-electric properties were experimentally characterized for the entire series of NaLnCoWO$_6$ compounds. All NaLnCoWO$_6$ compounds order antiferromagnetically below T_N which range from 4K to 13K. Curie-Weiss fits were performed to all compounds, yielding reasonable effective magnetic moments compared to the theoretical ones. Weiss temperatures were all determined to be negative further indicating that antiferromagnetic interactions are dominant in these systems. Magnetic structures were determined for NaLnCoWO$_6$ (Ln= Y, La, Tb, and Ho), providing two more examples about doubly ordered perovskites without and with magnetic rare-earth cations at the A'-site, respectively. For each compound, the magnetic space group was analyzed and a model among the best ones is discussed, nevertheless, there could be many models well explaining the observed NPD data. To determine unambiguously the magnetic structure of such materials, single crystal samples are needed. Sequential refinements on the temperature dependence of NPD data were performed for NaLnCoWO$_6$ (Ln=Y, Tb, Ho) to extract the magnetic moments evolution as a function of temperature. The Co^{2+} magnetic moment evolution curves show a classical second-order transition behavior. The moment evolutions of Tb^{3+} and Ho^{3+} demonstrated how the magnetic Ln cation is polarized by the magnetic ordering of the Co^{2+} sublattice.

Dielectric measurements were carried out on $NaLnCoWO_6$ (Ln=Y, La, Tb, and Ho). Magneto-dielectric coupling was experimentally observed in compounds $NaLnCoWO_6$ (Ln= Y, Tb, and Ho), which is indicated by an anomaly around the T_N in the Cp-T curve. The coupling of Y and Ho seems stronger than Tb. The dielectric measurements were also carried out at various magnetic fields up to 8T for Y, Tb, and Ho, as a function of temperature. The magneto-dielectric coupling was observed under each magnetic field, and the observed peaks shifted with the applied magnetic fields which further confirmed the magnetic and dielectric properties are coupled. In addition, magneto-capacitance plots were derived for all three samples, showing the effect of the applied magnetic field on the dielectric property at some fixed temperatures. Polarization was derived for Y and Ho from pyroelectric current measurement, however, only the $NaYCoWO_6$ compound demonstrates a polar behavior linked to the magnetic ordering which cannot be switched. The detectable polarization is rather small (~0.1 $\mu C/m^2$), but, this is the first evidence that electric polarization can be induced by the magnetic ordering in the $AA'BB'O_6$ class materials.

With all these observations, there are lots of questions to answer. Even if the compounds $NaLnCoWO_6$ (Ln= Y, La, Tb, Ho) share the same structure within the polar space group *P2₁* and order all antiferromagnetically, they display, however, very different magneto-electric coupling. The influence of the sites where the magnetic cations sit (A' or B) needs to be elucidated. Systematic studies by electric measurements and detailed structural studies across the magnetic transition may help to solve these issues.

Chapter 7: Summary and Perspectives

This thesis work focuses on exploring new magneto-electric multiferroic materials based on the very recently recognized HIF mechanism. Two classes of materials were concentrated on, namely, and the Ruddlesden-Popper oxides $NaRMO_4$ (R=Y, La; M= Mn, Cr) and the doubly ordered perovskites $AA'BB'O_6$. The study covers the synthesis of new materials, a structural study by X-ray powder diffraction, neutron powder diffraction, electron diffraction and electron microscopy, and characterizations of physical properties such as the magnetic, dielectric and themagneto-electric properties of these new phases.

Concerning the synthesis, attempts were made to introduce magnetic ions (Mn and Cr) into the Ruddlesden-Popper oxides $NaRTiO_4$ (R=Y, La), in order to promote a magnetic order in these compounds which have been confirmed to lift inversion symmetry by octahedral rotations. However, all these attempts including HT-HP synthesis failed to yield the target compounds. We turned to the doubly ordered perovskite family $NaLnCoWO_6$ (Ln=Y, La, Pr, Nd, Sm, Eu, Gd, Tb, Dy, Ho, Er, and Yb) which was little explored. Three compounds Ln=La, Pr, and Nd were obtained before and can be synthesized under conditions of high temperature and ambient pressure. Starting with the nitrate route[46] reported before, we did not get a pure $NaLaCoWO_6$ sample. After the optimization of parameters such as temperature and starting materials, a new synthesis method based on the carbonate route was found for $NaLaCoWO_6$. The other nine new phases (with smaller rare-earths) were obtained under HT-HP synthesis conditions. Intensive work was done to these nine compounds on optimizing the starting materials, and the effects of temperature and pressure to get pure samples. We also tried to synthesize at ambient pressure three other doubly ordered perovskites, namely, $NaLaNiWO_6$, $NaNdNiWO_6$, and $NaLaCuWO_6$. $NaLaNiWO_6$ was obtained by the nitrate route, however, it was difficult to get a pure sample. Due to time constraints the optimization of this synthesis was not pursued, but the carbonate route could be an alternative synthesis method to optimize the synthesis. In contrast, the latter two compounds were not obtained at all, HT-HP synthesis could help to stabilize these two phases.

A structural study was performed on the entire series of $NaLnCoWO_6$ compounds by high resolution SXRPD. Rietveld refinement was systematically performed to properly assign the space groups: *C2/m* for Ln=La, Pr, and Nd, and $P2_1$ for the other nine new compounds. In contrast to a previous report, the average structure of $NaLaCoWO_6$ was determined to have the *C2/m* symmetry instead of $P2_1/m$. The SXRPD patterns of both $NaPrCoWO_6$ and $NaNdCoWO_6$ can be fit by *C2/m* as well as $P2_1/m$, making it difficult to assign a unique space group to them. Finally, they were concluded to have *C2/m* symmetry as *C2/m* has a higher symmetry than $P2_1/m$ and in the refinement using *C2/m* it was easier to reach convergence. The nine new compounds were unambiguously determined to have the polar symmetry $P2_1$. The high quality SXRPD data allow to clearly distinguish $P2_1$ from $P2_1/m$ from the peak intensities, given that both space groups have the same extinction conditions. SHG measurements were performed on all these compounds in powder, and confirmed that the structure of the compounds with Ln=La, Pr, and Nd are centrosymmetric while the other nine compounds are non-centrosymmetric, confirming the correct space group assignment for all compounds. High resolution NPD data were refined for $NaYCoWO_6$, $NaTbCoWO_6$ and $NaHoCoWO_6$, in order to have complementary information on oxygen positions. A joint refinement combining the SXRPD and NPD data was carried out for these compounds which allowed us to obtain more precise models of the polar structures. The polar structures were decomposed in terms of symmetry modes, in order to get a deeper understanding on the induced HIF. Three major modes were identified: Γ_5^+, Γ_1^-, and Γ_5^-. The modes Γ_5^+ and Γ_1^- describe nonpolar oxygen octahedral rotations, and the mode Γ_5^- is the polar mode and induced by the two former nonpolar modes. The SXRPD symmetry modes refinements revealed that the magnitude of these three modes increases when decreasing the rare-earth cation's size. Considering a simple point charge model, the ferroelectric spontaneous polarization was estimated from the NPD refinements that ~20 μC/cm^2 for $NaYCoWO_6$, ~14 μC/cm^2 for $NaTbCoWO_6$, ~19 μC/cm^2 for $NaHoCoWO_6$. The estimated values are very close to the predicted polarization of the related compounds.

$NaLaCoWO_6$ manifested a very peculiar structural behavior showing an unusual hysteretic phase transition with respect to temperature and a modulated superstructure. The phase transition has a large temperature hysteresis of about 150 K, where the transition temperature was observed at ~ 330 K when heating up and ~180 K when cooling down from the temperature dependent NPD data. Extra peaks corresponding to the superstructure were also observed in the NPD pattern of the high temperature phase, which were hardly observed in the SXRPD pattern. In addition, the phase transition was also investigated by electron diffraction. The periodicity of the superstructure is $12a_p$ along either $[100]_p$ or $[010]_p$ indicated from both the spacings between the satellites and the modulated superstructure (S)TEM images. The reversibility of this phase transition was further confirmed by electron diffraction. Rietveld refinement of the low temperature phase SXRPD and NPD patterns revealed that it has the polar symmetry $P2_1$, and no superstructure was observed in the low temperature phase. The superstructure in the high temperature phase was deeply investigated by STEM. No evidence on chemical variation was observed in the superstructure, the stripe contrast was attributed to a structural effect such as octahedral tilt twinning. Three different models with oxygen octahedral tilt twinning were built based on the $P2_1/m$ (tilting scheme $a^-a^-c^0$) and $C2/m$ (tilting scheme $a^0b^-c^0$) refinements to explain the satellite reflections in the NPD and SXRPD patterns. The models with the tilting scheme $a^-a^-c^0$ are the better ones; even though it is impossible to distinguish between both possible directions of the propagation of the superstructure. Superstructures were also observed in $NaPrCoWO_6$ and $NaNdCoWO_6$. In contrast, the structures of $NaPrCoWO_6$ and $NaNdCoWO_6$ are more complicated and modulated along two coordinate axes. Further efforts on the understanding these two more complex superstructures are needed. Moreover, a phase diagram may be filled after further structural phase transition study. As shown in Figure 7.1, the La compound has been demonstrated in this study to possess local $P2_1/m$ symmetry in the high temperature phase and $P2_1$ symmetry in the low temperature phase. And then how about the other compounds? The compounds Pr and Nd have been investigated by NPD down to 2K, in addition, the Nd compound was also studied by NPD up to 1073K, no sign of phase transition was observed in both compounds. A transition might happen at a higher temperature, or no transition at all. All other smaller rare earth compounds are in polar $P2_1$ symmetry, the same as the low temperature phase of La, investigations on possible phase transition at higher temperature are needed for these compounds. However, the phase stability could be a hindrance for these compounds at high temperature, since they are all stabilized by high pressure synthesis.

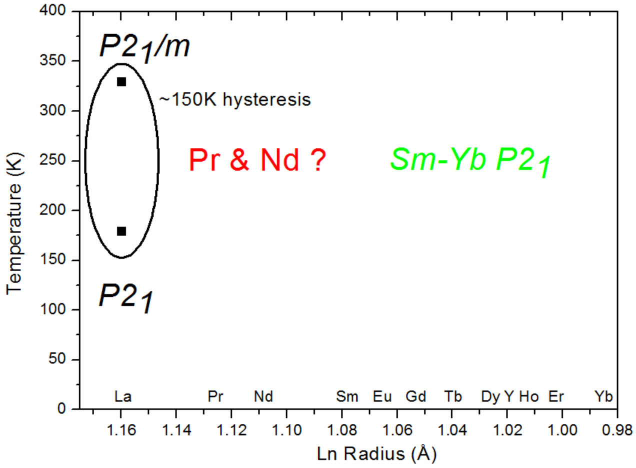

Figure 7.1 A possible phase diagram for the $NaLnCoWO_6$ family to be completed.

Characterizations of physical properties including magnetic properties, magnetic structures, magneto-electric and polarization measurements were carried out. All $NaLnCoWO_6$ compounds order antiferromagnetically below T_N which range from 4K to 13K. Curie-Weiss fits were performed for all compounds, yielding reasonable effective magnetic moments compared to the theoretical ones. Weiss temperatures were all determined to be negative further indicating that antiferromagnetic interactions are dominant in these systems. Isothermal magnetization curves were collected at a variety of magnetic fields, and metamagnetic transitions were observed in some compounds.

Magnetic structures were determined for $NaLnCoWO_6$ (Ln=Y, La, Tb, Ho), with two compounds without a magnetic Ln cation (Y and La) and two compounds with magnetic Ln cations (Tb and Ho). For each compound, the magnetic space group was analyzed and a model among the best ones is discussed, nevertheless, there could be many models well explaining the observed NPD data. To determine unambiguously the magnetic structure of such materials, single crystal samples are needed. Sequential refinements on the temperature dependence of NPD data were performed for $NaLnCoWO_6$ (Ln=Y, Tb, Ho) to extract the magnetic moments evolution as a function of temperature. The Co^{2+} magnetic moment evolution curves show a classical second-order transition behavior. The moment evolutions of Tb^{3+} and Ho^{3+} demonstrated how the magnetic Ln cation is polarized by the magnetic ordering of the Co^{2+} sublattice.

Dielectric measurements were carried out on $NaLnCoWO_6$ (Ln=Y, La, Tb, and Ho). Magneto-dielectric coupling was experimentally observed in the $NaLnCoWO_6$ (Ln= Y, Tb, and Ho) compounds, which is indicated by an anomaly around the T_N in the Capacitance-Temperature curve. The coupling of Y and Ho seems stronger than that of Tb. The dielectric measurements were also carried out at various magnetic fields up to 8T for Y, Tb, and Ho, as a function of temperature. The magneto-dielectric coupling was observed under each magnetic field, and the observed peaks shifted with the applied magnetic fields which further confirmed the magnetic and dielectric properties are coupled. In addition, magneto-capacitance plots were derived for all three samples, showing the effect of the applied magnetic field on the dielectric properties at some fixed temperatures. The polarization was derived for Y and Ho from pyroelectric current measurements, however, only the $NaYCoWO_6$ compound demonstrates a polar behavior which cannot be switched. The detectable polarization is rather small (~0.1 $\mu C/m^2$), but, this is the first evidence that electric polarization can be induced by the magnetic ordering in the AA'BB'O_6 class materials.

For pursuing the quest for magneto-electric multiferroics, a switchable polarization is a must. Further structural optimization is needed to decrease the switching energy barrier and increase the polarization. For this purpose, as discussed in Chapter 1, both the average tolerance factor and the difference of the tolerance factors of the building blocks have to be maximized. For example, to substitute Na by K at the A-site would meet both requirements. Furthermore, $NaYCoWO_6$ and $NaHoCoWO_6$ show comparable strengths of magneto-dielectric coupling, however, polarization was only experimentally measured in $NaYCoWO_6$. The reason has to be understood, is it experimental or intrinsic? In principle the magneto-electric coupling is mediated by the rotations of oxygen octahedra and would affect preferentially the magnetism on the B-site. The role of the magnetic ion which sits on the A'-site (the magnetic rare-earth) has still to be elucidated.

Recently, a theoretical study revealed that the related doubly ordered perovskites $NaLaFeMO_6$ (M=Ru, Re, Os) have a strong magneto-electric coupling by combining the ferroelectric and ferromagnetic effects.[115] The critical temperatures are believed to be above room temperature. Here, the B'-site employs the magnetic ions Ru, Re and Os, which could inspire new thoughts on optimizing the doubly ordered perovskites with respect to multiferroic effects.

References

[1] H. Schmid, “Multi-Ferroic magnetoelectrics,” *Ferroelectrics*, vol. 162, pp. 317–338, 1994.

[2] N. A. Spaldin, S. Cheong, and R. Ramesh, “Multiferroics : Past , present , and future feature,” *Physics Today*, vol. 63, no. 10, pp. 38-43,2010.

[3] M. Gajek, M. Bibes, S. T. Ephane, K. Bouzehouane, B. El, J. Fontcuberta, and A. G. N. Es, “Tunnel junctions with multiferroic barriers,” *Nature*, vol. 6, no. April, pp. 296–302, 2007.

[4] W. Eerenstein, N. D. Mathur, and J. F. Scott, “Multiferroic and magnetoelectric materials,” *Nature*, vol. 442, pp. 759–765, 2006.

[5] N. A. Spaldin, M. Fiebig,, “The renaissance of magnetoelectric multiferroics,” *Science*, vol. 309, pp. 391–392, 2005.

[6] D. Khomskii, “Classifying multiferroics : Mechanisms and effects,” *Physics*, vol. 2, p. 20, 2009.

[7] N. A. Hill, “Why are there so few magnetic ferroelectrics ?,” *J. Phys. Chem. B*, vol. 104, pp. 6694–6709, 2000.

[8] J. Wang, J. B. Neaton, H. Zheng, V. Nagarajan, S. B. Ogale, B. Liu, D. Viehland, V. Vaithyanathan, D. G. Schlom, U. V Waghmare, N. A. Spaldin, K. M. Rabe, M. Wuttig, and R. Ramesh, “Epitaxial BiFeO$_3$ multiferroic thin film heterostructures,” *Science*, vol. 299, pp. 1719–1722, 2003.

[9] N. Hur, S. Park, P. A. Sharma, J. S. Ahn, S. Guha, and S. Cheong, “Electric polarization reversal and memory in a multiferroic material induced by magnetic fields,” *Nature*, vol. 429, pp. 392–395, 2004.

[10] B. B. Van Aken, T. T. M. Palstra, A. Filippetti, N. A. Spaldin , “The origin of ferroelectricity in magnetoelectric YMnO$_3$,” *Nat. Mater.*, vol. 3, pp. 164–170, 2004.

[11] T. Kimura, T. Goto, H. Shintani, K. Ishizaka, T. Arima, and Y. Tokura, “Magnetic control of ferroelectric polarization,” *Nature*, vol. 426, pp. 55–58, 2003.

[12] O. Heyer, N. Hollmann, I. Klassen, S. Jodlauk, L. Bohaty, P. Becker, J. A. Mydosh, T. Lorenz, D. Khomskii, “A New Multiferroic Material: MnWO$_4$,” *J. phys.Condens. Matter*, vol. 18, pp. L471–L475, 2006 .

[13] Y. J. Choi, H. T. Yi, S. Lee, Q. Huang, V. Kiryukhin, and S. Cheong, “Ferroelectricity in an Ising chain magnet,” *Phys. Rev. Lett.*, vol. 100, p. 47601, 2008.

[14] D. Cufeo, “Ferroelectricity induced by proper-screw type magnetic order,” *Phys. Soc. Jpn.*, vol. 76, no. 7, p. 73702, 2007.

[15] N. A. Benedek and C. J. Fennie, “Hybrid improper ferroelectricity: a mechanism for controllable polarization-magnetization coupling,” *Phys. Rev. Lett.*, vol. 106, no. 10, p. 107204, 2011.

[16] E. Bousquet, M. Dawber, N. Stucki, C. Lichtensteiger, P. Hermet, S. Gariglio, J.-M. Triscone, and P. Ghosez, “Improper ferroelectricity in perovskite oxide artificial superlattices.,” *Nature*, vol. 452, pp. 732–736, 2008.

[17] A. Munkholm, S. K. Streiffer, M. V. R. Murty, J. A. Eastman, C. Thompson, O. Auciello, L. Thompson, J. F. Moore, and G. B. Stephenson, “Antiferrodistortive Reconstruction of the PbTiO$_3$

(001) Surface," *Phys. Rev. Lett.*, vol. 88, no. 1, p. 16101, 2002.

[18] C. Bungaro and K. M. Rabe, "Coexistence of antiferrodistortive and ferroelectric distortions at the $PbTiO_3$ (001) surface," *Phys. Rev. B*, vol. 71, p. 35420, 2005.

[19] W. Zhong and D. Vanderbilt, "Competing structural instabilities in cubic perovskites," *Phys. Rev. Lett.*, vol. 74, no. 13, pp. 2587–2590, 1995.

[20] N. A. Pertsev, A. K. Tagantsev, N. Setter , "Phase transition and strain-induced ferroelectricity in $SrTiO_3$ epitaxial thin films," *Phys. Rev. B*, vol. 61, no. 2, pp. R825–R829, 2000.

[21] C. Lin, C. Huang, G. Y. Guo, C. Lin, C. Huang, and G. Y. Guo, "Systematic ab initio study of the phase diagram of epitaxially strained Systematic ab initio study of the phase diagram of epitaxially strained $SrTiO_3$," *J. Appl. Phys.*, vol. 100, p. 84104, 2006.

[22] A. Vasudevarao, A. Kumar, L. Tian, J. H. Haeni, Y. L. Li, C. Eklund, Q. X. Jia, R. Uecker, P. Reiche, K. M. Rabe, L. Q. Chen, D. G. Schlom, and V. Gopalan, "Multiferroic domain dynamics in strained strontium titanate," *Phys. Rev. Lett.*, vol. 97, p. 257602, 2006.

[23] N. A. Benedek, A. T. Mulder, and C. J. Fennie , "Polar octahedral rotations: A path to new multifunctional materials," *J. Solid State Chem.*, vol. 195, pp. 11–20, Nov. 2012.

[24] J. M. Rondinelli and C. J. Fennie, "Octahedral Rotation-Induced Ferroelectricity in Cation Ordered Perovskites," *Advanced Materials*, 24, pp. 1961–1968, 2012.

[25] J. M. Rondinelli and N. A. Spaldin, "Substrate coherency driven octahedral rotations in perovskite oxide films," *Phys. Rev. B*, vol. 82, p. 113402, 2010.

[26] J. Young and J. M. Rondinelli, "Atomic scale design of polar perovskite oxides without Second-Order Jahn − Teller ions," *Chem. Mater.*, vol. 25, pp. 4545–4550, 2013.

[27] J. Young and J. M. Rondinelli, "Design of noncentrosymmetric perovskites from centric and acentric basic building units," *J. Mater. Chem. C*, vol. 4, pp. 4016–4027, 2016.

[28] A. M. Glazer, "The classification of tilted octahedra in perovskites," *Acta Crystallogr. Sect. B Struct. Crystallogr. Cryst. Chem.*, vol. 28, no. 11, pp. 3384–3392, Nov. 1972.

[29] A. T. Mulder, N. A. Benedek, J. M. Rondinelli, and C. J. Fennie, "Turning ABO_3 antiferroelectrics into ferroelectrics : design rules for practical rotation-driven ferroelectricity in double perovskites and $A_3B_2O_7$ Ruddlesden-Popper compounds," *Adv. Funct. Mater.*, vol. 23, pp. 4810–4820, 2013.

[30] Z. Zanolli, J. C. Wojdeł, J. Íñiguez, and P. Ghosez, "Electric control of the magnetization in $BiFeO_3/LaFeO_3$ superlattices," *Phys. Rev. B*, vol. 88, p. 060102(R), 2013.

[31] H. Sim, S. W. Cheong, and B. G. Kim, "Octahedral tilting-induced ferroelectricity in $ASnO_3/A'SnO_3$ superlattices (A,A'=Ca, Sr, and Ba)," *Phys. Rev. B*, vol. 88, p. 14101, Jul. 2013.

[32] N. Song, J. M. Rondinelli, and B. G. Kim, "Noncentrosymmetric structural transitions in ultrashort ferroelectric $AGaO_3/A'GaO_3$ superlattices," *Phys. Rev. B*, vol. 91, p. 134104, 2015.

[33] G. King, A. Wills, and P. Woodward, "Magnetic structures of $NaLMnWO_6$ perovskites (L=La,Nd,Tb)," *Phys. Rev. B*, vol. 79, p. 224428, 2009.

[34] T. Fukushima, A. Stroppa, S. Picozzi, and J. M. Perez-Mato, "Large ferroelectric polarization in the new double perovskite $NaLaMnWO_6$ induced by non-polar instabilities.," *Phys. Chem. Chem.*

Phys., vol. 13, pp. 12186–12190, 2011.

[35] J. Young, Al. Stroppa, S. Picozzi, and J. M. Rondinelli, “Tuning the ferroelectric polarization in AA’MnWO$_6$ double perovskites through A cation substitution,” *Dalt. Trans.*, vol. 44, pp. 10644–10653, 2015.

[36] P. V. Balachandran, D. Puggioni, and J. M. Rondinelli, “Crystal-chemistry guidelines for noncentrosymmetric A$_2$BO$_4$ ruddlesden-popper oxides,” *Inorg. Chem.*, vol. 53, pp. 336–348, 2014.

[37] H. Akamatsu, K. Fujita, T. Kuge, A. Sen Gupta, A. Togo, S. Lei, F. Xue, G. Stone, J. M. Rondinelli, L.-Q. Chen, I. Tanaka, V. Gopalan, and K. Tanaka, “Inversion symmetry breaking by oxygen octahedral rotations in the Ruddlesden-Popper NaRTiO$_4$,” *Phys. Rev. Lett.*, vol. 112, p. 187602, 2014.

[38] Y. S. Oh, X. Luo, F. Huang, Y. Wang, and S. Cheong, “Experimental demonstration of hybrid improper ferroelectricity and the presence of abundant charged walls in (Ca,Sr)$_3$Ti$_2$O$_7$ crystals,” *Nat. Mater.*, vol. 14, pp. 407–413, 2015.

[39] X. Q. Liu, J. W. Wu, X. X. Shi, H. J. Zhao, H. Y. Zhou, R. H. Qiu, W. Q. Zhang, and X. M. Chen, “Hybrid improper ferroelectricity in Ruddlesden-Popper Ca$_3$(Ti, Mn)$_2$O$_7$ ceramics,” *Appl. Phys. Lett.*, vol. 106, p. 202903, 2015.

[40] T. Sekiya, T. Yamamoto, Y. Torii, “Cation ordering in NaLaMgWO$_6$ with the perovskite structure,” *Bull. Chem. Soc. Jpn.*, vol. 57, pp. 1859–1862, 1984 .

[41] M. C. Knapp and P. M. Woodward, “A-site cation ordering in AA’BB’O$_6$ perovskites,” *J. Solid State Chem.*, vol. 179, pp. 1076–1085, 2006.

[42] G. King, L. M. Wayman, and P. M. Woodward, “Magnetic and structural properties of NaLnMnWO$_6$ and NaLnMgWO$_6$ perovskites,” *J. Solid State Chem.*, vol. 182, pp. 1319–1325, 2009.

[43] M. L. Lopez, M. L. Veiga, and C. Pico, “Cation ordering in distorted perovskites (MLa)(MgTe)O$_6$, M = Na, K,” *J. Mater. Chem.*, vol. 4, no. 4, p. 547, 1994.

[44] M. W. Licurse, A. Y. Borisevich, and P. K. Davies, “Nanoscale modulations in (KLa)(CaW)O$_6$ and (NaLa)(CaW)O$_6$,” *J. Solid State Chem.*, vol. 191, pp. 220–224, 2012.

[45] G. King, S. Thimmaiah, A. Dwivedi, and P. M. Woodward, “Synthesis and characterization of new AA’BWO$_6$ perovskites exhibiting simultaneous ordering of A-site and B-site cations,” *Chem. Mater.*, vol. 19, pp. 6451–6458, 2007.

[46] M. Retuerto, M. R. Li, A. Ignatov, M. Croft, K. V. Ramanujachary, S. Chi, J. P. Hodges, W. Dachraonui, J. Hadermann, T. Thao Tran, P. Shiv Halasyamani, C. P. Grams, J. Hemberger, and M. Greenblatt, “Polar and magnetic layered A‑site and rock salt B‑site-ordered NaLnFeWO$_6$ (Ln = La, Nd) perovskites,” *Inorg. Chem.*, vol. 52, pp. 12482–12491, 2013.

[47] M. A. Arillo, J. Gómez, M. L. López, C. Pico, and M. L. Veiga, “Structural characterization and properties of the perovskite (NaLa)(MW)O$_6$ (M=Co, Ni): two new members in the group–subgroup relations for the perovskite-type structures,” *J. Mater. Chem.*, vol. 7, pp. 801–806, 1997.

[48] M. A. Arillo, J. Gomez, M. L. Lopez, C. Pico, and M. Luisa Veiga, “Structural and electrical characterization of new materials with perovskite structure,” *Solid State Ionics*, vol. 95, pp. 241–

248, 1997.

[49] S. Vasala and M. Karppinen, “$A_2B'B''O_6$ perovskites : A review,” *Prog. Solid State Chem.*, vol. 43, pp. 1–36, 2015.

[50] C. J. Howard, B. J. Kennedy, and P. M. Woodward, “Ordered double perovskites - a group-theoretical analysis research papers,” *Acta Crystallogr. Sect. B*, vol. 59, pp. 463–471, 2003.

[51] P. K. Davies, H. Wu, A. Y. Borisevich, I. E. Molodetsky, and L. Farber, “Crystal chemistry of complex perovskites : new cation-ordered dielectric oxides,” *Annu. Rev. Mater. Res.*, vol. 38, pp. 369–401, 2008.

[52] G. King and P. M. Woodward, “Cation ordering in perovskites,” *J. Mater. Chem.*, vol. 20, no. 28, p. 5785, 2010.

[53] W. Dachraoui, T. Yang, C. Liu, G. King, J. Hadermann, G. Van Tendeloo, A. Llobet, and M. Greenblatt , “Short-Range layered A-Site ordering in double erovskites $NaLaBB'O_6$ (B=Mn, Fe; B’=Nb, Ta),” *Chem. Mater.*, vol. 23, pp. 2398–2406, 2011.

[54] S. Garcia-Martin, E. Urones-garrote, M. C. Knapp, G. King, and P. M. Woodward, “Transmission electron microscopy studies of $NaLaMgWO_6$: spontaneous formation of compositionally modulated stripes,” *J. Am. Chem. Soc.*, vol. 130, pp. 15028–15037, 2008.

[55] G. King, S. Garcia-Martin, and P. M. Woodward, “Octahedral tilt twinning and compositional modulation in $NaLaMgWO_6$,” *Acta Crystallogr. Sect. B Struct. Sci.*, vol. 65, pp. 676–683, 2009.

[56] S. Garcia-Martin, G. King, E. Urones-Garrote, G. Nénert, and P. M. Woodward, “Spontaneous superlattice formation in the doubly ordered perovskite $KLaMnWO_6$,” *Chem. Mater.*, vol. 23, pp. 163–170, 2011.

[57] M. W. Licurse and P. K. Davies, “Nanocheckerboard modulations in $(NaNd)(MgW)_6$,” *Appl. Phys. Lett.*, vol. 97, no. 12, p. 123101, 2010.

[58] S. Garcia-Martin, G. King, G. Nenert, C. Ritter, and P. M. Woodward, “The incommensurately modulated structures of the perovskites $NaCeMnWO_6$ and $NaPrMnO_6$,” *Inorg. Chemsitry*, vol. 51, pp. 4007–4014, 2012.

[59] C. De, T. H. Kim, K. H. Kim, and A. Sundaresan, “The absence of ferroelectric polarization in layered and rock-salt ordered $NaLnMnWO_6$ (Ln = La, Nd, Tb) perovskites.,” *Phys. Chem. Chem. Phys.*, vol. 16, pp. 5407–5411, 2014.

[60] J. N. Lalena, D. A. Cleary, E. E. Carpenter, *Inorganic materials synthesis and fabrication, Wiley Interscience,* 2008.

[61] J. V Badding, “High-Pressure synthesis, characterization, and tuning of solid state materials,” *Annu. Rev. Mater. Sci.*, vol. 28, pp. 631–658, 1998.

[62] E. Gilioli and L. Ehm, “High pressure and multiferroics materials: a happy marriage,” *IUCrJ*, vol. 1, pp. 590–603, 2014.

[63] I. L., Spain,J. Paauwe, *High Pressure Technology, Volume II, Applications and Processes,* Marcel Dekker, INC. New York and Basel, vol. II. 1977.

[64] E. W. Comings, *Chemical Engineering Series, High Pressure Technology,* McGraw-Hill Book

Company, INC. New York, Toronto, London, 1956.

[65] H. T. Hall, "Ultra-High-Pressure , High-Temperature Apparatus : the 'Belt' Ultra-High-Pressure , High-Temperature Apparatus : the ' Belt ,'" *Rev. Sci. Instrum.*, vol. 31, no. 2, pp. 125–131, 1960.

[66] N. A., Nikolaev, M. D. Shalimove, "Device for producing superhigh pressure and temperature, Patent,SU1332598," 1990.

[67] H. K. Hieu and N. N. Ha, "High pressure melting curves of silver , gold and copper," *AIP Adv.*, vol. 3, p. 112125, 2013.

[68] A. Kavner and R. Jeanloz, "High-pressure melting curve of platinum," *J. Appl. Phys.*, vol. 83, no. 12, pp. 7553–7559, 1998.

[69] R. C. Ropp, *Solid State Chemistry*. Elsevier Science B. V, ISBN: 0 444 510436 8.

[70] V. K., Pecharsky, P. Y. Zavalij , *Fundamentals of Powder Diffraction and Structural Characterization of Materials (second edition)*. Springer, 2009.

[71] *Monochromateur primaire de transmission pour le diffractometre D5000, Instructions*. Siemens, Ref. C79000-B3477-C160-01.

[72] *Monochromateur secondaire pour le diffractometer D5000, Instructions*. Siemens, Ref. C79000-B3477-C152-01.

[73] D. B. and W. D. Kaplan, *Microstructural Characterization of Materials (second edition),* John Wiley & Sons, Ltd, 2008. John Wiley & Sons, Ltd., 2008.

[74] G. King, "Structural, magnetic, and electronic studies of complex perovskites," Ph. D. Thesis, The Ohio State University, 2009.

[75] G. A. El-shobaky, A. S. Ahmad, A. N. Al-Noaimi, and H. G. El-Shobaky, "Thermal decomposition of basic cobalt and copper carbonates," *J. Therm. Anal.*, vol. 46, pp. 1801–1808, 1996.

[76] L. E. James, L. Crescentini and W. B. Fisher , "'Process for making a cobalt oxide catalyst', Patent, US4389339."

[77] M. Richard, "Contribution to the structural characterization of a sodium ytterium titanate layered perovskite and its protonated forms," *Mater. Res. Bull.*, vol. 30, no. 8, pp. 925–931, 1995.

[78] K. Toda, Y. Kameo, S. Kurita, and M. Sato, "Crystal structure determination and ionic conductivity of layered perovskite compounds $NaLnTiO_4$ (Ln = rare earth)," *J. Allyos Compd.*, vol. 234, pp. 19–25, 1996.

[79] V. Valvoda, "International Tables for Crystallography," vol. C, 2006, pp. 186–190.

[80] "https://www.synchrotron-soleil.fr/fr/lignes-de-lumiere/cristal."

[81] "https://www.ill.eu/instruments-support/instruments-groups/instruments/d2b/how-it-works/simulated-experiment/."

[82] "https://www.ill.eu/instruments-support/instruments groups/instruments/d1b/description/instrument-layout/."

[83] E. H. K. and C. J. Howard, *Applications of Neutron Powder Diffraction*. Oxford University Press, 2008.

[84] J. Rodriguez-carvajal, “Recent advances in magnetic structure determination by neutron powder diffraction,” *Phys. B*, vol. 192, pp. 55–69, 1993.

[85] R. A. Young, *The Rietveld Method*. Oxford University Press, 1993.

[86] B. H. Toby, “R factors in Rietveld analysis : How good is good enough ?,” *Powder Diffr.*, vol. 21, no. 1, pp. 67–70, 2006.

[87] J. Rodriguez-Carvajal, *An Introduction to the Prgram FullProf 2000, User Manual*. 2001.

[88] P. Thompson, D. E. Cox, and J. B. Hastings, “Rietveld refinement of Debye-Scherrer synchrotron X-ray data from Al_2O_3,” *J. Appl. Cryst.*, vol. 20, pp. 79–83, 1987 .

[89] L. W. Finger, “PROFVAL : functions to calculate powder-pattern peak profiles with axial-divergence asymmetry Picosecond Time Analyzer,” *J. Appl. Crystallogr.*, vol. 31, p. 111, 1998.

[90] K. Momma and F. Izumi, “VESTA 3 for three-dimensional visualization of crystal , volumetric and morphology data,” *J. Appl. Crystallogr.*, vol. 44, pp. 1272–1276, 2011.

[91] Y. U. Kurimura and Y. Yamamoto, “Optical second harmonic images of 90° domain structure in $BaTiO_3$ and periodically inverted antiparallel domains in $LiTaO_3$,” *Appl. Phys. Lett.*, vol. 66, pp. 2165–2167, 1995.

[92] W. Koechner, *Solid-State Laser Engine*. Springer, 1996.

[93] M. E. Lines, and A. M. Glass, *Principles and applications of ferroelectrics and related materials*. Oxford University Press, 1977.

[94] D. B. Williams, and C. B. Carter, *Transmission Electron Microscopy A Textbook for Materials Science*. Springer Science + business media, LLC 2009, 2009.

[95] E. Okunishi, H. Sawada, and Y. Kondo, “Experimental study of annular bright field (ABF) imaging using aberration-corrected scanning transmission electron microscopy (STEM),” *Micron*, vol. 43, pp. 538–544, 2012.

[96] S. Blundell, *Magnetism in Condensed Matter*. Oxford University Press, 2001.

[97] J. I. Hoppee, “Effective magnetic moment,” *J. Chem. Educ.*, vol. 49, no. 7, p. 505, 1972.

[98] “Quantum Design Inc. Magnetic Property Measurement System, User’s Manual.” 2009 .

[99] M. McElfresh, “Fundamentals of Magnetism and Magnetic Measurements Featuring Quantum Design’s Magnetic Property Measurement System.” Purdue University & Quantum Design, 1994.

[100] K. Skold, and D. L. Price, *Methods of Experimental Physics, vol. 23 Neutron Scattering*. Academic Press Inc., 1987.

[101] E. F. Bertaut, “Representation analysis of magnetic structures,” *Acta Cryst.*, vol. A24, pp. 217–231, 1968.

[102] A. S. Wills, “An introduction to the representative theory of magnetic structures.” NIST workshop, 2007.

[103] A. S. Wills, “A new protocol for the determination of magnetic structures using simulated annealing and representational analysis (SARA h),” *Phys. B*, vol. 276–278, pp. 680–681, 2000.

[104] D. Halliday, and R. Resnick, *Fundamentals of Physics*. Wiley.

[105] “Quantum Design, PPMS Manual.” 2008.

[106] “Physical property measurement system, Heat capacity option, user’s manual.” Quantum Design, 2004.

[107] “Agilent basics of measuring the dielectric properties of materials application note.” Agilent Technologies.

[108] T. Kimura, S. Kawamoto, I. Yamada, M. Azuma, M. Takano, and Y. Tokura, “Magnetocapacitance effect in multiferroic $BiMnO_3$,” *Phys. Rev. B*, vol. 67, p. 180401(R), 2003.

[109] R. D. Shannon, “Revised effective ionic radii and systematic studies of interatomie distances in halides and chaleogenides,” *Acta Cryst.*, vol. A32, pp. 751–767, 1976.

[110] M. D. Wei, “Preparation, Crystal Structure and Catalytic Properties of Ordered Perovskite-Type Oxides Contanining Tungsten and Molybdenum,” Ph. D. Thesis, Nagasaki Univeristy, 1999.

[111] J. M. D. Coey, *Magnetism and Magnetic Materials*. Cambridge University Press, 2009.

[112] Y. Takikawa, S. Ebisu, and S. N. Ã, “Van Vleck paramagnetism of the trivalent Eu ions,” *J. Phys. Chem. Solids*, vol. 71, pp. 1592–1598, 2010.

[113] E. Stryjewski and N. Giordano, “Metamagnetism,” *Adv. Phys.*, vol. 26, no. 5, pp. 487–650, 1977.

[114] J. M. Perez-Mato, S. V. Gallego, E. S. Tasci, L. Elcoro, G. de la Flor, and M. I. Aroyo, “Symmetry-Based computational tools for magnetic crystallography,” *Annu. Rev. Mater. Res.*, vol. 45, pp. 217–248, 2015.

[115] G. Song, G. Li, B. Gao, F. Liang, and J. Zhang, “Predicting room-temperature multiferroic phase of $NaLaFeMO_6$ (M = Ru , Re , Os) with strong magnetoelectric coupling,” *J. Alloys Compd.* vol. 690, pp. 923–929, 2017.

Appendix

Part I: SXPRD Refinements

SI.1. NaYCoWO$_6$:

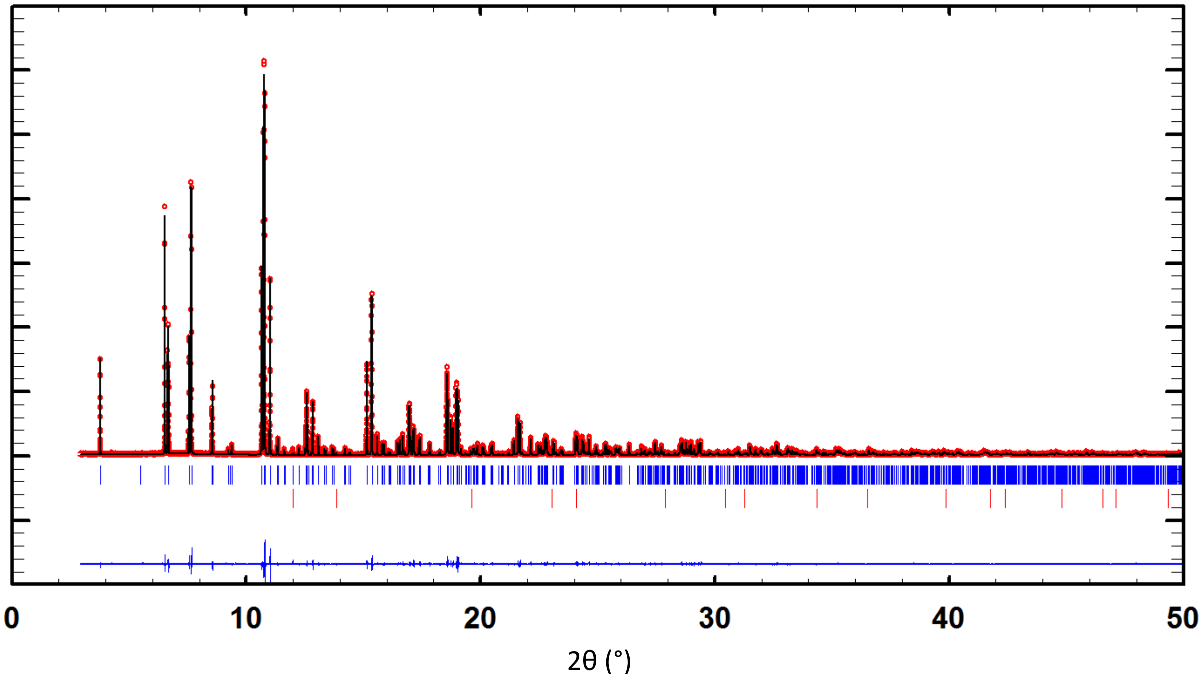

Figure S1. The SXRPD pattern refinement (*P2$_1$*) of the NaYCoWO$_6$ sample, the observed pattern (red circles), the calculated patterns (black lines), and the difference lines (blue, at the bottom) are shown. Blue tick marks in show allowed (*hkl*) reflections of the main phase NaYCoWO$_6$ (99.56(18) %). Red tick marks stand for allowed (*hkl*) reflections of CoO (0.44(2) wt%).

Table S2. Crystallographic parameters of NaYCoWO$_6$ from the SXRPD pattern refinement ($P2_1$) at room temperature.[a]

Atom	Wyckoff Symbol	x	y	z	B(Å^2)	Occupancy
Na	2a	0.250(2)	0.714(2)	0.001(1)	1.2(1)	1.0
Y	2a	0.2656(4)	0.8130(5)	0.5005(2)	0.60(2)	1.0
Co	2a	0.7493(6)	0.757(2)	0.2492(3)	0.52(2)	1.0
W	2a	0.7624(2)	0.75	0.76407(7)	0.477(5)	1.0
O1	2a	0.466(3)	0.553(3)	0.688(2)	0.49(5)	1.0
O2	2a	0.441(3)	0.526(3)	0.313(2)	0.49(5)	1.0
O3	2a	0.076(3)	-0.050(3)	0.214(2)	0.49(5)	1.0
O4	2a	0.056(3)	-0.070(3)	0.776(2)	0.49(5)	1.0
O5	2a	0.855(2)	0.713(3)	0.504(1)	0.49(5)	1.0
O6	2a	0.672(2)	0.782(3)	-0.012(1)	0.49(5)	1.0

[a] Space group $P2_1$, Z=2. Unit cell parameters: a= 5.34712(2) Å, b= 5.52411(2) Å, c= 7.78938(2) Å, β= 90.2946(1) °, V/Z= 115.04(0) Å^3. Discrepancy factors: χ^2 = 1.51, R_p=10.9%, R_{wp}= 13.2%, R_{Bragg}= 2.00%.

Table S3. Selected Bond lengths, Bond valence sums and bond angles of NaYCoWO$_6$ from the SXRPD refinement at room temperature.

Bond Lengths (Å)		Bond Valence Sums	
Co-O1	2.06(2)	Na	1.00(1)
Co-O2	2.15(2)	Y	2.98(2)
Co-O3	2.06(2)	Co	2.07(2)
Co-O4	2.10(2)	W	5.85(5)
Co-O5	2.07(1)	O1	1.92(2)
Co-O6	2.08(1)	O2	1.90(3)
Co-O Average	2.09	O3	2.03(3)
W-O1	2.01(1)	O4	1.99(3)
W-O2	1.97(1)	O5	1.95(2)
W-O3	1.88(1)	O6	2.11(2)
W-O4	1.86(1)	Bond Angles (°)	
W-O5	2.10(1)	Co-O1-W	143.1(4)
W-O6	1.82(1)	Co-O2-W	144.7(4)
W-O average	1.94	Co-O3-W	146.3(4)
		Co-O4-W	151.2(4)
		Co-O5-W	148.0(2)
		Co-O6-W	151.6(2)

SI.2. NaLaCoWO$_6$:

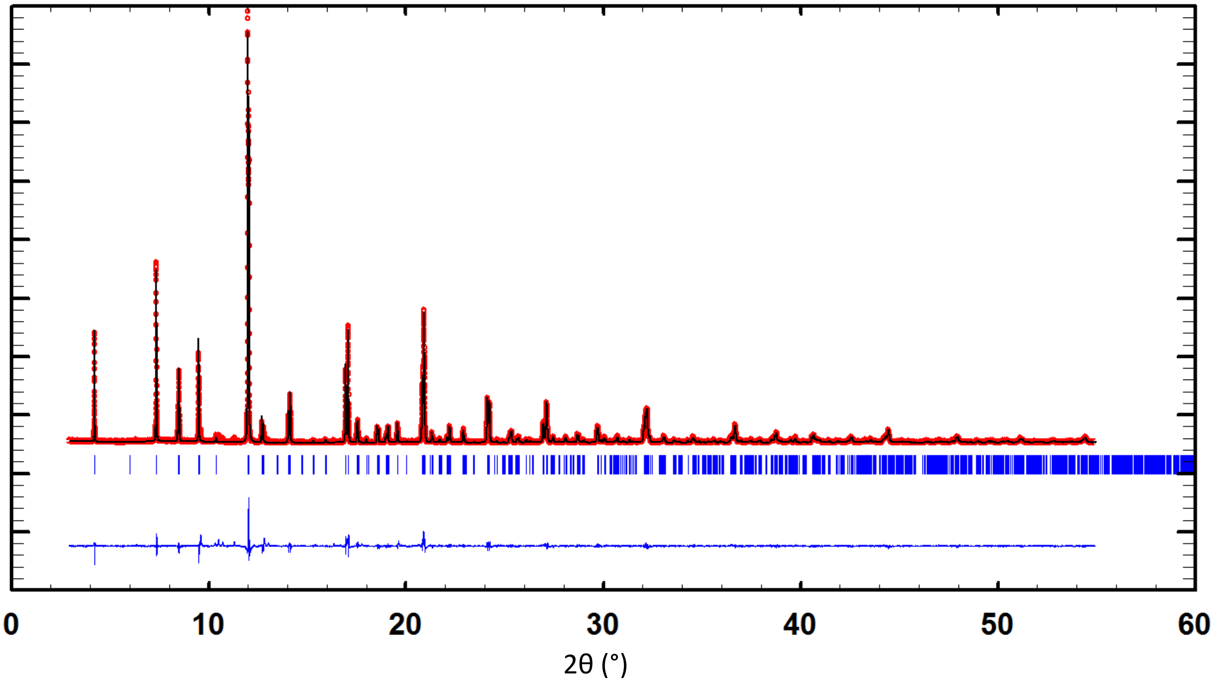

Figure S2. The SXRPD pattern refinement (*C2/m*) of the NaLaCoWO$_6$ sample, the observed pattern (red circles), the calculated patterns (black lines), and the difference lines (blue, at the bottom) are shown. Blue tick marks show allowed (*hkl*) reflections of the main phase NaLaCoWO$_6$.

Table S4. Crystallographic parameters of $NaLaCoWO_6$ from the SXRPD pattern refinement (*C2/m*) at room temperature.[b]

Atom	Wyckoff Symbol	x	y	z	B(Å^2)	Occupancy
Na	4g	0	0.245(8)	0.5	0.21(9)	0.5
La	4h	0	0.250(1)	0	0.77(2)	0.5
Co	4i	0.746(2)	0	0.747(1)	0.08(2)	0.5
W	4i	0.2484(7)	0	0.7331(4)	0.226(6)	0.5
O1	4i	0.01(1)	0	0.71(1)	1.4(1)	0.5
O2	8j	0.747(8)	0.263(7)	0.748(6)	1.4(1)	1.0
O4	4i	0.49(1)	0	0.803(9)	1.4(1)	0.5
O5	4i	0.800(8)	0	0.007(7)	1.4(1)	0.5
O6	4i	0.698(8)	0	0.486(7)	1.4(1)	0.5

[b] Space group *C2/m*, Z=4. Unit cell parameters: a= 7.8347(1) Å, b= 7.8430(1) Å, c= 7.8940(1) Å, β= 90.165(1) °, V/Z= 121.27(1) Å^3. Discrepancy factors: χ^2 = 3.12, R_p=15.6%, R_{wp}= 19.8%, R_{Bragg}= 5.52%.

Table S5. Selected Bond lengths, Bond valence sums and bond angles of NaLaCoWO$_6$ from the SXRPD refinement at room temperature.

Bond Lengths (Å)		Bond Valence Sums	
Co-O1	2.08(8)	Na	0.86(1)
Co-O2	2.07(6)	La	2.36(2)
Co-O3		Co	2.11(3)
Co-O4	2.07(8)	W	6.38(9)
Co-O5	2.10(5)	O1	1.70(5)
Co-O6	2.09(5)	O2	2.05(4)
Co-O Average	2.08	O3	
W-O1	1.89(8)	O4	2.07(4)
W-O2	1.86(6)	O5	1.77(2)
W-O3		O6	2.07(4)
W-O4	1.96(8)	Bond Angles (°)	
W-O5	2.08(5)	Co-O1-W	165.0(7)
W-O6	1.78(5)	Co-O2-W	176.2(5)
W-O average	1.91	Co-O3-W	
		Co-O4-W	151.2(7)
		Co-O5-W	157.9(4)
		Co-O6-W	156.1(5)

SI.3. NaPrCoWO$_6$:

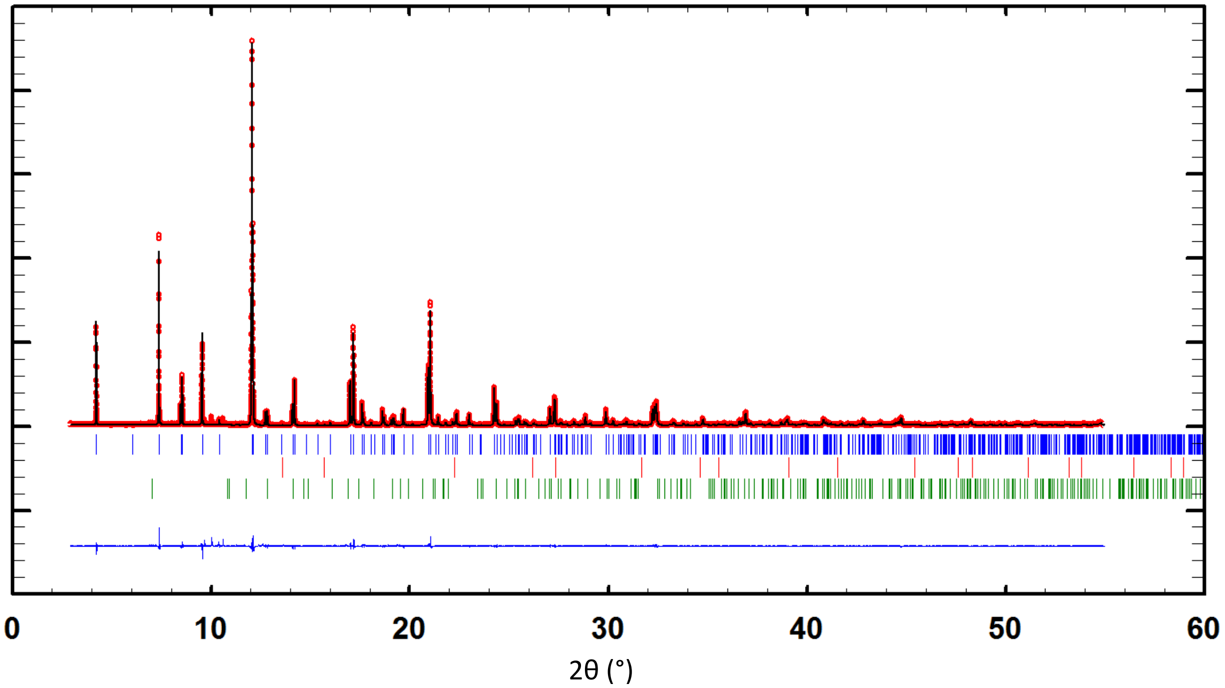

Figure S3. The SXRPD pattern refinement (*C2/m*) of the NaPrCoWO$_6$ sample, the observed pattern (red circles), the calculated patterns (black lines), and the difference lines (blue, at the bottom) are shown. Blue tick marks show allowed (*hkl*) reflections of the main phase NaPrCoWO$_6$ (99.17(20)wt%). Red tick marks stand for allowed (*hkl*) reflections of CoO (0.58(3) wt%). Green tick marks stand for allowed (*hkl*) reflections of NaPr(WO$_4$)$_2$ (0.24(2) wt%).

Table S6. Crystallographic parameters of $NaPrCoWO_6$ from the SXRPD pattern refinement ($C2/m$) at room temperature.[c]

Atom	Wyckoff Symbol	x	y	z	B(Å^2)	Occupancy
Na	4g	0	0.225(5)	0.5	1.1(2)	0.475(2)
Pr1	4g	0	0.225(5)	0.5	1.1(2)	0.025(2)
Pr2	4h	0	0.246(1)	0	1.03(1)	0.5
Co	4i	0.745(3)	0	0.7467(9)	0.12(2)	0.5
W	4i	0.250(1)	0	0.7338(2)	0.270(4)	0.5
O1	4i	0.02(1)	0	0.707(7)	0.6(1)	0.5
O2	8j	0.714(5)	0.261(7)	0.762(5)	0.6(1)	1.0
O4	4i	0.49(1)	0	0.820(8)	0.6(1)	0.5
O5	4i	0.805(5)	0	0.008(5)	0.6(1)	0.5
O6	4i	0.697(5)	0	0.485(5)	0.6(1)	0.5

[c] Space group $C2/m$, Z=4. Unit cell parameters: a= 7.7900(3) Å, b= 7.7913(3) Å, c= 7.86673(5) Å, β= 90.025(2) °, V/Z= 119.366(5) Å^3. Discrepancy factors: χ^2 = 15.2, R_p=11.2%, R_{wp}= 15.3%, R_{Bragg}= 4.16%.

Table S7. Selected Bond lengths, Bond valence sums and bond angles of NaPrCoWO$_6$ from the SXRPD refinement at room temperature.

Bond Lengths (Å)		Bond Valence Sums	
Co-O1	2.16(8)	Na	0.86(1)
Co-O2	2.05(5)	Pr	2.90(2)
Co-O3		Co	2.20(3)
Co-O4	2.04(8)	W	6.69(9)
Co-O5	2.11(4)	O1	2.13(6)
Co-O6	2.09(4)	O2	2.14(4)
Co-O Average	2.08	O3	
W-O1	1.81(8)	O4	2.17(4)
W-O2	1.89(5)	O5	1.93(2)
W-O3		O6	2.13(3)
W-O4	2.01(7)	Bond Angles (°)	
W-O5	2.08(4)	Co-O1-W	164.8(7)
W-O6	1.77(4)	Co-O2-W	161.9(4)
W-O average	1.91	Co-O3-W	
		Co-O4-W	143.8(7)
		Co-O5-W	155.2(3)
		Co-O6-W	156.3(4)

SI.4. NaNdCoWO$_6$:

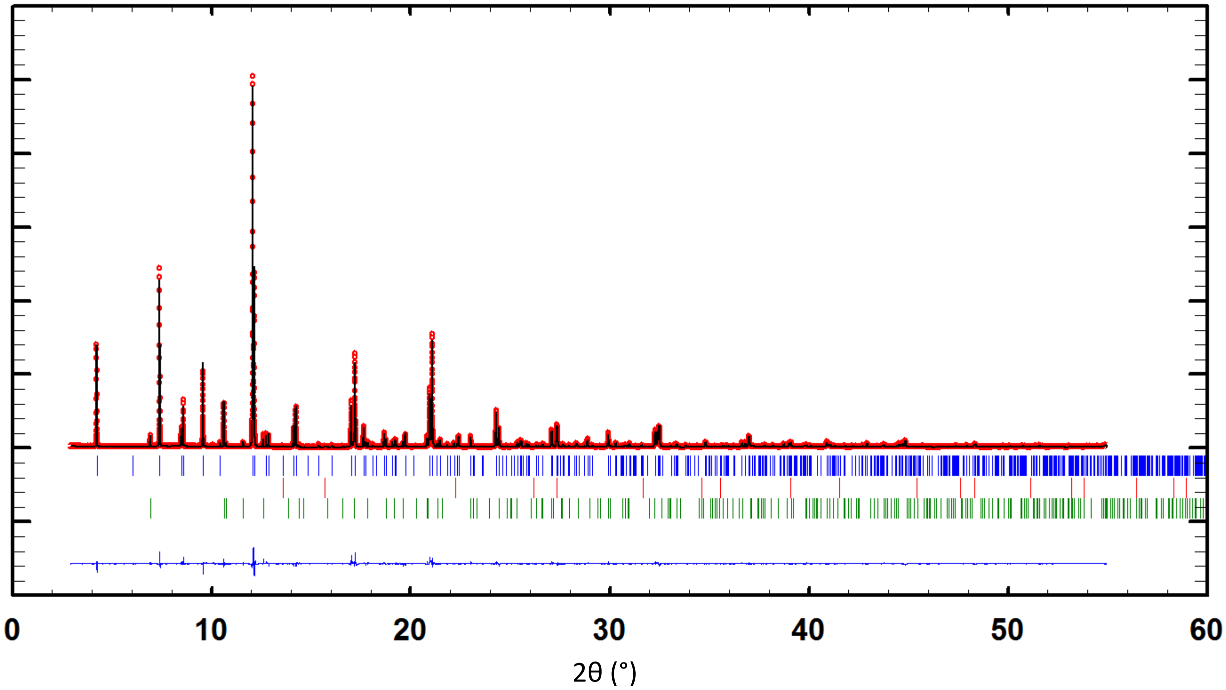

Figure S4. The SXRPD pattern refinement (*C2/m*) of the NaNdCoWO$_6$ sample, the observed pattern (red circles), the calculated patterns (black lines), and the difference lines (blue, at the bottom) are shown. Blue tick marks show allowed (*hkl*) reflections of the main phase NaNdCoWO$_6$ (91.98(18)wt%). Red tick marks stand for allowed (*hkl*) reflections of CoO (1.01(3) wt%). Green tick marks stand for allowed (*hkl*) reflections of NaNd(WO$_4$)$_2$ (7.01(4) wt%).

Table S8. Crystallographic parameters of $NaNdCoWO_6$ from the SXRPD pattern refinement (*C2/m*) at room temperature.[d]

Atom	Wyckoff Symbol	x	y	z	B(Å^2)	Occupancy
Na	4g	0	0.273(6)	0.5	0.7(1)	0.4710(8)
Nd1	4g	0	0.273(6)	0.5	0.7(1)	0.0290(8)
Nd2	4h	0	0.253(2)	0	1.33(1)	0.5
Co	4i	0.743(3)	0	0.745(1)	0.11(2)	0.5
W	4i	0.248(1)	0	0.7345(3)	0.216(4)	0.5
O1	4i	0.02(1)	0	0.708(8)	0.64(9)	0.5
O2	8j	0.720(7)	0.261(7)	0.765(5)	0.64(9)	1.0
O4	4i	0.48(1)	0	0.820(9)	0.64(9)	0.5
O5	4i	0.810(6)	0	0.013(6)	0.64(9)	0.5
O6	4i	0.690(6)	0	0.488(6)	0.64(9)	0.5

[d] Space group *C2/m*, Z=4. Unit cell parameters: a= 7.7736(2) Å, b= 7.7757(2) Å, c= 7.86181(6) Å, β= 90.023(2) °, V/Z= 118.801(3) Å^3. Discrepancy factors: χ^2 = 58.3, R_p= 11.9%, R_{wp}= 14.3%, R_{Bragg}= 4.71%.

Table S9. Selected Bond lengths, Bond valence sums and bond angles of $NaNdCoWO_6$ from the SXRPD refinement at room temperature.

Bond Lengths (Å)		Bond Valence Sums	
Co-O1	2.16(9)	Na	0.936(9)
Co-O2	2.04(5)	Nd	2.76(2)
Co-O3		Co	2.14(3)
Co-O4	2.12(9)	W	6.94(9)
Co-O5	2.17(5)	O1	1.98(6)
Co-O6	2.06(5)	O2	2.14(3)
Co-O Average	2.10	O3	
W-O1	1.79(9)	O4	2.31(5)
W-O2	1.89(5)	O5	1.88(2)
W-O3		O6	2.33(3)
W-O4	1.94(9)	Bond Angles (°)	
W-O5	2.04(5)	Co-O1-W	165.3(7)
W-O6	1.82(5)	Co-O2-W	163.8(4)
W-O average	1.89	Co-O3-W	
		Co-O4-W	143.6(7)
		Co-O5-W	153.3(3)
		Co-O6-W	152.7(3)

SI.5. NaSmCoWO$_6$:

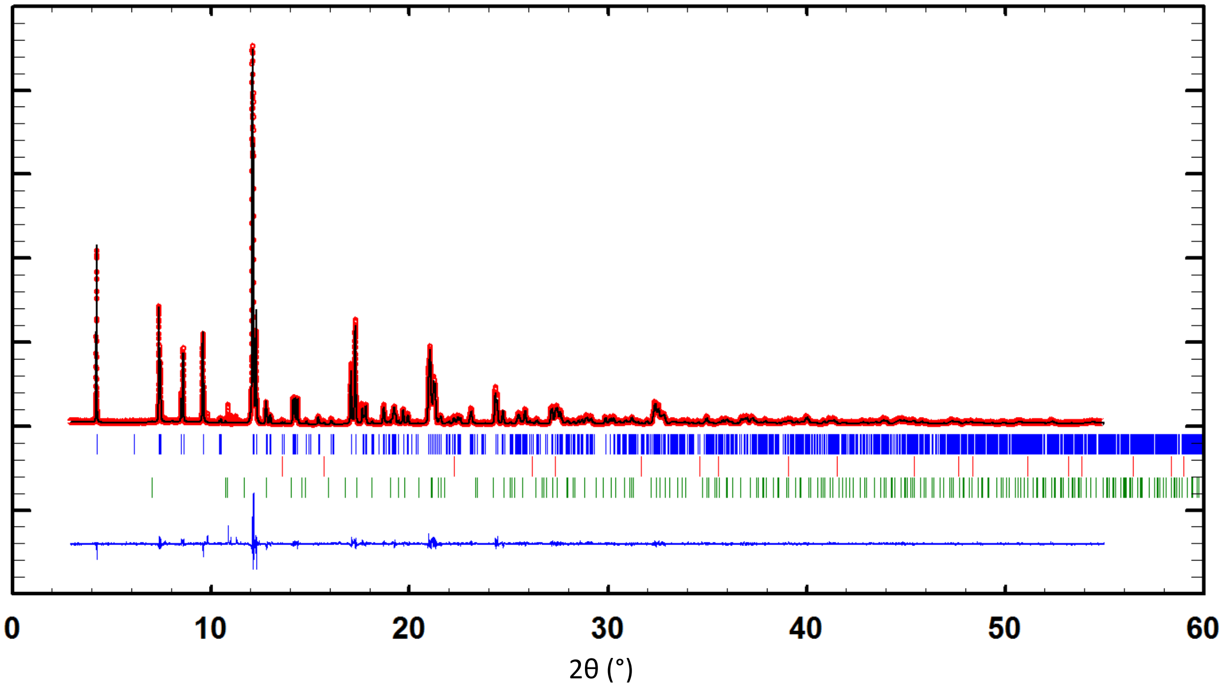

Figure S5. The SXRPD pattern refinement (*P2₁*) of the NaSmCoWO$_6$ sample, the observed pattern (red circles), the calculated patterns (black lines), and the difference lines (blue, at the bottom) are shown. Blue tick marks show allowed (*hkl*) reflections of the main phase NaSmCoWO$_6$ (98.50(21)wt%). Red tick marks stand for allowed (*hkl*) reflections of CoO (1.16(4)wt%). Green tick marks stand for allowed (*hkl*) reflections of NaSm(WO$_4$)$_2$ (0.34(2) wt%).

Table S10. Crystallographic parameters of $NaSmCoWO_6$ from the SXRPD pattern refinement ($P2_1$) at room temperature.[e]

Atom	Wyckoff Symbol	x	y	z	B(Å^2)	Occupancy
Na	2a	0.250(6)	0.743(6)	0.001(4)	0.8(1)	1.0
Sm	2a	0.2606(9)	0.803(1)	0.4999(6)	1.11(3)	1.0
Co	2a	0.751(2)	0.763(4)	0.2476(8)	0.67(5)	1.0
W	2a	0.7580(6)	0.75	0.7660(3)	0.94(1)	1.0
O1	2a	0.488(7)	0.531(8)	0.694(7)	0.43(8)	1.0
O2	2a	0.453(8)	0.510(8)	0.287(7)	0.43(8)	1.0
O3	2a	0.047(8)	-0.059(7)	0.186(5)	0.43(8)	1.0
O4	2a	0.041(7)	-0.069(8)	0.766(6)	0.43(8)	1.0
O5	2a	0.828(5)	0.706(7)	0.503(4)	0.43(8)	1.0
O6	2a	0.666(5)	0.757(9)	-0.015(3)	0.43(8)	1.0

[e] Space group $P2_1$, Z=2. Unit cell parameters: a= 5.43629(6) Å, b= 5.51765(6) Å, c= 7.8402(1) Å, β= 90.297(1) °, V/Z= 117.585(2) Å^3. Discrepancy factors: χ^2 = 3.60, R_p= 12.7%, R_{wp}= 15.6%, R_{Bragg}= 3.57%.

Table S11. Selected Bond lengths, Bond valence sums and bond angles of $NaSmCoWO_6$ from the SXRPD refinement at room temperature.

Bond Lengths (Å)		Bond Valence Sums	
Co-O1	2.02(5)	Na	1.13(2)
Co-O2	2.16(4)	Sm	2.83(4)
Co-O3	1.95(4)	Co	2.17(3)
Co-O4	2.15(4)	W	5.89(7)
Co-O5	2.07(3)	O1	2.03(4)
Co-O6	2.11(3)	O2	2.02(4)
Co-O Average	2.08	O3	1.85(3)
W-O1	1.98(5)	O4	2.06(4)
W-O2	1.88(4)	O5	1.97(3)
W-O3	2.04(4)	O6	2.09(4)
W-O4	1.83(4)	Bond Angles (°)	
W-O5	2.11(3)	Co-O1-W	149.0(7)
W-O6	1.79(3)	Co-O2-W	156.5(6)
W-O average	1.94	Co-O3-W	143.7(6)
		Co-O4-W	154.5(6)
		Co-O5-W	153.2(4)
		Co-O6-W	151.1(4)

SI.6. NaEuCoWO$_6$:

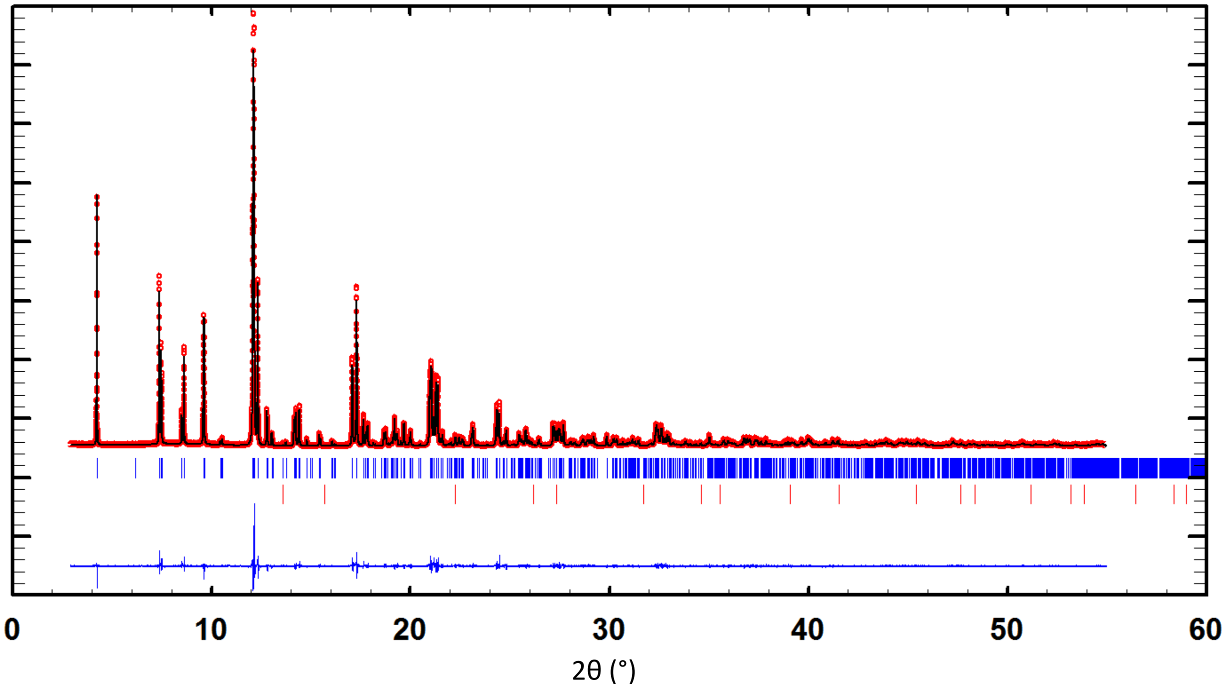

Figure S6. The SXRPD pattern refinement (*P2$_1$*) of the NaEuCoWO$_6$ sample, the observed pattern (red circles), the calculated patterns (black lines), and the difference lines (blue, at the bottom) are shown. Blue tick marks show allowed (*hkl*) reflections of the main phase NaEuCoWO$_6$ (99.48(16)wt%). Red tick marks stand for allowed (*hkl*) reflections of CoO (0.52(4)wt%).

Table S12. Crystallographic parameters of $NaEuCoWO_6$ from the SXRPD pattern refinement ($P2_1$) at room temperature.[f]

Atom	Wyckoff Symbol	x	y	z	B(Å^2)	Occupancy
Na	2a	0.249(3)	0.728(3)	0.002(2)	0.5(1)	1.0
Eu	2a	0.2616(4)	0.8028(9)	0.5004(3)	0.68(2)	1.0
Co	2a	0.749(1)	0.753(4)	0.2475(5)	0.51(3)	1.0
W	2a	0.7586(3)	0.75	0.7660(1)	0.525(8)	1.0
O1	2a	0.477(4)	0.546(5)	0.691(4)	0.59(6)	1.0
O2	2a	0.450(4)	0.524(4)	0.302(4)	0.59(6)	1.0
O3	2a	0.067(4)	-0.041(4)	0.210(3)	0.59(6)	1.0
O4	2a	0.039(4)	-0.064(4)	0.779(3)	0.59(6)	1.0
O5	2a	0.847(3)	0.708(4)	0.504(2)	0.59(6)	1.0
O6	2a	0.670(3)	0.756(5)	-0.011(2)	0.59(6)	1.0

[f] Space group $P2_1$, Z=2. Unit cell parameters: a= 5.41229(2) Å, b= 5.52448(2) Å, c= 7.82945(5) Å, β= 90.3220(3) °, V/Z= 117.049(1) Å^3. Discrepancy factors: χ^2 = 3.14, R_p= 10.5%, R_{wp}= 12.1%, R_{Bragg}= 2.52%.

Table S13. Selected Bond lengths, Bond valence sums and bond angles of $NaEuCoWO_6$ from the SXRPD refinement at room temperature.

Bond Lengths (Å)		Bond Valence Sums	
Co-O1	2.09(3)	Na	0.92(1)
Co-O2	2.10(3)	Eu	2.81(3)
Co-O3	2.09(3)	Co	2.05(2)
Co-O4	2.10(3)	W	6.00(6)
Co-O5	2.09(2)	O1	1.99(3)
Co-O6	2.07(1)	O2	1.93(3)
Co-O Average	2.09	O3	1.80(3)
W-O1	1.98(2)	O4	2.03(4)
W-O2	1.96(2)	O5	1.97(2)
W-O3	1.87(2)	O6	2.07(3)
W-O4	1.84(2)	Bond Angles (°)	
W-O5	2.12(2)	Co-O1-W	145.2(6)
W-O6	1.81(1)	Co-O2-W	148.5(6)
W-O average	1.93	Co-O3-W	150.4(6)
		Co-O4-W	155.6(6)
		Co-O5-W	149.3(3)
		Co-O6-W	152.6(3)

SI.7. NaGdCoWO$_6$:

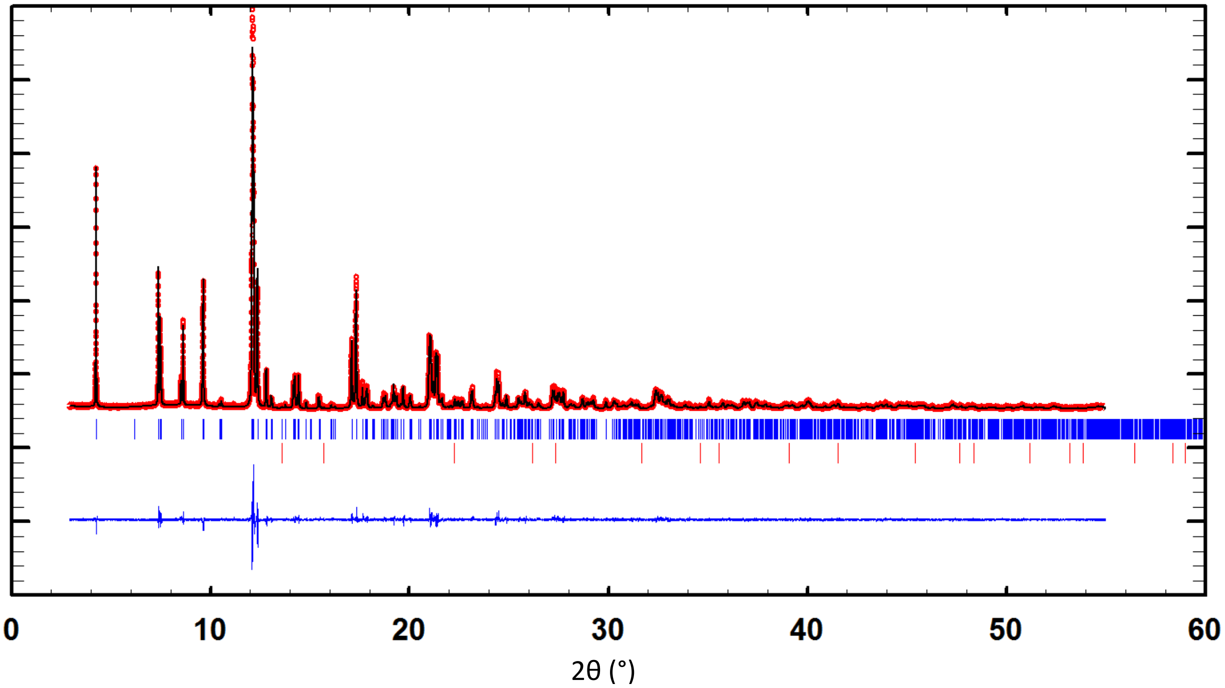

Figure S7. The SXRPD pattern refinement (*P2*$_1$) of the NaGdCoWO$_6$ sample, the observed pattern (red circles), the calculated patterns (black lines), and the difference lines (blue, at the bottom) are shown. Blue tick marks show allowed (*hkl*) reflections of the main phase NaGdCoWO$_6$ (99.35(17)wt%). Red tick marks stand for allowed (*hkl*) reflections of CoO (0.65(4)wt%).

Table S14. Crystallographic parameters of $NaGdCoWO_6$ from the SXRPD pattern refinement ($P2_1$) at room temperature.[g]

Atom	Wyckoff Symbol	x	y	z	B(Å^2)	Occupancy
Na	2a	0.248(4)	0.729(3)	0.005(2)	0.2(1)	1.0
Gd	2a	0.2643(6)	0.8083(9)	0.5003(4)	0.79(2)	1.0
Co	2a	0.746(2)	0.762(4)	0.2463(7)	0.37(5)	1.0
W	2a	0.7596(5)	0.75	0.7654(2)	0.64(1)	1.0
O1	2a	0.474(5)	0.544(6)	0.693(5)	0.51(7)	1.0
O2	2a	0.448(6)	0.526(5)	0.304(5)	0.51(7)	1.0
O3	2a	0.064(6)	-0.020(5)	0.210(4)	0.51(7)	1.0
O4	2a	0.042(5)	-0.057(5)	0.788(4)	0.51(7)	1.0
O5	2a	0.858(4)	0.686(5)	0.500(3)	0.51(7)	1.0
O6	2a	0.664(4)	0.751(5)	-0.013(3)	0.51(7)	1.0

[g] Space group $P2_1$, Z=2. Unit cell parameters: a= 5.40023(5) Å, b= 5.52331(5) Å, c= 7.82229(8) Å, β= 90.2976(6) °, V/Z= 116.657(1) Å^3. Discrepancy factors: χ^2 = 3.28, R_p= 11.3%, R_{wp}= 13.0%, R_{Bragg}= 2.45%.

Table S15. Selected Bond lengths, Bond valence sums and bond angles of $NaGdCoWO_6$ from the SXRPD refinement at room temperature.

Bond Lengths (Å)		Bond Valence Sums	
Co-O1	2.02(3)	Na	1.07(2)
Co-O2	2.12(3)	Gd	3.15(4)
Co-O3	2.12(3)	Co	2.04(3)
Co-O4	2.12(3)	W	6.08(7)
Co-O5	2.12(3)	O1	2.00(3)
Co-O6	2.07(2)	O2	1.97(3)
Co-O Average	2.09	O3	2.26(5)
W-O1	2.00(3)	O4	1.96(4)
W-O2	1.97(3)	O5	2.07(3)
W-O3	1.78(3)	O6	2.07(3)
W-O4	1.87(3)	Bond Angles (°)	
W-O5	2.17(3)	Co-O1-W	145.7(6)
W-O6	1.81(2)	Co-O2-W	148.1(6)
W-O average	1.93	Co-O3-W	153.7(6)
		Co-O4-W	154.7(6)
		Co-O5-W	142.5(4)
		Co-O6-W	151.2(4)

SI.8. $NaTbCoWO_6$:

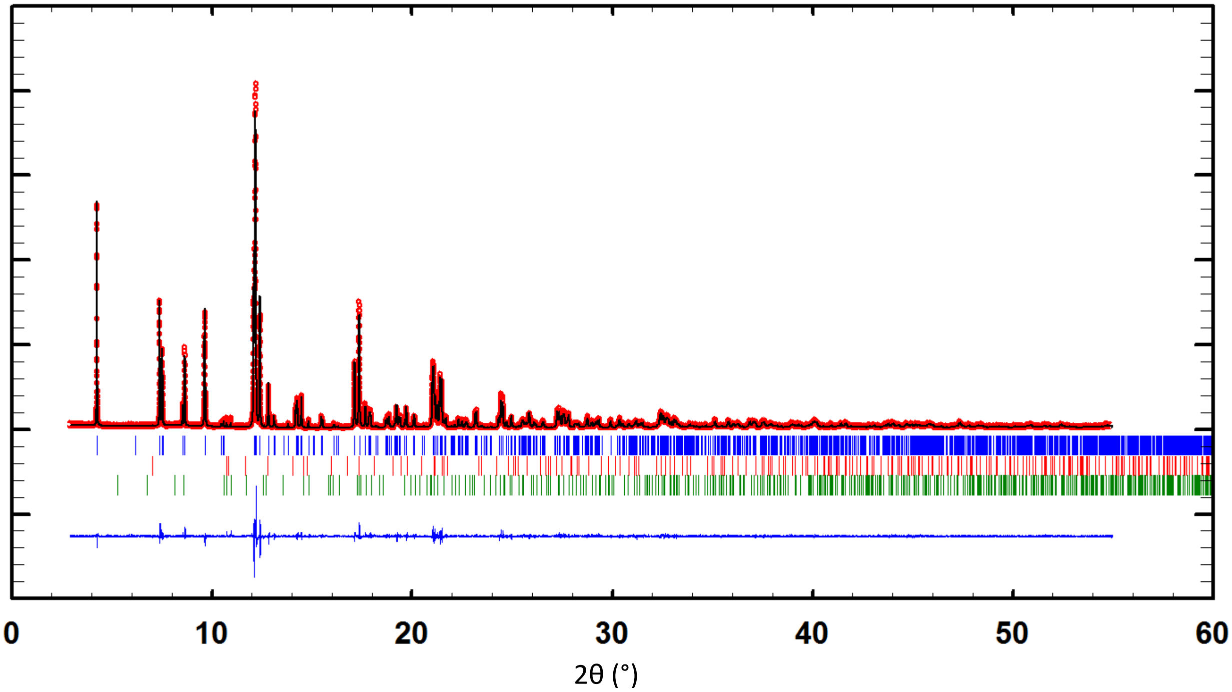

Figure S8. The SXRPD pattern refinement ($P2_1$) of the $NaTbCoWO_6$ sample, the observed pattern (red circles), the calculated patterns (black lines), and the difference lines (blue, at the bottom) are shown. Blue tick marks show allowed (*hkl*) reflections of the main phase $NaTbCoWO_6$ (99.36(20)wt%). Red tick marks stand for allowed (*hkl*) reflections of $NaTb(WO_4)_2$ (0.32(2)wt%). Green tick marks stand for allowed (*hkl*) reflections of Tb_6W (0.32(2)wt%).

Table S16. Crystallographic parameters of $NaTbCoWO_6$ from the SXRPD pattern refinement ($P2_1$) at room temperature.[h]

Atom	Wyckoff Symbol	x	y	z	B(Å^2)	Occupancy
Na	2a	0.247(4)	0.725(3)	0.001(2)	0.8(1)	1.0
Tb	2a	0.2638(5)	0.8098(9)	0.5007(3)	0.74(2)	1.0
Co	2a	0.748(1)	0.760(3)	0.2479(6)	0.38(5)	1.0
W	2a	0.7602(4)	0.75	0.7652(2)	0.54(1)	1.0
O1	2a	0.473(5)	0.549(5)	0.690(4)	0.50(8)	1.0
O2	2a	0.441(5)	0.534(5)	0.302(4)	0.50(8)	1.0
O3	2a	0.063(5)	-0.023(5)	0.216(4)	0.50(8)	1.0
O4	2a	0.043(5)	-0.063(5)	0.783(4)	0.50(8)	1.0
O5	2a	0.855(4)	0.692(5)	0.498(3)	0.50(8)	1.0
O6	2a	0.671(3)	0.757(5)	-0.012(3)	0.50(8)	1.0

[h] Space group $P2_1$, Z=2. Unit cell parameters: a= 5.38318(2) Å, b= 5.51974(5) Å, c= 7.80868(5) Å, β= 90.3017(5) °, V/Z= 116.011(1) Å^3. Discrepancy factors: χ^2 = 3.09, R_p= 12.3%, R_{wp}= 14.8%, R_{Bragg}= 2.47%.

Table S17. Selected Bond lengths, Bond valence sums and bond angles of $NaTbCoWO_6$ from the SXRPD refinement at room temperature.

Bond Lengths (Å)		Bond Valence Sums	
Co-O1	2.05(3)	Na	1.03(2)
Co-O2	2.12(3)	Tb	2.94(3)
Co-O3	2.09(3)	Co	2.07(3)
Co-O4	2.12(3)	W	6.17(7)
Co-O5	2.07(2)	O1	1.96(3)
Co-O6	2.07(2)	O2	1.90(3)
Co-O Average	2.09	O3	2.24(5)
W-O1	1.99(3)	O4	2.05(4)
W-O2	1.98(3)	O5	1.98(3)
W-O3	1.79(3)	O6	2.09(3)
W-O4	1.84(3)	Bond Angles (°)	
W-O5	2.17(2)	Co-O1-W	144.7(6)
W-O6	1.81(2)	Co-O2-W	147.4(6)
W-O average	1.93	Co-O3-W	154.7(6)
		Co-O4-W	154.1(6)
		Co-O5-W	144.6(4)
		Co-O6-W	152.9(4)

SI.9. $NaDyCoWO_6$:

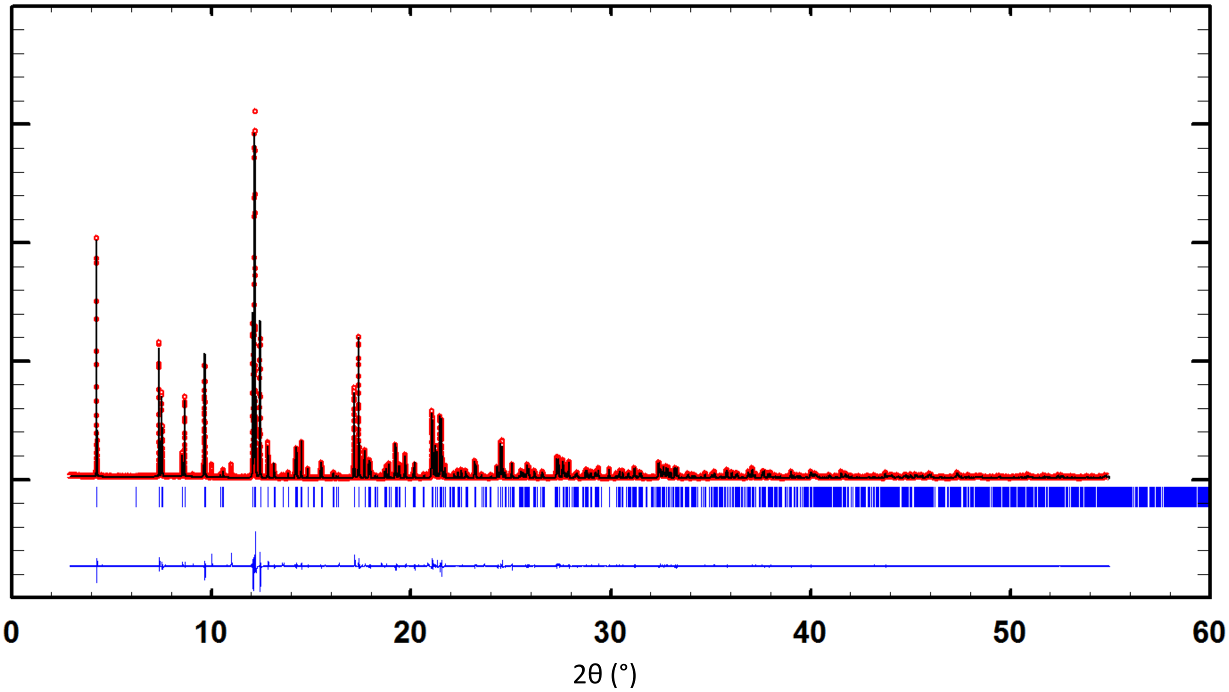

Figure S9. The SXRPD pattern refinement (*$P2_1$*) of the $NaDyCoWO_6$ sample, the observed pattern (red circles), the calculated patterns (black lines), and the difference lines (blue, at the bottom) are shown. Blue tick marks show allowed (*hkl*) reflections of the main phase $NaDyCoWO_6$.

Table S18. Crystallographic parameters of $NaDyCoWO_6$ from the SXRPD pattern refinement ($P2_1$) at room temperature.[i]

Atom	Wyckoff Symbol	x	y	z	B(Å^2)	Occupancy
Na	2a	0.244(5)	0.723(5)	0.005(3)	0.9(1)	1.0
Dy	2a	0.2646(7)	0.811(1)	0.5004(5)	0.70(2)	1.0
Co	2a	0.750(2)	0.758(5)	0.250(1)	0.57(4)	1.0
W	2a	0.7617(5)	0.75	0.7646(3)	0.579(9)	1.0
O1	2a	0.475(7)	0.555(8)	0.699(6)	0.46(7)	1.0
O2	2a	0.447(8)	0.526(8)	0.310(6)	0.46(7)	1.0
O3	2a	0.078(8)	-0.047(7)	0.220(6)	0.46(7)	1.0
O4	2a	0.053(7)	-0.065(8)	0.773(6)	0.46(7)	1.0
O5	2a	0.854(6)	0.711(7)	0.505(4)	0.46(7)	1.0
O6	2a	0.678(6)	0.771(8)	-0.010(4)	0.46(7)	1.0

[i] Space group $P2_1$, Z=2. Unit cell parameters: a= 5.36328(4) Å, b= 5.52198(4) Å, c= 7.79760(4) Å, β= 90.2986(4) °, V/Z= 115.465(1) Å^3. Discrepancy factors: χ^2 = 23.4, R_p= 12.0%, R_{wp}= 15.6%, R_{Bragg}= 3.18%.

Table S19. Selected Bond lengths, Bond valence sums and bond angles of $NaDyCoWO_6$ from the SXRPD refinement at room temperature.

Bond Lengths (Å)		Bond Valence Sums	
Co-O1	2.08(5)	Na	0.85(1)
Co-O2	2.12(5)	Dy	2.72(3)
Co-O3	2.08(5)	Co	2.09(2)
Co-O4	2.08(5)	W	6.02(6)
Co-O5	2.08(4)	O1	1.91(3)
Co-O6	2.06(3)	O2	1.83(3)
Co-O Average	2.08	O3	2.05(4)
W-O1	1.94(4)	O4	1.95(3)
W-O2	1.97(4)	O5	1.90(2)
W-O3	1.86(4)	O6	2.04(3)
W-O4	1.87(4)	Bond Angles (°)	
W-O5	2.10(4)	Co-O1-W	147.8(5)
W-O6	1.82(3)	Co-O2-W	146.5(5)
W-O average	1.93	Co-O3-W	147.6(5)
		Co-O4-W	152.9(5)
		Co-O5-W	147.8(3)
		Co-O6-W	154.2(3)

SI.10. $NaHoCoWO_6$:

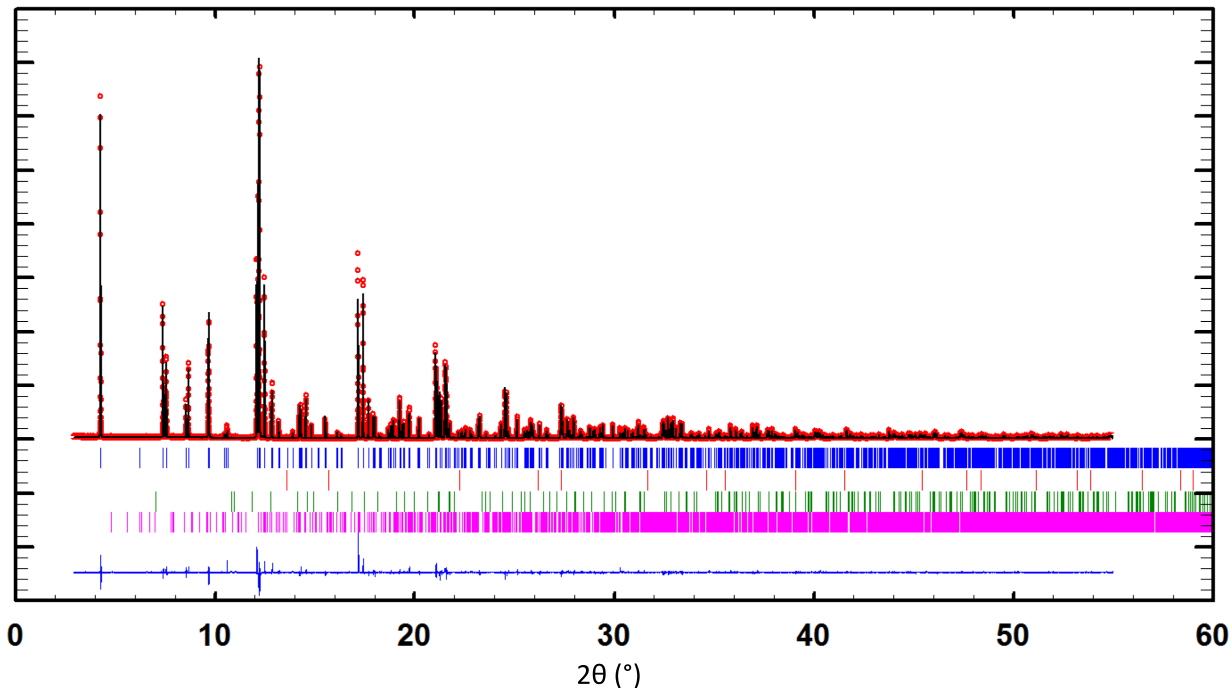

Figure S10. The SXRPD pattern refinement ($P2_1$) of the $NaHoCoWO_6$ sample, the observed pattern (red circles), the calculated patterns (black lines), and the difference lines (blue, at the bottom) are shown. Blue tick marks show allowed (*hkl*) reflections of the main phase $NaHoCoWO_6$ (99.19(22)wt%). Red tick marks stand for allowed (*hkl*) reflections of CoO (0.35(3)wt%). Green tick marks stand for allowed (*hkl*) reflections of $NaHo(WO_4)_2$ (0.13(1)wt%). Purple tick marks stand for allowed (*hkl*) reflections of $Na_2WO_4{\cdot}2H_2O$ (0.33(3)wt%).

Table S20. Crystallographic parameters of $NaHoCoWO_6$ from the SXRPD pattern refinement ($P2_1$) at room temperature.^{j}

Atom	Wyckoff Symbol	x	y	z	B(Å^2)	Occupancy
Na	2a	0.244(4)	0.718(4)	0.003(2)	0.4(1)	0.786(9)
Ho	2a	0.2655(4)	0.8123(8)	0.5006(3)	0	1.0
Co	2a	0.750(1)	0.759(4)	0.2488(6)	0.80(4)	1.0
W	2a	0.7617(3)	0.75	0.7647(2)	0	1.0
O1	2a	0.466(5)	0.553(5)	0.701(3)	0.50(6)	1.0
O2	2a	0.449(5)	0.524(5)	0.297(3)	0.50(6)	1.0
O3	2a	0.088(5)	-0.058(5)	0.223(3)	0.50(6)	1.0
O4	2a	0.066(5)	-0.077(5)	0.772(3)	0.50(6)	1.0
O5	2a	0.844(4)	0.723(5)	0.506(2)	0.50(6)	1.0
O6	2a	0.680(4)	0.780(5)	-0.014(2)	0.50(6)	1.0

^{j}Space group $P2_1$, Z=2. Unit cell parameters: a= 5.34661(1) Å, b= 5.52114(1) Å, c= 7.78969(2) Å, β= 90.2836(2) °, V/Z= 114.972(0) Å^3. Discrepancy factors: χ^2 = 3.40, R_p= 13.8%, R_{wp}= 16.5%, R_{Bragg}= 5.46%. Preferred Orientation 0.906(1). Anisotropic displacement parameters: (Ho) $B11$= 0.0073(3), $B22$= 0.0049(2), $B33$= 0.0046(1), $B12$= -0.0003(3), $B13$= -0.0006(1), $B23$= -0.0001(1); (W) $B11$= 0.0060(2), $B22$= 0.0044(2), $B33$= 0.00402(9), $B12$= 0.0001(2), $B13$=0.0000(1), $B23$= 0.0002(1).

Table S21. Selected Bond lengths, Bond valence sums and bond angles of $NaHoCoWO_6$ from the SXRPD refinement at room temperature.

Bond Lengths (Å)		Bond Valence Sums	
Co-O1	2.03(3)	Na	1.06(1)
Co-O2	2.10(3)	Ho	2.79(2)
Co-O3	2.08(3)	Co	2.11(2)
Co-O4	2.10(3)	W	6.03(6)
Co-O5	2.08(2)	O1	1.95(3)
Co-O6	2.08(2)	O2	1.93(3)
Co-O Average	2.08	O3	1.97(3)
W-O1	1.98(3)	O4	1.91(3)
W-O2	1.95(3)	O5	1.91(2)
W-O3	1.88(3)	O6	2.08(3)
W-O4	1.89(3)	Bond Angles (°)	
W-O5	2.07(2)	Co-O1-W	147.6(5)
W-O6	1.79(2)	Co-O2-W	151.4(5)
W-O average	1.93	Co-O3-W	143.7(5)
		Co-O4-W	147.8(5)
		Co-O5-W	151.8(3)
		Co-O6-W	154.0(3)

SI.11. NaErCoWO$_6$:

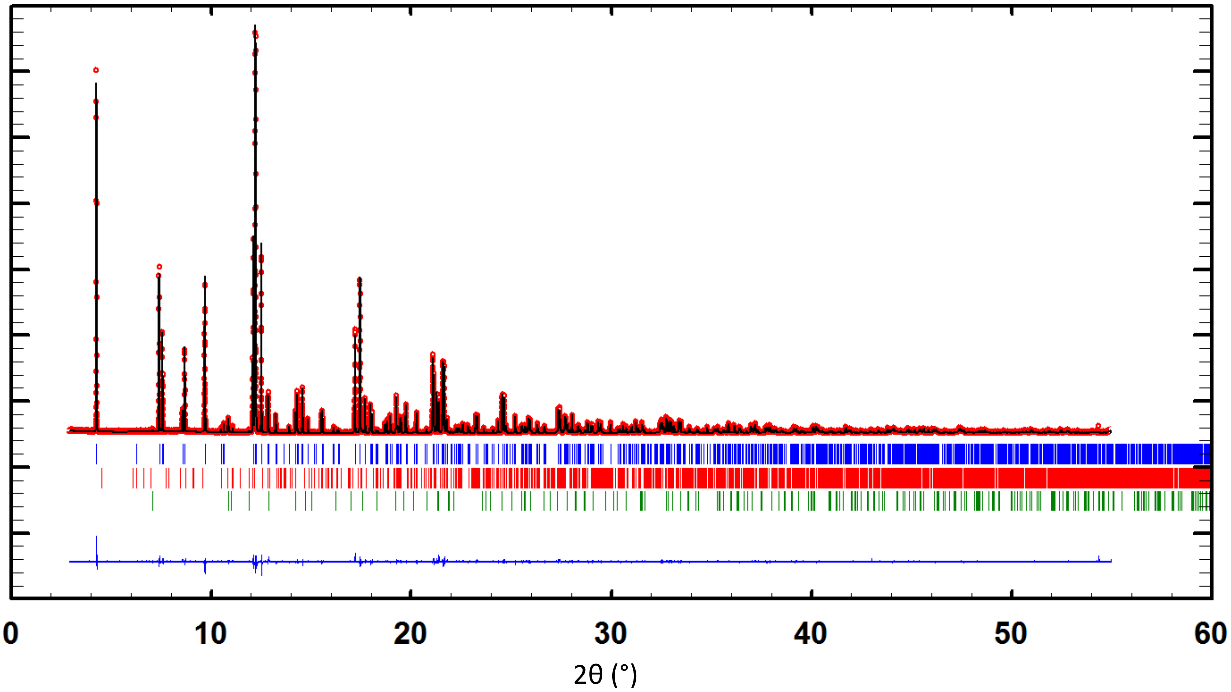

Figure S11. The SXRPD pattern refinement (*P2$_1$*) of the NaErCoWO$_6$ sample, the observed pattern (red circles), the calculated patterns (black lines), and the difference lines (blue, at the bottom) are shown. Blue tick marks show allowed (*hkl*) reflections of the main phase NaErCoWO$_6$ (96.29(18)wt%). Red tick marks stand for allowed (*hkl*) reflections of Er$_2$WO$_6$ (0.47(2)wt%). Green tick marks stand for allowed (*hkl*) reflections of NaEr(WO$_4$)$_2$ (3.24(4)wt%).

Table S22. Crystallographic parameters of $NaErCoWO_6$ from the SXRPD pattern refinement ($P2_1$) at room temperature.[k]

Atom	Wyckoff Symbol	x	y	z	B(Å^2)	Occupancy
Na	2a	0.247(2)	0.783(2)	0.001(1)	1.3(1)	1.0
Er	2a	0.2663(3)	0.6854(4)	0.5001(2)	0.52(1)	1.0
Co	2a	0.7496(8)	0.741(2)	0.2505(4)	0.54(3)	1.0
W	2a	0.7629(2)	0.75	0.7638(1)	0.467(8)	1.0
O1	2a	0.560(3)	0.473(3)	0.684(3)	0.49(6)	1.0
O2	2a	0.530(3)	0.446(3)	0.314(2)	0.49(6)	1.0
O3	2a	-0.061(3)	0.070(3)	0.230(2)	0.49(6)	1.0
O4	2a	-0.082(3)	0.054(3)	0.778(2)	0.49(6)	1.0
O5	2a	0.856(3)	0.787(3)	0.504(2)	0.49(6)	1.0
O6	2a	0.673(2)	0.720(3)	-0.013(2)	0.49(6)	1.0

[k] Space group $P2_1$, Z=2. Unit cell parameters: a= 5.33276(1) Å, b= 5.51783(1) Å, c= 7.78224(2) Å, β= 90.2758(1) °, V/Z= 114.496(0) Å^3. Discrepancy factors: χ^2 = 2.39, R_p= 11.1%, R_{wp}= 13.9%, R_{Bragg}= 2.63%.

Table S23. Selected Bond lengths, Bond valence sums and bond angles of $NaErCoWO_6$ from the SXRPD refinement at room temperature.

Bond Lengths (Å)		Bond Valence Sums	
Co-O1	2.15(2)	Na	0.91(1)
Co-O2	2.07(2)	Er	2.90(3)
Co-O3	2.09(2)	Co	2.07(2)
Co-O4	2.07(2)	W	5.88(6)
Co-O5	2.06(2)	O1	1.86(3)
Co-O6	2.09(1)	O2	1.91(3)
Co-O Average	2.09	O3	1.98(3)
W-O1	1.97(2)	O4	2.01(3)
W-O2	1.99(2)	O5	1.90(2)
W-O3	1.87(2)	O6	2.10(3)
W-O4	1.87(2)	Bond Angles (°)	
W-O5	2.10(2)	Co-O1-W	143.9(4)
W-O6	1.81(1)	Co-O2-W	143.1(4)
W-O average	1.94	Co-O3-W	150.5(4)
		Co-O4-W	145.2(4)
		Co-O5-W	147.5(3)
		Co-O6-W	151.9(3)

SI.12. $NaYbCoWO_6$:

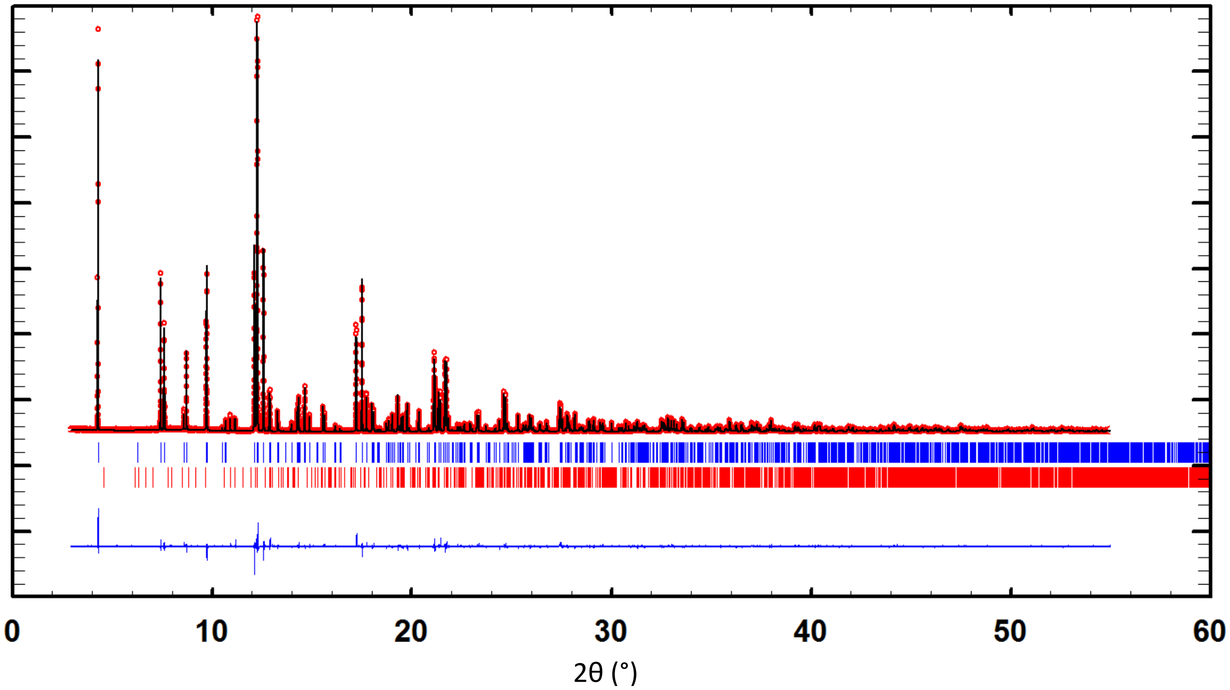

Figure S11. The SXRPD pattern refinement (*$P2_1$*) of the $NaYbCoWO_6$ sample, the observed pattern (red circles), the calculated patterns (black lines), and the difference lines (blue, at the bottom) are shown. Blue tick marks show allowed (*hkl*) reflections of the main phase $NaYbCoWO_6$ (97.89(20)wt%). Red tick marks stand for allowed (*hkl*) reflections of Yb_2WO_6 (2.11(3)wt%).

Table S24. Crystallographic parameters of $NaYbCoWO_6$ from the SXRPD pattern refinement ($P2_1$) at room temperature.[1]

Atom	Wyckoff Symbol	x	y	z	B(Å^2)	Occupancy
Na	2a	0.250(3)	0.785(2)	0.005(2)	0.4(1)	1.0
Yb	2a	0.2676(3)	0.6828(5)	0.5003(2)	0.44(1)	1.0
Co	2a	0.749(1)	0.741(2)	0.2510(6)	0.36(4)	1.0
W	2a	0.7633(3)	0.75	0.7632(2)	0.386(9)	1.0
O1	2a	0.562(5)	0.467(4)	0.672(3)	0.53(7)	1.0
O2	2a	0.536(4)	0.444(4)	0.323(3)	0.53(7)	1.0
O3	2a	-0.048(4)	0.067(4)	0.225(3)	0.53(7)	1.0
O4	2a	-0.081(5)	0.044(4)	0.775(3)	0.53(7)	1.0
O5	2a	0.859(4)	0.802(4)	0.506(3)	0.53(7)	1.0
O6	2a	0.669(3)	0.726(4)	-0.015(2)	0.53(7)	1.0

[1] Space group $P2_1$, Z=2. Unit cell parameters: a= 5.30692(1) Å, b= 5.50727(1) Å, c= 7.76784(2) Å, β= 90.2815(2) °, V/Z= 113.513(0) Å^3. Discrepancy factors: χ^2 = 2.77, R_p= 13.2%, R_{wp}= 15.6%, R_{Bragg}= 4.34%.

Table S25. Selected Bond lengths, Bond valence sums and bond angles of NaYbCoWO$_6$ from the SXRPD refinement at room temperature.

Bond Lengths (Å)		Bond Valence Sums	
Co-O1	2.16(3)	Na	0.96(1)
Co-O2	2.07(3)	Yb	3.04(3)
Co-O3	2.11(3)	Co	1.99(2)
Co-O4	2.08(3)	W	6.12(7)
Co-O5	2.09(2)	O1	1.85(3)
Co-O6	2.11(2)	O2	1.91(3)
Co-O Average	2.10	O3	2.12(4)
W-O1	2.01(2)	O4	2.14(4)
W-O2	2.02(2)	O5	1.95(3)
W-O3	1.82(2)	O6	2.15(3)
W-O4	1.82(2)	Bond Angles (°)	
W-O5	2.09(2)	Co-O1-W	139.0(5)
W-O6	1.80(2)	Co-O2-W	139.3(5)
W-O average	1.93	Co-O3-W	153.4(5)
		Co-O4-W	147.4(5)
		Co-O5-W	144.7(4)
		Co-O6-W	151.5(4)

Part II: Joint Refinements

SII.1. $NaYCoWO_6$:

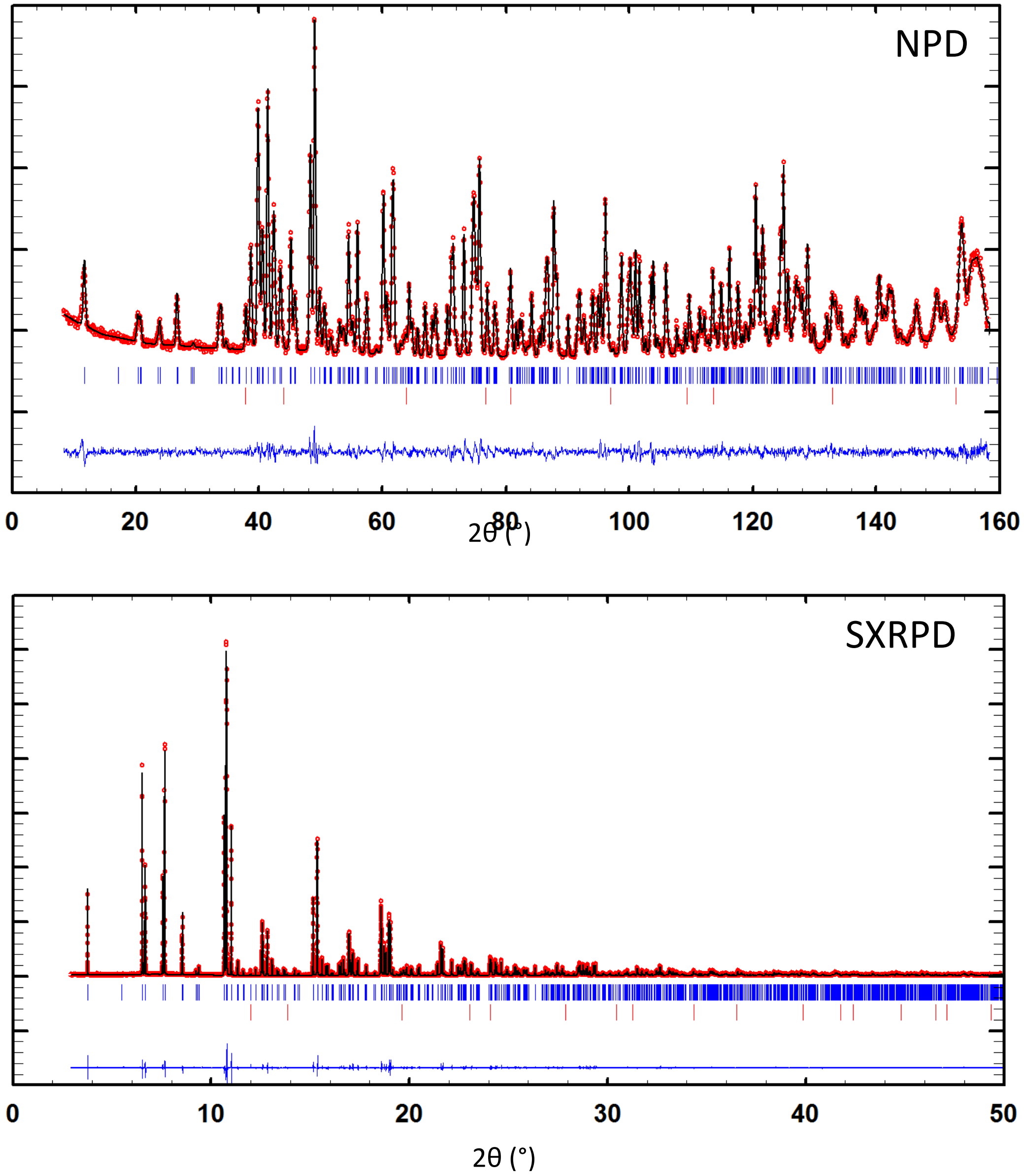

Figure S12. The joint refinement (*$P2_1$*) of the $NaYCoWO_6$ sample, the NPD pattern is on the top and the SXRPD pattern is at the bottom. In both patterns, the observed patterns (red circles), the calculated patterns (black lines), and the difference lines (blue, at the bottom) are shown. Blue tick marks show allowed (*hkl*) reflections of the main phase $NaYCoWO_6$ (99.45(57)wt% from NPD pattern). Red tick marks stand for allowed (*hkl*) reflections of CoO (0.55(4)wt% from NPD pattern).

Table S26. Crystallographic parameters of $NaYCoWO_6$ from the joint refinement (*$P2_1$*) at room temperature.[m]

Atom	Wyckoff Symbol	x	y	z	B(Å^2)	Occupancy
Na	2a	0.250(2)	0.715(2)	0.002(1)	1.03(8)	1.0
Y	2a	0.2658(5)	0.8129(6)	0.5005(3)	0.19(2)	1.0
Co	2a	0.7497(8)	0.759(2)	0.2487(5)	0.06(3)	1.0
W	2a	0.7624(2)	0.75	0.7642(1)	0.022(7)	1.0
O1	2a	0.465(1)	0.555(2)	0.6862(7)	0.32(1)	1.0
O2	2a	0.439(1)	0.526(1)	0.3146(8)	0.32(1)	1.0
O3	2a	0.077(1)	-0.051(1)	0.2159(7)	0.32(1)	1.0
O4	2a	0.053(1)	-0.070(2)	0.7787(7)	0.32(1)	1.0
O5	2a	0.855(1)	0.713(1)	0.5050(8)	0.32(1)	1.0
O6	2a	0.673(1)	0.778(1)	-0.0114(7)	0.32(1)	1.0

[m] Space group $P2_1$, Z=2. Unit cell parameters: a= 5.34712 Å, b= 5.52411 Å, c= 7.78938 Å, β= 90.29462 °, V/Z= 115.04 Å^3. Discrepancy factors: (NPD) χ^2 = 2.39, R_p= 7.92%, R_{wp}= 8.36%, R_{Bragg}= 2.48%; (SXRPD) χ^2 = 1.68, R_p= 11.7%, R_{wp}= 14.0%, R_{Bragg}= 2.29%.

Table S27. Selected Bond lengths, Bond valence sums and bond angles of $NaYCoWO_6$ from the joint refinement at room temperature.

Bond Lengths (Å)		Bond Valence Sums	
Co-O1	2.06(1)	Na	0.926(8)
Co-O2	2.16(1)	Y	3.01(1)
Co-O3	2.06(1)	Co	2.05(1)
Co-O4	2.11(1)	W	5.88(3)
Co-O5	2.087(9)	O1	1.93(1)
Co-O6	2.067(7)	O2	1.90(1)
Co-O Average	2.09	O3	1.98(2)
W-O1	2.013(7)	O4	2.00(2)
W-O2	1.965(7)	O5	1.95(1)
W-O3	1.877(7)	O6	2.10(1)
W-O4	1.848(7)	Bond Angles (°)	
W-O5	2.092(7)	Co-O1-W	142.2(4)
W-O6	1.822(5)	Co-O2-W	143.8(4)
W-O average	1.936	Co-O3-W	146.2(4)
		Co-O4-W	151.3(4)
		Co-O5-W	147.9(2)
		Co-O6-W	152.1(2)

SII.2. NaTbCoWO$_6$:

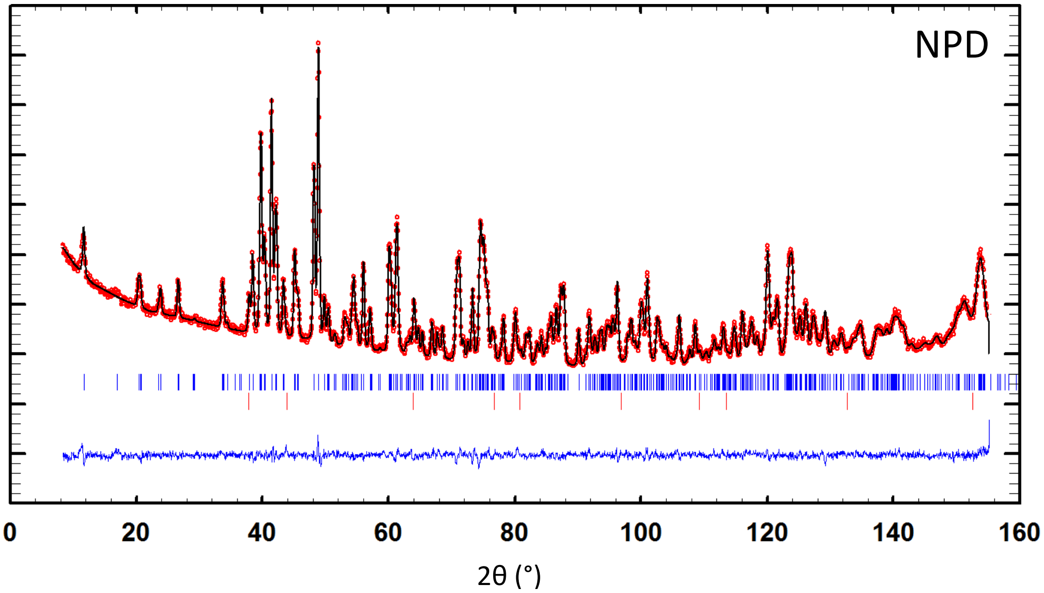

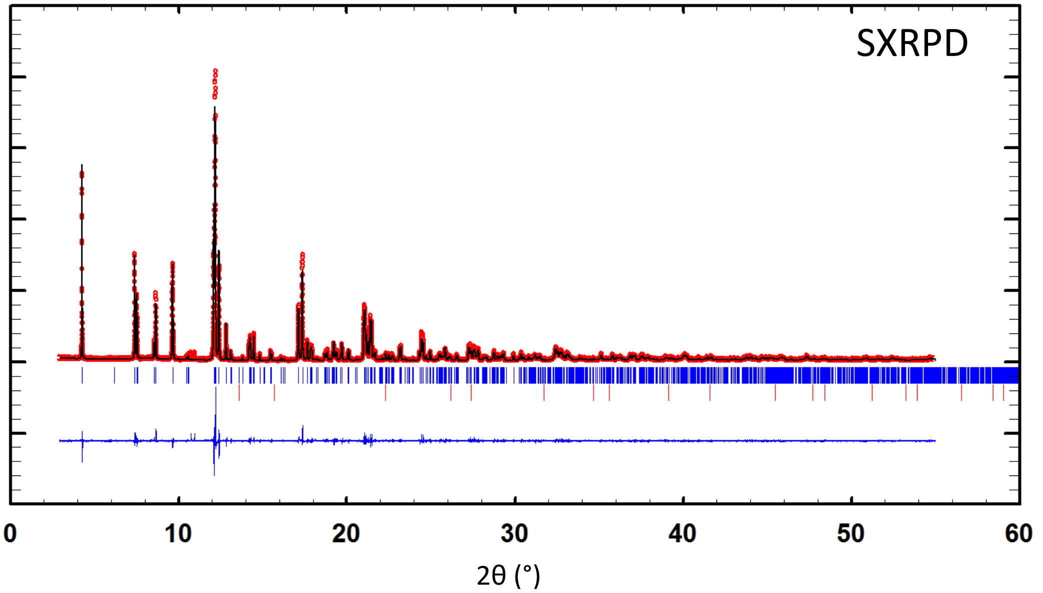

Figure S13. The joint refinement (*P2$_1$*) of the NaTbCoWO$_6$ sample, the NPD pattern is on the top and the SXRPD pattern is at the bottom. In both patterns, the observed patterns (red circles), the calculated patterns (black lines), and the difference lines (blue, at the bottom) are shown. Blue tick marks show allowed (*hkl*) reflections of the main phase NaTbCoWO$_6$ (99.71(54)wt% from NPD pattern). Red tick marks stand for allowed (*hkl*) reflections of CoO (0.29(3)wt% from NPD pattern).

Table S28. Crystallographic parameters of $NaTbCoWO_6$ from the joint refinement ($P2_1$) at room temperature.[n]

Atom	Wyckoff Symbol	x	y	z	B(Å^2)	Occupancy
Na	2a	0.250(2)	0.719(2)	0.001(2)	0.68(8)	1.0
Tb	2a	0.2637(6)	0.810(1)	0.5003(4)	0.38(3)	1.0
Co	2a	0.748(2)	0.761(3)	0.2482(8)	0.07(6)	1.0
W	2a	0.7606(5)	0.75	0.7653(2)	0.19(2)	1.0
O1	2a	0.470(1)	0.559(2)	0.6905(9)	0.30(1)	1.0
O2	2a	0.441(1)	0.527(2)	0.313(1)	0.30(1)	1.0
O3	2a	0.073(1)	-0.044(2)	0.2173(9)	0.30(1)	1.0
O4	2a	0.049(1)	-0.063(2)	0.7799(9)	0.30(1)	1.0
O5	2a	0.850(1)	0.718(2)	0.506(1)	0.30(1)	1.0
O6	2a	0.675(1)	0.777(2)	-0.0108(9)	0.30(1)	1.0

[n] Space group $P2_1$, Z=2. Unit cell parameters: a= 5.38318 Å, b= 5.51974 Å, c= 7.80868 Å, β= 90.3017 °, V/Z= 116.011 Å^3. Discrepancy factors: (NPD) χ^2 = 2.99, R_p= 7.55%, R_{wp}= 7.59%, R_{Bragg}= 2.33%; (SXRPD) χ^2 = 3.27, R_p= 12.6%, R_{wp}= 15.2%, R_{Bragg}= 3.11%.

Table S29. Selected Bond lengths, Bond valence sums and bond angles of $NaTbCoWO_6$ from the joint refinement at room temperature.

Bond Lengths (Å)		Bond Valence Sums	
Co-O1	2.07(2)	Na	0.880(9)
Co-O2	2.15(2)	Tb	2.95(1)
Co-O3	2.06(2)	Co	2.05(2)
Co-O4	2.11(2)	W	6.02(3)
Co-O5	2.09(1)	O1	2.00(2)
Co-O6	2.057(9)	O2	1.91(2)
Co-O Average	2.09	O3	2.02(2)
W-O1	1.969(9)	O4	1.94(2)
W-O2	1.968(9)	O5	1.92(1)
W-O3	1.856(9)	O6	2.11(2)
W-O4	1.864(9)	Bond Angles (°)	
W-O5	2.093(9)	Co-O1-W	143.5(5)
W-O6	1.814(8)	Co-O2-W	144.3(5)
W-O average	1.927	Co-O3-W	148.6(5)
		Co-O4-W	153.3(6)
		Co-O5-W	149.2(3)
		Co-O6-W	153.3(3)

SII.3. NaHoCoWO$_6$:

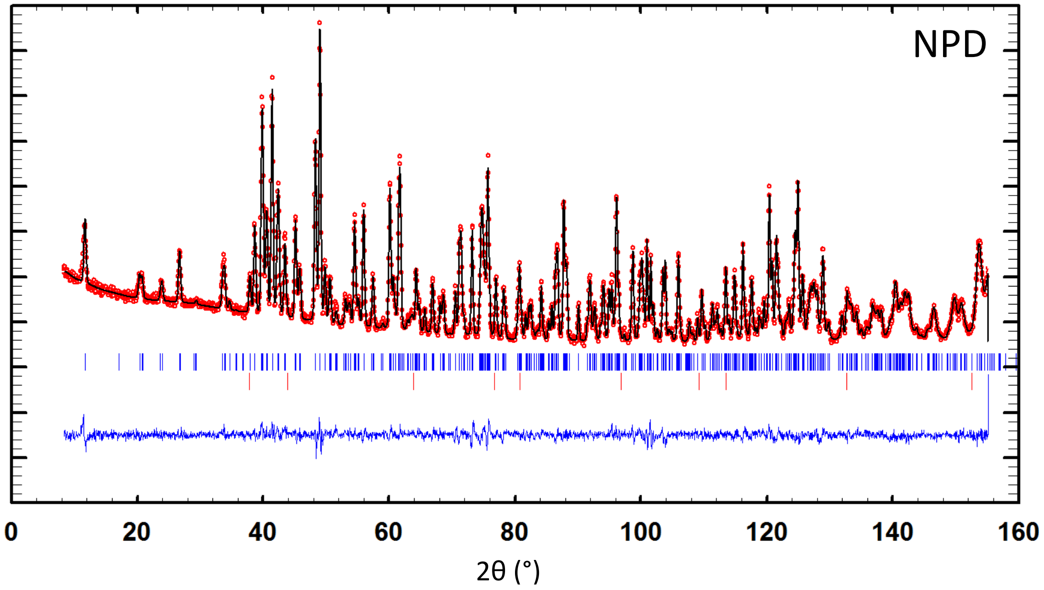

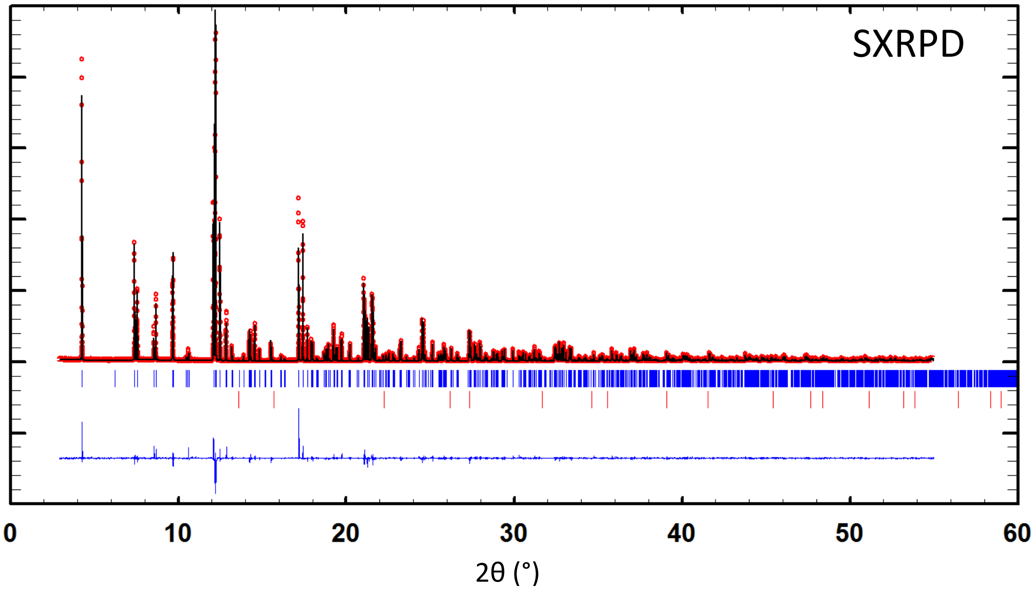

Figure S14. The joint refinement (*P2$_1$*) of the NaHoCoWO$_6$ sample, the NPD pattern is on the top and the SXRPD pattern is at the bottom. In both patterns, the observed patterns (red circles), the calculated patterns (black lines), and the difference lines (blue, at the bottom) are shown. Blue tick marks show allowed (*hkl*) reflections of the main phase NaHoCoWO$_6$ (99.70(75)wt% from NPD pattern). Red tick marks stand for allowed (*hkl*) reflections of CoO (0.30(4)wt% from NPD pattern).

Table S30. Crystallographic parameters of $NaHoCoWO_6$ from the joint refinement (*$P2_1$*) at room temperature.[o]

Atom	Wyckoff Symbol	x	y	z	B(Å^2)	Occupancy
Na	2a	0.249(2)	0.712(2)	0.002(1)	1.3(1)	1.0
Ho	2a	0.2656(4)	0.8120(6)	0.5005(2)	0.20(2)	1.0
Co	2a	0.749(1)	0.755(3)	0.2498(6)	0.25(5)	1.0
W	2a	0.7615(3)	0.75	0.7645(2)	0.04(1)	1.0
O1	2a	0.465(1)	0.554(2)	0.6876(9)	0.68(2)	1.0
O2	2a	0.440(1)	0.527(2)	0.315(1)	0.68(2)	1.0
O3	2a	0.076(1)	-0.051(2)	0.2172(8)	0.68(2)	1.0
O4	2a	0.055(1)	-0.071(2)	0.7781(9)	0.68(2)	1.0
O5	2a	0.854(1)	0.713(2)	0.505(1)	0.68(2)	1.0
O6	2a	0.673(1)	0.778(2)	-0.0120(9)	0.68(2)	1.0

[o] Space group *$P2_1$*, Z=2. Unit cell parameters: a= 5.34661 Å, b= 5.52114 Å, c= 7.78969 Å, β= 90.28355 °, V/Z= 114.972 Å^3. Discrepancy factors: (NPD) χ^2 = 2.19, R_p= 9.84%, R_{wp}= 9.76%, R_{Bragg}= 3.24%; (SXRPD) χ^2 = 3.75, R_p= 14.6%, R_{wp}= 17.3%, R_{Bragg}= 6.76%.

Table S31. Selected Bond lengths, Bond valence sums and bond angles of $NaHoCoWO_6$ from the joint refinement at room temperature.

Bond Lengths (Å)		Bond Valence Sums	
Co-O1	2.07(2)	Na	0.915(9)
Co-O2	2.15(1)	Ho	3.05(2)
Co-O3	2.06(1)	Co	2.06(2)
Co-O4	2.10(2)	W	5.89(3)
Co-O5	2.07(1)	O1	1.94(2)
Co-O6	2.082(8)	O2	1.93(2)
Co-O Average	2.09	O3	1.97(2)
W-O1	2.008(8)	O4	2.01(2)
W-O2	1.968(8)	O5	1.96(1)
W-O3	1.879(8)	O6	2.12(2)
W-O4	1.853(8)	Bond Angles (°)	
W-O5	2.094(8)	Co-O1-W	142.9(4)
W-O6	1.813(7)	Co-O2-W	143.5(4)
W-O average	1.936	Co-O3-W	147.2(4)
		Co-O4-W	150.9(5)
		Co-O5-W	148.2(3)
		Co-O6-W	152.2(3)